NANO-ENGINEERED POLYMER COMPOSITE FOR STRUCTURAL HEALTH MONITORING IN FIBER-REINFORCED POLYMER STRUCTURES

TING YUI WONG

PhD

The Hong Kong Polytechnic University

2026

The Hong Kong Polytechnic University

Department of Civil and Environmental Engineering

Nano-engineered Polymer Composite for Structural Health Monitoring in Fiber-reinforced Polymer Structures

Ting Yui Wong

A thesis submitted in partial fulfilment of the requirements for the degree of

Doctor of Philosophy

Aug 2025

CERTIFICATE OF ORIGINALITY

I hereby declare that this thesis is my own work and that, to the best of my knowledge and belief, it reproduces no material previously published or written, nor material that has been accepted for the award of any other degree or diploma except where due acknowledgement has been made in the text.

_____ (Signed)

Ting Yui Wong (Name of student)

This work is dedicated to my wife, who has been a constant source of strength, and my younger self, who decided to embark on this challenging journey.

ABSTRACT

Fiber reinforced polymer (FRP) composites have found their structural applications in many sectors like aerospace, automotive, marine, and construction because of their high strength-to-weight ratio, good resistance to corrosion and fatigue, and flexibility in design. Durable and cost-effective monitoring techniques are required to help gain long-term observations of structural deterioration and provide solutions for structural health monitoring (SHM). Self-sensing polymer nanocomposites are alternative SHM methodology with attractive advantages including inherently integrated nature with trivial weight penalty, great potential of multifunctionality, and capability to detect matrix-dominated damages.

Despite the excellence and great potential shown in using self-sensing nanocomposites for SHM in FRP composites, more work is required to promote the application of this methodology in real-life industrial structures. The aim of this PhD study is to develop SHM methodology for FRP structures using nano-engineered polymer composites through a mechanistic study on the piezoresistivity of carbon nanotube (CNT)/epoxy nanocomposites and investigations into the application of CNT/epoxy nanocomposites for self-sensing strain and damage in FRP structures.

This study started with investigation on the effect of curing conditions on the piezoresistivity of CNT/epoxy nanocomposites under tensile loading. CNT/epoxy nanocomposite samples were fabricated using different curing cycles, including room temperature curing followed by post-curing and direct heat curing at temperatures ranging from 40 to 100 °C. Quasi-static tensile tests with simultaneous electrical resistance measurements revealed that the piezoresistivity of the nanocomposites is significantly affected by the curing conditions. Samples cured at room temperature exhibited non-monotonic piezoresistive behavior, with an inversion in piezoresistivity occurring at critical strains. In contrast, samples

cured at elevated temperature demonstrated monotonic piezoresistive behavior until failure. The monotony of the piezoresistive behavior and the critical strain were found to be independent of the nanofiller content.

The microstructural origin of the nonmonotonic piezoresistive behavior in the nanocomposites was investigated using coarse-grained molecular dynamics (CGMD) simulations. The experimental results of the piezoresistive behavior of CNT/epoxy nanocomposites transitioning from nonmonotonic to monotonic with increasing curing temperature were reproduced by the CGMD simulations. Analysis revealed that the inter-nanofiller junction geometry governs the monotony of the piezoresistive behavior. Mechanistically, monotonically increasing resistance responses under tension can be achieved by promoting active diffusion that causes van der Waals force-driven barrier crossing of nanofillers (resulting in direct contact between nanofillers, e.g., at elevated curing temperatures) during curing; thus, during deformation, nanofillers primarily move away from one another. Conversely, suppressing diffusion during curing causes barrier crossing of nanofillers, which results in resistance reduction, under deformation owing to stress-driven local rearrangement of polymer molecules in heterogeneous shear transformation zones. The molecular structure of the polymer matrix also influenced nanofiller diffusion, modulating the inter-nanofiller junction geometry and piezoresistive behavior. The mechanistic insights provided by this study can guide the design of next-generation, advanced strain-sensing materials in the future.

Then, the piezoresistive behaviors of glass fiber reinforced polymer (GFRP) composite laminates and tubes using CNT-dispersed epoxy as matrix were investigated, focusing on the effect of fiber orientation. CNT/GFRP laminates and tubes with different fiber orientations were prepared using a wet lay-up process and a filament winding process, respectively. The results revealed that the piezoresistive behavior of CNT/GFRP composites is significantly

affected by fiber orientation. Laminates with fibers oriented nearly perpendicular to the tensile direction exhibited a monotonic increase in resistance with strain, while those with off-axis fibers, i.e. oriented around 45°, showed a nonmonotonic response with a relatively low critical strain. Laminates with fibers aligned nearly parallel to the tensile axis demonstrated a nonmonotonic response with higher critical strains. Similarly, tubes with fibers oriented parallel or perpendicular to the tensile direction displayed monotonic piezoresistivity, whereas those with off-axis fibers exhibited a nonmonotonic response.

The microstructural origin of the fiber orientation dependent piezoresistive behavior in CNT/GFRP composites was investigated using a multiscale finite element analysis (FEA) based electromechanical framework. The model included microscale for unit cells of yarn and matrix, and mesoscale for geometric pattern of yarn and matrix, involving both mechanical and electrical domains. Digital image correlation (DIC) and FEA revealed that the strain distribution heterogeneity varies with fiber orientation, and localized transverse compression may lead to the inversion in piezoresistivity. The means of tunneling distance provided microscopic insights into the changes in the CNT network during the transition from positive to negative piezoresistivity, which was accompanied by increase and then decrease in tunneling distance between CNTs, for composites with off-axis fibers. The monotonic or nearly monotonic positive piezoresistive behaviors of composites with parallel or perpendicular fibers were attributed to the increase in tunneling distance under CNT separation. The study highlighted the intricate relationship between fiber orientation, deformation mechanisms, and CNT network reconfiguration in CNT/GFRP composites under tensile loading, contributing to the design of tailored composites with optimized piezoresistive performance for SHM applications.

The nonmonotonic piezoresistive behavior of [±55] GFRP composites, which are widely used in real-world structures, poses challenges for self-sensing. Design of CNT/GFRP

composites with desired monotonic piezoresistive behavior using the multiscale FE modeling was attempted with support of experimental validations. The effects of yarn width, matrix Poisson's ratio, and stacking sequence on the piezoresistive response of the composites were explored. Numerical results suggested that narrower yarns and lower matrix Poisson's ratios improve the monotony of the piezoresistive behavior, but these parameters alone may be insufficient for achieving a monotonic response. The inclusion of [0] layer was found to be crucial for obtaining monotonic piezoresistive behavior. Experimental validations using multi-layered composite tubes with different stacking sequences confirmed the effectiveness of the [0] layer in improving the monotony of the piezoresistive response. The [±55/90/0] stacking sequence exhibited the best self-sensing performance with a monotonic piezoresistive behavior, demonstrating its potential for practical sensing applications. The resistance change-stress relationships of the CNT/GFRP composite tubes revealed two distinct stages: an initial smooth increase in resistance associated with elastic deformation, followed by fluctuations and step increases indicating damage initiation and propagation. This study highlighted the importance of fiber orientation and stacking sequence in tailoring the piezoresistive behavior of CNT/GFRP composites for SHM applications.

In summary, this PhD study has performed in-depth investigations on the piezoresistive properties of CNT/epoxy nanocomposites and the development of self-sensing CNT/GFRP composite structures. The study contributes to the development of advanced composites with optimized piezoresistive performance for SHM applications.

LIST OF PUBLICATIONS

Journal Papers

Wong, T. Y., Yu, T., & Zou, F. (2023). Effect of curing condition on the piezoresistivity of multi-walled carbon nanotube/epoxy nanocomposites. *Composites Communications*, 39, 101557.

Wong, T. Y., Lin, K., Yu, T., & Zou, F. (2025). Microstructural Origin of Nonmonotonic Piezoresistivity in Polymer Nanocomposites. *Advanced science*, e04381.

Wong, T. Y., Yu, T., & Zou, F. On the Piezoresistivity of Conductive Nanofiller-Filled Fiber-Reinforced Polymer Composites: Effect of Fiber Orientation. (*Under review*).

Wong, T. Y., Yu, T., & Zou, F. Unravelling Fiber Orientation Dependent Piezoresistivity of Carbon Nanotube/Epoxy/Fiberglass Composites for Designing Self-sensing Fiber-reinforced Polymer Composite Structures. (*Under preparation*).

Conference Presentations/Publications

Wong, T. Y., Zou, F., Yu, T. (2024). "Microstructural origin of non-monotonic piezoresistivity in CNT/epoxy nanocomposite", *APS March Meeting 2024*, 3-8 March 2024, Minneapolis, Minnesota, USA.

Wong, T. Y., Zou, F., Yu, T. (2023). "Relationships between curing temperature, microstructure, and piezoresistivity of CNT/epoxy nanocomposites", *International Functional Nanomaterials and Nanodevices Conference 2023*, 27-30 August 2023, Warsaw, Poland.

Wong, T. Y., Zou, F., Yu, T. (2022). "Piezoresistivity in hierarchical MWNT-GFRP composites", *The 15th International Conference on Fibre-Reinforced Polymers for Reinforced*

Concrete Structures (FRPRCS-15) and The 8th Asia-Pacific Conference on FRP in Structures (APFIS-2022), 10-14 December 2022, Shenzhen, China (Online via Zoom).

AKOWNLEDGEMENT

First and foremost, I would like to express my deepest gratitude to my supervisor, Professor Tao Yu, for his constructive feedback and academic support. His mentorship and encouragement have played a critical role in shaping my academic development and research direction.

I would also like to sincerely thank my co-supervisor, Dr. Fangxin Zou, for his invaluable guidance, unwavering support, and insightful advice throughout the course of my PhD study. I am grateful to Dr. Yu Xiang for his constructive feedback and academic support as my co-supervisors. Their perspectives have been instrumental in refining the scope and quality of this research.

Special thanks go to Dr. Lin Kui, whose expertise and mentorship in molecular dynamics simulations greatly enhanced the scientific rigour of this thesis.

I gratefully acknowledge the financial support provided by the Theme-based Research Project – Sustainable Marine Infrastructure Enabled by the Innovative Use of Seawater Sea-Sand Concrete and Fibre-Reinforced Polymer Composites, which made this research possible.

Furthermore, I am genuinely grateful for the discussions, support, and cooperation of my fellow members of the Advanced Engineering Materials Group throughout my PhD journey. I truly admire their dedication and commitment.

I also extend my appreciation to the technical staff who provided essential assistance throughout my experimental work. In the AAE Department, I would like to thank Yin Chiu Kan, Jasmine Choi, Ricky Fong, Jenny, and Yan Lung Li. In the CEE Department, my thanks go to Jonathan Chan, Paul Choi, Bosco Tam, and David. I am also grateful to the engineering staff at the Industrial Center: Dr. Mabel Ho, Hoi-cheung Leung, Gary Shum, and Eric Tsang. Furthermore, I would like to acknowledge the support of staff at UMF, particularly Dr. Hardy

Lui and Pendy Ho, and at ULS, Dr. Rachel Li and Dr. Carol Tsang, for their technical contributions to various stages of this research.

On a personal note, I am profoundly thankful to my mother and my wife for their unconditional love, patience, and unwavering belief in me throughout this journey. Their support has been my greatest source of strength and motivation. Without them, this would not have been possible.

Lastly, I would like to extend my gratitude to all those who, directly or indirectly, have contributed to the completion of this work. Your support has been truly appreciated.

Thank you everyone.

TABLE OF CONTENTS

CHAPTER 1 INTRODUCTION

1.1 Background

Fiber reinforced polymer (FRP) composites have found their structural applications in many sectors like aerospace, automotive, marine, and construction because of their high strength-to-weight ratio, good resistance to corrosion and fatigue, and flexibility in design and multifunctional. Wide ranges of diverse features and properties of composite materials can be achieved from combinations of constituent elements, like matrix and fiber types, as well as the manufacturing techniques, such as resin transfer molding (RTM), pressure laminating, and filament winding (Rajak, Pagar, Menezes, & Linul, 2019). Many research studies have been carried out to reveal their physical, mechanical, electrical, and thermal properties, as well as fatigue behavior, impact behavior, and failure mechanisms etc. With better knowledge of FRP composites, advanced structures can be designed using these materials and applied to different situations and environmental conditions (Frigione & Lettieri, 2018). For instance, concrete-filled FRP tubes (CFFTs), which are formed by concrete cores and FRP tubes for confinement, has become one of the attractive forms of hybrid members in civil infrastructure (Bazli, Zhao, Bai, Singh Raman, & Al-Saadi, 2019; Li, Teng, Zhao, & Singh Raman, 2018; Xie, Lin, Teng, & Jiang, 2020; Zhang, Yu, & Teng, 2015). The FRP tubes are usually manufactured using synthetic fibers as reinforcement, including glass, carbon, and basalt fibers, and thermosetting polymers such as epoxy and vinyl ester resins as matrix.

While the potential of FRP composites can be exploited thanks to the extensive literature on designing composite structures, the demand for monitoring techniques that can provide information on the conditions of the structures has arisen not only for monitoring the structure health but also enabling more advanced approach of studying the material and structural

deterioration. It is inevitable that manufacturing defects and in-service damages, such as interfacial debonding, matrix cracking, delamination, and fiber breakage, will occur in FRP composite structures. Furthermore, FRPs differ from traditional materials in that they exhibit complex failure mechanisms, such as matrix cracking, fiber breakage, interfacial debonding, and delamination, which frequently occur without visible signs. This complexity necessitates the use of advanced analytical and numerical tools to accurately predict their mechanical behavior, as well as the initiation and progression of damage, to enhance performance, reliability, and reduce maintenance requirements. Numerous non-destructive evaluation (NDE) techniques have already been developed to identify and characterize these defeats and damages, with ultrasonic testing, thermography, radiographic testing, electromagnetic testing, and acoustic emission being the most commonly used (Gholizadeh, 2016). Despite the excellence of these NDE techniques, they are employed as off-line inspection, i.e. when the parts are at shutdowns or taken out of service. Therefore, structural health monitoring (SHM) has emerged with the aim of detecting damages and monitoring structural integrity continuously during operation (Güemes, Fernandez-Lopez, Pozo, & Sierra-Pérez, 2020). In SHM, sensors or transducers are permanently attached or embedded into the structures, instead of being removable for NDE. Fiber optic and piezoelectric sensors are widely used in SHM, and their corresponding techniques have been relatively mature. For example, fiber Bragg grating (FBG) sensor, a common type of fiber optic sensors, can measure tensile or compressive strain at high sensitivity and accuracy through measuring the shift in peak frequency of the reflected light signals, which is proportional to the period of the gratings printed into the core of an optical fiber (Takeda, Okabe, & Mizutani, 2007). Concerning piezoelectric sensors, an active damage detection system can be established by mounting array of lead zirconium titanate (PZT) ceramic wafers on the surface of FRP structures, for example filament wound tubes (Beard & Chang, 1997). Although these sensors have found success in SHM for composite structures,

embedding or surface-mounting them means non-structural features are introduced into the structures, causing concern of degradation in mechanical performance.

An alternative approach in self-sensing provides the opportunity of SHM without the need of additional embedded or mounted sensors. Self-sensing can be achieved when detectable signal can be sensed from the material and information about its own condition, such as strain, damage, temperature, can be extracted from the signal (Rana, Subramani, Fangueiro, & Correia, 2016). It was demonstrated that in carbon fiber reinforced polymer (CFRP) composites, electrical resistance measurement using conductive carbon fibers can reflect the internal health status through an electromechanical phenomenon "piezoresistivity", i.e. "the electrical resistivity of a material changes reversibly with strain" (Chung, 2020; Park, Kwon, Wang, & Devries, 2015). The carbon fibers form electrically conductive paths. Variation in conductivity of the fibers with strain and altered conductive paths due to damage or breakage of the fibers cause the overall electrical resistance of the composite to change. Hence the change in electrical signal can be used to detect strain and damage in the composite. However, this electrical resistance change method requires the composite material to contain a conducting element. This restricted the application of the method to CFRP as other typical materials like glass fiber and epoxy are electrical insulators. Another setback was that this approach is ineffective for detecting matrix microcracking that associates the damage initiation and propagation in FRP composites because the response is principally sensitive to fiber-dominated damage mechanisms including fiber-matrix debonding and fiber breakage (Park et al., 2015).

With recent advancement of nanotechnology, researchers have been able to develop new multifunctional composites that possess unique mechanical, electrical, and thermal properties (Balasubramaniam, Sathiyan, Palani, Iyer, & Gupta, 2019; Gu et al., 2016). Polymer nanocomposites have shown increasingly rapid advances in the last decades because the mechanical and physical properties of the composites can be modified by the inclusion of nano-

sized fillers (Fu, Sun, Huang, Li, & Hu, 2019; Naskar, Keum, & Boeman, 2016). Carbon nanotubes (CNTs) have been used as the fillers in many classic studies that aimed at enhancing the mechanical properties of the composites or developing multifunctional materials due to their remarkable mechanical, electrical, and thermal properties of CNTs (Chou, Gao, Thostenson, Zhang, & Byun, 2010; Thostenson, Ren, & Chou, 2001). One of the dominant features of polymer composites filled with CNTs is the electrical percolation of low thresholds enabled by the high aspect ratio and conductivity of CNT, especially in thermosetting polymers with low processing viscosity (Bauhofer & Kovacs, 2009). Piezoresistivity utilizing the electrically conducting network of CNTs in polymer composite is a major area of interest within the field of multifunctional composites as the coupled electromechanical response is a fundamental property of strain sensing (Alamusi et al., 2011; Chung, 2020; C. Li, Thostenson, & Chou, 2008).

Extensive research has shown that the applications of piezoresistive polymer composites are vast, from stretchable, skin-mountable, and wearable strain sensors (Amjadi, Kyung, Park, & Sitti, 2016), to smart materials for in situ strain and damage sensing (Avilés, Oliva-Avilés, & Cen-Puc, 2018). CNTs have been the subject of studies in self-sensing nanocomposites for SHM of FRPs (H. Zhang, Bilotti, & Peijs, 2015). Relevant technique has been demonstrated on single fiber composites or laminate composites, and verified in standardized composite tests, such as ASTM D3039 for tensile fatigue testing. The advantages of CNT sensing techniques compared to other SHM methodologies are the inherently integrated nature with trivial weight penalty, great potential of multifunctionality, and the capability to detect matrix-dominated damages.

The research of self-sensing polymer composites using CNTs has already attracted attention from the industry as there is a patent granted to Boeing and University of Delaware on the application of CNTs for SHM in composite structures of aircraft (Patent No.

US9329021B1, 2016). The cost of CNTs was a concern for real applications but large quantities have been commercially available at lower prices with the demand rising. Industrial multi-walled carbon nanotubes (MWNTs) can be purchased at around USD100.00 per kilogram at present, i.e. additional material cost of USD0.25 for every kilogram of FRP with 0.5% by weight MWNT reinforcement in the matrix. Furthermore, fabrication of CNT-reinforced FRP composites has been proven to be fully compatible with conventional manufacturing techniques, such as wet-layup, resin infusion, and filament winding (Jia, Zhu, Li, Chen, & Yang, 2015; Kara, Kırıcı, Tatar, & Avcı, 2018; Taşyürek & Tarakçioğlu, 2017). These show the feasibility of using CNTs in advanced FRP composites for practical applications.

Despite the excellence and great potential shown in using self-sensing nanocomposite for SHM in FRP composites, more work is required to promote the application of this method in real-life industrial structure. One of the aspects that research needs, as addressed by Cawley (2018), is to focus on realistic structures. While the aforementioned studies on coupon or flat plate structures are encouraging, difficulties may arise when the techniques are applied on real structures with practical geometries or operating environment, such as CFFTs. Durable and cost-effective monitoring techniques are required to help making long-term observations of structural deterioration in FRP composites and providing solutions for structural health monitoring (SHM). Thomas et al. (2019) conducted a study to explore the Electrical Resistance Tomography (ERT) technique for damage detection in a thin-walled filament wound GFRP composite tube with CB-modified epoxy matrix. This study revealed the effect of tube aspect ratio and damage position on the sensitivity of ERT, hence suggesting the need for future work on extending research of self-sensing nanocomposite for real applications.

1.2 Aim and Objectives

The aim of this PhD study is to develop SHM method for FRP structures using nano-engineered polymer composites. To achieve this, epoxy nanocomposites are utilized as the matrix for developing advanced composite materials with performance enhancement and potential multifunctionality. CNT/epoxy nanocomposite is a promising piezoresistive material for incorporating self-sensing capability to FRP composite. On the other hand, thin-walled filament wound GFRP composite tube with CNT-modified epoxy matrix is a compelling candidate for extending research of self-sensing nanocomposite to structures with practical geometries. The findings should make an important contribution to promote the application of this method in real-life industrial structure.

This thesis involves in-depth investigations on the piezoresistive properties of CNT/epoxy nanocomposites and the development of self-sensing CNT/GFRP composite structures, concentrating on addressing the following challenges and objectives.

The first part is a mechanistic study on the piezoresistivity of CNT/epoxy nanocomposites for using as the matrices of FRP structures with self-sensing capability. The key objectives of this part are:

1. The first objective of this PhD study is to investigate the piezoresistive behavior of CNT/epoxy nanocomposites through electromechanical tests and establish key factors influencing the electromechanical properties.
2. The second objective of this PhD study is to address the challenge of nonmonotonic piezoresistive behavior and achieve complete control over the monotony of the piezoresistivity of CNT/epoxy nanocomposite employing both physical experiments and coarse-grained molecular dynamics (CGMD) simulations.

The second part concentrates on the application of nano-engineered polymer composites in SHM of FRP structures. The key objectives of this part are:

3. The third objective of this PhD study is to conduct a comprehensive investigation on the piezoresistive behavior of CNT/GFRP composite structures through electromechanical tests and identify key factors influencing the electromechanical properties.
4. The fourth objective of this PhD study is to address the challenge of fiber orientation dependent, nonmonotonic piezoresistive behavior of CNT/GFRP composites employing multiscale finite element-based electromechanical framework.
5. The fifth objective of this PhD study is to design CNT/GFRP composites with desired monotonic piezoresistive behavior for SHM in FRP structures using self-sensing polymer composites.

1.3 Outline of Thesis

This PhD thesis tackles the obstacles of nonmonotonic piezoresistive behavior in CNT/epoxy nanocomposites and CNT/GFRP composites for their SHM applications. The outline of the thesis is as follows:

CHAPTER 1 provides an overview of SHM in FRP composite structures, introduces nano-engineered polymer composites for SHM applications, and briefly explains piezoresistivity and its relevance in SHM. It states the main research aim, lists specific objectives, and highlights the significance of the study.

CHAPTER 2 systematically reviews related research progress, covering piezoresistivity of polymer nanocomposites, molecular dynamic simulations of polymer and polymer nanocomposites, self-sensing polymer nanocomposites for SHM of FRP composite structures,

and numerical methods including finite element analysis (FEA) and multiscale modeling approaches, for FRP composite.

CHAPTER 3 examines the effect of curing condition on the piezoresistivity of CNT/epoxy nanocomposites. The chapter analyzes electrical conductivity data, interprets electromechanical test results, and discusses the relationship between curing conditions and piezoresistivity.

CHAPTER 4 investigates the microstructural origin of nonmonotonic piezoresistivity in polymer nanocomposites through experimental and computational approaches. The chapter analyzes curing-dependent piezoresistivity and establishes inter-nanofiller junction geometry as the microstructural parameter governing the monotony of the piezoresistive behavior.

CHAPTER 5 focuses on the importance of fiber orientation on the piezoresistivity of CNT/GFRP composites. The chapter analyzes electrical percolation and piezoresistive behaviors in CNT/epoxy nanocomposites and examines effects of fiber orientation on the piezoresistivity of CNT/GFRP laminates and tubes.

CHAPTER 6 investigates the microstructural origin of nonmonotonic piezoresistivity in CNT/GFRP composites through experimental and computational approaches. The chapter analyses effect of fiber orientation on the piezoresistive and tensile behaviors and reveals the complex relationship between fiber orientation, deformation mechanisms, and CNT network reconfiguration in CNT/GFRP composites under tensile loading.

CHAPTER 7 focuses on achieving monotonic piezoresistive behavior in CNT/GFRP composites for SHM applications. The chapter analyzes numerical results, validates tailored monotonic piezoresistive behavior experimentally, and discusses optimizing CNT/GFRP composites for SHM applications.

CHAPTER 8 summarizes the main research findings from each chapter and proposes future studies to address remaining research gaps and challenges.

CHAPTER 2 LITERATURE REVIEW

2.1 Piezoresistivity in CNT/epoxy Nanocomposites

This section explores the piezoresistive behavior of nanocomposites, primarily focusing on CNT nanofillers within epoxy polymer matrix. The literature investigates how the electrical resistance of these materials changes under mechanical strain, a phenomenon crucial for strain sensing and structural health monitoring. They discuss experimental methods for characterization, analyze the impact of filler concentration, dispersion, and morphology on conductivity and sensitivity, and propose theoretical and computational models to explain observed behaviors, including percolation theory, tunneling effects, and the influence of CNT deformation and network reconstruction.

2.1.1 Underlying Mechanisms

The piezoresistive response of polymer nanocomposite originates from the conducting network that comprises of electrically conductive nanofillers within the insulating polymer matrix. The nanofillers act as discrete conductors and form paths that delocalized electrons can flow through under applied voltage. The filler network configuration determines the equivalent resistance of the network and subsequently the composite. It is similar to a resistor circuit, of which the equivalent resistance significantly depends on how the resistor elements are connected. It has been widely accepted that the piezoresistivity of polymer nanocomposites is a consequence of changes in the equivalent resistance of the filler network R_{eq} induced by changes in network configuration under mechanical deformation. The underlying mechanisms have been discussed by a number of review papers and are summarized here (Amjadi et al.,

2016; Avilés et al., 2018). There are three types of changes in the filler network that contribute to the piezoresistivity of polymer nanocomposite, including modification in the filler-to-filler interparticle distance, changes in the intrinsic resistance of the filler, and formation and destruction of the conducting path. Figure 2.1 schematically illustrates the underlying mechanisms of piezoresistivity in polymer nanocomposites.

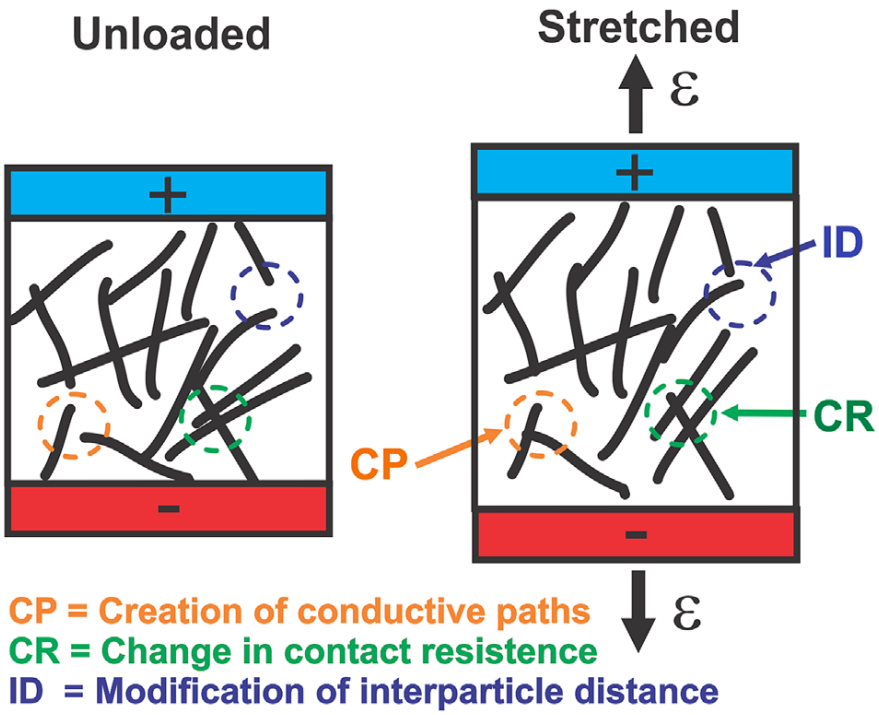

Figure 2.1. Underlying mechanisms of piezoresistivity in polymer nanocomposites (Avilés et al., 2018). (Adapted from Avilés et al., 2018. Copyright 2025, with permission from Wiley).

In polymer nanocomposites, electron can flow between fillers separated by a layer of polymer matrix that is sufficiently thin to allow the quantum tunneling effect. Simmons' formula for tunneling resistance R_{tunnel} have been extensively used to estimate the tunneling resistance between nanofillers pair of tunneling junctions (Simmons, 1963)

$$R_{tunnel} = \frac{h^2}{A_{tunnel} e^2 \sqrt{2m\lambda}} \exp\left(\frac{4\pi d}{h}\sqrt{2m\lambda}\right) \quad (2.1)$$

where h is Planck's constant, A_{tunnel} is the cross-section area of the tunneling junction, e is the charge of electron, m is the mass of electron, λ is the height of energy barrier for the polymer layer, d is the filler-to-filler interparticle distance. With an exponential dependance on d, R_{tunnel} increases rapidly with interparticle distance. Therefore, the tunneling resistance is highly sensitive to changes in interparticle distance or thickness of polymer layer. The tunneling effect has been regarded as the dominant mechanism governing the piezoresistivity in polymer nanocomposites due to the discrete nature of the nanofillers participating in the conductive network (De Vivo et al., 2014; N. Hu, Karube, Yan, Masuda, & Fukunaga, 2008). In practice, a cutoff distance (d_{cutoff}) is applied to turn off the tunneling mechanism when the value of R_{tunnel} reaches the level of insulator so that a conducting path can be well defined. Other than d, the level of R_{tunnel} also depends on A_{tunnel} and λ, which reflect the physical properties of the fillers and the polymer matrix. Therefore, d_{cutoff} varies with different types of nanofillers and polymer matrix. For example, for CNT-based polymer composites, d_{cutoff} can be taken as 1.8 nm (C. Li, Thostenson, & Chou, 2007).

While the tunneling effect is dominant, the intrinsic resistance of the filler contributes to the equivalent resistance of the filler network as well. As illustrated in Figure 2.1, the portion of the filler between two contact points that electron flows across neighboring fillers may vary when strain is applied on the composite. Treating the filler as a classical conductor, the intrinsic resistance of the filler $R_{intrinsic}$ is given by

$$R_{intrinsic} = \frac{L}{\sigma_{filler} A_{filler}} \quad (2.2)$$

where L is the length of filler between two tunneling junctions, σ_{filler} is the electrical conductivity of the filler, and A_{filler} is the cross-section area of the filler. These are physical

parameters of the filler so the contribution of $R_{intrinsic}$ to the piezoresistivity depends on the type of the filler predominantly. The aspect ratio is one of the major parameters that decide the weight of $R_{intrinsic}$ in the piezoresistivity. For spherical or zero-dimensional (0D) fillers such as CB with aspect ratio close to one, the change of $R_{instrinsic}$ is negligible regardless of the state of strain. On the other hand, for one-dimensional (1D) or two-dimensional (2D) fillers, including CNTs, graphene, and metal nanowires, the range of variation in L could be large due to the large aspect ratio. Hence, $R_{intrinsic}$ should not be overlooked when studying polymer nanocomposites with 1D or 2D fillers. The terms σ_{filler} and A_{filler} may change if the filler is inherently piezoresistive and strained. However, a considerable number of studies have indicated the contribution of inherent piezoresistivity of the nanofiller is expected to be negligible or small. This could be mainly attributed to the weak interfacial strength between nanofillers and polymer matrix, which leads to inefficient stress transfer (N. Hu et al., 2010; N. Hu, Karube, et al., 2008; Ren & Seidel, 2013; Yin et al., 2011).

During the early stage of deformation, the change in R_{eq} is mainly driven by the tunneling effect and changes in intrinsic resistance when the number of conducting paths has not been altered much yet. The number of paths varies with the generation or demolition of tunneling junctions. When the interparticle distance of a tunneling junction becomes larger than d_{cutoff}, the original path is no longer considered as conductive because of the cessation of quantum tunneling for electron transport between two neighboring fillers. On the contrary, fillers may move closer to within d_{cutoff} and hence create a new conducting path. An increase (decrease) in number of conducting path causes R_{eq} of the network to increase (decrease). This mechanism can be accounted for by incorporating the relation for number of path N as a function of strain ε into the resistance-strain expression (Al-Solamy, Al-Ghamdi, & Mahmoud, 2012; Boland et al., 2016; Y. Li, Wang, & Su, 2018). For example, Al-Solamy et al. (2012) proposed a theoretical model that different forms of resistance-strain relation were used for

different range of strain. At small deformations, the resistance-strain relation was derived based on the tunneling effect only. Change in number of conducting paths was included at large deformations and yield a resistance-strain relation as

$$\ln R_{eq} = \ln R_0 + \ln(1+\varepsilon) + \alpha\varepsilon + \beta\varepsilon^2 + \tau\varepsilon^3 + \delta\varepsilon^4 \quad (2.3)$$

where R_0 is the initial resistance under zero strain, ε is the strain of the composite, α, β, τ, and δ are constants that can be fitted by experiments. Equation (2.3) fit well the experimental data of acrylonitrile butadiene rubber (NBR) loaded with 0.5 phr of GNPs for compressive strain above 0.1. This illustrates that formation and destruction of the conducting path could produce significant influence on the piezoresistivity of polymer nanocomposites.

2.1.2 Piezoresistive Responses of CNT/epoxy Nanocomposites

The mechanisms mentioned in Chapter 2.1.1 are general to polymer nanocomposites featuring an electrically insulating matrix and conductive fillers. Researchers have been studying the piezoresistive behavior of nanocomposites with different types of polymer matrix and nanofillers. Researchers have shown great interest in epoxy nanocomposites because of their high mechanical properties, good chemical resistance, versatility, and hence wide range of application in fields of aeronautic, civil, and mechanical engineering as coatings, adhesives, structural components (Gu et al., 2016). Epoxy resins filled with CNTs are one of the most studied systems regarding their piezoresistive behavior because of their great potential for the development of multi-functional hierarchical composites (Khan & Kim, 2011; Qian, Greenhalgh, Shaffer, & Bismarck, 2010; H. Zhang et al., 2015). The most relevant results and findings of these composites are reviewed in this section. It is noted that the results presented in this review should be taken as of bulk specimens, which are defined with thickness of few millimeters, except otherwise specified.

2.1.2.1 Monotonic Piezoresistive Behavior

Most of the studies have reported research on the piezoresistivity of CNT/epoxy composites under tensile loading. Monotonic or even linear relations between resistance change and strain can be found in several of them. Thostenson and Chou (2006) and Fernberg et al. (2009) have both shown highly linear lines of electrical resistance against displacement or strain for 0.5 wt.% CNT/epoxy composites loaded in quasi-static tension. A research group of Guadagno and Vertuccio has published a series of papers studying the piezoresistive properties of CNT/epoxy composites with different epoxy precursors and filler concentrations (Guadagno, Lamberti, Tucci, & Vertuccio, 2021; Spinelli, Lamberti, Tucci, Vertuccio, & Guadagno, 2018; L. Vertuccio et al., 2016; Luigi Vertuccio, Vittoria, Guadagno, & De Santis, 2015). The resistance monotonically increased until the failure of specimens at around 3 – 3.5% tensile strain for the two precursors, tetrafunctional tetraglycidyl methylene dianiline (TGMDA) and bifunctional bisphenol A diglycidyl ether (DGEBA). In comparison, the DGEBA system resulted in slightly higher sensitivity, which can be quantified in terms of gauge factor k calculated by

$$k = \frac{\Delta R/R_0}{\varepsilon} \tag{2.4}$$

where ΔR is the resistance change. Filler concentrations affected the sensitivity and also the linearity of the resistance-strain relations (Luigi Vertuccio et al., 2015). It was found that the sensitivity decreased when the filler concentrations increased (0.025 – 0.5 wt.%). Nonlinear curve was found in the 0.025 wt.% sample, which was close to the percolation threshold. These findings could be explained by the tunneling effect being the dominant mechanism when the proportion of tunneling junctions along the conductive paths is high, leading to the exponential behavior.

2.1.2.2 Nonmonotonic Piezoresistive Behavior

While monotonic and linear piezoresistive behaviors are desired for strain sensing applications, literature has emerged that offers contradictory findings about the nonmonotonic trend of the electromechanical response in CNT/DGEBA epoxy composites (X. Cao et al., 2017; Meeuw, Viets, Liebig, Schulte, & Fiedler, 2016; Panozzo, Zappalorto, & Quaresimin, 2017; Vadlamani, Chalivendra, Shukla, & Yang, 2012; Wichmann, Buschhorn, Gehrmann, & Schulte, 2009). Wichmann et al. (2009) investigated the piezoresistive response of a DGEBA epoxy cured by anhydride hardener filled with multi-walled CNTs. It was observed that the electrical resistance increased monotonically initially but the trend changed from positive to negative (inversion of piezoresistivity) when the strain increased to above 4% (Figure 2.2a). The critical strain (ε_c) corresponding to the peak of resistance change at 4% was observed to be the same for the 0.1 and 0.3 wt.% composites in the study. The negative piezoresistivity was ascribed to viscoelastic and inelastic deformation of the epoxy matrix, which could promote the formation of conducting paths by reorientating and aligning the CNTs, because it appeared to occur with the onset of yielding judging from the stress-strain curves.

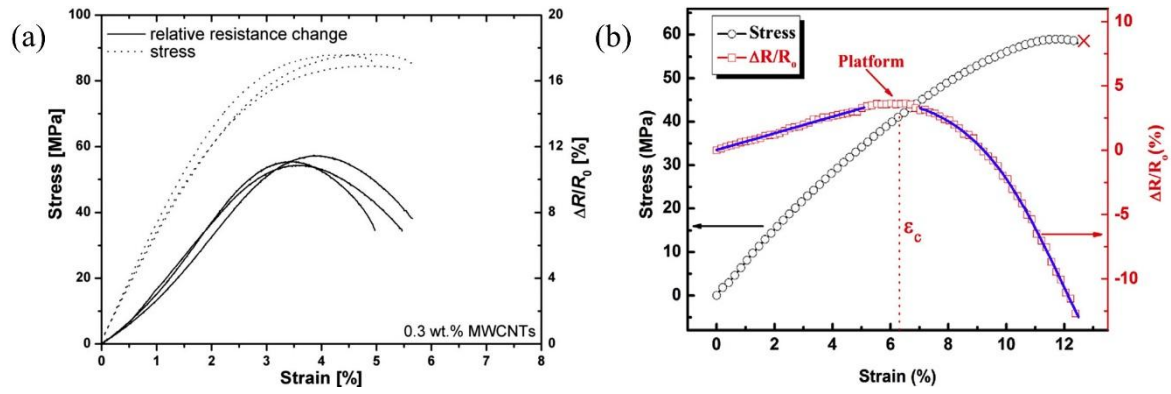

Figure 2.2. Nonmonotonic piezoresistive behaviors of (a) 0.3 wt.% CNT/epoxy composites in (Wichmann et al., 2009), (Adapted from Wichmann et al., 2009. Copyright 2025, with

permission from American Physical Society), and (b) 0.15 vol.% CNT/epoxy composites in (Cao et al., 2017). (Adapted from Cao et al., 2017. Copyright 2025, with permission from Elsevier).

Inversion of piezoresistivity leads to undefined response in strain sensing, i.e. one resistance reading corresponding to two strain values. Therefore, several attempts have been made to identify the factors that affect the trend of resistance change. Among the studies on CNT/epoxy nanocomposites, the most extensively examined factor is the filler concentration. However, there are conflicting findings regarding whether an increase in filler concentration enhances the monotony of piezoresistive behavior. Vadlamani et al. (2012) examined the piezoresistivity of samples loaded with 0.1, 0.3, and 0.5 wt.% and found that the values of ε_c were 1.5, 1.9, and 3.9% respectively. Only the 0.5 wt.% composites exhibited similar piezoresistive behavior to those in (Wichmann et al., 2009). The results of the 0.1 and 0.3 wt.% composites demonstrated that the inversion of piezoresistivity may occur in earlier stage of applied tensile strain and provided evidence that it may not coincides with the macroscopic yielding of the composites. Similar behavior can be found in the study of Cao et al. (2017). Figure 2.2b shows the plots of resistance change against tensile strain and the stress-strain curve. The author also reported that the value of ε_c increased with CNT content. The values of ε_c for the 0.15 vol.% and 0.25 vol.% specimens were about 6% and 9% respectively. The explanation for this finding was that the higher original number of conducting paths in composite with higher filler concentration delayed the stage that the formation and destruction of conducting path became the dominant mechanism. It is noted that direct comparison of ε_c across individual study should be avoided because the epoxy system used as matrix and the method of measuring applied strain were different.

On the other hand, the value of ε_c was found to decrease with filler concentration in other studies. The experimental data in the study of Panozzo et al. (2017) indicated that the maximum in resistance change curve occurred at lower value of strain with higher filler concentration. When the CNT concentration was at 0.1 wt.%, the maximum appeared near the failure of specimen at about 3% strain. The resistance change-strain curves of the 0.25 and 0.5 wt.% specimens were almost identical, and the inversion of piezoresistivity was more apparent with the values of ε_c both at about 2.2% strain. The occurrence of maximum in resistance change curves was attributed to local matrix plastic and viscoelastic flow, which cause locally thinner polymer layers between nanoparticles, as well as re-orientation of nanoparticles. Meeuw et al. (2016) investigated the influence of network morphology on the piezoresistive behavior of MWNT modified epoxy nanocomposites in bulk or film form. Nonmonotonic trend of resistance change against strain was found in almost all samples despite a wide variety of parameters investigated, such as aspect ratio, filler concentration, and orientation. Increase of filler concentration and aspect ratio induced the inversion of piezoresistivity at lower strains in either bulk or film specimens. The effect of filler alignment was explored in film specimens of about 100 μm thick. It was found that alignment of CNTs using AC electric field could significantly delay the inversion of piezoresistivity. While the values of ε_c of the composites with randomly dispersed 0.03 wt.%, 100 μm long MWNTs and 0.02 wt.%, 1000 μm long CNTs were both around 1.25% strain, the piezoresistive behavior of the specimens with aligned fillers became linear and monotonic in the range of 4% strain. This finding indicated that the reorientation of nanotubes contributed to the occurrence of inversion of piezoresistivity.

Nonmonotonic piezoresistive behavior has often been observed in polymer nanocomposites, severely affecting the application prospects of this material class. Boland et al. (2016) associated the nonmonotonic piezoresistive behavior of a graphene-filled lightly crosslinked polysilicone nanocomposite with the viscoelasticity of the polymer. They proposed

that, during mechanical deformation, a low matrix viscosity enables the movement of nanofillers by diffusion or under an applied electric field, leading to nanofiller network relaxation and a decrease in resistance. Similar undesirable piezoresistive behavior has also been observed in other elastomer nanocomposites (Paliy et al., 2016; Tendo Innocent et al., 2021). Beyond elastomers, which are generally highly viscoelastic, thermosetting polymers, another type of extensively explored matrix material, have shown large variations in the monotony of their piezoresistive behaviors (X. Cao et al., 2017; Meeuw et al., 2016; Panozzo et al., 2017; Vadlamani et al., 2012; Wichmann et al., 2009). Thus far, the emergence of nonmonotonic piezoresistive behavior has been mainly attributed to matrix plasticity, transverse nanofiller movement under Poisson's effect, and nanofiller network rearrangement under a large strain (Avilés et al., 2018).

2.1.2.3 Strain Sensing Performance

The strain sensing capability of CNT/epoxy composites has been evaluated under cyclic tensile loading (X. Cao et al., 2017; Meeuw et al., 2016; Panozzo et al., 2017; Spinelli et al., 2018; L. Vertuccio et al., 2016; Luigi Vertuccio et al., 2015; Wichmann et al., 2009). In case of monotonic piezoresistive behavior, Vertuccio et al. (2016) and Spinelli et al. (2018) loaded and unloaded the samples to maximum strains of increasing value (0.83%, 1.65%, and 2.42%) while monitoring the resistance change. The resistance change and strain corresponded well throughout the loading-unloading process. When the maximum strains were at 0.83% and 1.65%, the resistance returns to the original values with strain (i.e. no residual resistance). This was expected as these levels of deformation were in the elastic region (2% strain) identified by quasi-static tensile tests. Positive residual resistance was observed after the samples were stretched to 2.42%, which was in the plastic region, even though the strain value returned to

zero. The residual resistance was attributed to the plastic deformation occurred beyond the elastic region in the samples that disrupted the CNT network irreversibly. This demonstrates the great potential of the composites for strain sensing application with the ability to detect yielding in the structure.

The resistance change behavior of the composites under cyclic tensile loading was found to be more complicated if the composites possess nonmonotonic piezoresistive behavior. When the maximum strains were below ε_c by a margin, for example 1% with respect to values of ε_c above 2%, the resistance change followed the strain well and was able to return to the original value (X. Cao et al., 2017; Meeuw et al., 2016; Panozzo et al., 2017). The strain sensing capability still prevails with elastic deformation only. However, the inversion of piezoresistivity could be detrimental to the sensing performance. Residual resistance occurred when the strain levels reached the vicinity of ε_c, suggesting that there were irreversible changes in the filler network configuration due to plastic and viscoelastic deformation in the matrix. Cao et al. (2017) applied 10s cycles of loading-unloading to several maximum strain levels on composites with the inversion of piezoresistivity occurring at about 6% strain. Positive residual resistance was observed for strain amplitude of 4%, similar to the monotonic cases. Further increases in the strain amplitude beyond the values of ε_c lead to negative residual strains which could accumulate (X. Cao et al., 2017; Meeuw et al., 2016; Wichmann et al., 2009). Wichmann et al. (2009) performed single and incremental loading-unloading tensile tests. The samples with ε_c of 4% were loaded to 6% strain and then unloaded to zero stress in the single cycle test. The residual resistance was negative with residual strain of about 0.5%. The authors hence denoted that the 6% total strain was composed of 5.5% elastic and viscoelastic deformation and 0.5% plastic deformation. Also, the negative residual resistance should be the result of molecular level viscoelastic and plastic processes such as alignment of CNTs in high local deformation area because the composites were elongated macroscopically. In the incremental

loading-unloading tests, as well as the cyclic tensile tests with maximum strains above ε_c performed by (X. Cao et al., 2017), the magnitude of negative residual resistance was found to be increasing. This could be the consequence of irreversible changes in the MWNT network configuration under the plastic deformation accumulated in the matrix.

It can be summarized that the strain sensing performance of CNT/epoxy nanocomposites would be deteriorated by the inversion of piezoresistivity. The resistance change could be used to monitor tensile strain unambiguously in the elastic region. The onset of plastic deformation would be accompanied by residual strain and resistance change but nonmonotonic piezoresistive behavior has been found to cause either positive or negative resistance change. This ambiguity limits the working range of strain sensing and the capability of damage detection using the composites for SHM in advanced multiscale composites.

2.1.3 Numerical Modeling

In view of the attractive potential of the electrical and piezoresistive properties in CNT/polymer composites demonstrated through extensive experimental studies, researchers have developed theoretical methods such as analytical models and numerical simulations to predict and gain deeper understanding of them. The theoretical methods in the literature can be briefly classified into three categories, which are analytical models, computational micromechanics-based models, and equivalent resistor network models (Koo & Tallman, 2020). Analytical models refer to those attempted to derive a relationship between electrical properties and strain (Al-Solamy et al., 2012; Boland et al., 2016; Cattin & Hubert, 2014; Han et al., 2018; Koo & Tallman, 2020; Matos, Pinho, & Tagarielli, 2019; Panozzo et al., 2017; Tallman & Wang, 2013; Wichmann et al., 2009). Equation (2.3) is an example. The relationships derived can be fitted to experimental data to determine coefficients or physical parameters (Al-Solamy et al.,

2012; Boland et al., 2016; Cattin & Hubert, 2014; Koo & Tallman, 2020). A major advantage of analytical models is low computational cost. They can be readily integrated with finite element methods for macroscale analysis (Koo & Tallman, 2020; Matos et al., 2019; Tallman & Wang, 2013). However, assumptions are inevitably made regarding some phenomenon on nanoscale such as nanofiller movement during the homogenization of the representative volume elements (RVEs). Computational micromechanics-based models, on the other hand, focus on simulating the nanoscale interactions between the nanofillers and the matrix using finite element methods (Alian & Meguid, 2019; Ren, Chaurasia, & Seidel, 2016; Ren & Seidel, 2013). The matrix and the fillers are both meshed in a RVE and the interactions between them, including stress transfer and electron transport, are explicitly simulated. Therefore, these models are suitable for studying the coupling effects of mechanical and electrical phenomenon that may affect the piezoresistive properties, such as how damage-induced local mechanical properties fluctuations in matrix could alternate local current pathways between nanofillers (Ren et al., 2016). The limitation of these models is high computational cost due to high number of mesh required and unscalable. Equivalent resistor network models simulate the changes in the configuration and hence the electrical properties of CNT network in a microscale RVE under deformation (Alian & Meguid, 2019; Gbaguidi & Kim, 2018; Gbaguidi, Namilae, & Kim, 2019; Gong et al., 2018; Gong & Zhu, 2014; B. Hu et al., 2012; N. Hu, Karube, et al., 2008; Jung et al., 2019; Matos, Tagarielli, Baiz-Villafranca, & Pinho, 2018; Taya, Kim, & Ono, 1998; Theodosiou & Saravanos, 2010). Since it has been generally accepted that the conductive network formed by CNTs gives rise to the electrical conductivity of nanocomposite, it is physically intuitive to treat the CNT network as resistor circuit. The configuration of resistors and individual resistance value of the resistors determine the overall effective resistance of the circuit, as discussed in Chapter 2.1.1. The general approach of equivalent resistor network model involves randomly generating large number of CNTs to form a network that spans the

RVE, and monte Carlo method is usually used to determine the effective resistance from tens to thousands of random networks. Therefore, the computational cost of such models is also high. The numerical modeling of the piezoresistive effect in CNT/polymer nanocomposites involves a variety of methods, focusing on different aspects of the nanocomposite's behavior. Here is an overview of some significant numerical methods.

2.1.3.1 Equivalent resistor network model

Equivalent resistor network models are by far the most adopted numerical methods in simulating the piezoresistive behavior of CNT/polymer composites. Hu et al. (2008, 2010) developed a 3D resistor network model that considers the tunneling effect and changes in the intrinsic resistance of CNTs as the mechanism, then combined it with a 3D fiber reorientation model for controlling the movement of CNTs to simulate the piezoresistivity of CNT/polymer composites. The influence of filler concentration and alignment were investigated, and good agreement was observed between the numerical results and the experimental measurements of CNT/epoxy composites. Gong et al. (2014) incorporated an additional mechanism, which was the deformation of CNT at the tunneling junction, into the 3D resistor network model and found that the proposed new mechanism may play a significant role in the piezoresistivity of CNT/polymer composites. Other than exploring the involving mechanisms, the influence of network morphology can be studied using equivalent resistor network model as well. The simplest way for modeling CNTs is treating them as straight lines. It is sufficient for qualitatively acceptable results. For achieving more realistic CNT network, curved CNT can be described as a set of straight-line segments (Jung et al., 2019) or p-splines (Matos et al., 2018). Gbaguidi et al. (2019) investigated the effect of CNT agglomeration on the percolation and piezoresistive behaviors of nanocomposites with CNTs only or hybrid of CNT and

graphene nanoplatelets (GNPs) through a parametric study using a 2D resistor network model considering the tunneling effect as the primary mechanism. The variety of equivalent resistor network models found in the literature suggests that this numerical method is versatile and fit for studying different factors in the piezoresistive behavior of CNT/polymer composites.

The algorithm for calculating the effective resistance of a resistor network is given in the papers by Li and Chou (2007, 2008) and Jung et al. (2019). This is critical for simulation using equivalent resistor network model, so it is presented here. Assuming a RVE with randomly dispersed CNTs modeled as straight lines connecting the two end points is generated, the first step is to identify a network consisting of CNTs that can form paths for electrons to flow from one side to the opposite side of the RVE, i.e. a spanning cluster. Union-find algorithm (Jung et al., 2019) or Hoshen-Kopelman algorithm (C. Li & Chou, 2007) can be used to put CNTs that are within in a defined cutoff distance into the same cluster. The algorithm output the sets of CNTs that are grouped into clusters of which the spanning clusters can be identified. In order to model the CNT network as a resistor network, resistor with two nodes as shown in Figure 2.3. Schematic of (a) a resistor element (b) a resistor network (Li & Chou, 2007). are used to represent individual resistor element of the network. The resistance of a resistor element R^e depends on the type of segment it is representing. Considering the tunneling effect and intrinsic conductance of CNT as the mechanisms of electron transport along the conducting paths (and piezoresistivity as discussed in Chapter 2.1.1), there are two classes of resistor of which one is for CNT segment between two nodes at tunneling junctions and the other one is for tunneling junction between two nodes on adjacent CNTs. Figure 2.3(b) shows an example of a resistor network on a 2D space of nodes. As a result, the CNT network is transformed into a resistor network. Modified nodal analysis (MNA) method can be applied to adapt the matrix of resistor network to calculate the effective resistance under a boundary condition of applied voltage between two opposite sides of the RVE (Alian & Meguid, 2019). The problem of resistor

network is usually a large-scale matrix of linear system, which can be solved by iterative equation solver such as conjugate gradient method. After nodal voltages are solved, the effective resistance can be readily calculated using Ohm's law.

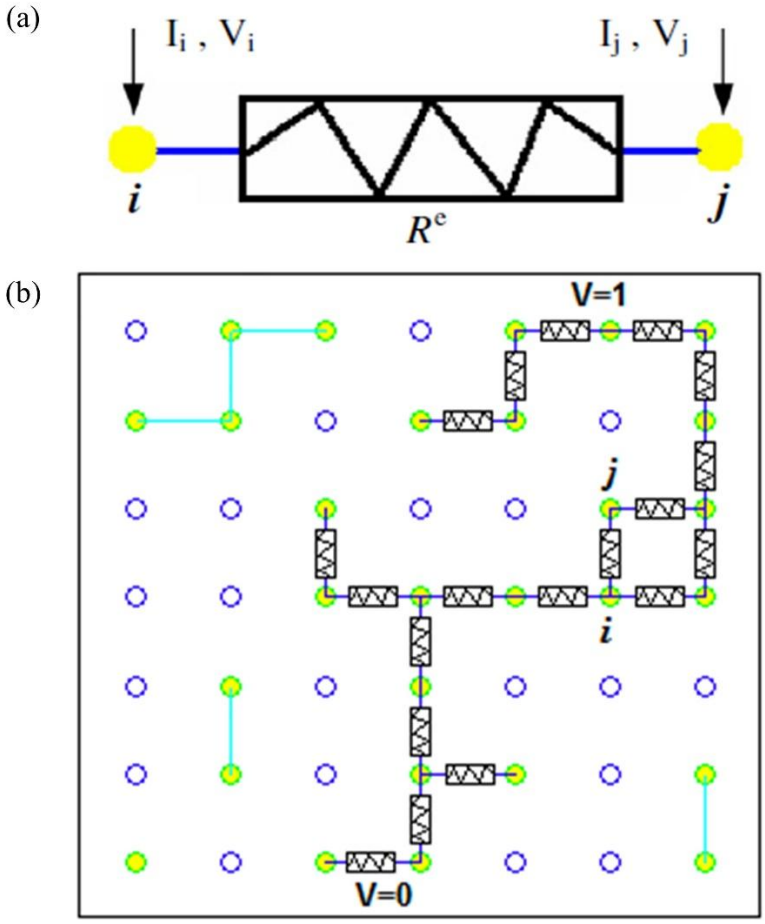

Figure 2.3. Schematic of (a) a resistor element (b) a resistor network (Li & Chou, 2007). (Adapted from Li & Chou, 2007. Copyright 2025, with permission from IOP Publishing).

2.1.3.2 Finite Element Analysis-Based Multiscale Modeling

3D computational multiscale micromechanics models based on FEA have been developed to predict the macroscale piezoresistive response of polymer nanocomposite. These models often use RVEs to capture the distribution and interaction of nanofillers within the

polymer matrix under various loading conditions, e.g. uniaxial tension, compression, shear, and even multiaxial strain states (Matos et al., 2019, 2018). Alian and Meguid (2019) developed a multiscale electromechanical model for CNT/polymer nanocomposites. Figure 2.4 shows the schematic illustration of the proposed multiscale model. As an attempt to link the material properties at nanoscale to the electromechanical coupling behavior of CNT/polymer nanocomposites, their model employed molecular dynamics (MD) simulations for nanoscale properties, hybrid FE-MD model for structural response, and equivalent resistor network model for electrical response. The results showed limitation at strains higher than 3.0% which the authors attributed it to the straight CNT constraint and hence the inability of the model to account for any induced bending of CNTs at large deformations. Matos et al. (2019, 2018) presented FE simulations to predict piezoresistive response of CNT/epoxy nanocomposites using realistic RVEs with CNTs of arbitrary complexity, e.g. representing curved CNTs by penalized basis splines. They later applied machine learning to reduce computational cost and handle more complex problems like arbitrary geometry and multiaxial strain field. Ren and Seidel (2016, 2013) focused on computational micromechanics to model inherent piezoresistivity and its effect on macroscale response. Their work suggests that inherent CNT piezoresistivity alone may not fully explain the observed macroscale response, implying other mechanisms like the tunneling effect and nanofiller contact play important roles. They also explored the coupled effect of continuum damage and piezoresistivity, showing good correlation between damage and piezoresistive response, supporting its use for damage detection.

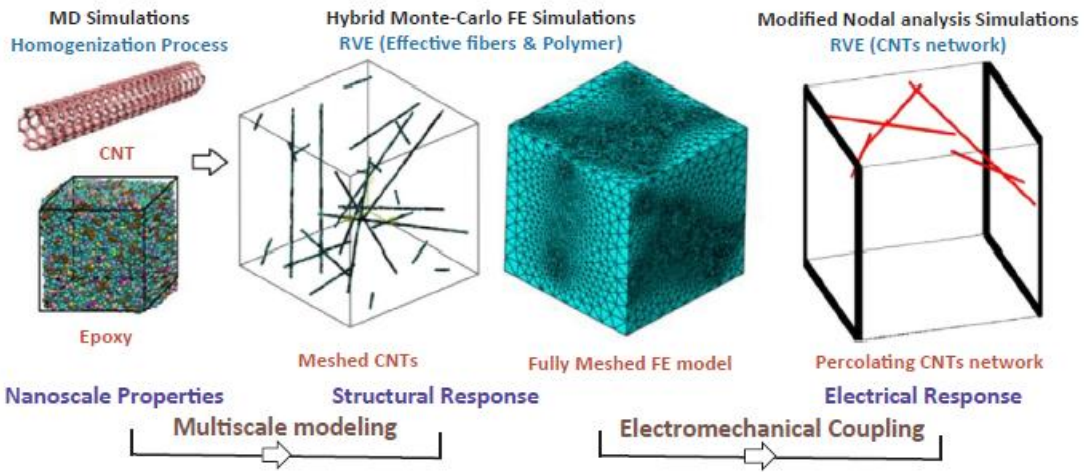

Figure 2.4. Schematic illustration of the multiscale electromechanical model for CNT/polymer nanocomposites proposed by Alian and Meguid (Alian & Meguid, 2019). (Adapted from Alian & Meguid, 2019. Copyright 2025, with permission from Elsevier).

In general, this approach involves several key aspects, from generating realistic microstructures to accurately representing both nanofiller and matrix material. Randomness of dispersed CNTs is commonly handled by Monte Carlo simulations (Alian & Meguid, 2019; Grabowski, Zbyrad, Uhl, Staszewski, & Packo, 2017; Matos et al., 2019). This allows researchers to study and predict the behavior of materials containing randomly distributed CNTs without needing to create physical samples for every possible configuration cost-effectively and time-efficiently. While the generation of realistic RVEs is crucial, accurately representing the CNTs within these structures is equally important. CNTs are typically modeled as equivalent beam elements (Grabowski et al., 2017; Matos et al., 2019, 2018) or solid cylinders (Alian & Meguid, 2019; Han et al., 2018). The polymeric matrix is often discretized into brick elements, and CNTs are modeled as embedded elements that are assumed to be perfectly bonded to the matrix.

For electromechanical coupling, these models employ a sequentially coupled approach. First, mechanical loading is simulated to determine the structural response and updated CNT

locations and/or deformations. Mechanical properties of nanofillers and the polymer matrix for these models can be derived from MD simulations, allowing for a multiscale analysis that links nanoscale material properties to microscale and macroscale responses (Alian & Meguid, 2019; Grabowski et al., 2017). Second, an electrical model, e.g. equivalent resistor network model, is employed to calculate the corresponding electrical resistance of the nanocomposite based on the deformed state. Electrical properties are usually obtained by integration of mechanisms, including the tunneling effect, changes in network configuration, inherent nanofiller piezoresistivity, as described in Chapter 2.1.1.

2.1.3.3 Analytical Formulations

Analytical formulations provide a powerful and computationally efficient approach to predicting the piezoresistive response of polymer nanocomposite. Unlike computationally intensive equivalent resistor network- or FEA-based models that output discrete data points, analytical models offer generalized knowledge on parameter dependencies through approximate, closed-form expressions, which is highly desirable for designing multifunctional sensing materials. They are less computationally expensive because they do not simulate individual nanofillers explicitly, making them more amenable to macroscale analyses and integration with FE methods. Several key mechanisms that govern the change in electrical resistance under mechanical deformation, including the tunneling effect, changes in network configuration, inherent nanofiller piezoresistivity, are typically incorporated during the development of these analytical formulations.

Several analytical models have been developed, each with distinct features and assumptions. Panozzo, Zappalorto, and Quaresimin (2017) developed an analytical model to predict the electrical resistance change of CNT-modified polymers as a function of applied

strain (only the elastic, reversible part). This model accounted for three-dimensional random orientation, waviness, and entangling of CNTs. The final equation correlated overall resistance change to average thickness variation of the matrix for a given value of deformation, accounting for many physical and mechanical properties of the matrix and CNTs, emphasizing the dominant role of tunneling resistance in piezoresistivity. The model required inputs like CNT concentration, Poisson's ratio, and an estimation of a global morphological parameter (K), showing good agreement with both new experimental data and those from the literature. The experimental results were nonmonotonic at higher strains.

A considerable number of analytical models is based on percolation theory. Tallman and Wang (2013) developed an analytical piezoresistivity model for arbitrary strains that can be integrated with FEA, bridging the gap between materials-level (RVE) and structures-level analysis (complicated macroscopic structures subjected to arbitrary strain). The analytical approach was mainly based on percolation theory and excluded volume theory. Their model considered the influence of strain on volume fraction, critical volume fraction, percolation probability, and average inter-filler spacing. The model fitted well with experimental data in the literature in tensile strain range up to 6000 micron-strain but less accurate in compressive strain range, especially from -4000 to -6000 micro-strain where the model fails to capture the piezoresistive saturation. Cattin and Hubert (2014) introduced another percolation theory-based model for positive piezoresistive behavior in polymer nanocomposites containing high aspect ratio particles, i.e. CNT, graphene, and high structure carbon black. This percolation theory-based model related the variation in electrical resistance to compressive strain and accurately fitted experimental data from the literature without relying on assumptions about particle nature or network configuration, but rather on experimentally definable parameters. It explained the piezoresistitivity by a mechanical deformation-induced change in the distribution of local conductance described by a strain-dependent conductivity exponent. The authors

believed the change is caused by reorientation, reshaping, and relative movement of fillers. However, only qualitative explanation was given in this paper. Wang et al. (2019) proposed another percolation theory-based model where pressure increases the volume fraction of conductive filler particles, leading to piezoresistivity. They argued this model provides a simpler physical mechanism and a more accurate fit to data than the tunneling models. The model itself was quite straightforward, but it may not be applicable to 1D or 2D fillers like CNT or graphene because the underlying percolation law is different from the one used for lattice percolation model in this study.

Analytical models for piezoresistive behavior of polymer nanocomposites are crucial for designing innovative materials as these models strike a balance between computational efficiency and physical insight, focusing on primary mechanisms like the tunneling effect, network changes, and filler reorientation. While they often rely on simplified assumptions and might need experimental calibration, their ability to offer generalized relationships makes them indispensable for researchers looking to harness the piezoresistive effect in strain sensing and damage detection applications using polymer nanocomposites.

2.2 Molecular Dynamic Simulations of Polymer and Polymer Nanocomposites

Owing to the diverse range of microstructures present in various polymer nanocomposites and the complex interactions among their constituents, achieving control over the monotony of piezoresistive behavior in polymer nanocomposite has not yet been demonstrated. The most extensively studied factor in this regard is the nanofiller content; however, experimental outcomes remain inconsistent, and its impact on the monotony is notably limited (Boland et al., 2016; Panozzo et al., 2017; Vadlamani et al., 2012; Wichmann et al., 2009). Meeuw et al. investigated the effect of nanofiller alignment, revealing that

aligning nanofillers in the direction of the load through the application of an electric field significantly enhanced monotony, thereby underscoring the importance of network morphology (Meeuw et al., 2016). While MD simulations have offered insights into the microstructural origins of hysteretic piezoresistive responses (Jin et al., 2018), the causes of nonmonotonic responses remain inadequately explained. The primary obstacles in achieving control over the monotony of piezoresistive behaviors in polymer nanocomposites are the intricate microstructures of the constituents and the complex interactions between them, which impede effective control over changes in the nanofiller network morphology in response to mechanical deformation (Kinloch, Suhr, Lou, Young, & Ajayan, 2018).

In this regard, MD simulation is a powerful computational tool used to investigate the behavior of polymer systems at the molecular level, offering insights into phenomena that are difficult or impossible to study experimentally (Rahmat & Hubert, 2011). These include understanding the structure, dynamics, and various physical and mechanical properties of polymers and polymer-based nanocomposites. They address the limitations of spatial and temporal scales inherent in traditional FE simulations by modeling the behavior of atoms and molecules over time. This allows researchers to derive molecular-level insights into phenomena such as plastic deformation, glassy behavior, and the response of polymeric systems to variations in pressure and temperature. This has become more essential for understanding the physical properties of polymer nanocomposites and can aid in the interpretation of experimental data, thereby facilitating the development of innovative nanocomposite designs.

2.2.1 Type of MD models

Various MD models and simulation approaches have been employed to capture the complex behavior of polymers. All-Atomistic MD (AAMD) approach captures the physical and chemical interactions between individual atoms in polymer molecules and/or fillers, i.e. at a fundamental length scale. It has been used to investigate CNT reinforcement effects on polymer deformation, including molecular chain entanglement, covalent bond elongation, and bond dissociation (J. Yang et al., 2022; Zhu, Pan, & Roy, 2007). However, AAMD is computationally intensive, limiting its application to small-scale systems and making it unable to capture microscale damage mechanisms or simulate realistic CNT lengths in microns.

To overcome the computational limitations of AAMD, CGMD models approximate atomic structures and polymer molecules using "coarser bead particles" or "super atoms". A common coarse-grained (CG) approach where polymer chains are represented by connected beads is called bead-spring models. This model can incorporate chain stiffness by including angular bending potentials. These beads interact through effective force fields calibrated to match AAMD or experimental data, significantly reducing computational cost while maintaining molecular details (Arash, Park, & Rabczuk, 2015). CG models can include conformationally relevant degrees of freedom like angles and dihedrals, that can be derived from quantum mechanical simulations (Aramoon, Breitzman, Woodward, & El-Awady, 2016).

2.2.2 Polymers

MD simulation has been demonstrated as an effective technique to better understand the relations between the molecular structure of the crosslinked network and the physical properties of epoxies and their nanocomposites. Through numerically simulating the movement of mutually interacting atoms and molecules in a period of time, physical properties

of the system can be analyzed. Bead-spring model is the most popular model for describing polymer molecules, where a bead can represent a single atom (atomistic system) or a group of atoms (coarse-grained system) and spring refers to the chemical or physical interaction between beads. Variety of polymer molecular structures can be generated controlling the physical parameters of beads and springs (Aoki, Shundo, Kuwahara, Yamamoto, & Tanaka, 2019a; Aramoon et al., 2016; Arash et al., 2015; Moreira, Zhang, Müller, Stuehn, & Kremer, 2015; Varshney, Patnaik, Roy, & Farmer, 2008; W. Yang, Wei, Jin, & Liao, 2007).

A considerable amount of literature has been published on using MD simulations to study the mechanical properties of highly cross-linked polymers (Chowdhury, Elder, Sirk, & Gillespie, 2020; Hoy & Robbins, 2006; Panico, Narayanan, & Brinson, 2010; Tsige, Lorenz, & Stevens, 2004; Shaorui Yang & Qu, 2014). Tsige et al. (2004) established a correlation between the tensile stress-strain behavior and the network structure of highly cross-linked polymers using CGMD simulations. It was found that the failure strain and stress were decreased and increased respectively when the functionality of cross-linker and degree of cross-linking increased, indicating more brittle behavior. Crazing was observed when the functionality and degree of cross-linking were both low. This finding corresponded to the phenomenon induced by high molecular mobility due to heterogeneity in the network structure of epoxy reported by Zhang et al. (2009). Panico et al. (2010) reported similar findings using CGMD simulations as well. More insight was given regarding the strain-hardening stage and the related molecular level processes. Strain-hardening was referred as orientation hardening during the post-yield deformations accompanied by chain scission and chain disentanglement. Highly cross-linked network for thermosetting polymer caused the brittle behavior due to rapid chain scission and inhibited disentanglement. With lower degree of cross-linking, chain disentanglement was favored and lead to localized plastic deformation including crazing. CGMD simulations are well-suited for studying the localized plastic deformation originated in

the network structure of epoxy. For example, Yang and Qu (2014) performed MD simulations on CG model of epoxy phenol novolacs (EPN)-bisphenol A (BPA) and the results were in accordance with previous studies of highly cross-linked polymers.

2.2.3 Polymer Nanocomposites

Various studies have attempted to investigate the physical properties of polymer nanocomposite using MD simulations (Arash et al., 2015; Y. Gao et al., 2015, 2014; Ge, Kalathi, Halverson, Grest, & Rubinstein, 2017; Ma et al., 2017; Papakonstantopoulos, Doxastakis, Nealey, Barrat, & De Pablo, 2007; Zhu et al., 2007). Papkonstantopoulos et al. (2007) studied the impact of spherical nanoparticle on the local mechanical properties of the polymer matrix. Heterogeneity in elastic moduli was induced by the formation of glassy layer, which is region of higher elastic moduli around the nanoparticles. Nonaffine displacement field analysis found that there was tendency for the non-affinely displaced polymer segments to form 'clusters' under deformation. Zhu et al. (2007) performed MD simulations to study the mechanical reinforcement effect of CNT on epoxy using an atomistic system composed of single CNT embedded in EPON 862, which is a matrix of bisphenol F diglycidyl ether (DGEBF). The size of RVE for such atomistic system would be limited due to computational cost.

Therefore, CG systems are preferred for simulations of longer simulation time and larger length scales so that expanded insight into polymer nanocomposites can be afforded on molecular level. Ma et al. (2017) provided molecular insight into the underlying mechanism of the Mullins effect, which has been observed in both filled and unfilled rubber or materials similar to rubber, through large scale MD simulations on CD model of styrene-butadiene-rubber (SBR) filled with saline-functionalized silica nanoparticles. Irreversible disentanglement of polymer chains was identified as the molecular level process occurred

within the polymer matrix that provoke strongly heterogeneous deformation of the nanocomposite and hence the stress softening termed Mullins effect. Gao et al. (2014, 2015) performed CGMD simulations to study the effect of polymer-filler interaction, aspect ratio of nanorods, filler-filler interaction etc. on the mechanical properties and electrical percolation of polymer composite filled with nanorods. The results confirmed the applicability of CGMD models in simulating polymer nanocomposites as processes such as orientation hardening and formation of conductive network could be observed. Analysis on the dispersion states of nanorods was allowed by the large scale of system. Furthermore, the wide range of parameters reflected the efficiency of CGMD simulations.

It is noteworthy that Jin et al. (2018) investigated the microstructural origin of resistance-strain hysteresis in CNT thin film conductors, which are essential for stretchable electronics applications. The researchers used a combination of experiments, coarse-grained molecular statics (CGMS) simulations, and analytic modeling to study this phenomenon. They found that the hysteretic resistance-strain behavior is controlled by a microstructural parameter ξ, which is the ratio of the mean projected CNT length over the film length. The CGMS simulations revealed that the asymmetric behavior of CNT caused the hysteresis. The CNTs re-align and slide during stretching but buckle during unloading (Figure 2.5). Shorter CNTs or those with larger diameters exhibited smaller hysteresis of resistance change on a loading and unloading cycle, which is suitable for strain sensing applications. The CNT concentration had minimal effect on the piezoresistive behavior when it was far above the percolation threshold.

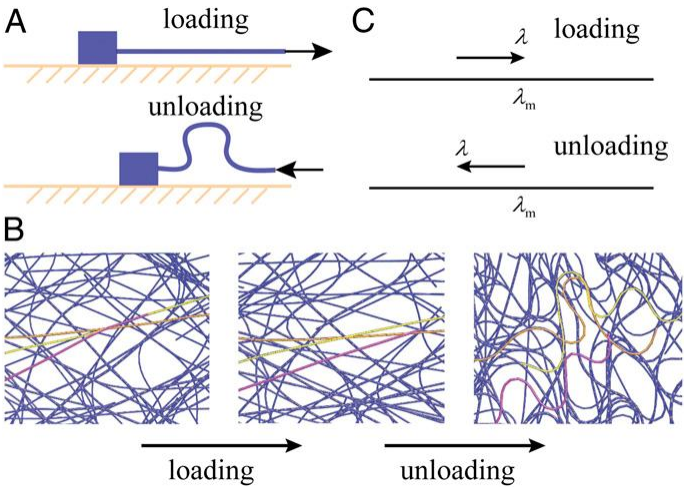

Figure 2.5. Schematic and results of the CNTs morphology during loading and unloading (Jin et al., 2018).

While the study did not directly discuss piezoresistive behavior of polymer nanocomposites, its findings had significant implications for understanding and potentially improving such materials. The study identified a key microstructural parameter (ξ) that governs the resistance-strain hysteresis in CNT films. This insight could be applied to work aiming at better understanding and controlling piezoresistivity. The combined use of experiments, simulations, and analytic modeling in this study provided a comprehensive approach that could be adapted to study piezoresistive behavior in polymer nanocomposites.

2.3 Self-sensing Polymer Nanocomposites for SHM of FRP Composite Structures

Recent advancements in self-sensing polymer nanocomposite materials for SHM of FRP composites have focused on their ability to detect strain and damage through changes in electrical resistance. The core innovation lies in incorporating conductive nanoparticles, such as CNTs and graphene, into insulating polymer matrices. These nanoparticles form a conductive network that exhibits piezoresistive behavior, allowing the composite material itself

to act as a sensor. This "self-sensing" capability offers significant advantages over traditional SHM methods, including reduced intrusion, lower weight, and the potential for multifunctionality. This technique enables real-time, in-situ monitoring of various damage mechanisms, including matrix microcracking, fiber/matrix debonding, delamination, and even fiber breakage, often with higher sensitivity than conventional strain gauges. Advanced sensing techniques, e.g. electrical resistance tomography (ERT), can be integrated with self-sensing composites to localize and characterize damage in both planar and complex geometries.

2.3.1 Laminates

Conductive carbon nanostructures such as CB, CNTs, and graphene have gained much attention and yielded novel nano-engineered FRP composites that demonstrate self-sensing capability (Böger, Wichmann, Meyer, & Schulte, 2008a; Fernberg et al., 2009; L. Gao, Thostenson, Zhang, & Chou, 2009; Ku-Herrera, Pacheco-Salazar, Ríos-Soberanis, Domínguez-Rodríguez, & Avilés, 2016a; Y. Li, Wang, et al., 2018; Monti, Natali, Petrucci, Kenny, & Torre, 2011; Naghashpour & Hoa, 2013; Nofar, Hoa, & Pugh, 2009; Park et al., 2007; Thostenson & Chou, 2006a, 2008). Thostenson and Chou (2006a) processed glass fiber-epoxy composites with 0.5 wt.% multi-walled CNTs dispersed in the epoxy matrix as distributed sensors to detect the onset and evolution of damage in the composites in situ. The CNTs formed electrical conducting paths which impart conductivity to the matrix phase. The changes in electrical resistance were captured simultaneously with applied tensile and flexural loads. The resistance changes were smooth and continuous before the occurrence of damage when the deformation is small. Sharp increases in resistance were associated with the occurrence and accumulation of damages in the composites, which altered and broke the CNT conducing network. Figure 2.6 shows the electromechanical responses of unidirectional and cross-ply

composites indicating the potential capability of strain sensing and damage detection. Further work by the pair (Thostenson & Chou, 2008) and Gao et al. (2009) demonstrated that dispersing CNTs in the matrix phase can be used as a technique to monitor the accumulated damage in real time via electrical resistance change and study the damage evolution and failure mechanism of glass fiber reinforced polymer (GFRP) structures under cyclic loading. The strain sensing capability was demonstrated by the matching curves of resistance change and strain against time with the range of applied strain below 0.2%. The onset of microcrack and accumulation of damage can be detected from the deviation of resistance curve from the strain curve as shown in Figure 2.7. Böger et al. (2008) showed that similar electrical resistance method via nanofiller-modified matrix can be achieved using CB as well. Besides dispersing nanofillers in the matrix, Ku-Herrera et al. (2016) deposited CNTs on to the glass fibers in unidirectional GFRP composites and compared the self-sensing behaviors resulted from two different architectures. Both architectures can self-sense the onset and accumulation of damages during cyclic tensile loading, but the electromechanical responses showed different sensitivity to matrix or fiber-dominated damage. An interesting finding was reported by Nahgasphour and Hoa (2013). In their work, they attempted to measure the through-thickness strain in GFRP laminates using dispersed CNTs in the epoxy matrix and expected that the resistance would decrease with the thickness when the specimen is loaded lengthwise in tension. However, the resistance change was inversely proportional to the through-thickness strain. While the proposed explanation was the increase in separation between CNTs due to lengthwise load, the authors noted the need of further work for clarification.

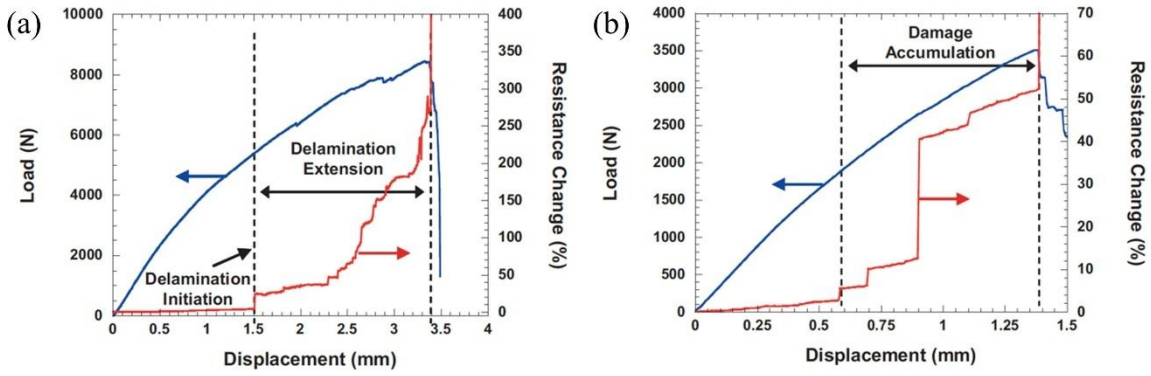

Figure 2.6. Load-displacement and resistance change-displacement curves for (a) the $[0]_5$ specimen with center ply cut to initiate delamination and (b) the $[0/90]_s$ specimen (Thostenson & Chou, 2006). (Adapted from Thostenson & Chou, 2006. Copyright 2025, with permission from Wiley).

Beside GFRP composites, Wang et al. (2018) presented a study on the strain and damage self-sensing capabilities of basalt fiber reinforced polymer (BFRP) composite laminates fabricated with carbon nanofibers (CNFs)/epoxy nanocomposites under tensile loadings. This study explored the effects of CNF content, temperature, and cyclic loading on the piezoresistive response, providing insights into the potential use of these materials for SHM applications. A key finding was the nonmonotonic piezoresistive behavior observed in both CNF/epoxy nanocomposites and CNF/BFRP composites. The phenomenon was explained by the complex interplay of damage accumulation, which tends to increase resistivity, and Poisson's contraction of the matrix and CNF reorientation, which form new conductive networks and decrease resistivity. The study demonstrated that nonmonotonic piezoresistive behavior could occur in FRP composites.

Beyond quasi-static and low-frequency large magnitude cyclic loadings, Li et al. (2018) developed a self-sensing system with dispersed graphene in the epoxy matrix of GFRP laminate that is capable of monitoring strain and damage under quasi-static tensile strains, low-frequency dynamic vibration strains, and ultrasonic guided wave signals. The capability to

capture ultrasonic guided wave signals enabled the self-sensing system to locate barely visible impact damage (BVID) without using conventional lead zirconate titanate (PZT) sensors, hence providing a "sensor-less" methodology for SHM in FRP composites (2020, 2018). Another approach called ERT for detecting and locating damage was proposed recently (Baltopoulos, Polydorides, Pambaguian, Vavouliotis, & Kostopoulos, 2015; Thomas et al., 2019; Viets, Kaysser, & Schulte, 2014). The ERT system developed by Baltopoulos et al. (Baltopoulos et al., 2015) consisted of peripheral electrodes close to the edge of the GFRP composite plate with CNT-modified matrix. Conductivity changes due to crack, notch and delamination etc. can be detected by the electrode array to assess and locate the damages according to the conductivity distribution.

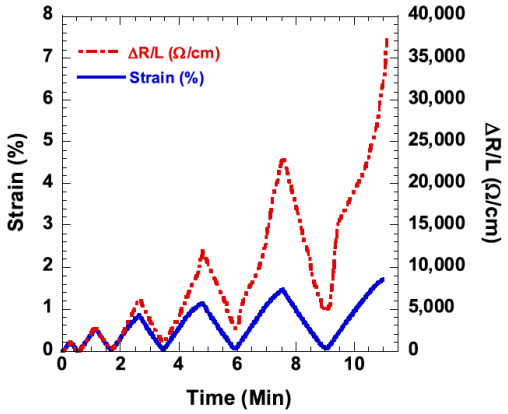

Figure 2.7. Strain-time and resistance change-time curves of a cross-ply laminate under incremental cyclic tensile loading (Thostenson & Chou, 2008). (Adapted from Thostenson & Chou, 2008. Copyright 2025, with permission from IOP Publishing).

2.3.2 Tubes

Despite the excellence and great potential shown in using self-sensing nanocomposites for structural health monitoring in FRP composites, much work is required to promote the

application of this method in real-life industrial non-planar structures. Thomas et al. (2019) and Homa et al. (2019) in particular explored ERT for damage mapping in CB/epoxy GFRP composite tubes. While the technique could detect through-hole and BVID, the sensitivity to damage decreased with the distance between the location of damage and the electrode array. This indicated that there may be a limit of detectability, and the configuration of electrode array requires optimization with respect to the geometries of FRP tube, such as aspect ratio. Yao et al. (2024) developed a piezoresistive behavior-based self-sensing method for composite pipes. Self-sensing joints were manufactured using short carbon fiber composites for SHM of composite pipes. Their performance was evaluated through cyclic internal pressure tests and bursting tests. The self-sensing joints demonstrated high sensitivity to internal pressure changes and damage initiation in composite pipes and exhibited strong correlation between monitoring resistance and the degree of joint damage. By quantitatively characterizing joint damage and analyzing the failure modes, critical monitoring resistance changes that indicate structural safety or potential damage in pipe joints were established. The study concluded that this self-sensing method offers a promising approach for real-time, non-destructive monitoring of composite pipes, providing valuable insights for safety assessment and maintenance decisions. Despite that the self-sensing joints were not FRP composites, these results provided supporting evidence for the application of nano-engineered polymer composites in SHM of FRP structures.

2.4 Numerical Methods for FRP Composites

Numerical methods, particularly FEA and multiscale modeling, have become indispensable tools for predicting, understanding, and optimizing the physical behaviors of composite materials. These methods have enabled studies of composite behavior across different scales, from the nanoscale interactions of fillers to the macroscale response of entire

structures. This section synthesizes current advancements in the numerical analysis of FRP composites, covering multiscale modeling, damage prediction, and the integration of nanofillers.

2.4.1 Finite Element Analysis and Multiscale Modeling Approach

FEA is a widely used and powerful numerical tool for analyzing a broad range of physical behaviors in both FRP composites and hybrid composites with nanofillers (Liew, Pan, & Zhang, 2019; P. F. Liu & Zheng, 2010). These FE models replicate the complex microstructures within FRP composites, including fiber yarns, resin-rich areas, and nanofillers, and consider the interfacial properties between these components. Software like TexGen can be used to generate geometric models of 3D mesoscale RVEs with varying shear angles (Brown & Long, 2020). The heterogeneous mesoscale structure of FRP composites significantly influences their physical properties. To accurately capture this complexity, various multiscale modeling approaches have been developed (Elmasry, Azoti, El-Safty, & Elmarakbi, 2023).

Concurrent multiscale analysis is a method that can accurately capture mechanical behavior across different scales, leveraging properties of mesoscale components to forecast structural responses without relying solely on macroscale constitutive laws. It considers the internal mesoscale structure heterogeneity due to yarn and matrix. For instance, a concurrent multiscale simulation method based on self-consistent clustering analysis (SCA) has been proposed to model the mechanical behavior of profiled composite structures, validated against experimental data for various shear deformations (Z. Liu, Bessa, & Liu, 2016). This approach involves generating a RVE database in an offline stage and coupling macroscale and mesoscale solutions in an online stage. Hierarchical modeling approach has been used for systematic computational studies of hybrid composites with nanofillers. This method can address the

significant difference in dimension scale between FRP composites (mesoscale) and nanoscale reinforcements like CNTs (Dai & Mishnaevsky, 2015).

Homogenization has been an essential technique in multiscale modeling for predicting the macroscopic behavior of heterogeneous composite materials by deriving their effective properties from their micro- or mesoscale components (S. Li, Jeanmeure, & Pan, 2015). It aims to substitute a complex heterogeneous material with an equivalent homogeneous material that possesses the same overall mechanical properties, which is particularly pertinent for materials such as FRP composites with complex mesoscale structures. Homogenization techniques are often applied to RVEs to determine effective orthotropic properties, considering the stiffness of yarn and pure matrix, and the fiber architecture. For example, micromechanical models like the bending-restrained model (BRM) and three-dimensional series-parallel model (3D-SPM) were used for predicting composite properties from constituent yarns and matrices (López-Santos, Hernández-Pérez, Ledesma-Orozco, & Avilés, 2024). Homogenization has been employed in studies for predicting tensile properties, damage evolution, and failure mechanisms in composite structures, aiding in structural design and process optimization.

2.4.1.1 Damage Mechanisms

FEA has been extensively used for damage and failure analysis to simulate damage initiation and propagation in FRP composites. Progressive damage analysis (PDA) is a typical technique that involves determining the onset of material degradation in fiber yarn and matrix (intralaminar) using criteria like Hashin failure criterion, which considers four modes: matrix tension, fiber tension, matrix compression, and fiber compression, and then incorporating the progressive damage, usually through stiffness reduction of damaged elements and redistribution of stress, throughout the models until laminate failure. For interlaminar

delamination, cohesive zone model (CZM) is commonly employed to simulate crack growth and delamination between layers under various loading modes (e.g., Mode I and Mode II tension and shear).

Building upon these established modeling frameworks, Liu et al. (2025) proposed a novel concurrent multiscale analysis method for profiled composite structures that considers the forming process. The method combined preforming simulation of woven fabric composites with a feature reduction scheme to capture the heterogeneous mesoscale structure resulting from the forming process. The approach utilized SCA to efficiently model the mechanical behavior of these structures at multiple scales. Their method was validated against experimental data for various shear deformations and apply it to analyze the progressive failure of a U-shape composite structure. The results demonstrated that the proposed method can accurately predict the nonlinear mechanical behavior and failure mechanisms of profiled composite structures at both macroscale and mesoscale levels, while accounting for the effects of the preforming process.

It is possible to consider the geometrical arrangement of yarns in the composite utilizing FEA. Li et al. (2024) conducted a detailed investigation into the effects of yarn gaps on the tensile failure behavior of multi-layered, multidirectional CFRP composite laminates containing open holes. Through a combination of experimental testing using digital image correlation (DIC), scanning electron microscopy (SEM), and FEA, the study compared the mesoscale model with explicit yarn gaps incorporated to a conventional macroscale model and demonstrates the superior accuracy of the mesoscale model. The researchers identified that the yarn gaps and multi-directionality significantly alter stress distribution and failure mechanisms. It was concluded that accounting for yarn gaps is essential for accurately predicting the mechanical performance of real-world composite structures.

The effectiveness of PDA also depends on the incorporation of damage evolution after initiation. Ferreira, Graciani, and París (2019) presented a study on predicting the failure load of a non-crimp fabric composite using a 3D FE model that incorporates progressive damage. The research focused on a $[0/90]_n$ laminate under compressive loading, utilizing a mesoscale 3D RVE. The study employed various failure criteria, including non-interactive (Maximum Stress and Maximum Strain) and interactive (Hashin and Puck) criteria, to determine the onset of material degradation in the fiber yarns. The material property degradation (MPDG) method was used to incorporate damage evolution. The research examined the progressive damage throughout the mesoscale RVE, from damage initiation to laminate failure, and identified the mechanism responsible for failure. The study found satisfactory agreement between numerical and experimental results for failure stress, failure strain, and compressive stress-strain curves when using the MPDG method with Maximum Stress, Hashin's, or Puck's failure criteria.

2.4.1.2 Mechanical Properties

Fiber orientation plays a critical role in governing the mechanical performance of FRP composites. Wang et al. (2014) developed a FE model to study the effect of fiber orientation on Young's modulus in unidirectional GFRP composites. The results showed a U-shaped dependency of Young's modulus on fiber orientation, with the highest stiffness at 0° (along fiber direction) and the lowest around 60°. The research also explored the impact of shear modulus of fiber and fiber volume content on the Young's modulus. The findings demonstrated the importance of fiber orientation for the microstructural optimization of FRP composites. Gonabadi et al. (2022) presented a comprehensive study on the effects of fiber orientation in GFRP composites, focusing on their tensile and shear properties. The research employed a combined approach using FEA, DIC, and microscopy to assess how fiber orientation impacts

the mechanical properties and failure modes of woven GFRP composites. The study revealed that strain distribution is strongly related to the microstructure and fiber orientation. The research also highlighted the importance of optimizing stacking sequences in composite structures to improve performance. The results indicated that FE models can accurately predict strain distributions in FRP composites and provided insights into heterogeneous localized strains behavior.

For hybrid composites with nanofillers, multiscale FEA was performed by Malekimoghadam and Icardi (2019), who developed a 3D multiscale FE model of hybrid carbon nanotube-carbon fiber (CNT-CF) composites to study the mechanical properties. The 3D multiscale model considered debonding damage across both nano- and macroscales. CZM was employed to model the interfacial interactions and debonding at the interphase of CNT and matrix. The model revealed that CNTs exhibit extraordinary influence on fiber-matrix interfacial properties, and significant enhancements were observed when coated on fibers compared to those with CNTs dispersed in the matrix.

2.4.1.3 Piezoresistive Behaviors

Regarding self-sensing polymer nanocomposites for SHM of FRP composite, Li and Chou (2008) presented FE simulations on strain and damage sensing in cross-ply GFRP composites using embedded CNT networks. Electrical resistance was calculated using equivalent resistor network model considering the tunneling effects when damage progression was simulated using FEA. Information on modeling of nanotube network (e.g., matrix representation of resistor network and Kirchhoff's current law) was comprehensive. The results demonstrated that the nanotube network can detect the onset and evolution of matrix cracking

through measurable changes in electrical resistance. The model captured essential parameters affecting the piezoresistive behavior and shows potential as a tool for SHM of FRP composites.

Nevertheless, there are several limitations in its modeling approach and methodology. These include the use of a simplified 2D model, which may overestimate nanotube contact and conductivity, and a smaller model size with reduced fiber dimensions due to computational constraints. The 2D model also leads to higher stress concentrations at nanotube ends compared to a 3D model. These limitations highlight the challenges in balancing computational feasibility with accurate representation of complex nanocomposite materials. Nevertheless, the continuous progress in computational modeling of FRP composites, particularly with self-sensing capabilities enabled by nanotechnology, is crucial for the design and optimization of future advanced composite materials.

2.5 Summary

This review provides a comprehensive analysis of piezoresistive behavior-based SHM methods for self-sensing polymer composites. It highlights the key results from literature that focused on establishing accurate correlations between electrical resistance and structural health parameters. The review first discusses the underlying mechanism of piezoresistivity in polymer nanocomposites, then identifies a controversy in the monotony of piezoresistive behavior in CNT/epoxy nanocomposites. A synopsis of the numerical methods related to the study of piezoresistivity in polymer nanocomposites are provided. MD simulation may be a promising method to tackle the problem of nonmonotonic piezoresistive behavior, which have not been adequately addressed by current methods like resistor network, analytical, or micromechanics models. The review then moved on to the application of nano-engineered self-sensing polymer nanocomposites for SHM of FRP composite structures. Relevant literature has demonstrated

that accurate extraction of damage features from electrical parameters can be achieved on planar laminates but those for non-planar structures like tubes remain rather limited. The review concludes with an overview of numerical methods on the physical behavior of FRP composites, noting scant attention in the research of numerical investigation on piezoresistive behavior of FRP composites.

CNT/epoxy nanocomposites have been regarded as promising candidates for strain sensing applications, especially for FRP structures. However, the unpredictable variations in electrical resistance when subjected to tensile stress, thereby limiting their practical utility. The root cause of this erratic behavior remains elusive, with various studies proposing brief explanations. Thus far, nonmonotonic piezoresistive behaviors of polymer nanocomposites have been attributed to the viscoelasticity of polymer matrix, the plasticity of matrix, lateral filler movement, and realignment of nanofiller. Controlling this behavior in polymer nanocomposites remains a challenge. Identifying a key microstructural factor may open new approach to tune the monotony of piezoresistive behaviors and provide effect design rule for strain-sensing polymer nanocomposites.

Recent advancements in self-sensing polymer nanocomposite materials have enabled real-time, in-situ monitoring of strain and damage in FRP composites. This self-sensing capability has been demonstrated mainly in FRP laminates, allowing for the detection of various damage mechanisms, including matrix microcracking, fiber/matrix debonding, delamination, and fiber breakage. Challenges remain in applying the methodology to non-planar structures for real-life industrial applications such as FRP tubes, of which the choice of fiber orientation depends on the applications. However, the piezoresistive behavior of nano-engineered FRP composite tubes has not been closely examined.

CHAPTER 3 EFFECT OF CURING CONDITION ON THE PIEZORESISTIVITY OF CARBON NANOTUBE/EPOXY NANOCOMPOSITES

3.1 Introduction

Carbon nanomaterial/polymer composites have shown increasingly rapid advances in the last decades, because the mechanical and physical properties of such a nanocomposite could essentially be customized by choosing the right nanofiller and matrix (Fu et al., 2019; Meng, Fan, Ma, Du, & Geng, 2019). Due to their remarkable mechanical, electrical and thermal properties, carbon nanotubes (CNTs) have been used as the nanofillers in many classic works that aimed at enhancing the mechanical properties of the host materials or at developing new multifunctional materials (Chou et al., 2010; Thostenson et al., 2001). One of the most dominant features of CNT/polymer nanocomposites is that they can achieve electrical percolation at low nanofiller contents, thanks to the high aspect ratio and electrical conductivity of CNTs (Bauhofer & Kovacs, 2009). In the context of multifunctionality, the piezoresistivity of CNT/polymer nanocomposites, which is enabled by conductive CNT networks, represents a major area of interest, because it is fundamental to strain sensing (Alamusi et al., 2011; Chung, 2020; C. Li et al., 2008). Moreover, epoxy has received wide recognition as an ideal matrix material for nanocomposites, owing to its outstanding mechanical properties, chemical resistance and versatility (Gu et al., 2016).

Several studies have reported research on the piezoresistivity of CNT/epoxy nanocomposites under tensile loading. Wichmann et al. (2009) observed that the electrical resistance of a CNT/epoxy nanocomposite would initially increase monotonically and exponentially with tensile strain, but the direction would change from positive to negative when the strain reaches 4%. The critical strain (ε_c) of 4% is common to both the 0.1 wt.% CNT

content sample and the 0.3 wt.% CNT content sample that were used in their study. The negative resistance change vs. strain relationships were ascribed to molecular-level processes that would take place during the viscoelastic and inelastic deformation of an epoxy matrix in the plastic regime, because beyond 2% strain, the resistance change curves appeared to deviate from the exponential behavior and the gradients of the stress-strain curves began to decline. As inversions in piezoresistivity would lead to undefined responses in strain sensing, i.e., one resistance measurement could correspond to two strain values, several attempts have been made to identify the factors that would affect the trend of the piezoresistivity of CNT/epoxy nanocomposites. The most extensively discussed factor is nanofiller content. Vadlamani et al. (Vadlamani et al., 2012) examined the piezoresistive behaviors of CNT/epoxy nanocomposites that are filled with 0.1 wt.%, 0.3 wt.% and 0.5 wt.% of CNTs, and found that the critical strains were 1.5%, 1.9% and 3.9%, respectively. Only the 0.5 wt.% CNT content sample demonstrated a similar critical strain to (Wichmann et al., 2009), and the results of the other samples indicated that an inversion in piezoresistivity could occur at an earlier stage under tensile loading and may not coincide with the plastic regime of the epoxy matrix where the stress-strain curve would show a downturn trend. Although in the literature most CNT/epoxy nanocomposites exhibited non-monotonic piezoresistivity (X. Cao et al., 2017; Meeuw et al., 2016; Panozzo et al., 2017; Vadlamani et al., 2012; Wichmann et al., 2009), contradictory observations have also been made. For instance, Vertuccio et al. (L. Vertuccio et al., 2016; Luigi Vertuccio et al., 2015) fabricated CNT/epoxy nanocomposites with nanofiller contents of 0.025 – 0.5 wt.%, and noticed that the resistance of a sample would increase monotonically with tensile strain all the way until it fails at 3 – 3.5% strain, despite the fact that the sample would enter the plastic regime at 2% strain.

For CNT/epoxy nanocomposites, the divergence in their piezoresistivity remains a critical issue that limits their applicability in strain sensing. Haghoo et al. (Haghgoo, Ansari,

Hassanzadeh-Aghdam, & Nankali, 2022; Haghgoo, Ansari, Kazem Hassanzadeh-Aghdam, Tian, & Nankali, 2022) investigated analytically how the physical properties of the CNT nanofillers in a CNT/polymer nanocomposite would influence the piezoresistive properties of the nanocomposite. However, little attention has been paid to the role of the polymer matrix. In fact, the mechanisms that underpin the electromechanical response of a CNT/polymer nanocomposite are highly complex and built upon molecular-level phenomena that are related to the physical properties of both the CNT nanofillers and the polymer matrix, as well as the interactions between the two constituents (Avilés et al., 2018). Since it has been shown that both the electrical and the mechanical properties of CNT/epoxy nanocomposites can be modified by adopting different curing conditions (Ci & Bai, 2006; de Villoria, Miravete, Cuartero, Chiminelli, & Tolosana, 2006; Faiella et al., 2012; N. Hu, Masuda, et al., 2008; Montazeri, Khavandi, Javadpour, & Tcharkhtchi, 2010), it is reasonable to speculate that their piezoresistivity, which essentially reflects the coupling between their electrical and mechanical responses, would be influenced by curing condition. However, such correlation has not yet been explicitly demonstrated.

In this study, different curing cycles were employed to fabricate CNT/epoxy nanocomposite samples. The electromechanical responses of the samples were acquired via quasi-static tensile tests. Based on the experimental results obtained, the effect of curing condition on the piezoresistivity of CNT/epoxy nanocomposites was preliminarily established.

3.2 Methods

3.2.1 Materials and Sample Fabrications

Chemical vapor deposition-grown multiwalled carbon nanotubes (purity: >95%, outer diameter: 50–90 nm, aspect ratio: >100) were purchased from Sigma-Aldrich, USA. Bisphenol

A diglycidyl ether-based epoxy resin (EL2) and cycloaliphatic amine-based epoxy hardener (AT30 Slow) were supplied by Easy Composites, UK. The fabrication process for CNT/epoxy nanocomposite samples is schematically illustrated in Figure 3.1a. CNTs were dispersed into epoxy resin through a mechanical approach. At first, CNT/epoxy resin mixture was mechanically stirred for 1 h at 2000 rpm using an overhead stirrer (Hei-TORQUE Core, Heidolph Instruments, Germany) with a radial flow impeller (TR 21, Heidolph Instruments, Germany). During stirring, the mixture was heated to 60 °C to reduce viscosity. Then, the mixture was sonicated in an ultrasonic bath (RS PRO Ultrasonic Cleaner, RS Components, UK) for 30 min. After degassing it at 40 °C in a vacuum oven for 1 h, the mixture was blended with epoxy hardener at a resin-to-hardener weight ratio of 10:3. Finally, the CNT/epoxy resin/epoxy hardener mixture was poured into a silicone mold of dumbbell-shaped tensile specimens and cured under one of the cycles shown in Table 3.1. Both Cycle A and Cycle B consist of a 24 h or 12 h room temperature curing stage and a 6 h, 60 °C post-curing stage. On the other hand, direct heat curing was applied in Cycle C (40 – 60 °C), Cycle D (60 °C) and Cycle E (80 °C). These curing cycles were selected based on manufacturer recommendations and preliminary trial. Samples with different CNT contents (i.e., 0.1 wt.%, 0.2 wt.%, and 0.3 wt.%) were prepared under Cycle A and Cycle D, in order to further evaluate the influence of curing condition on the piezoresistivity of CNT/epoxy nanocomposites at different nanofiller contents. The samples are labelled as X-CNT/epoxy-Y, where X indicates the curing cycle adopted, and Y the CNT content of the sample.

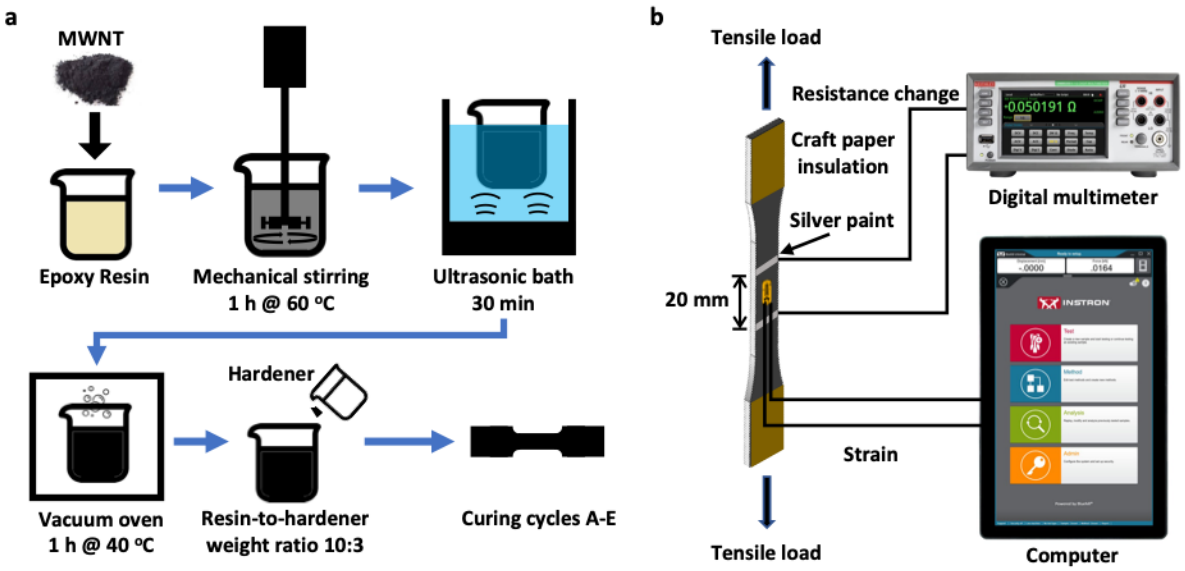

Figure 3.1. Fabrication and electromechanical test setup. a) Fabrication procedures of CNT/epoxy nanocomposite samples. b) Experimental setup for quasi-static tensile tests with simultaneous electrical resistance measurements.

Table 3.1. Processing conditions of CNT/epoxy nanocomposites.

Curing cycle	Nanofiller content [wt.%]	Curing temperature and time	Post-curing temperature and time
A	0.1, 0.2, 0.3	Room temperature for 24 h	60 °C for 6 h
B	0.3	Room temperature for 12 h	60 °C for 6 h
C	0.3	40 °C for 2 h, 50 °C for 2 h, 60 °C for 5 h	N/A
D	0.1, 0.2, 0.3	60 °C for 6 h	N/A
E	0.3	80 °C for 6 h	N/A

3.2.2 Electrical Conductivity Measurement

The electrical resistances of the MWNT/epoxy nanocomposite samples were measured via the two-probe method using a digital multimeter (DMM6500, Keithley Instruments, USA). On every sample, a pair of parallel electrodes were marked using conductive silver paint (RS PRO Conductive Lacquer, RS Components, UK), 20 mm apart from each other, as shown in Figure 3.1b. The electrical conductivity (ρ) of each sample was calculated by

$$\rho = \frac{L}{A \cdot R} \tag{3.1}$$

where L is the distance between the two electrodes, A is the cross-sectional area of the sample, and R is the resistance of the sample.

3.2.3 Electromechanical Tests

Quasistatic tensile tests were performed on the CNT/epoxy nanocomposite samples using a universal testing machine (5982, Instron, USA). A minimum of three specimens were tested for each sample. The specimens were loaded at a crosshead speed of 1 mm min^{-1} until failure. During loading, the electrical resistance and axial deformation of the specimens were measured simultaneously, as illustrated in Figure 3.1b. Craft paper was bonded to the gripping areas of the specimens using a cyanoacrylate adhesive to electrically insulate the conductive specimens using a universal testing machine. Strain measurements were acquired through uniaxial strain gauges (gauge length: 5 mm, gauge factor: 2.07, resistance: 120 Ω; BFLA-5-3-1LJB, Tokyo Measuring Instruments Laboratory, Japan).

3.3 Results and Discussion

CNT/epoxy nanocomposite samples (CNT purity: >95%, CNT outer diameter: 50-90 nm, CNT aspect ratio: >100) were cured under different cycles. The CNT content was fixed at 0.3 wt.%, which is just beyond the percolation region as shown in Figure 3.2. Figure 3.3 compares the electrical conductivities of samples with 0.3 wt.% nanofillers that were cured under different cycles. The results indicate that the electrical conductivity of a sample could be increased by either a reduction in room-temperature curing time (Cycle A and Cycle B) or an increase in curing temperature (Cycle C, Cycle D, and Cycle E). This observation is in line with previous studies (Faiella et al., 2012; N. Hu, Masuda, et al., 2008) which showed that a higher curing temperature would enhance the formation of a conductive network due to temperature-induced agglomeration of nanofillers, leading to a higher electrical conductivity in the resultant CNT/epoxy nanocomposite.

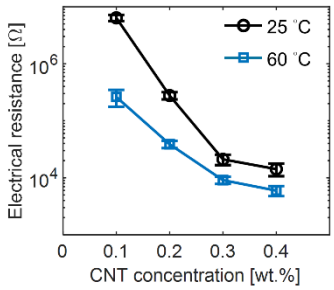

Figure 3.2. Experimental electrical resistance of CNT/EL2 nanocomposites at different CNT concentrations. At least three specimens were tested for each sample. Error bar represents ±1 standard deviation.

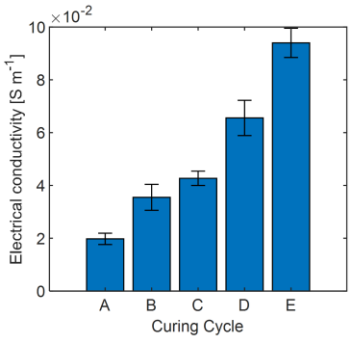

Figure 3.3. The electrical conductivities of CNT/epoxy-0.3 samples that were cured under different cycles (for each sample, three specimens were tested and the mean measurement is plotted (error bar: ±1 standard deviation)).

Figure 3.4 shows the electromechanical responses of samples with 0.3 wt.% nanofillers that were cured under different cycles. The most striking finding that emerged from these results is that samples that are cured under two different cycles could exhibit drastically different electrical resistance change vs. tensile strain relationships. For the Cycle A, Cycle B and Cycle C samples, inversions in piezoresistivity occurred at around 0.28% strain, 0.36% strain and 0.89% strain, respectively. The resistance of each of these samples first increased with strain, reaching its maximum at the respective critical strain, and then decreased until the sample failed. On the other hand, both the Cycle D and Cycle E samples demonstrated monotonic piezoresistive behavior until failure. For each of these samples, the resistance increased exponentially when the strain was below ~1%, most likely because in the early stage of the tensile deformation of a CNT/epoxy nanocomposite, the quantum tunneling effect is the dominant cause of the resistance change (N. Hu, Karube, et al., 2008; Panozzo et al., 2017; Wichmann et al., 2009). For a material that is oriented towards strain sensing, having a monotonic piezoresistive behavior, even if it is nonlinear, would be absolutely crucial (Meeuw et al., 2016; Luigi Vertuccio et al., 2015). The results presented indicate that the piezoresistivity of CNT/epoxy nanocomposites can be significantly affected by curing condition.

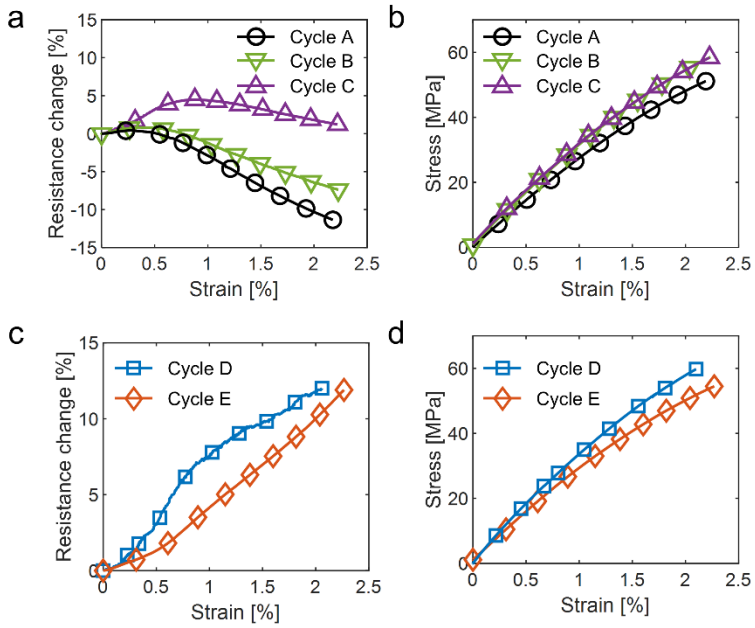

Figure 3.4. a,c) Piezoresistive behaviors and b,d) stress-strain curves of CNT/epoxy-0.3 samples that were cured under different cycles (for each sample, three specimens were tested, and the mean response is plotted).

A phenomenological description that incorporates the underlying mechanisms discussed in Chapter 2.1.1 is proposed to explain the nonmonotonic piezoresistive behavior of the Cycle A, Cycle B and Cycle C samples. First of all, it has been widely accepted that the piezoresistivity of polymer nanocomposites is mainly driven by deformation-induced construction and destruction of conductive path, which are governed by the distances between adjacent nanofillers (Avilés et al., 2018). Under a tensile deformation, the CNTs in a nanocomposite should move away from each other, and as a result, the number of conductive paths in the nanocomposite should decrease and the electrical resistance of the nanocomposite should increase. However, in previous studies as well as this work, negative resistance change vs. strain relationships have been observed in CNT/epoxy nanocomposites beyond certain strain levels, indicating that there were processes that, under tensile strain, reduced the

distances between adjacent nanofillers and/or increased the number of conductive paths (X. Cao et al., 2017; Meeuw et al., 2016; Panozzo et al., 2017; Vadlamani et al., 2012; Wichmann et al., 2009). These processes were likely to be molecular motions that pertain to the viscoelastic and plastic deformations of the polymer matrices, e.g., plastic flow, alignment of molecular chains, and elongation of entangled molecular chain clusters.

The electromechanical responses of all samples, including the Cycle A and Cycle D samples with 0.1 wt.% and 0.2 wt.% nanofillers, are presented in Figure 3.5, Figure 3.6, and Figure 3.7. From the results, it can be seen that while the strain sensitivity (i.e., the gradient of the resistance change vs. strain curve) of a CNT/epoxy nanocomposite would decrease with nanofiller content, nanofiller content would not affect the monotony of the piezoresistive behavior of the nanocomposite nor the critical strain of the nanocomposite.

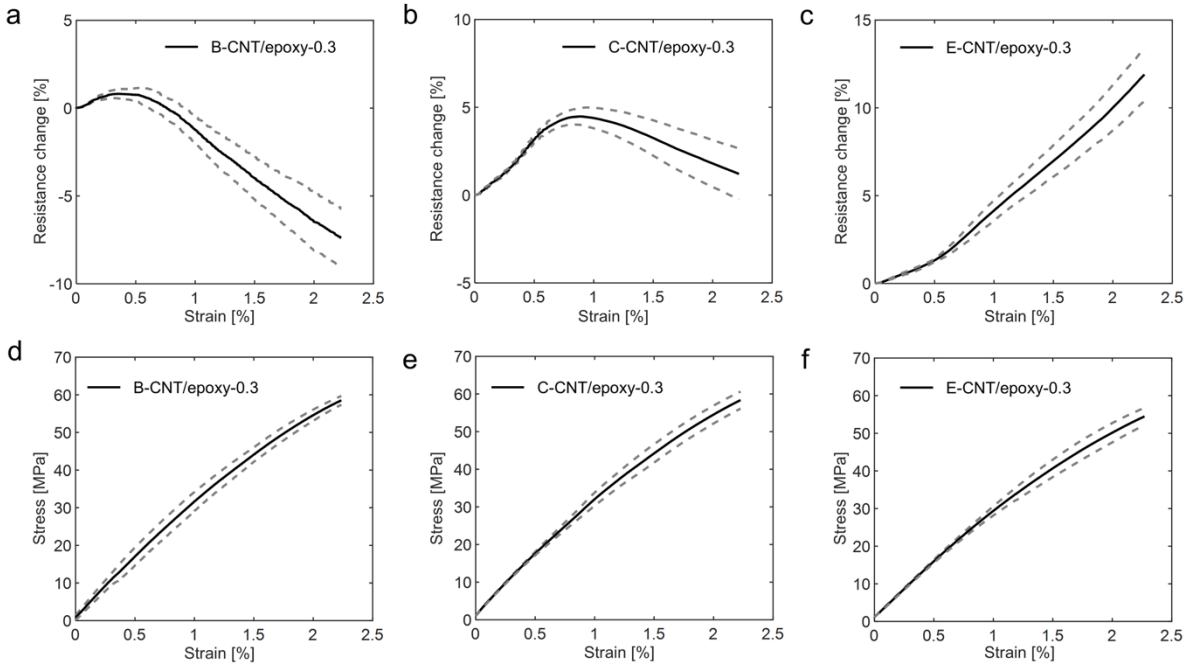

Figure 3.5. The electromechanical responses of a,d) B-CNT/epoxy-0.3, b,e) C-CNT/epoxy-0.3, and c,f) E-CNT/epoxy-0.3 (for each sample, three specimens were tested and the mean response is plotted (dotted lines: ±1 standard deviation)).

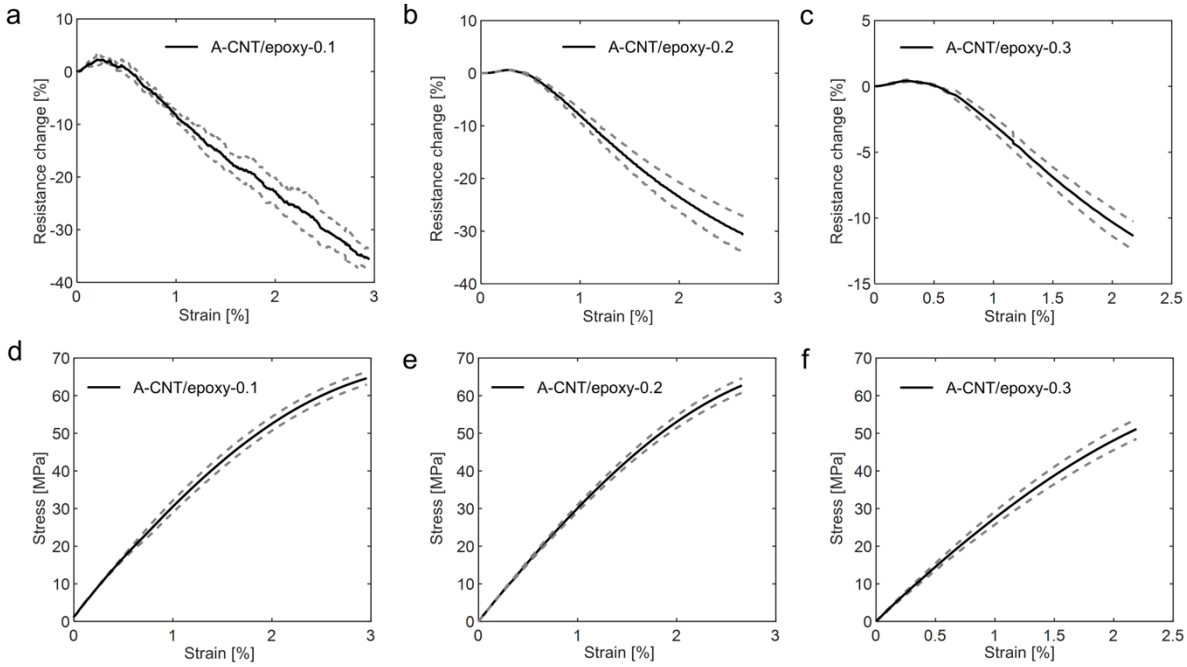

Figure 3.6. The electromechanical responses of a,d) A-CNT/epoxy-0.1, b,e) A-CNT/epoxy-0.2, and c,f) A-CNT/epoxy-0.3 (for each sample, three specimens were tested and the mean response is plotted (dotted lines: ±1 standard deviation)).

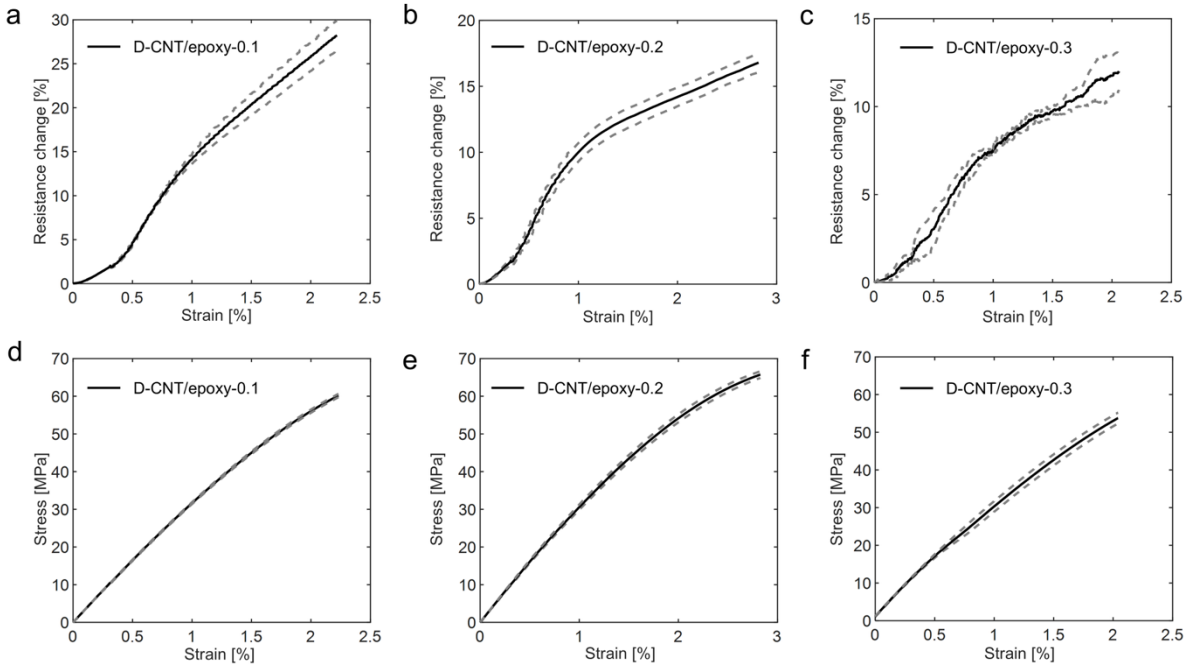

Figure 3.7. The electromechanical responses of a,d) D-CNT/epoxy-0.1, b,e) D-CNT/epoxy-0.2, and c,f) D-CNT/epoxy-0.3 (for each sample, three specimens were tested and the mean response is plotted (dotted lines: ±1 standard deviation)).

In addition, pristine EL2 epoxy resin samples were prepared and cured under Cycle A and Cycle D. Comparing the stress versus strain relationships between pristine samples in Figure 3.8 and CNT/epoxy nanocomposites in Figure 3.5d-f, Figure 3.6d-f, and Figure 3.7d-f, the mechanical properties remained similar with different curing conditions and nanofiller contents. The tensile strength and Young's modulus were around 50 MPa and 3 GPa, respectively. Both pristine resins and nanocomposites exhibited brittle fractures, indicating that the presence of CNTs did not modify the inherent brittle nature of epoxy.

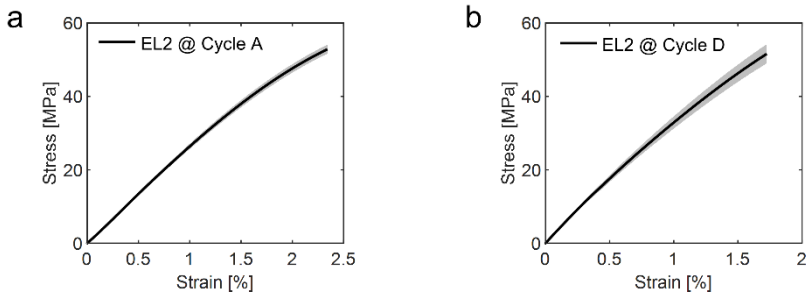

Figure 3.8. Experimental stress versus strain relationships of EL2 epoxy resin cured under (a) Cycle A and (b) Cycle D. For each sample, three specimens were tested and the mean response is plotted (shaded area: ±1 standard deviation).

3.4 Conclusion

This chapter examines the effect of curing condition on the piezoresistivity of CNT/epoxy nanocomposites under tensile loading. The results reveal that the piezoresistivity changed from non-monotonic to monotonic when the curing temperature increased from room temperature to 60 °C. The findings reported here shed new light on the mechanisms that govern the piezoresistivity of CNT/epoxy nanocomposites, which will be elucidated by further molecular dynamic simulations and experimentation.

CHAPTER 4 MICROSTRUCTURAL ORIGIN OF NONMONOTONIC PIEZORESISTIVITY IN POLYMER NANOCOMPOSITES

4.1 Introduction

In this study, both physical experiments and CGMD simulations are employed to address the challenge of nonmonotonic piezoresistive behavior of CNT/epoxy nanocomposites, demonstrating that complete control over the monotony of the piezoresistivity can be achieved by regulating the initial inter-nanofiller junction geometry. Our experimental results, together with numerical evidence, suggest that during curing, barrier crossing of nanofillers due to van der Waals (vdW) interactions occurs, leading to direct contact between nanofillers. In addition, the initial inter-nanofiller junction geometry of the developed nanofiller network is directly determined by the degree of diffusion. During deformation, stress-driven local rearrangements of polymer molecules in heterogeneous shear transformation zones can trigger barrier crossing of the nanofillers, further modifying the inter-nanofiller junction geometry. For a nanofiller network that is developed under active diffusion, the agglomerated nanofillers would, by and large, move away from each other during deformation, causing the overall resistance to increase. However, when diffusion is suppressed, re-agglomeration of the nanofillers occurs during deformation, resulting in a reduction in resistance. The initial inter-nanofiller junction geometry, which governs the monotony of the piezoresistive behavior of polymer nanocomposites, can be modulated by the curing temperature, polymer molecular structure, and alignment of the nanofiller, all of which influence nanofiller mobility during curing.

4.2 Methods

4.2.1 Materials and Sample Fabrications

The methodology employed here follows that described in Chapter 3.2.1, with the following modifications:

Another high-purity bisphenol A diglycidyl ether (DGEBA) liquid epoxy resin (DER332), and a polypropylene glycol-based polyetheramine curing agent, with an average molecular weight of approximately 230, were purchased from Sigma-Aldrich, USA. The CNT/epoxy nanocomposite samples, using either the DER332/polyetheramine system or the EL2/AT30 Slow system, were fabricated using a mechanical approach (Figure 4.1a). After blending the mixture with an epoxy hardener at a resin-to-hardener weight ratio of 1000:344 for the DER332/polyetheramine system and 10:3 for the EL2/AT30 Slow system, it was degassed in a vacuum oven. Finally, the CNT/epoxy resin/epoxy hardener mixture was poured into a silicone mold of dumbbell-shaped tensile specimens and cured at various temperatures ranging from room temperature to 100 °C (Table 4.1). For the DER332/polyetheramine system, the curing conditions were selected based on the crosslinking dynamics of the curing process characterized using Fourier-transform infrared spectroscopy as described in Chapter 4.2.5 and Appendix A2. For the EL2/AT30 Slow system, three curing conditions that correspond to Cycle A, Cycle D, and Cycle E in CHAPTER 3 were selected to demonstrate its curing dependent piezoresistive behavior. The CNT content is fixed at 0.3 wt. % based on the results in CHAPTER 3.

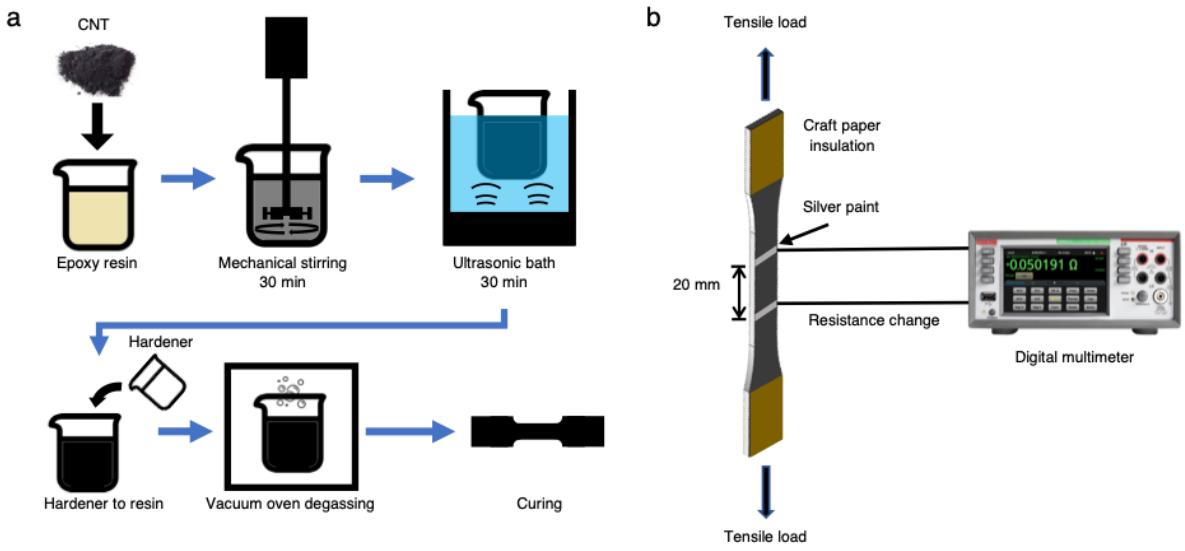

Figure 4.1. Fabrication and electromechanical test setup. a) Fabrication procedures of CNT/epoxy nanocomposite samples. b) Experimental setup for quasi-static tensile tests with simultaneous electrical resistance measurements.

Table 4.1. Processing conditions of CNT/epoxy nanocomposites.

Samples	Curing temperature [°C]	Curing time [h]	Post-curing temperature [°C]	Post-curing time [h]
CNT/DER332	60	6	125	3
	70	4		
	80	3		
	100	1		
CNT/EL2	25	24	60	6
	60	6	n/a	
	80	6		

4.2.2 Electromechanical Tests

The methodology employed here follows that described in Chapter 3.2.3, with the following modifications:

The deformation of the specimens was calculated using machine crosshead displacement (Figure 4.1b).

4.2.3 Microstructural Analysis

The morphology of the CNT network was imaged using a field-emission scanning electron microscope (FESEM; MAIA3, TESCAN, Czech Republic) operating at 5 kV. The imaging surfaces were processed using an ultramicrotome (PowerTome-XL, RMC Boeckler, USA) and coated with a thin layer of gold via sputtering (MCM-200, NanoImages, USA). Micrographs were collected at four or more locations on each specimen to characterize the dispersion state of the CNTs.

4.2.4 Electrical Conductivity Measurement

The methodology employed here follows that described in Chapter 3.2.2.

4.2.5 Fourier Transform Infrared Spectrometry

Fourier transform infrared spectra were collected *in situ* using an IR spectrometer (Spectrum Two, PerkinElmer, Waltham, MA, USA) equipped with a deuterated triglycine sulfate detector. A mixture of DER332 and a polyetheramine curing agent was sandwiched between potassium bromide windows using a 2-mm PTFE spacer. All the spectra were obtained

in the region of 8000–4000 cm^{-1} with a resolution of 4 cm^{-1} and 16 scans during isothermal curing. Spectral analysis was performed using the Spectrum 10 software (PerkinElmer, USA).

4.2.6 Dynamic Shear Rheology

Dynamic rheological measurements were performed using an oscillatory rheometer (MCR702 TwinDrive Rheometer, Anton Paar, Austria) to determine the shear flow characteristics of the DER332 and EL2 epoxy matrices. A 25-mm diameter parallel plate with a 1-mm gap configuration were used. The steady shear viscosity was measured at a shear rate of 0.1–100 s^{-1} and temperatures ranging from 20 to 80 °C.

4.2.7 Molecular Dynamic Simulations

To investigate the microstructural origin of the nonmonotonic piezoresistive behavior in CNT/epoxy nanocomposites, the CGMD method was utilized to simulate and analyze the dynamic percolation of CNTs and the dynamic crosslinking process of epoxy at different temperatures, as well as the CNT movement and morphological changes in the CNT network under deformation, using the MD package LAMMPS (Thompson et al., 2022) and a post-processing visualization tool OVITO (Stukowski, 2010). The unit cell contained randomly dispersed CNTs and an epoxy polymer matrix, both of which were represented by a bead-spring model. A reduced-unit formalism is adopted. All physical quantities are expressed as multiples of fundamental quantities, mass (m), energy (ϵ), distance (σ) and Boltzmann constant (k_B) which are all set equal to one in the simulation. This approach has been widely adopted in MD simulations to focus on relative interactions and dynamics rather than absolute physical values, particularly when the goal is to capture qualitative trends and mechanisms.

4.2.7.1 Pair Potential

The nonbonded or van der Waals interactions between all beads are represented by the truncated and shifted Lennard-Jones (LJ) potential

$$U_{\mathrm{LJ}}(r) = 4\varepsilon\left[\left(\frac{\sigma}{r-\Delta}\right)^{12} - \left(\frac{\sigma}{r-\Delta}\right)^{6}\right] \tag{4.1}$$

where r is the distance between beads, ε is the interaction parameter or the depth of the potential, σ is the distance parameter or the zero-crossing distance for the potential, and Δ is the shift factor for the change in the size of bead, with a cutoff distance of 2.5 σ. Each CNT or polymer chain is discretized into a series of beads that interact with adjacent bonded beads on the same molecule, the stretching stiffness of which is accounted for by a stiff finite extensible nonlinear elastic (FENE) bond potential

$$U_{\mathrm{FENE}}(r) = -0.5K_{\mathrm{FENE}}R_0^2\, ln\left[1 - \left(\frac{r-\Delta}{R_0}\right)^2\right] \tag{4.2}$$

where K_{FENE} is the coefficient for the stretching stiffness of the bond, and $R_0 = 1.5\,\sigma$ is the equilibrium bond length. The stretching stiffness coefficients for the polymer and CNT chains are set as 30 $\epsilon\,\sigma^{-2}$ and 80 $\epsilon\,\sigma^{-2}$ respectively to reflect the higher stretching stiffness of CNT than polymer. The bending stiffness of the CNT was introduced using a harmonic angle potential

$$U_{\mathrm{angle}}(\theta) = K_{\mathrm{angle}}(\theta - \theta_0)^2 \tag{4.3}$$

where θ is the bond angle of CNT beads, $K_{\mathrm{angle}} = 10\,\epsilon\,\sigma^{-2}$ is the coefficient for the bending stiffness of the chain, and $\theta_0 = 180^{\mathrm{o}}$ is the equilibrium value of the angle potential. These parameters (e.g., interaction strength ϵ, bond stiffness K_{FENE}, and bending stiffness K_{angle}) are tuned to qualitatively represent the relative differences in interactions (e.g., higher stiffness for CNTs compared to polymer chains) rather than to match exact physical ratios. In addition, the

mass of a CNT bead (m_{CNT}) was set to 2 m when the diameter was 1 σ and scaled with its diameter to better reflect the differences in the CNT and polymer matrices.

4.2.7.2 Simulation Methods

The initial configurations of the CNTs are randomly created with the relative orientation of consecutive bonds ($\theta - \theta_0$) less than a maximum deviation angle to account for the waviness of CNT (Matos et al., 2018). The simulation boxes are then filled by a liquid mixture of two-bead, three-bead or five-bead chains representing the epoxy resin molecules and crosslinker beads to a desired number density of $\sim 1\ \sigma^{-3}$ (Tsige et al., 2004). The functionalities of the epoxy and crosslinker beads were set to 1 and 4, respectively, to simulate a typical DGEBA/diamine epoxy system. The number ratio between the resin molecules and crosslinker beads was set using stoichiometry.

The overlap between the randomly placed beads was first removed by applying a cosine-pairwise potential

$$U_{\mathrm{soft}} = A\left[1 + cos\left(\frac{\pi r}{r_{\mathrm{cutoff,soft}}}\right)\right] \tag{4.4}$$

where $r_{\mathrm{cutoff,soft}}$ is the cutoff distance, and is set as the bead diameter. The amplitude A is increased from 0.0 to 30.0 $\epsilon\ \sigma^{-2}$ over the span of 500,000 time steps for the overlapping removal stage. Then, the nonbonded interaction is switched back to the LJ potential and equilibrated at $T = 1.0\ \epsilon\ k_B^{-1}$ for 500,000 time steps. To disperse the CNTs, the interaction parameter between CNT and polymer beads ε_{np} is set to 2.0 ϵ (Y. Gao et al., 2015) and further run the simulations for 500,000 time steps. The dispersed state is verified by a single strong peak at approximately $r = \sqrt{3}\ \sigma$ in the radial distribution function of the CNT beads $g_{nn}(r)$, as shown in Figure 4.2. Subsequently, the systems are cooled to the curing temperature, which

is varied from 0.3 to 0.7 $\epsilon\, k_B^{-1}$, over 250,000 time steps. After setting ε_{np} to 1.0 ϵ, further equilibrium is performed at their respective curing temperatures for 1,000,000 time steps.

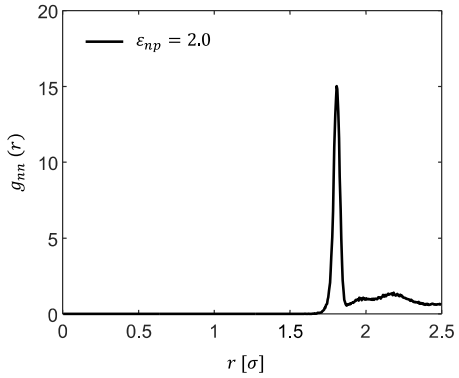

Figure 4.2. Radial distribution function of CNT beads $g_{nn}(r)$ for interaction parameter between CNT and polymer beads ε_{np} set to 2.0 ϵ.

Liquid mixtures of resin molecules and crosslinker beads were dynamically crosslinked to form a three-dimensional molecular network of the epoxy (Shaorui Yang & Qu, 2014). Bonds between the epoxy beads and crosslinker beads are formed when their separation is less than 1.3 σ. Possible bonding sites are checked every 10 time steps, and a probability of 0.1 for bond formation is assigned to avoid drastic changes in the system energy. This dynamic crosslinking process was conducted until a conversion degree of 95% was reached or stopped when no more bonds were formed within 100 time steps. Thereafter, the systems are quenched from their respective curing temperature to 0.3 $\epsilon\, k_B^{-1}$, which is below the glass transition temperature of such CGMD model for epoxy (0.5 $\epsilon\, k_B^{-1}$) (Tsige et al., 2004), over a span of 500,000 time steps and equilibrated for 3,000,000 time steps.

To simulate the piezoresistive behavior, tensile deformation is applied by elongating the simulation cell along the x direction at a strain rate of $2\times10^{-5}\ \tau^{-1}$, where $\tau = \sqrt{m\sigma^2/\epsilon}$ is the reduced unit of time (Panico et al., 2010), while adjusting the cell sizes in the y and z directions

to maintain zero-stress state. Periodic boundary conditions were applied in all the three directions throughout the simulation. The configurations of the CNT networks are outputted every 10,000 time steps or 50 τ for calculation of electrical resistance using a resistor network model, as discussed in Chapter 4.2.8.

4.2.8 Resistor Network Model

The resistance-strain relationship was obtained by calculating the electrical resistance of the CNT network in discrete strain increments using the equivalent resistor network method (Jin et al., 2018). The CNT network was transformed into an equivalent resistor circuit with each CNT bead as a node in the circuit such that nodal analysis could be applied to calculate the electrical resistance (Figure 4.3). Two transport mechanisms, intrinsic conductance and the tunnelling effect, are considered to contribute to the electrical conduction path of the CNT network. In the intrinsic conductance mechanism, charge transport along each CNT is described by a series of resistors connecting neighboring nodes with resistance, given by

$$R_{\text{node}} = \frac{R_{\text{CNT}}}{N_{\text{node}} - 1} \tag{4.5}$$

where R_{CNT} is the total resistance of a CNT and N_{node} is the number of nodes per CNT. Notably, in a given configuration, all the CNTs have the same length or number of nodes. It is assigned that $R_{\text{CNT}} = 17.3\ \text{k}\Omega$ even though the overall resistance change is largely unaffected by R_{node} or R_{CNT}, which, in reality, is multiple orders of magnitude smaller than the tunnelling resistance R_{tunnel}. For the tunnelling mechanism, when the distance between the CNT beads from two CNTs is smaller than the tunnelling cutoff distance d_{cutoff}, which is set as 2.5 σ, the charge transport between the CNT pair is described by a resistor connecting the node pair with the lowest separation d_{tunnel}, given by

$$R_{\text{tunnel}} = \frac{h}{2e^2}\frac{1}{MT_{\text{prob}}} \tag{4.6}$$

where h is Planck's constant, e is the electron charge, and M = 400 is the total number of conduction channels (Büttiker, Imry, Landauer, & Pinhas, 1985). The transmission probability T_{prob} was estimated by solving the Schrödinger equation with a rectangular potential barrier as

$$T_{\text{prob}} = \exp\left(-\frac{d_{\text{tunnel}}}{d_{\text{char}}}\right) \tag{4.7}$$

with the tunnelling characteristic length given by

$$d_{\text{char}} = \frac{h}{2\pi\sqrt{8m_e W}} \tag{4.8}$$

where m_e is the electron mass and $W = 1.5$ eV is the work function difference between the CNTs and the polymer barrier (N. Hu, Karube, et al., 2008). The tunnelling distance d_{tunnel} was transformed from LJ units to real (SI) units as

$$d_{\text{tunnel,real}} = d_{\text{vdW,real}} + \frac{(d_{\text{cutoff,real}} - d_{\text{vdW,real}}) \times (d_{\text{tunnel,LJ}} - d_{\text{vdW,LJ}})}{d_{\text{cutoff,LJ}} - d_{\text{vdW,LJ}}} \tag{4.9}$$

where $d_{\text{vdW,real}} = 0.34$ nm is the van der Waals distance between CNTs in real unit, $d_{\text{cutoff,real}} = 1.0$ nm is the tunnelling cutoff distance in real unit (N. Hu, Karube, et al., 2008), and $d_{\text{vdW,LJ}} = 2^{1/6}\,\sigma$ is the van der Waals distance between CNTs in LJ unit. Periodic boundary conditions were applied in the y and z directions to minimize the influence of the simulation cell size (Bao, Meguid, Zhu, & Meguid, 2011; Jin et al., 2018).

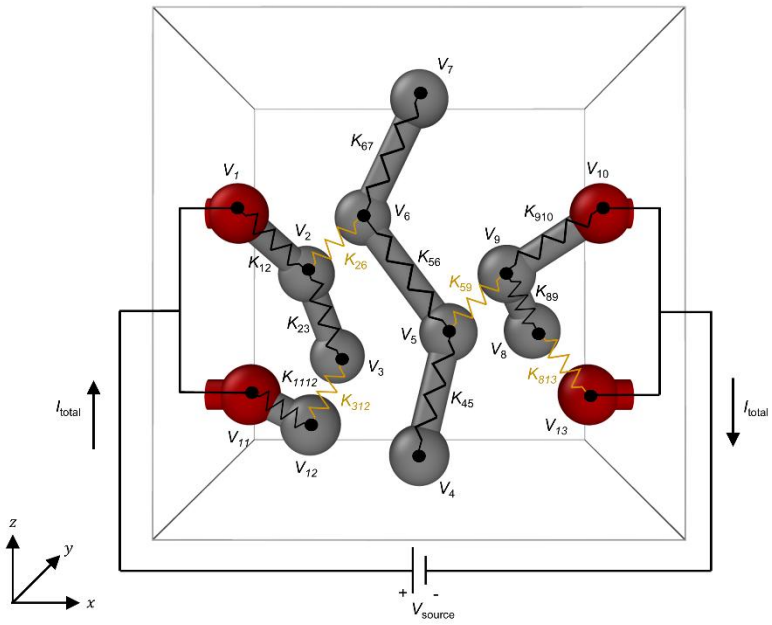

Figure 4.3. Schematic of the equivalent resistor network model.

According to Kirchhoff's current law, the elemental matrix representation of the relation between the external input current I passing through a resistor connecting nodes i and j and the nodal voltage V is

$$\begin{Bmatrix} I_i^e \\ I_j^e \end{Bmatrix} = [K_{ij}^e] \begin{Bmatrix} V_i \\ V_j \end{Bmatrix} = \frac{1}{R_{ij}^e} \begin{bmatrix} 1 & -1 \\ -1 & 1 \end{bmatrix} \begin{Bmatrix} V_i \\ V_j \end{Bmatrix} \tag{4.10}$$

where K_{ij}^e is the element conductance and R^e is the element resistance (C. Li & Chou, 2007). The elemental matrices for all the resistors were then assembled into a system of algebraic equations for the entire CNT network as

$$\mathbf{I}=\mathbf{KV} \tag{4.11}$$

where $\mathbf{V} = \{V_1, V_2, \dots, V_n\}^T$ is the vector of the nodal voltages, $\mathbf{I} = \{I_1, I_2, \dots, I_n\}^T$ is the vector of the external input current, and $\mathbf{K}$ is the global conductance matrix

$$\mathbf{K} = \sum_{e=1}^{m} [K_{ij}^e] \tag{4.12}$$

where m is the number of resistance elements. To solve Equation (4.11), it is assumed that a source voltage V_{source} of 1 V was applied at the two boundaries of the loading direction; that

is, at the two y-z surfaces. Under the periodic boundary condition and applied voltage, an external input current term is introduced at any node i near the high-potential boundary (i.e., the left y-z surface) that is bonded to a node near the low-potential boundary (i.e., the right y-z surface) as $I_i = I_{\text{source}} = V_{\text{source}}/R_{\text{node}}$ (e.g., for the model shown in Figure 4.3, an external input current term is introduced at Node 1, which is bonded to Node 10, and Node 11, which is bonded to Node 13). After solving for the nodal voltages, the total current passing through the simulation cell is calculated using the total current of the nodes connected across the high-potential boundary (e.g., nodes 1 and 11) as (Jin et al., 2018)

$$I_{\text{total}} = \sum_{e=1}^{m} \frac{1}{R_{ij}^{e}} (V_{\text{source}} - V_i) \tag{4.13}$$

Finally, the equivalent resistance of the CNT network is obtained using Ohm's law.

$$R_{\text{equivalent}} = \frac{V_{\text{source}}}{I_{\text{total}}} \tag{4.14}$$

4.3 Results and Discussion

4.3.1 Curing Dependent Piezoresistivity

CNT/epoxy nanocomposites were fabricated by curing DER332 epoxy resin, containing well-dispersed multiwalled CNTs, at 60, 70, 80, and 100 °C for 6, 4, 3, and 1 h, respectively, followed by applying post-curing treatment at 125 °C for 3 h (Figure 4.1a and Table 4.1). The samples were then loaded under tension until failure (Figure 4.1b). The piezoresistive behavior transformed from nonmonotonic to monotonic as the curing temperature increased (Figure 4.4a,b), while the mechanical properties remained similar (Figure 4.5). For the 60 and 70 °C samples, the resistance first increases with strain, and after reaching the maximum at the critical strain (ε_c), decreases until the failure of specimen, i.e. inversion of piezoresistivity. The ε_c of

the 70 °C sample is larger than that of the 60 °C sample. Upon reaching 80 °C, the resistance monotonically increased until failure.

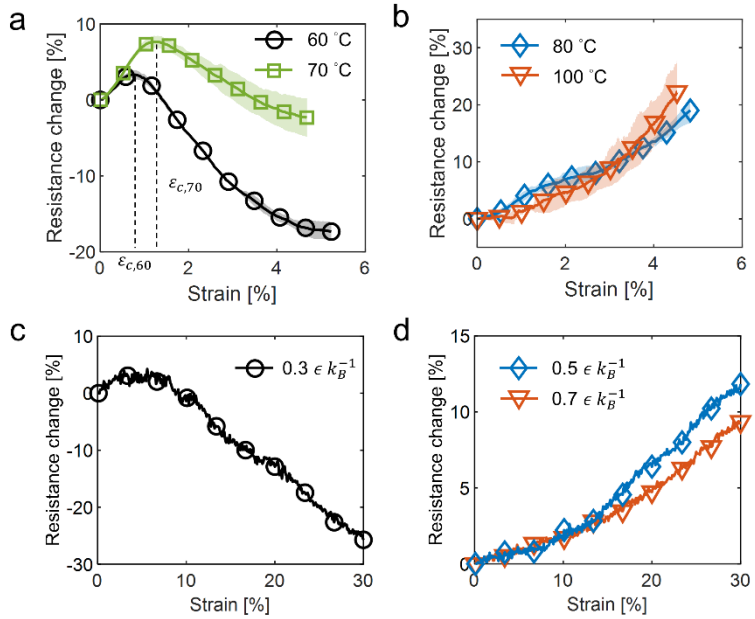

Figure 4.4. Experimental and CGMD simulation results of piezoresistive behaviors of polymer nanocomposites. a,b) Experimental resistance change versus strain relationships of CNT/epoxy nanocomposites cured at 60, 70, 80, and 100 °C for 6, 4, 3, and 1 h, respectively, followed by applying post-curing treatment at 125 °C for 3 h. At least three specimens were tested for each sample and the mean response is plotted (shaded area: ±1 standard deviation). c,d) Simulated resistance change versus strain relationships of CNT/epoxy nanocomposites cured at 0.3, 0.5, or 0.7 ϵ k_B^{-1}. The CGMD model parameters are CNT concentration = 5 vol.%, number of beads per CNT = 100, CNT diameter = 1.0 σ, CNT waviness in terms of maximum deviation angle = 10°, and simulation cell size = 150 σ. The liquid epoxy structure is two-bead mixture.

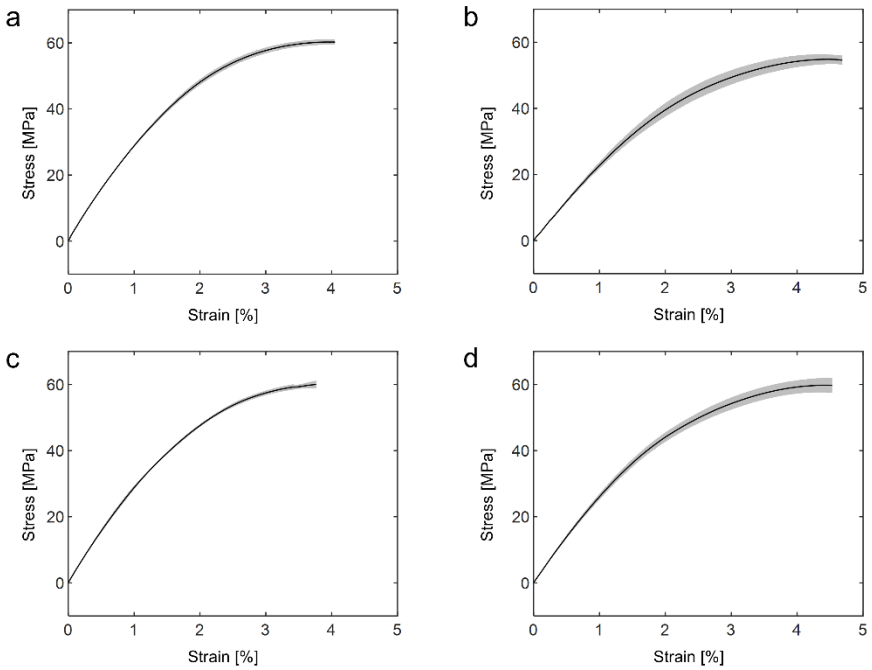

Figure 4.5. Experimental results of stress versus strain relationships of CNT/epoxy nanocomposites. a-d) Experimental stress versus strain relationships of CNT/epoxy nanocomposites cured at 60 °C for 6 h (a), 70 °C for 4 h (b), 80 °C for 3 h (c) or 100 °C for 1 h (d), all post-cured at 125 °C for 3 h. For each sample, three specimens were tested, and the mean response is plotted (shaded area: ±1 standard deviation).

The transformation of the piezoresistive behavior with the curing temperature suggests differential changes in the CNT network configuration under tensile deformation. The electrical properties and piezoresistive behavior of polymer nanocomposites, including CNT/epoxy nanocomposites, are largely determined by the quantum tunnelling effect, which depends on the distance between adjacent nanofillers (N. Hu, Karube, et al., 2008). Under tensile deformation, the nanofillers move apart, thereby increasing the inter-nanofiller distance and electrical resistance. However, the inversion of piezoresistivity indicates processes that reduce the inter-nanofiller distance, likely due to molecular-level phenomena at the nanometer scale involving nanofiller-matrix interactions. The unclear microstructural origin of nonmonotonic

piezoresistivity necessitates a mechanistic study to advance our understanding and achieve controllability of piezoresistivity in polymer nanocomposites.

To accomplish this task, MD simulations were employed and a CGMD model of a periodically repeating unit cell representing CNT/epoxy nanocomposites was constructed (Jin et al., 2018). Since our aim is to pinpoint the microstructural origin, the reduced units formalism, i.e. expressing all physical quantities as multiples of fundamental quantities: mass (m), energy (ϵ), distance (σ) and Boltzmann constant (k_{B}), each set to one, which allow us to focus on the relative interactions and dynamics, was adopted (Y. Gao et al., 2015; Tsige et al., 2004; Tsige & Stevens, 2004). The simulated resistance-strain curves reproduced the experimentally observed temperature dependence of the piezoresistive behavior of the CNT/epoxy nanocomposites (Figure 4.4c,d). The curve is nonmonotonic for 0.3 $\epsilon\, k_B^{-1}$ and becomes monotonic for 0.5 and 0.7 $\epsilon\, k_B^{-1}$. The resemblance between the simulations and experiments, although qualitative owing to the simplification of molecular details into beads and springs in this study, suggests that the microstructural origin of the nonmonotonic piezoresistive behavior can be traced through analysis of the simulations. Quantitative alignment with experimental data, which requires further calibration of the model parameters, can be attempted in future investigations.

4.3.2 Inter-nanofiller Junction Geometry and Microstructural Origin

Upon increasing the curing temperature, the nanotube microstructure became more visibly agglomerated, as shown in the representative FESEM images (Figure 4.6a) and slice images of the CGMD simulation cells (Figure 4.6b). The dispersion state was quantitatively characterized using free-space length analysis and electrical conductivity measurements on at least four specimens for each sample (Faiella et al., 2012). Khare and Burris adopted a method

for quantifying the dispersion state (Khare & Burris, 2010). Its principle is to compute the free-space length L_f which correlates with the continuous area free of nanoparticles. Specifically, statistically substantial numbers of squares of different sizes were randomly positioned throughout the SEM image to create a histogram displaying the probability that a given number of nanoparticles existed within a square (e.g., in this study, 10 000 squares of each square size were used). The free-space length L_f is defined as "the largest square size for which the most probable number of intersecting nanoparticles in a randomly placed square is zero." The electrical conductivity of each sample was calculated as

$$\rho = \frac{D}{A \cdot R} \tag{4.15}$$

where D is the distance between the two electrodes, A is the cross-sectional area of the sample, and R is the measured resistance of the sample.

For uniform dispersion, nanoparticles are distributed in a regular fashion throughout the micrograph, so the space between nanoparticles or agglomerates, and hence the free-space length, is minimized. In a system near the percolation threshold like our CNT/epoxy nanocomposite, uniform dispersion leads to the presence of an insulating polymer layer surrounding each nanoparticle and lower electrical conductivity, as in the case of the 60 and 70 °C cured samples (Figure 4.6c). However, when nanoparticles migrate closer to each other in local agglomerates, continuous areas free of nanoparticles emerge and expand between the agglomerates, leading to a larger free-space length. Local agglomerates of nanoparticles facilitate the formation of electrical conduction paths, resulting in higher electrical conductivity. It can be observed from Figure 4.6c that an increase in curing temperature leads to larger free-space lengths and higher conductivities in the 80 and 100 °C samples compared to the 60 and 70 °C samples.

The above procedures are repeated on the CGMD simulations, using the images of slices with thickness of 1 σ to mimic the FESEM images (Figure 4.6b). The slices were extracted

from three locations along each coordinate axis in the 3D simulation box, i.e. a total of nine slices for each model. An increase in the curing temperature led to a higher conductivity and free-space length, resembling the experimental data (Figure 4.6d). The agglomerated dispersion leads to a larger free-space length and facilitates the formation of electrical conduction paths, resulting in higher electrical conductivity (Vigolo, Coulon, Maugey, Zakri, & Poulin, 2005). The free-space lengths and the electrical conductivities are higher for the 80 and 100 °C or 0.5 and 0.7 $\epsilon\, k_B^{-1}$ samples which exhibit monotonic piezoresistive behavior (Figure 4.6c,d). These observations are consistent with the previous experimental results (Faiella et al., 2012). At a low temperature 0.3 $\epsilon\, k_B^{-1}$, a strong radial distribution function (RDF) peak is detected near 2σ for the nanotube beads ($g_{\mathrm{nn}}(r)$) before deformation, representing a perfectly dispersed state with all nanotubes surrounded by the polymer beads and all inter-nanotube junctions formed with a polymer layer barrier (green circle in Figure 4.6e). A peak near 1σ, which represents inter-nanotube junctions in direct contact (yellow circle in Figure 4.6e), emerges at 0.5 $\epsilon\, k_B^{-1}$. The 1σ and 2σ peaks compete with each other; as the curing temperature increases, the height of the former increases, whereas that of the latter shrinks, suggesting the occurrence of thermally activated processes that affect the inter-nanotube junction geometry (Boland et al., 2016). Notably, the free-space length and conductivity of the 100 °C sample were lower than those of the 80 °C sample. While this observation seems to counteract our claim that thermally activated barrier-crossing events drive changes in the inter-nanotube junction geometry during curing, a possible explanation for the validity of our claim based on the shorter gelation time under more rapid crosslinking is provided (Boland et al., 2016; X. Zhang et al., 2013). Further details on the influence of crosslinking dynamics on the dynamic percolation of nanofillers are provided in Appendix A2.

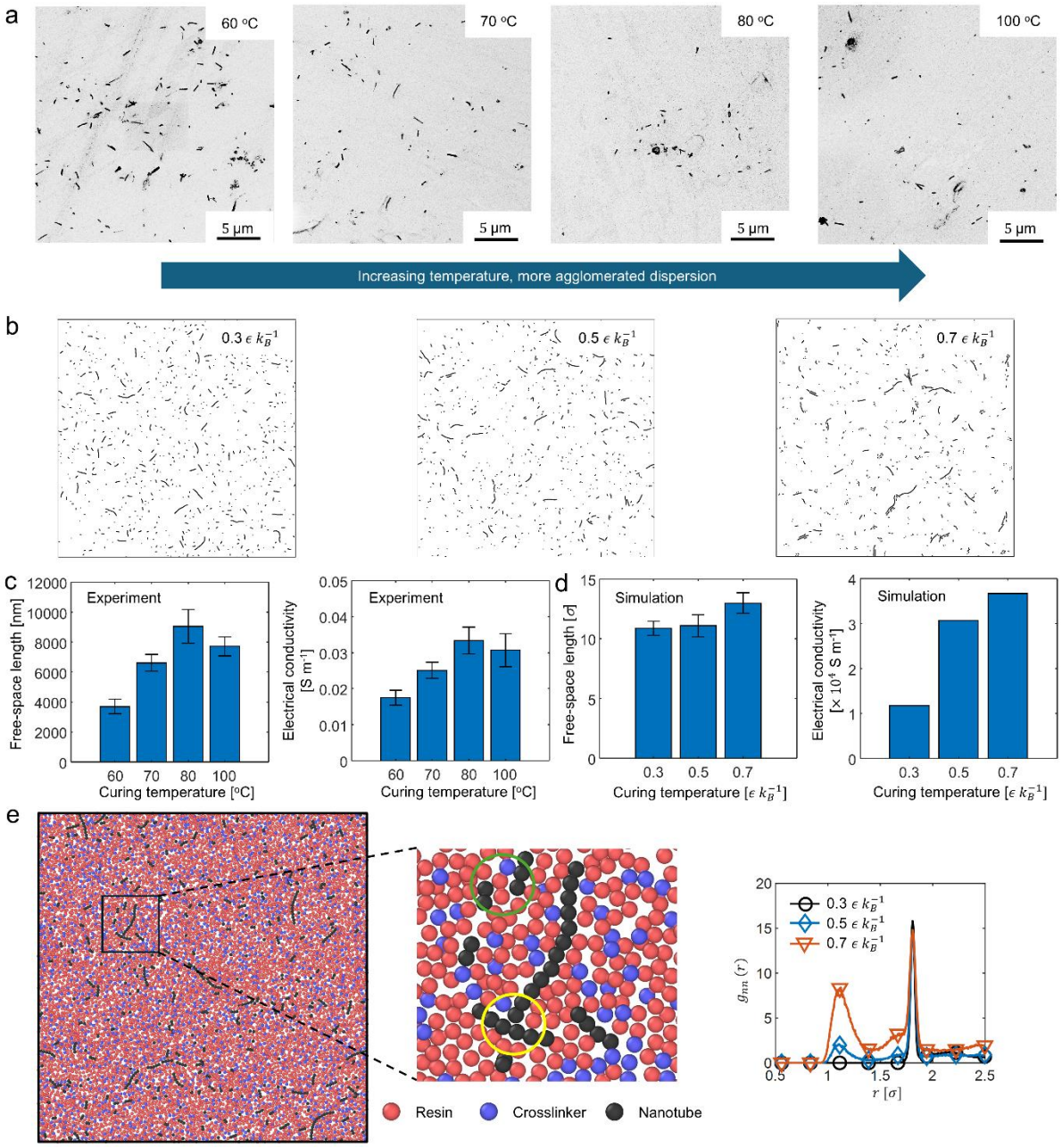

Figure 4.6. Experimental and CGMD simulation results of inter-nanofiller junction geometries and electrical conductivities of polymer nanocomposites. a,b) FESEM images and CGMD model slices showing the morphologies of CNT networks developed under different curing temperatures. Black and white are inverted in FESEM images for better visibility. c,d) Experimental and simulation results of the free-space lengths and electrical conductivities of CNT/epoxy nanocomposites cured at different temperatures. For the experimental results, at least four specimens were tested for each sample. For the simulations results, nine slices from

each model were used for free-space length analysis. Error bar represents ±1 standard deviation. e) CGMD model slice demonstrating the inter-nanotube junction morphology in direct contact or with polymer barrier which corresponds to 1σ or 2σ peak in the RDF of nanotube beads. The CGMD model setup is CNT concentration = 5 vol.%, number of beads per CNT = 200, CNT diameter = 1.0 σ, CNT waviness in terms of maximum deviation angle = 10°, and simulation cell size = 100 σ. The liquid epoxy structure is two-bead mixture.

The changes in the initial inter-nanotube junction geometry are ascribed to nanotube propagation via diffusion in a viscous medium, such as epoxy resin (Boland et al., 2016); this phenomenon reflects thermally activated energy barrier crossing (Lyons, Devi, Hoffer, Woodside, & Ka Shing, 2024). Because diffusion is suppressed at low temperatures ($0.3\ \epsilon\ k_B^{-1}$), the inter-nanotube junction geometry remains unchanged unlike the dispersed state (Figure 4.2 and Figure 4.6e). Diffusion is thermally activated at higher temperatures (0.5 or $0.7\ \epsilon\ k_B^{-1}$), allowing barrier-crossing transitions between 1σ and 2σ peaks. The vdW interaction between nanotubes plays a vital role in the occurrence and growth of 1σ peak, as the attractive force brings the nanotube beads closer from 2σ peak to the energy minimum of the Lennard-Jones potential at $2^{1/6} \approx 1.12\sigma$ (Girifalco, Hodak, & Lee, 2000; Vigolo et al., 2005). For the electrical properties, electron transport between nanotubes is conducted through the insulating barrier under the tunnelling mechanism, which is commonly described by the Simmons formula (Simmons, 1963) or the Landauer–Büttiker formula (Büttiker et al., 1985). A common feature of these formulae for describing the tunnelling resistance between nanotubes is the exponential dependence of the inter-nanotube distance. When thermally activated diffusion induces the agglomeration of nanotubes at higher temperatures, the tunnelling resistance is reduced owing to the smaller inter-nanotube separation. Therefore, even with only small portion of nanotube beads transitioning from 2σ peak to 1σ peak through barrier-crossing at $0.5\ \epsilon\ k_B^{-1}$, as indicated

by the similar free-space lengths for 0.3 and 0.5 $\epsilon\ k_B^{-1}$ (Figure 4.6d) and the RDF plots (Figure 4.6e), the emergence of direct contact between nanotube beads results in significantly higher electrical conductivity.

The piezoresistivity of polymer nanocomposites is primarily influenced by alterations in filler network configuration under mechanical deformation, governed by the distance between neighboring nanofillers (Avilés et al., 2018). Under tensile deformation, nanofillers within the nanocomposite move apart. This separation widens, increasing the tunnelling resistance and overall electrical resistance. To determine the microstructural origin of nonmonotonic piezoresistive behavior, changes in the tunnelling distance (d_{tunnel}) distribution, which reflect the movement of junction-forming nanotube pairs in CGMD simulations, were monitored. The bistable feature of distance distribution was preserved, suggesting inter-nanotube geometry was governed by vdW interactions during deformation. It is observed that in the 0.3 $\epsilon\ k_B^{-1}$ case, considerable amount of inter-nanotube junctions originally with polymer layer barrier (at 2σ peak) become in direct contact (at 1σ peak) through barrier-crossing process (Figure 4.7a), leading to reduced inter-nanotube distance and decrease in resistance. In particular, the increase and decrease in the numbers of counts under the 1σ and 2σ peaks, respectively, coincide with the inversion of piezoresistivity, which occurs within the strain range of 5–30% (Figure 4.4d). Conversely, for the 0.5 and 0.7 $\epsilon\ k_B^{-1}$ cases that exhibit monotonic piezoresistive behavior, the number of counts under the 1σ peak does not increase.

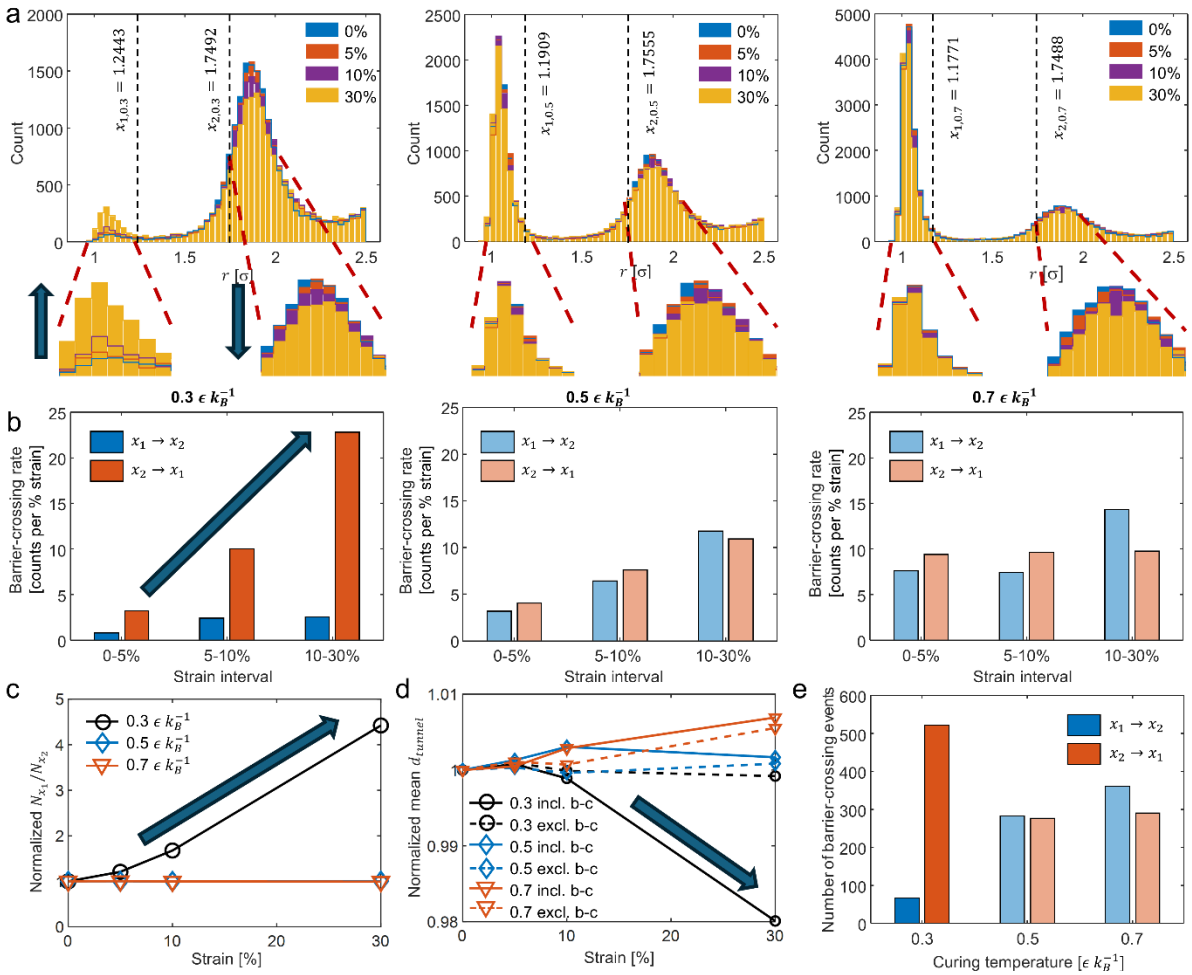

Figure 4.7. CGMD simulation results and analysis of changes in inter-nanofiller junction geometry under tensile deformation. Key results related to the nonmonotonic piezoresistive behavior are highlighted. a) Evolutions of inter-nanotube tunnelling distance distribution with respect to strain. Positions of peaks are determined by Gaussian fitting. b) Rates of barrier-crossing events from x_1 to x_2 and vice versa. c) Ratios between numbers of inter-nanotube junctions with distance smaller than x_1 and with distance greater than x_2, normalized with respect to the initial ratio at 0% strain. d) Changes in normalized mean d_{tunnel} including or excluding junctions exhibiting barrier-crossing during stretching. e) Total numbers of barrier-crossing events. The curing temperatures are 0.3, 0.5, and 0.7 $\epsilon\, k_B^{-1}$. The CGMD model setup is CNT concentration = 5 vol.%, number of beads per CNT = 100, CNT diameter = 1.0 σ,

CNT waviness in terms of maximum deviation angle = 10°, and simulation cell size = 150 σ. The liquid epoxy structure is two-bead mixture.

Barrier-crossing events induce tunnelling distance transitions between 1σ and 2σ peaks. The middle two-thirds of the distance between the two peaks are defined as the barrier region (Lyons et al., 2024); therefore, the two boundaries for the two peaks are x_1 and x_2. Identifying changes in inter-nanotube junction distance from smaller than x_1 to greater than x_2 ($x_2 \rightarrow x_1$) and vice versa ($x_1 \rightarrow x_2$) as transition paths, the rate of barrier-crossing events with respect to strain at discrete strain intervals, which could be correlated to the observed changes in the tunnelling distance distribution, was calculated. The increase and decrease in the numbers of counts under the 1σ and 2σ peaks, respectively, in the $0.3\ \epsilon\ k_B^{-1}$ case, which cause the inversion of piezoresistivity, can be attributed to the increase in the $x_2 \rightarrow x_1$ crossing rate, whereas the $x_1 \rightarrow x_2$ crossing rate remains unchanged (Figure 4.7b). The former increases from approximately three times that of the latter to approximately ten times. The imbalance between the two types of barrier-crossing events increases the ratio between the number of junctions in the 1σ peak and that in the 2σ peak (N_{x_1}/N_{x_2}); this ratio is normalized with respect to the initial ratio at 0% strain (Figure 4.7c). When the two crossing rates hold in fair balance in the 0.5 and 0.7 $\epsilon\ k_B^{-1}$ cases, the ratio N_{x_1}/N_{x_2} remains similar during deformation. Even though the $x_2 \rightarrow x_1$ crossing rate is mostly higher, the mean d_{tunnel} shows increasing trend in the 0.5 and 0.7 $\epsilon\ k_B^{-1}$ cases, as well as at the initial stage in the $0.3\ \epsilon\ k_B^{-1}$ case (Figure 4.7d). This result indicates that the nanotubes generally moved apart, leading to positive piezoresistivity. When the junctions exhibiting barrier crossing are excluded, the mean d_{tunnel} does not decrease in the 5–30% strain range in the $0.3\ \epsilon\ k_B^{-1}$ case. The effect of the imbalance between the two types of barrier-crossing events on the mean d_{tunnel} is apparent. The $x_2 \rightarrow x_1$ crossing is the major contributor to

the decrease in d_{tunnel} and hence the nonmonotonic piezoresistive behavior. For the monotonic 0.5 and 0.7 $\epsilon\ k_B^{-1}$ cases, the influence of barrier-crossing events on the change in d_{tunnel} is much smaller, since the rates of the two opposite events are similar. The total number of barrier-crossing events shows a distinct correlation with N_{x_1} and N_{x_2}, i.e., more junctions in the 1σ (or 2σ) peak results in more $x_1 \rightarrow x_2$ (or $x_2 \rightarrow x_1$) barrier-crossing events (Figure 4.7e), whereas the initial N_{x_1} and N_{x_2} are influenced by thermally activated diffusion as elucidated earlier.

Understanding the distinction between barrier-crossing events that occur prior to and during deformation is crucial. As discussed earlier, barrier-crossing events are thermally activated and diffusion-driven before the build-up of viscosity of the epoxy matrix that accompanies the crosslinking process. They are suppressed at low curing temperature (0.3 $\epsilon\ k_B^{-1}$) (Figure 4.6e). However, during stretching which takes place at 0.3 $\epsilon\ k_B^{-1}$in the CGMD simulations, barrier-crossing events do occur, implying that an alternative mechanism is required. For amorphous, highly cross-linked epoxy network structure in response to stretching, a prevailing framework known as "shear transformation zones" (STZs) introduces discrete molecular rearrangements, in conjunction with interactions with their local surroundings, as the fundamental microstructural mechanisms driving the viscoplasticity (Chevalier et al., 2018; Falk & Langer, 1998; Nicolas, Ferrero, Martens, & Barrat, 2018). The random, heterogeneous activation of STZs induces energy-barrier-crossing processes that conform to a fractal potential energy landscape (PEL), describing the energetics and dictating configurational changes within individual STZs (P. Cao, Short, & Yip, 2019; Mayr, 2006; Nicolas et al., 2018). Regions of local molecular rearrangement by the nonaffine squared displacement (D^2_{min}) field can be identified, where a nonzero value indicates a molecular displacement deviating from a linear elastic manner (Cubuk et al., 2017; Falk & Langer, 1998), and look for inter-nanotube junctions that bypass the polymer layer barrier under attraction via vdW interactions between neighboring nanotubes (Figure 4.8a). In the region of relatively high nonaffine displacement

(green), barrier-crossing events that lead to an increase in current (from red to orange) due to lower inter-nanotube separation can be correlated (Figure 4.8b). The occurrence of barrier-crossing events during deformation at 0.3 $\epsilon\ k_B^{-1}$, and their inhibition during curing at the same temperature, can be attributed to the stress-induced flattening of a local minimum on the PEL of an STZ; this feature reduces the activation energy required for configurational changes (Figure 4.8d). Considering the stochastic nature of STZ activation, higher numbers of nanotube junctions result in a higher probability of local molecular rearrangement-induced barrier-crossing events (Figure 4.7e). The activation of STZs progresses with strain; thus, the resistance decreases gradually. In other words, barrier-crossing events are locally plasticity-enabled and stress-driven during stretching, as opposed to the thermally activated diffusion-driven events in a viscous medium during curing.

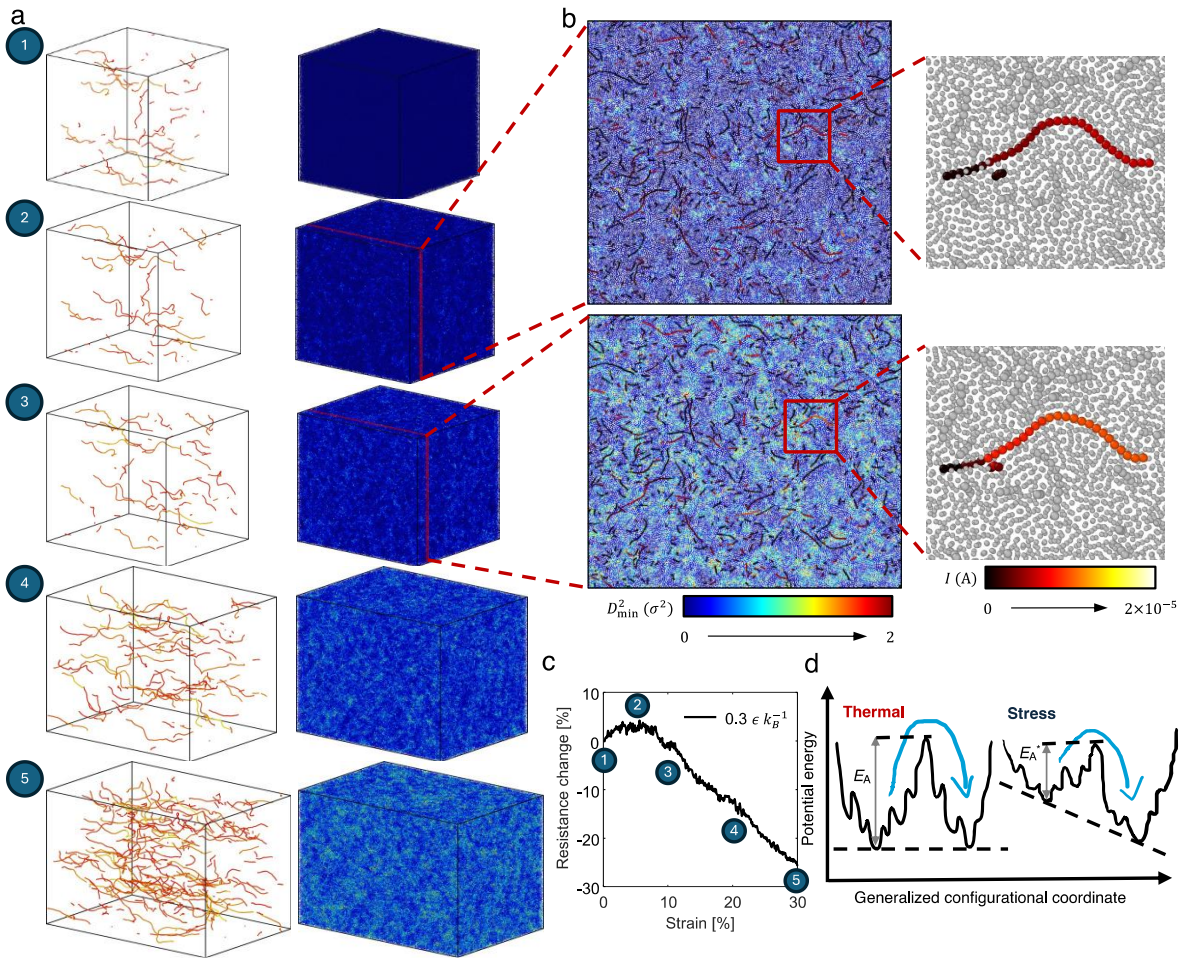

Figure 4.8. Correlation between local molecular rearrangement and barrier-crossing process that trigger nonmonotonic piezoresistive behavior under tensile deformation. a) Evolution of main current-carrying portion of CNT network and spatial distribution of nonaffine displacement ($D^2_{\min}$) with respect to strain. b) Closeups illustrating the association between local barrier-crossing events and inversion of resistance change. c) Simulated resistance change versus strain relationships of CNT/epoxy nanocomposite cured at 0.3 ϵ k_B^{-1}. d) Schematic of a fractal PEL and barrier-crossing processes of a STZ triggered by thermal and stress activations. The CGMD model setup is CNT concentration = 5 vol.%, number of beads per CNT = 100, CNT diameter = 1.0 σ, CNT waviness in terms of maximum deviation angle = 10°, and simulation cell size = 150 σ. The liquid epoxy structure is two-bead mixture.

4.3.3 Structural-Property Relationships

Based on the agreement between the experimental results and the CGMD simulations, the nanoscale dispersion state or inter-nanofiller junction geometry is identified as the dominant microstructural feature for the piezoresistive behavior (Figure 4.9). Here, it is further demonstrated the controllability of the monotony of the piezoresistive behavior through the inter-nanotube junction geometry using the CGMD model. The piezoresistive behaviors of the CNT/epoxy nanocomposites with different epoxy matrices, namely, DER332 and EL2, which are both bisphenol A diglycidyl ethers-based, are compared. The curing temperatures for DER332 and EL2 matrices to attain monotonic piezoresistive behavior are 80 °C and 60 °C respectively (Figure 3.4a,c and Figure 4.4a,b). This suggests that the influence of the matrix on the inter-nanofiller junction geometry is indispensable and warrants further investigation.

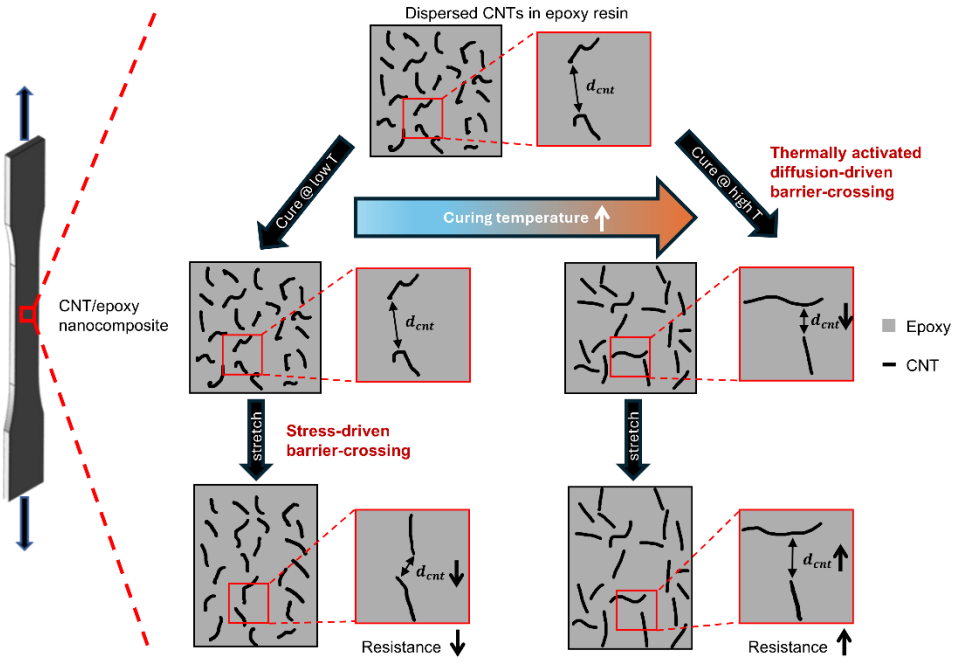

Figure 4.9. Schematic of the morphological change in CNT network induced by thermally activated diffusion-driven and stress-driven barrier-crossing that determines the piezoresistive behavior of CNT/epoxy nanocomposite under tensile deformation.

In liquid epoxy resins, nanotube diffusion is dictated by the viscosity of the surrounding polymer molecules, which imposes an energy barrier (Boland et al., 2016; Kharchenko, Douglas, Obrzut, Grulke, & Migler, 2004). Therefore, the zero-shear viscosity (η_o) of the epoxy matrices was measured, and the data were fitted by the Arrhenius equation to obtain the activation energy (E_a) for viscous flow. Both the DER332 and EL2 epoxy resins exhibited Newtonian behavior, that is, shear-rate-independent viscosity. The thermal activation energy E_a for a viscous flow can be calculated using the Arrhenius model

$$\ln \eta_0 = \ln A + \frac{E_a}{RT} \tag{4.16}$$

where η_0 is the zero-shear viscosity, A is the prefactor, R is the gas constant, and T is the temperature. Owing to the Newtonian behavior, η_0 can be taken as the viscosity measured. The η_o of DER332 and EL2 at 20 °C were 8.488 ± 0.022 and 2.824 ± 0.026 Pa·s respectively. This

indicates that the M_W of DER332 is higher than that of EL2, as η_0 is related to molecular weight (M_W), i.e., $\eta_0 \sim M_W$ (Takahashi, Noda, & Nagasawa, 1985). From the viscosity-temperature relationships, the E_a for the viscous flow of DER332 (76.425 kJ mol^{-1}) is higher than that of EL2 (63.881 kJ mol^{-1}) (Figure 4.10a). These results suggest that the activation energy for nanofiller diffusion would be higher in polymer matrix with higher viscosity and molecular weight.

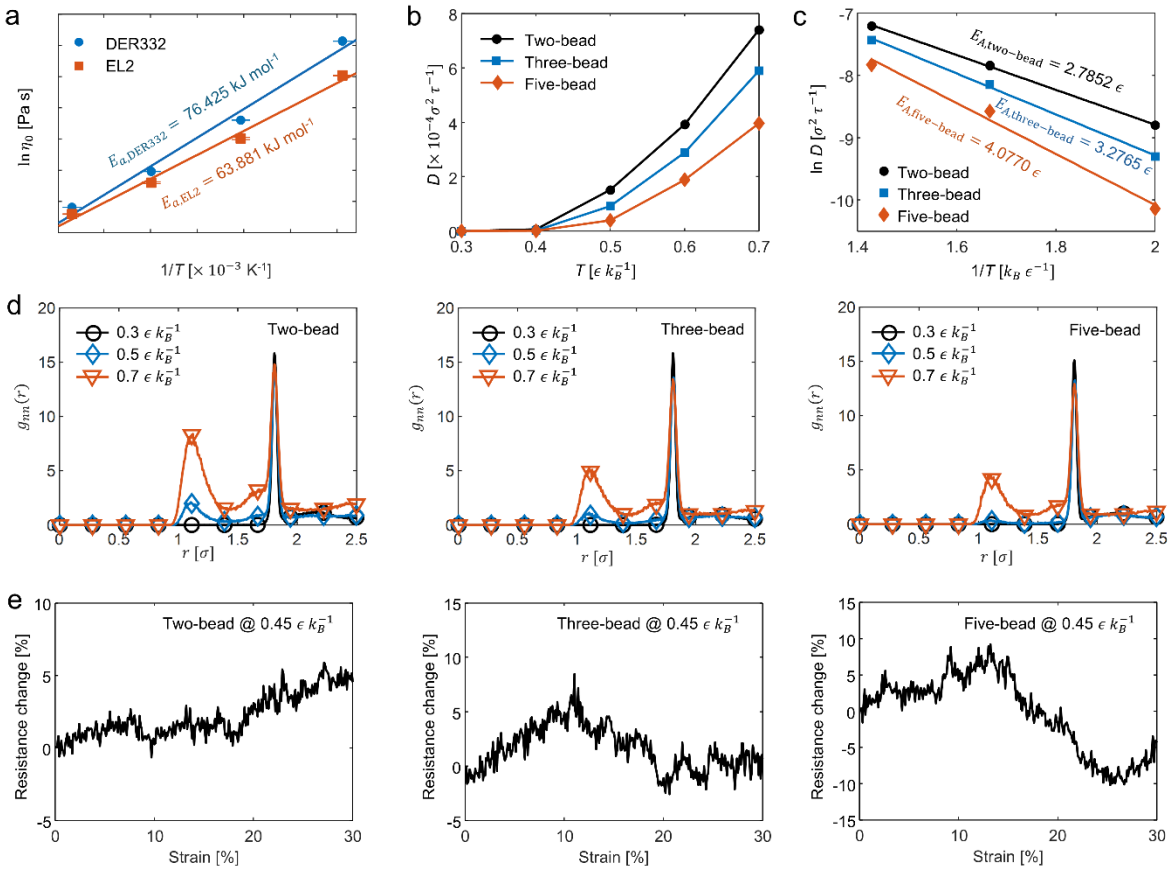

Figure 4.10. Experimental and CGMD simulation results of influence of polymer molecular structure on inter-nanofiller junction geometries and piezoresistive behavior in polymer nanocomposites. a) Experimental Arrhenius plots of activation energy (E_a) for viscous flow of DER332 and EL2 epoxy resins. Each data point represents the mean of three measurements. Error bar represents ±1 standard deviation. b) Simulated diffusivity versus temperature relationships of nanotube beads. c) Simulated Arrhenius plots of activation

energy (EA) for nanotube diffusion. d) Simulated RDFs of nanotube beads at 0.3, 0.5, or 0.7 $\epsilon\, k_B^{-1}$. e) Simulated resistance change versus strain relationships at 0.45 $\epsilon\, k_B^{-1}$. The CGMD model setup is CNT concentration = 5 vol.%, number of beads per CNT = 100, CNT diameter = 1.0 σ, CNT waviness in terms of maximum deviation angle = 10°, and simulation cell size = 100 σ. The liquid epoxy structures are composed of two-bead, three-bead, and five-bead mixtures.

Therefore, the initial structure of the epoxy matrix in the CGMD model was varied by replacing two-bead resin molecules with three-bead and five-bead molecules (Figure 4.11a). To characterize the mobility of the nanotube under diffusion (Boland et al., 2016) and describe its thermally activated nature, the activation energy E_A for the diffusion of CNTs in liquid two-bead, three-bead, and five-bead epoxy mixtures was calculated (Maździarz, Rojek, & Nosewicz, 2018; Zhou, Jones, & Gruber, 2017) (Figure 4.11a). From the CGMD simulations, diffusivity *D* is related to the mean square displacement (MSD) by

$$D = \lim_{t\to\infty} \frac{1}{6t} \langle |\vec{r}(t) - \vec{r}(0)|^2 \rangle \tag{4.17}$$

where $\vec{r}(0)$ and $\vec{r}(t)$ represent the position vectors of an atom at the initial time and time *t* respectively, and < > is the average over all nanotube beads. The value of *D* was obtained from the slope of the MSD vs. time curve, as shown in Figure 4.11b. The diffusivities for the nanotube beads at T = 0.3, 0,4, 0.5, 0.6, and 0.7 $\epsilon\, k_B^{-1}$ are calculated and compared in Figure 4.10b. The diffusion is thermally activated at T = 0.5 $\epsilon\, k_B^{-1}$ regardless of the epoxy resin structure, whereas it becomes increasingly restricted in three-bead and five-bead mixtures.

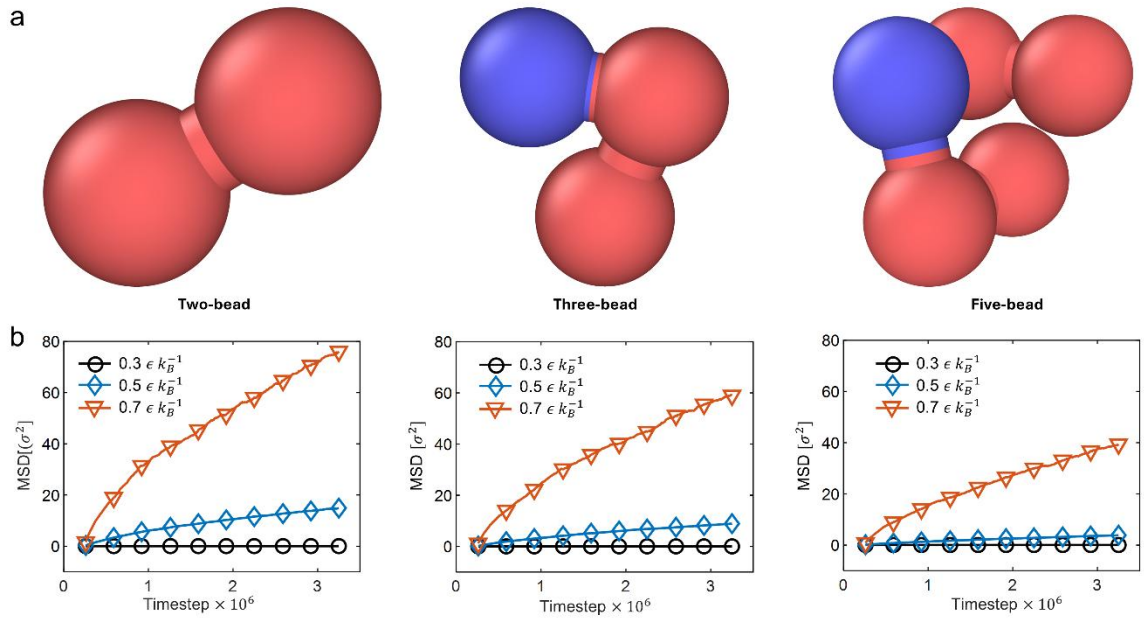

Figure 4.11. Influence of epoxy molecular structure on mobility and thermally activated diffusion of CNTs. a) Schematics of two-bead, three-bead, and five-bead polymer strands. b) MSD against time step for the nanotube beads at 0.3, 0.5, and 0.7 $\epsilon\ k_B^{-1}$ in two-bead, three-bead, and five-bead mixture.

It is assumed that the temperature dependence of the diffusivity of nanotubes can be described by the Arrhenius form of a thermally activated process:

$$\ln D = \ln D_0 - \frac{E_A}{k_B T} \tag{4.18}$$

where D_0 is the prefactor. The energy barrier E_A can be obtained from the slope of $\ln D$ vs. $1/T$ for the range of 0.5 to 0.7 $\epsilon\ k_B^{-1}$, in which barrier-crossing events are activated. The results are shown in Figure 4.10c, which indicates that the E_A for the diffusion of nanotube beads increases with the length of the polymer strand.

The movement of nanotube is activated when the temperature approaches 0.5 $\epsilon\ k_B^{-1}$ with higher mobility in mixture of shorter polymer strand (Figure 4.10b and Figure 4.11b). The increase in diffusivity with temperature in the simulations parallels the decrease in viscosity with increasing temperature in the experiments (Figure 4.10a), both of which indicate enhanced

molecular mobility at higher temperatures. The E_A for nanotube diffusion increases with the length of polymer strand, from 2.7852 ϵ for two-bead mixture, to 3.2765 ϵ and 4.0770 ϵ for three-bead mixture for five-bead mixtures respectively (Figure 4.10c). This is analogous to the higher E_a for viscous flow in DER332 than in EL2, which requires higher curing temperatures to achieve similar CNT mobility and overcome the E_A for nanotube re-agglomeration under diffusion. The temperature dependence of the inter-nanotube junction geometry was affected by the molecular structure of the resin, as shown by the RDF plots for polymer strands of different lengths (Figure 4.10d). In particular, the height of 1σ peak decreases with longer polymer strands, indicating suppressed diffusion-driven barrier-crossing events.

While a direct one-to-one conversion between reduced units ($\epsilon\, k_B^{-1}$) and real temperatures (°C) is not straightforward due to the coarse-grained nature of the model (Aramoon et al., 2016; Y. Gao et al., 2015; Tsige & Stevens, 2004; Shaorui Yang & Qu, 2014), a qualitative correlation based on the observed piezoresistive and diffusive behaviors in both simulations and experiments is provided here. The simulation temperatures of 0.3 to 0.7 $\epsilon\, k_B^{-1}$ represent a range of thermal activation levels that influence the diffusion of CNTs. At 0.3–0.4 $\epsilon\, k_B^{-1}$, diffusion is suppressed, leading to a well-dispersed CNT state with polymer barriers between nanotubes, resulting in nonmonotonic piezoresistive behavior. This corresponds qualitatively the 0.3–0.4 $\epsilon\, k_B^{-1}$ range to the lower experimental curing temperatures (e.g., 20–60 °C). The corresponding resistance change-strain curves at curing temperature of 0.45 $\epsilon\, k_B^{-1}$ is monotonic in two-bead mixture but nonmonotonic in three-bead and five-bead mixtures (Figure 4.10e), whereas the monotony remains unchanged at 0.3 and 0.7 $\epsilon\, k_B^{-1}$ (Figure 4.12). This corresponds to the experimental observation that EL2-based nanocomposites exhibit monotonic piezoresistive behavior at a curing temperature of 60 °C, whereas DER332-based nanocomposites remain nonmonotonic at the same temperature. Owing to the larger viscosity and higher E_a of DER332, a higher temperature was required to induce CNT diffusion and re-

agglomeration during the low-viscosity stage of curing to attain monotonic piezoresistive behavior. At 0.5–0.7 $\epsilon\, k_B^{-1}$, thermally activated diffusion enables barrier-crossing events and CNT re-agglomeration, leading to direct inter-nanotube contacts and monotonic piezoresistive behavior. Specifically, the onset of significant diffusion as observed at 0.5 $\epsilon\, k_B^{-1}$ in simulations aligns with the glass transition temperature (T_g) of the CGMD model as reported in the literature (Tsige et al., 2004; Tsige & Stevens, 2004), which indicates a transition in material behavior analogous to real epoxy systems near typical curing temperatures. This mirrors the experimental results at higher curing temperatures (e.g., 80–100 °C).

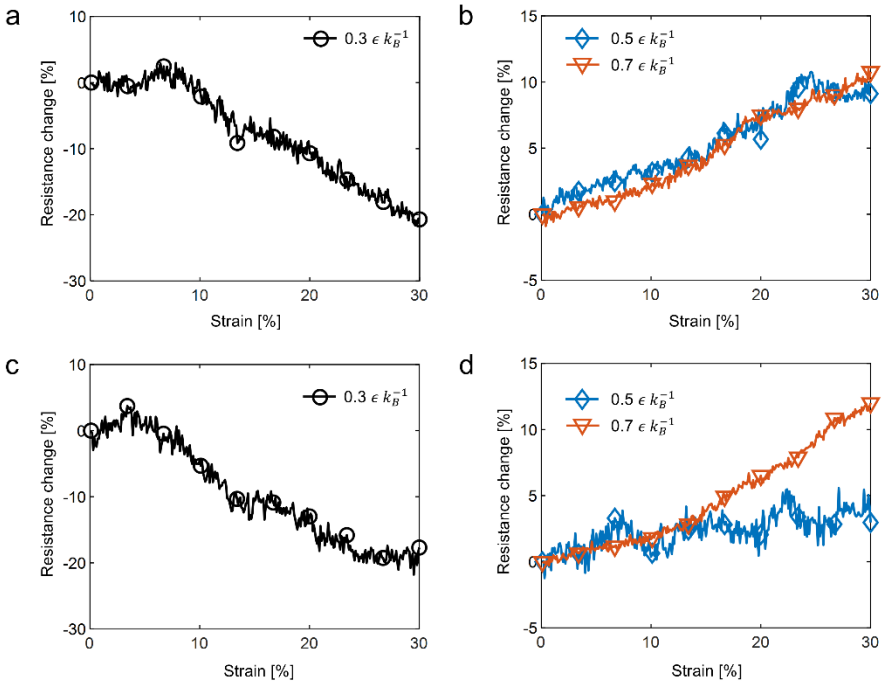

Figure 4.12. CGMD simulation results of the effect of liquid epoxy structure on piezoresistive behavior of CNT/epoxy nanocomposites. a–d) Simulated resistance change versus strain relationships of CNT/epoxy nanocomposites with three-bead mixture (a,d) or five-bead mixture (c,d).

4.3.4 Nanofiller-related Parameters

Other control simulations, in which nanofiller-related parameters, including concentration, length, diameter, and waviness, were varied, were carried out (Figure 4.13–Figure 4.17). Note that all simulations were performed with cell size of at least 100 σ. This size was selected based on the results showing that using a cell size of 50 σ led to noisy data (Figure 4.13a,b). The data approached stability with a cell size for 100 σ (Figure 4.13c,d). Within the range of 4-6 vol.% CNT concentrations (Figure 4.14), 50-200 beads per CNT (Figure 4.15), 1.5-2 σ CNT diameters (Figure 4.16), and 30-60° maximum deviation angles for CNT waviness (Figure 4.17), the piezoresistive behavior remained nonmonotonic for 0.3 ϵ k_B^{-1} and monotonic for 0.5 and 0.7 ϵ k_B^{-1}. The general dependence of the piezoresistive behavior on the curing temperature remained similar, demonstrating the limited impact of these nanofiller-related factors. These results reinforce our proposal that the inter-nanofiller junction geometry is the dominant factor for the monotony of piezoresistive behavior. In addition to the curing temperature and polymer molecular structure that modulate the inter-nanofiller junction geometry through diffusion under attraction via vdW interactions, the alignment of the nanofiller in an electric field during curing (Meeuw et al., 2016) can alternatively drive the direct contact of neighboring nanofillers owing to electrostatic interactions associated with the applied voltage (Boland et al., 2016). For nanotechnology applications, it may be possible to design and optimize strain-sensing polymer nanocomposites based on the curing temperature dependence of the piezoresistive behavior on the viscosity of the polymer matrix. For example, a higher curing temperature may be required for epoxy resins with higher viscosity, or a less viscous resin may be adopted if a lower curing temperature is preferred.

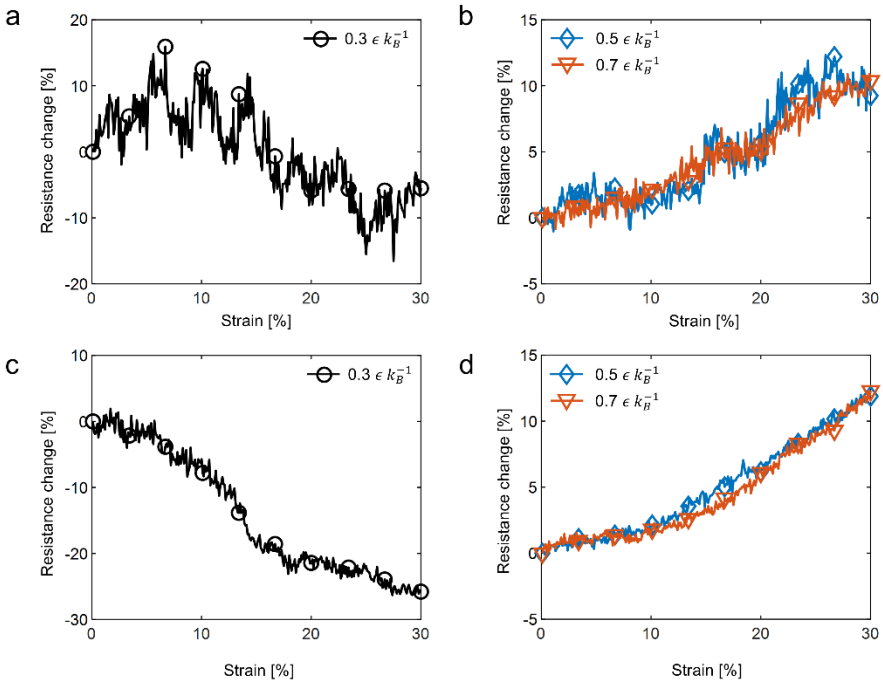

Figure 4.13. CGMD simulation results of the effect of simulation cell size on curing temperature-dependent piezoresistive behavior of CNT/epoxy nanocomposite. a–d) Simulated resistance change versus strain relationships of CNT/epoxy nanocomposites obtained with cell size of 50 σ (a,b) or cell size of 100 σ (c,d).

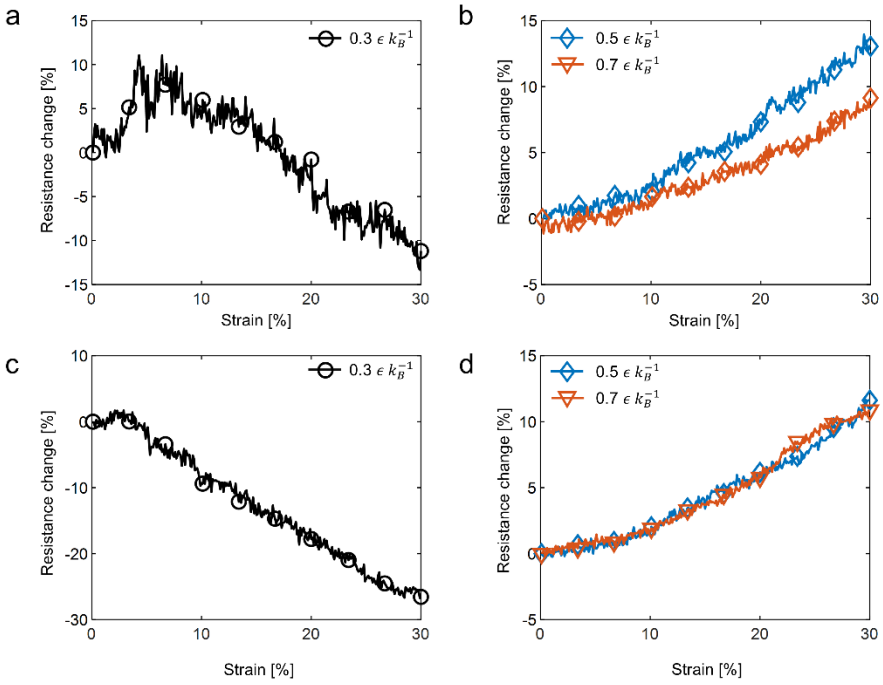

Figure 4.14. CGMD simulation results of the effect of CNT concentration on curing temperature-dependent piezoresistive behavior of CNT/epoxy nanocomposite. a,b) Simulated

resistance change versus strain relationships of CNT/epoxy nanocomposites with CNT concentration of 4 vol.% (a,b) or CNT concentration of 6 vol.% (c,d).

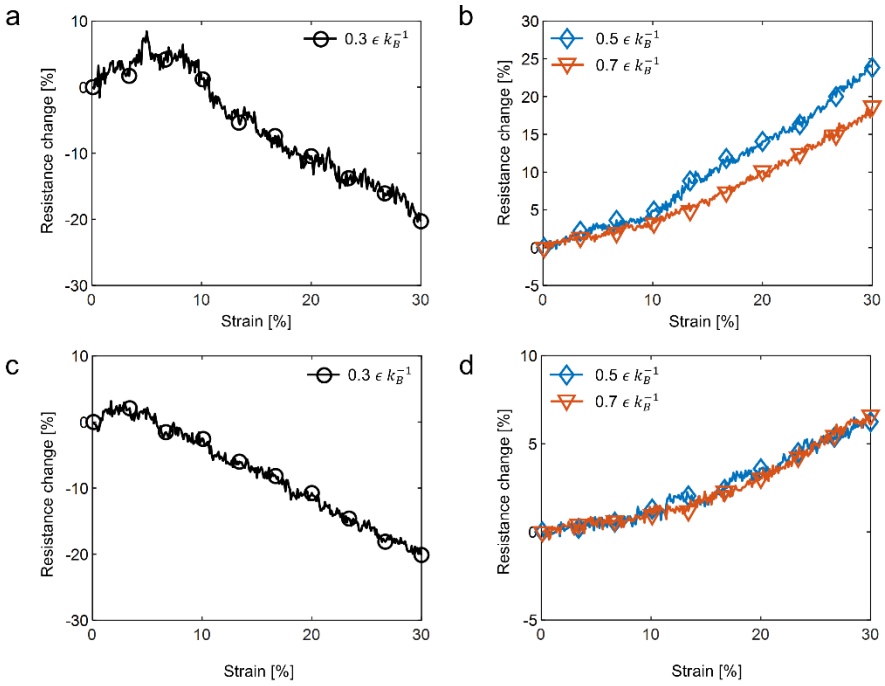

Figure 4.15. CGMD simulation results of the effect of CNT length on curing temperature-dependent piezoresistive behavior of CNT/epoxy nanocomposite. a–d) Simulated resistance change versus strain relationships of CNT/epoxy nanocomposites with CNT length of 50 beads per chain (a,b) or CNT length of 200 beads per chain (c,d).

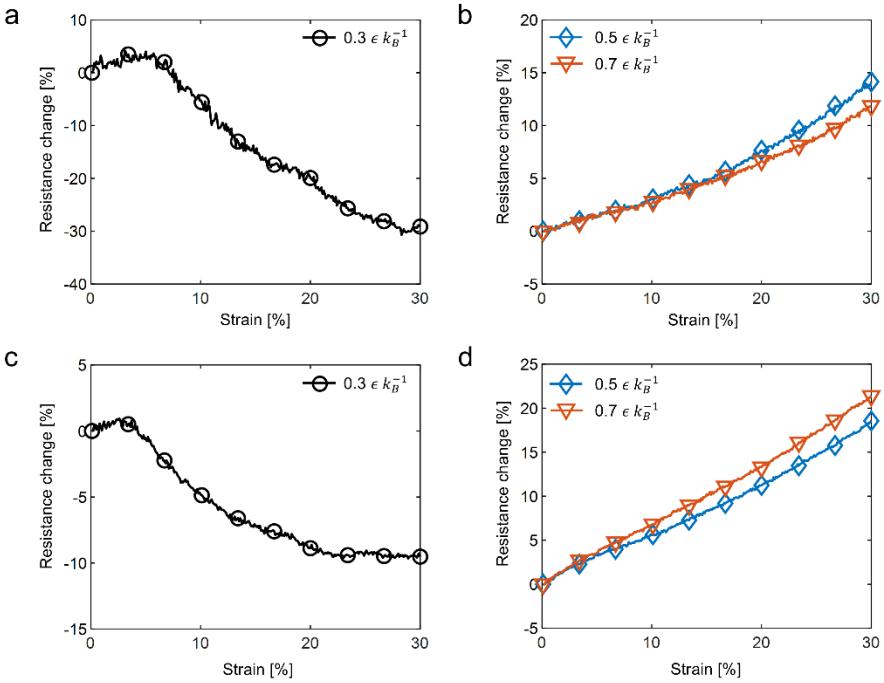

Figure 4.16. CGMD simulation results of the effect of CNT diameter on curing temperature-dependent piezoresistive behavior of CNT/epoxy nanocomposite. a–d) Simulated resistance change versus strain relationships of CNT/epoxy nanocomposites with CNT diameter of 1.5 σ (a,b) or CNT diameter of 2 σ (c,d).

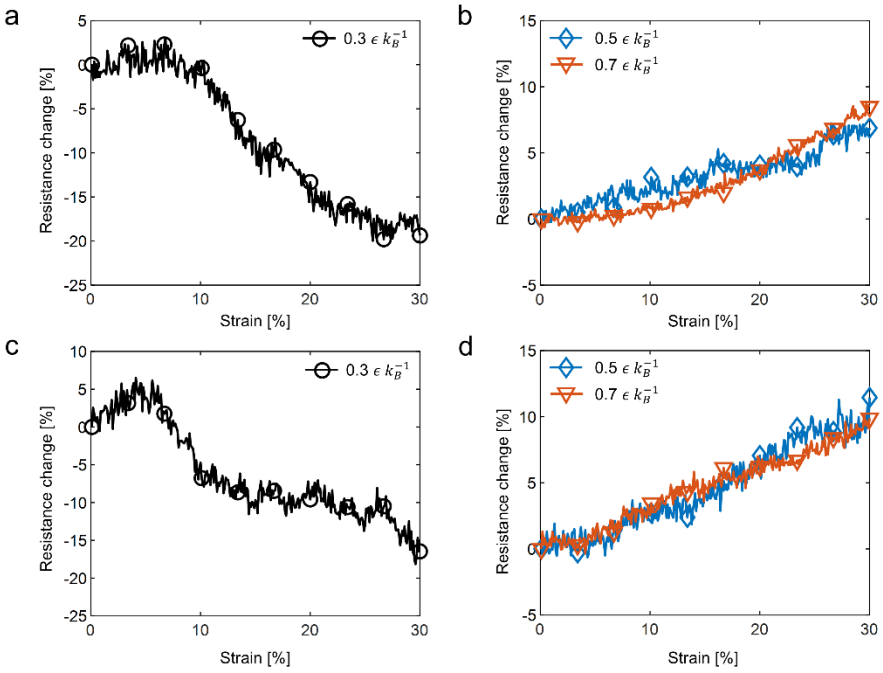

Figure 4.17. CGMD simulation results of effect of the CNT waviness on curing temperature-dependent piezoresistive behavior of CNT/epoxy nanocomposites. a–d) Simulated resistance

change versus strain relationships of CNT/epoxy nanocomposites with CNT waviness of 30° (a,b) or CNT waviness of 60° (c,d).

4.4 Conclusion

This chapter presents the results of an in-depth investigation of the microstructural origin of the nonmonotonic piezoresistive behavior of polymer nanocomposites. The experimental results indicate that the piezoresistive behavior transitions from nonmonotonic to monotonic with increasing curing temperature, and the CGMD simulations reproduce this temperature dependence. Through further analysis, the inter-nanofiller junction geometry is identified as a microstructural parameter governing the monotony of the piezoresistive behavior. During curing, thermally activated diffusion at high temperatures induces re-agglomeration of and direct contact between nanofillers in the liquid polymer matrix owing to vdW interactions. As a result, monotonic piezoresistive behavior is attained, as agglomerated nanofillers generally dissociate during stretching. For a nanofiller network developed under suppressed diffusion at low curing temperatures, re-agglomeration of the nanofiller is stimulated during stretching by molecular rearrangements in stress-activated STZs, which are associated with the viscoplastic deformation of the polymer matrix, leading to a decrease in resistance.

Modulating inter-nanofiller junction geometry enables control over the monotony of piezoresistive behavior in polymer nanocomposites. The molecular structure of the polymer matrix, which affects nanofiller diffusion, also plays an important role in the modulation of the inter-nanofiller junction geometry and piezoresistive behavior. Other nanofiller-related factors, such as nanofiller concentration, aspect ratio, and waviness, have limited impact, as briefly assessed by the simulations. Therefore, the influence of these factors is beyond the scope of the current work but may be further studied in future investigations. By developing

nanocomposites with monotonic piezoresistive behaviors, high-performance strain-sensing materials with extended operating ranges can be developed for real applications. The findings contribute to understanding electromechanical properties of polymer nanocomposites and provide a framework for designing advanced strain-sensing materials.

CHAPTER 5 EFFECT OF FIBER ORIENTATION ON THE PIEZORESISTIVITY OF CARBON NANOTUBE/EPOXY/GLASS FIBER COMPOSITES

5.1 Introduction

FRP composites have found increasing demand for structural applications in many engineering sectors because of their high strength-to-weight ratio, good resistance to corrosion and fatigue, and flexibility in design and multifunctionality. Many research studies have been carried out to reveal their physical, mechanical, electrical, and thermal properties, as well as fatigue behaviour, impact behaviour, and failure mechanisms etc. With better knowledge of FRP composites, advanced structures can be designed using these materials and applied to different situations and environmental conditions (Frigione & Lettieri, 2018). For instance, concrete-filled FRP tubes, which are formed by concrete cores and FRP tubes for confinement, have become one of the attractive forms of hybrid members in civil infrastructure (Bazli, Zhao, Bai, Singh Raman, & Al-Saadi, 2019; Y. L. Li, Teng, Zhao, & Singh Raman, 2018; Xie, Lin, Teng, & Jiang, 2020; B. Zhang, Yu, & Teng, 2015).

While the potential of FRP composites can be exploited thanks to the extensive research on designing composite structures, the demand for monitoring techniques that can monitor the health of the structures has arisen. With recent advancement of nanotechnology, researchers have been able to develop new multifunctional nanocomposites that possess unique mechanical, electrical, and thermal properties (Balasubramaniam, Sathiyan, Palani, Iyer, & Gupta, 2019; Gu et al., 2016). Piezoresistivity utilizing the electrically conducting network of carbon nanotubes (CNTs) in polymer nanocomposite is a major area of interest within the field of multifunctional composites as the coupled electromechanical response is a fundamental property of strain sensing (Böger, Wichmann, Meyer, & Schulte, 2008; Ku-Herrera, Pacheco-

Salazar, Ríos-Soberanis, Domínguez-Rodríguez, & Avilés, 2016; Thostenson & Chou, 2006). Thostenson and Chou (2006) fabricated cross-ply and unidirectional glass fibre reinforced polymer (GFRP) laminates with 0.5 wt.% multi-walled CNTs dispersed into the epoxy matrix and used the nanofiller network as distributed sensors for *in situ* strain and damage sensing under tensile and flexural loads. Böger et al. (2008) demonstrated that similar self-sensing nanocomposites can be used for strain and damage monitoring in GFRP laminates under incremental tensile tests and fatigue tests. Ku-Herrera et al. (2016) showed that using dispersed nanofillers in the epoxy matrix can achieve better sensitivity to matrix dominated damages such as matrix microcracking and fiber-matrix debonding in unidirectional GFRP laminates.

Despite the excellence and great potential shown in using self-sensing nanocomposites for structural health monitoring in FRP composites, much work is required to promote the application of this method in real-life industrial structures. For FRP tubes, the choice of fibre orientation depends on the applications, ranging from 55° for close ended pipes (e.g. hydrogen tank) (Taşyürek & Tarakçioğlu, 2017; Üstün, Eskizeybek, & Avci, 2016; Üstün, Ulus, et al., 2016), to 80° for concrete-filled FRP tubes (Xie et al., 2020; B. Zhang et al., 2015). However, in the preliminary investigations, when piezoresistive CNT/epoxy nanocomposites were applied to filament wound CNT/GFRP composite tubes, nonmonotonic and monotonic resistance change-strain relationships were observed for [±55] and [±80] samples under split-disk tests respectively. This observation suggests that the fiber orientation may significantly influences the piezoresistive behavior of CNT/GFRP composites, yet the effect of fiber orientation has not been closely examined.

Therefore, this study aims to conduct a comprehensive investigation on the effect of fiber orientation on the piezoresistive behavior of GFRP composites reinforced with CNTs. Glass fibers were aligned at different angles with respect to the uniaxial and hoop tension in laminates and tubes respectively using epoxy with dispersed CNTs as matrix. The electromechanical

responses of the samples were acquired via quasi-static tensile tests, and the strains were measured by a digital image correlation (DIC) system. The resistance change-strain relationships indicates that the piezoresistive behavior of CNT/GFRP composite structures exhibit profound fiber orientation-dependence and warrants further investigations.

5.2 Methods

5.2.1 Materials and Sample Fabrications

The methodology employed here follows that described in Chapter 4.2.1, with the following modifications:

Industrial multiwalled carbon nanotubes (purity: >95%, inner diameter: 5–15 nm, outer diameter: 30–80 nm, length: <100 μm) were purchased from XFNANO, China. Bisphenol A diglycidyl ether-based epoxy resin (EL2) and cycloaliphatic amine-based epoxy hardener (AT30 Slow) were supplied by Easy Composites, UK.

The fabrication processes for CNT/epoxy nanocomposite and CNT/GFRP composite laminate samples are schematically illustrated in Figure 5.1. The first step was the dispersion of CNTs into the resin. The second step was the fabrication of CNT/epoxy nanocomposites and CNT/GFRP laminates via a manual lay-up process. Nanocomposite samples with CNT concentrations from 1 to 3 wt.% were prepared to determine the percolation threshold. Unidirectional glass fiber fabrics were wetted with the CNT/epoxy mixture and stacked on a flat aluminum mold to produce laminates with fiber orientations from 0° to 90°. Note that in this study the 90° is defined as the longitudinal direction. The CNT concentration was fixed at 2 wt.% for laminate samples based on the electrical percolation behavior presented in Chapter 5.3.1. The laminates consisted of four plies. The lay-ups were compacted using vacuum

bagging and then cured at room temperature for 24 h followed by 60 °C for 6 h. Additional $[\pm 55]_2$, $[\pm 80]_2$, and $[90/0]_s$ specimens were fabricated using direct heat curing at 60 °C for 6 h, in order to evaluate the influence of curing condition on the piezoresistive behavior of CNT/GFRP composites. The nominal thickness of wet-layup laminates was about 2 mm.

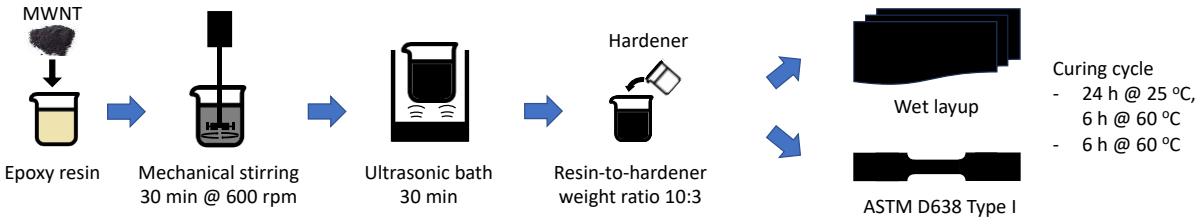

Figure 5.1. Procedures for fabricating CNT/epoxy nanocomposites and CNT/GFRP laminates.

The fabrication process for CNT/GFRP tube samples is schematically illustrated in Figure 5.2. The first step was the dispersion of CNTs into the resin. The procedures were same as the laminate samples. The second step was the fabrication of CNT/GFRP tubes via a filament winding process using a X-Winder desktop filament winder. Glass fiber rovings were wetted with the CNT/epoxy mixture and wound on a mandrel to produce tubes with fiber orientations from 25° to 89°. The fiber orientation is controlled by the relative speed between mandrel rotation and carriage lateral movement when the reinforcing fibers in fiber bundles were arranged on a mandrel. The CNT concentration is also fixed at 2.0 wt.% for tube samples. The tubes were configured as $[\pm\theta]$, where θ is the angle between the fiber and the longitudinal axis, and cured at room temperature for 24 h. The nominal inner diameter and thickness of filament wound tubes were about 53 and 2 mm respectively.

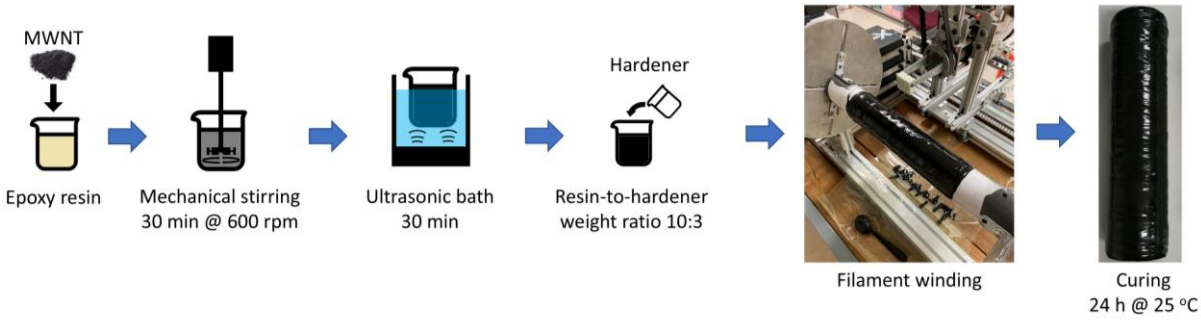

Figure 5.2. Procedures for fabricating CNT/GFRP filament wound tubes.

5.2.2 Electromechanical Tests

Quasistatic tensile tests were performed on the CNT/epoxy nanocomposite and CNT/GFRP laminate samples using a universal testing machine (5982, Instron, USA) as shown in Figure 5.3a. Rectangular tensile test specimens were precisely cut from the laminates using an abrasive waterjet system (ProtoMax, OMAX) to dimensions complying with specifications in ASTM D3039, i.e. width of 25 mm and length of 250 mm. A minimum of three specimens were tested for each sample. The specimens were loaded along the 90° direction at a crosshead speed of 1 mm min^{-1} until failure. During loading, the electrical resistance and axial deformation of the specimens were measured simultaneously. Craft papers and non-conducting GFRP composites were bonded to the gripping areas of the nanocomposite and laminate specimens using a cyanoacrylate adhesive and 3M™ Scotch-Weld™ Epoxy Adhesive 2216 respectively, to electrically insulate the conductive specimens from the universal testing machine. Strain measurements were acquired through a digital image correlation (DIC) system as shown in Figure 5.3b and described in Chapter 5.2.3. Electrical resistances were measured via the two-probe method using a digital multimeter (DMM6500, Keithley Instruments). On every specimen, a pair of parallel electrodes were marked using conductive silver paint (SPI Supplies), 2 mm apart from each other.

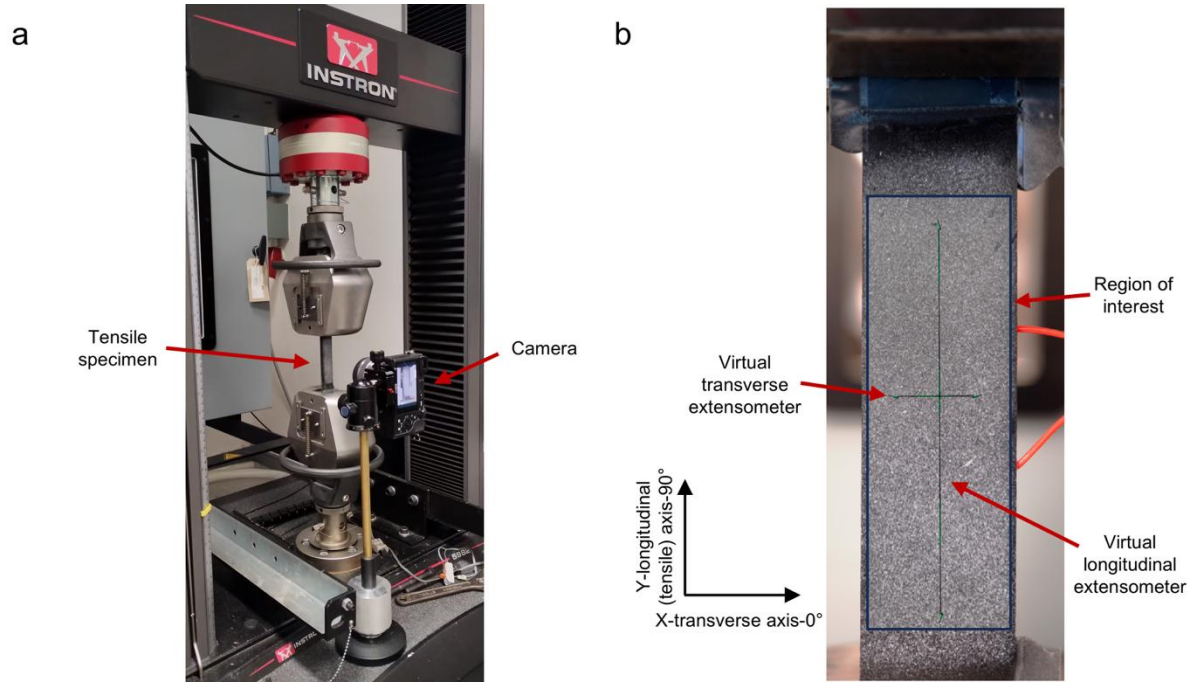

Figure 5.3. Experimental setup for a) quasistatic tensile test with camera for DIC image capture, and b) sprayed random speckle pattern on tensile test specimen surface with region of interest and virtual extensometers for strain analysis.

Quasistatic split-disk tests were performed on the CNT/GFRP tube samples using a universal testing machine (5982, Instron, USA) to study the piezoresistive properties of the composite structures under hoop tension (Figure 5.4). Ring tensile test specimens were precisely cut from the tubes to dimensions complying with specifications in ASTM D2290, i.e. width of 20 mm. A minimum of three specimens were tested for each sample. The specimens were loaded along the hoop (90°) direction at a crosshead speed of 1 mm min^{-1} until failure. The ring coupons were mounted on the testing machine with high-pressure grease applied between the rings and the electrical insulating tape-covered steel half-disks to prevent friction effect and electrically insulate the conductive specimens from the machine. During loading, the electrical resistance, hoop and longitudinal deformation of the specimens were measured simultaneously. Strain measurements were acquired through uniaxial strain gauges (gauge length: 2 mm, gauge factor: 2.11, resistance: 120 Ω; BFLA-5-3-1LJB, Tokyo Measuring

Instruments Laboratory) outside of the middle gap region to eliminate bending effect at the gaps (Bazli et al., 2019; B. Zhang et al., 2015). Electrical resistances were measured via the two-probe method using a digital multimeter (DMM6500, Keithley Instruments). On every specimen, a pair of parallel electrodes were marked using conductive silver paint (SPI Supplies), 2 mm apart from each other.

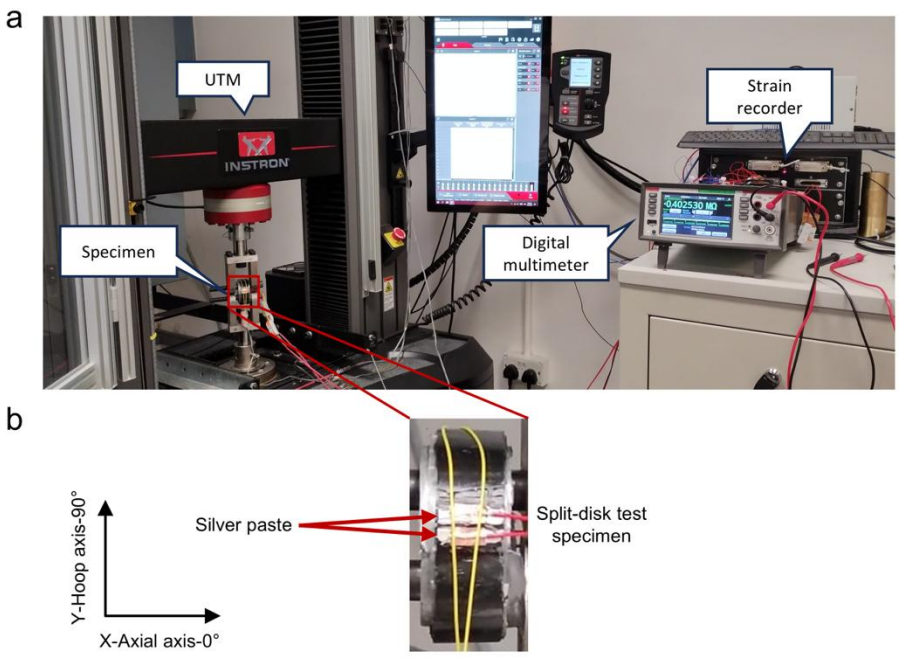

Figure 5.4. Electromechanical split-disk test setup of CNT/GFRP composite tubes.

5.2.3 Digital Image Correlation

Strain field was obtained using a DIC system (Figure 5.3b). Speckle patterns were applied onto the surface of specimens by firstly spraying black paint to produce uniform background, followed by generating random pattern using white paint speckles. A camera (ILCE-6400, Sony) equipped with a 30 mm focal length lens (E 30mm F3.5 Macro, Sony) is positioned perpendicular to the specimen surface, capturing images as the surface is loaded (Figure 5.3a). Images were taken at five-second intervals. Image correlation analysis is

performed using the GOM Correlate 2019 software, with a facet size set at 30 × 30 pixels and a separation of 10 pixels. The virtual extensometer feature was employed for longitudinal and transverse strain measurements to construct the stress-strain curves.

5.3 Results and Discussion

5.3.1 Electrical Percolation and Piezoresistive Behaviors of CNT/Epoxy Nanocomposites

Based on the electrical percolation behavior of CNT/EL2 nanocomposite samples as shown in Figure 5.5, the percolation threshold was at or below 2 wt.% CNTs, therefore the CNT concentration was chosen to be 2 wt.% for the following studies. Figure 5.6 shows the electromechanical responses of the CNT/epoxy nanocomposite samples cured at room temperature and 60 °C. The curing dependent piezoresistive behavior is observed from the resistance change-strain relationships displayed in Figure 5.6.

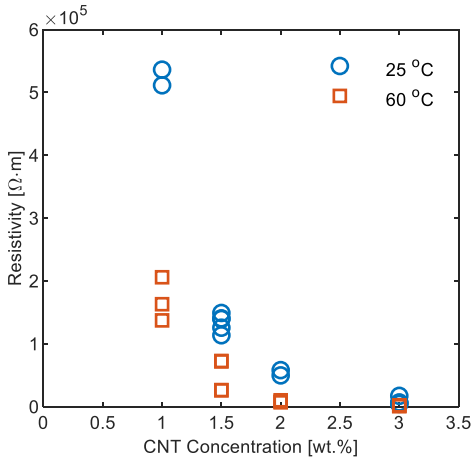

Figure 5.5. Experimental electrical resistance of CNT/EL2 nanocomposites of different CNT concentrations cured at different temperatures.

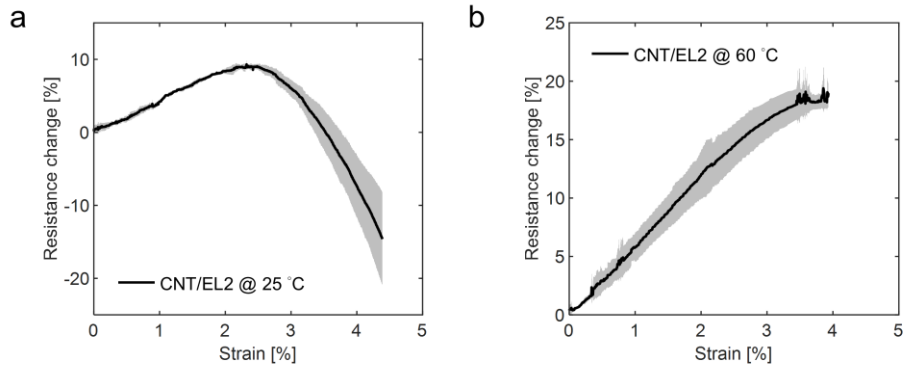

Figure 5.6. Resistance change-strain relationships of CNT/epoxy nanocomposite samples that were cured at a) room temperature and b) 60 °C (for each sample, three specimens were tested, and the mean response is plotted with shaded area representing ±1 standard deviation).

5.3.2 Effect of Fiber Orientation on Piezoresistive Behaviors of CNT/GFRP Laminates

Figure 5.7 shows the electromechanical responses of $[\pm 55]_2$, $[\pm 80]_2$, and $[90/0]_s$ laminate samples with 2 wt.% nanofillers that were cured under different cycles. The piezoresistive behaviors of laminate samples appear to be influenced more significantly by fiber orientation than by curing temperature within the range of curing conditions examined. For the $[\pm 55]_2$ and $[\pm 80]_2$ laminate samples cured at room temperature, inversions in piezoresistivity occurred at around 0.73 and 1.35% strain respectively. The values are 1.12%, 1.24% when the laminates were cured at 60 °C. The resistance of each of these samples first increased with strain, reaching its maximum at the respective critical strain (γ_c), and then decreased until the sample failed. On the other hand, both the room temperature- and 60 °C-cured cross-ply $[90/0]_s$ samples demonstrated monotonic piezoresistive behavior until failure. For a material that is oriented towards strain sensing, having a monotonic or nonmonotonic with relatively high γ_c piezoresistive behavior would be absolutely crucial (Meeuw et al., 2016; Luigi Vertuccio et al.,

2015). The results presented indicate that the piezoresistive behaviors of CNT/GFRP composites can be significantly affected by fiber orientation.

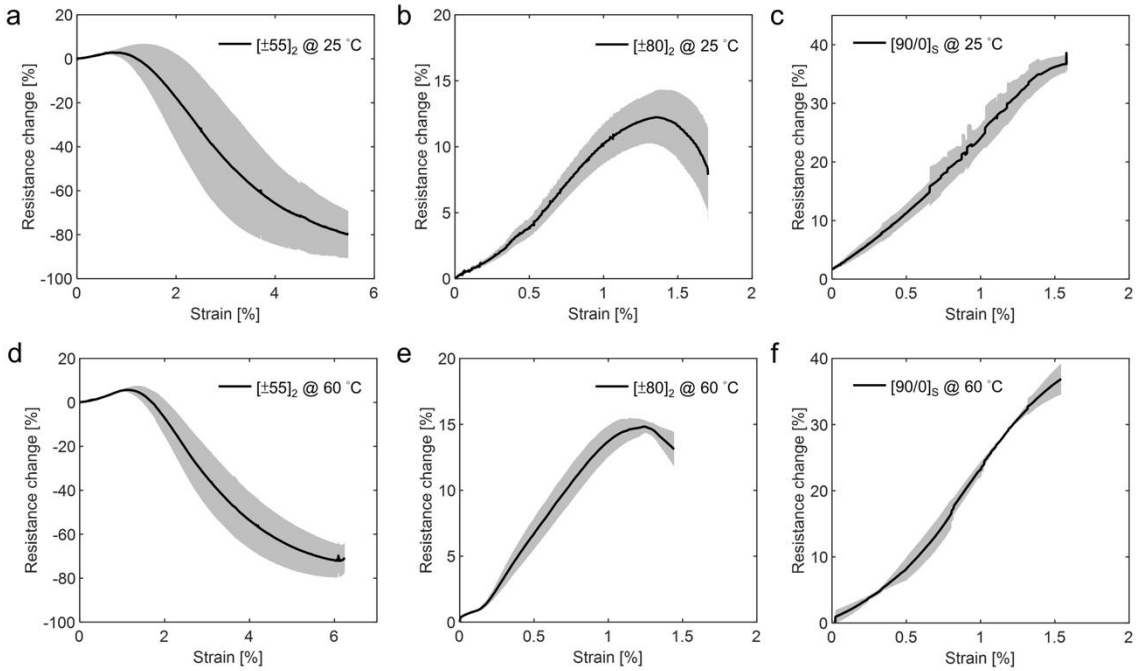

Figure 5.7. Resistance change-strain relationships of a,d) $[\pm55]_2$, b,e) $[\pm80]_2$, and c,f) $[90/0]_s$ CNT/GFRP composite laminate samples that were cured at a-c) room temperature and d-f) 60 °C (for each sample, three specimens were tested, and the mean response is plotted with shaded area representing ±1 standard deviation).

To provide a more comprehensive understanding of the composite system, the mechanical properties of the CNT/GFRP samples are displayed in Figure 5.8. The stress-strain responses of the $[\pm55]_2$ samples show clear yielding and higher failure strain, indicating ductile behavior. The yield stress and strain were 72.07±4.20 MPa and 1.85±0.09% respectively when the samples were cured at room temperature. The values were similar with a higher curing temperature of 60 °C, at 73.66±2.66MPa and 1.79±0.03% respectively. When the composites contained fiber aligned near the loading direction, i.e. $[\pm80]_2$ and $[0/90]_s$, the stress-strain

curves exhibited more brittle behavior with higher modulus and tensile strength. Figure 5.9 compared the Young's modulus and tensile strength of the CNT/GFRP composites with different fiber orientations and curing temperature. Both parameters increased from $[\pm 55]_2$ to $[0/90]_s$, reaching a maximum in $[\pm 80]_2$. Similar to the piezoresistive behavior, the mechanical properties were dominated by fiber orientation and appeared barely influenced by curing temperature.

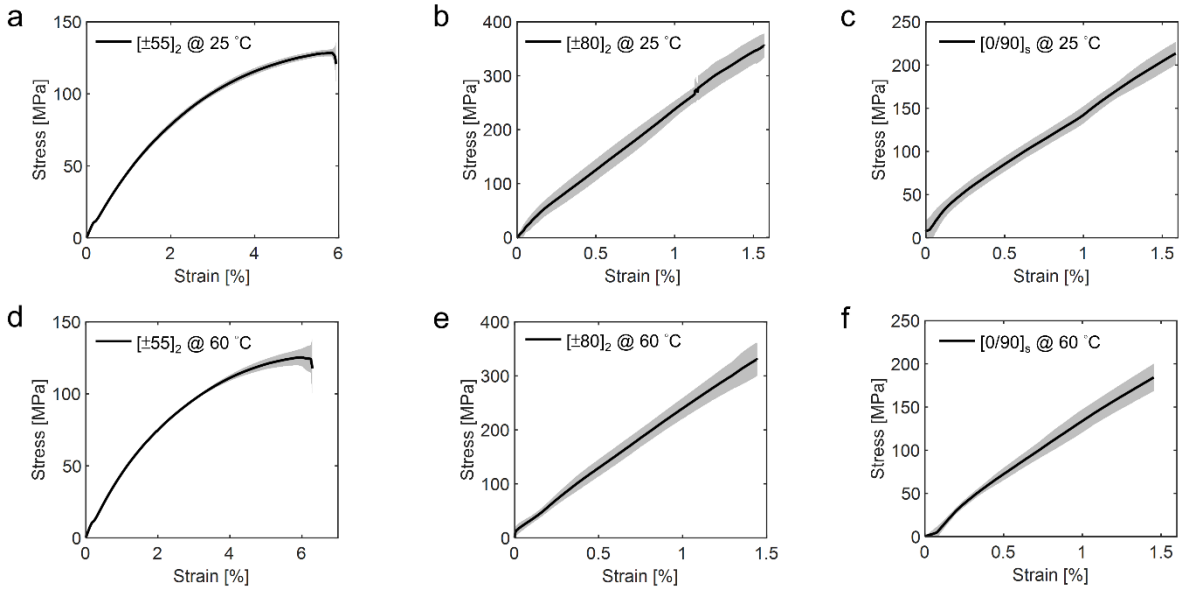

Figure 5.8. Stress-strain relationships of a,d) $[\pm 55]_2$, b,e) $[\pm 80]_2$, and c,f) $[90/0]_s$ CNT/GFRP composite laminate samples that were cured at a-c) room temperature and d-f) 60 °C (for each sample, three specimens were tested, and the mean response is plotted with shaded area representing ±1 standard deviation).

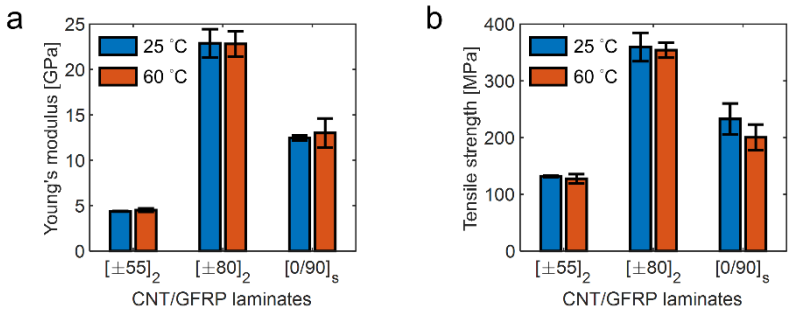

Figure 5.9. a) Young's modulus and b) tensile strength of $[\pm 55]_2$, $[\pm 80]_2$, and $[90/0]_s$ CNT/GFRP composite laminate samples that were cured at room temperature and 60 °C. For each sample, three specimens were tested and the mean measurement is plotted (error bar: ±1 standard deviation).

To further investigate the influence of fiber orientation, laminate samples with fiber orientations from 0° to 90° were prepared and tested for their electromechanical responses. The resistance change-strain relationships of the laminate samples are presented in Figure 5.10. From the results, it can be seen that there are three types of piezoresistive behavior, i.e. monotonic (Figure 5.10a-c), nonmonotonic with relatively low γ_c (Figure 5.10d-f), and nonmonotonic with relative high γ_c (Figure 5.10g-i), which exhibit clear dependence on fiber orientations. Laminates containing fibers oriented nearly perpendicular to the tensile direction (e.g., $[0]_4$, $[\pm 15]_2$, $[90/0]_s$) demonstrated a monotonic increase in resistance as strain increases. Laminates with fibers oriented around 45° to the tensile direction (e.g., $[\pm 35]_2$, $[\pm 45]_2$, $[\pm 55]_2$) exhibited a nonmonotonic resistance change-strain response. This response type is characterized by an initial increase in resistance, followed by a decrease upon reaching a critical strain, which is relatively low (e.g., ~0.73% for $[\pm 55]_2$). When fibers were aligned nearly parallel to the tensile axis (e.g., $[\pm 75]_2$, $[\pm 80]_2$, $[90]_4$), the resistance change-strain response remained nonmonotonic; however, the strains at which resistance peaks are closer to the failure strains.

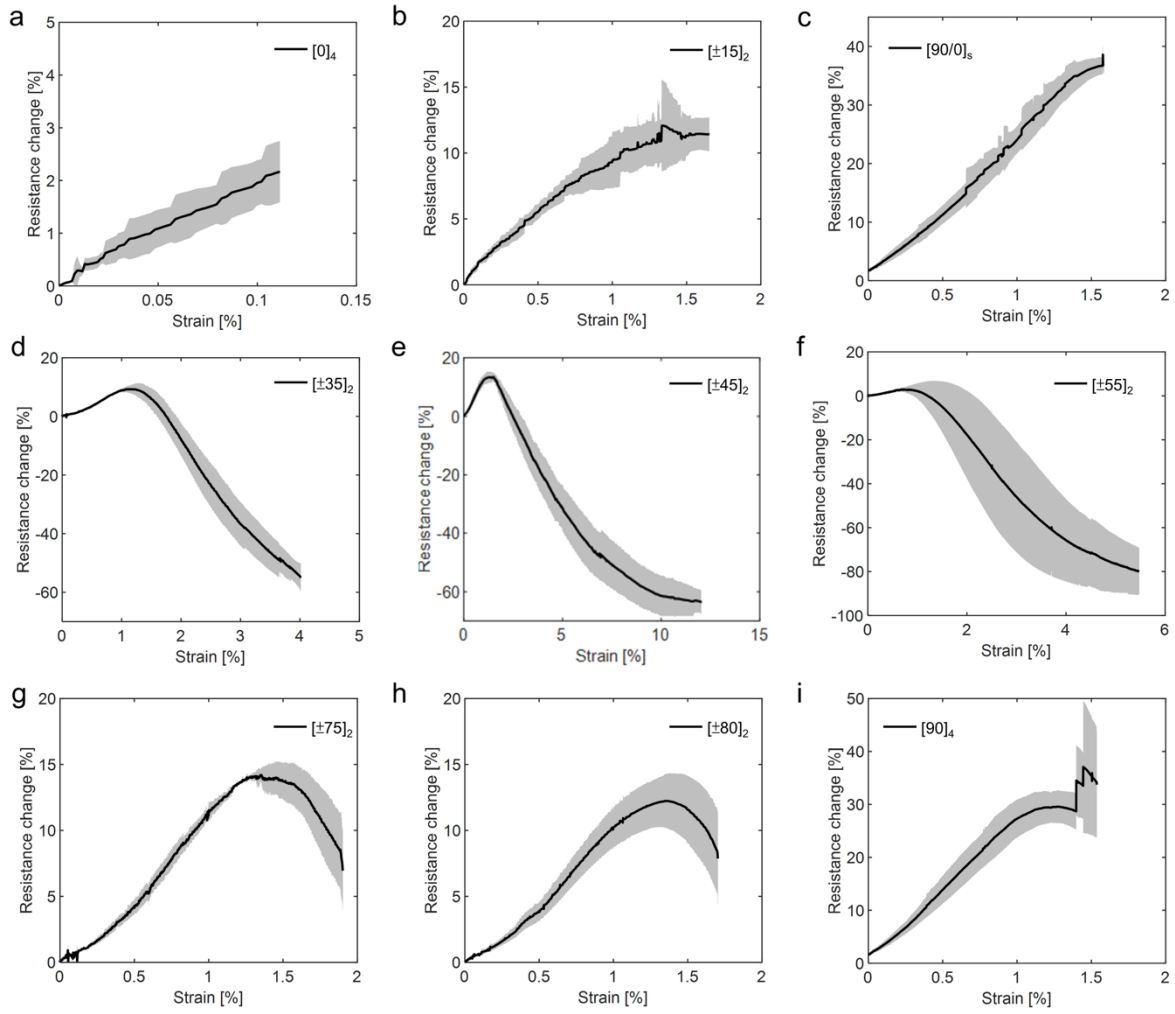

Figure 5.10. Resistance change-strain relationships of a) $[0]_4$, b) $[\pm15]_2$, c) $[90/0]_s$, d) $[\pm35]_2$, e) $[\pm45]_2$, f) $[\pm55]_2$, g) $[\pm75]_2$, h) $[\pm80]_2$, and i) $[90]_4$ CNT/GFRP composite laminate samples that were cured at room temperature (for each sample, three specimens were tested and the mean response is plotted (shaded area: ±1 standard deviation)).

5.3.3 Effect of Fiber Orientation on Piezoresistive Behaviors of CNT/GFRP Tubes

It is important to examine the influence of fiber orientation on non-planer structures for realistic real-world applications. Therefore, tube samples with fiber orientations from 25° to 89° were prepared and tested for their electromechanical responses. The resistance change-

strain relationships of the tube samples are presented in Figure 5.11. From the results, there are two types of piezoresistive behavior, i.e. monotonic and nonmonotonic, which exhibit clear dependence on fiber orientations. Tubes with fiber orientations of ±25° and ±35° or near parallel to the tensile direction (e.g., ±75°, ±80°, ±89°) demonstrate monotonic increase in resistance as strain increases. Tubes with fibers oriented around 55° to the tensile direction (e.g., [±45], [±55], and [±65]) exhibit nonmonotonic resistance change-strain response. This response type is characterized by an initial increase in resistance, followed by a decrease upon reaching a critical strain (e.g., ~0.76% for [±55] tube).

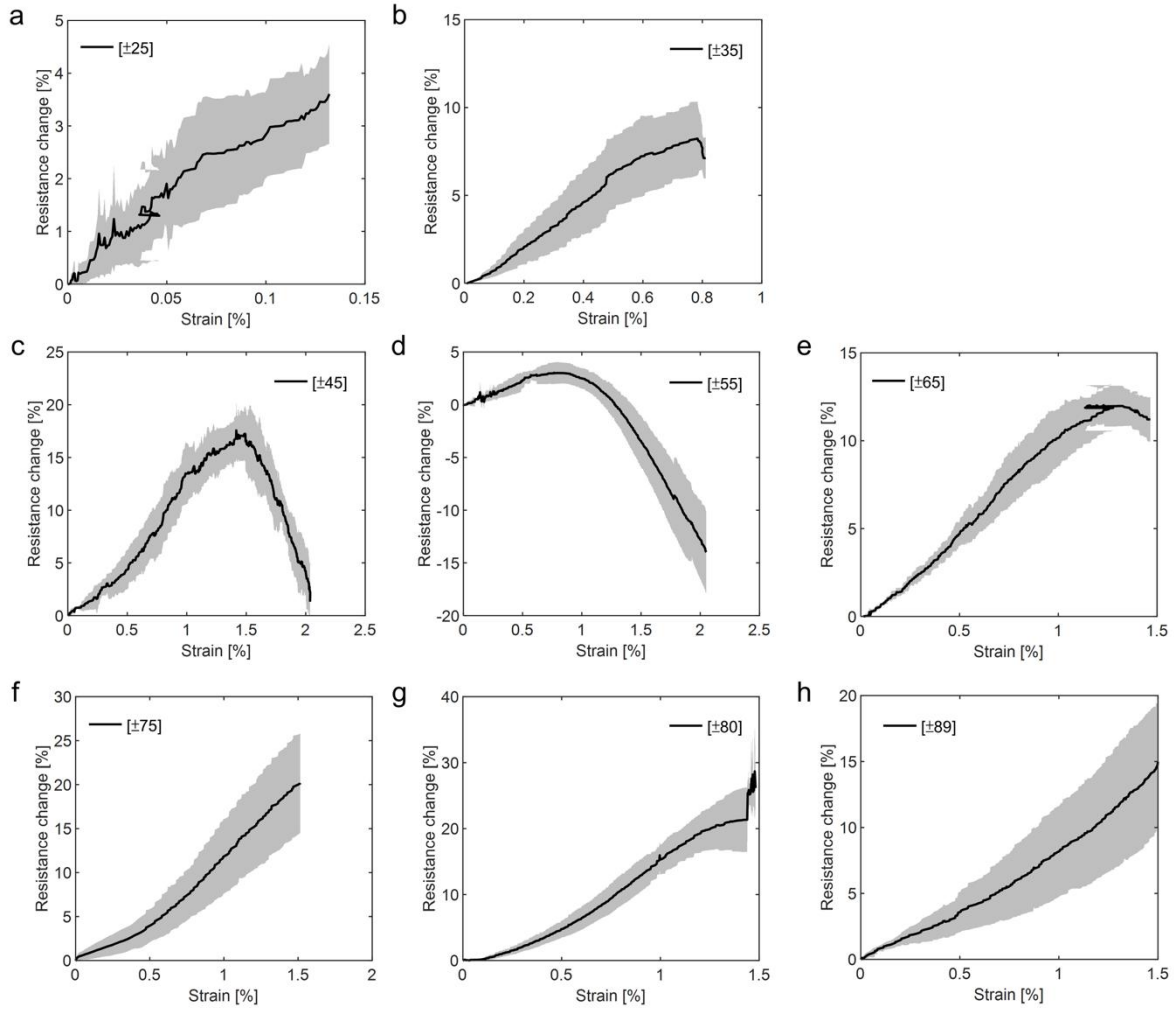

Figure 5.11. Resistance change-strain relationships of a) [±25], b) [±35], c) [±45], d) [±55], e) [±65], f) [±75], h) [±80], and i) [±89] CNT/GFRP composite tube samples that were cured at

room temperature (for each sample, three specimens were tested and the mean response is plotted (shaded area: ±1 standard deviation)).

The piezoresistive behaviors of the CNT/GFRP composite laminates and tubes both exhibit dependence on fiber orientation. This correlation provides valuable insights into the piezoresistivity and deformation mechanisms of the material as the changes in CNT conducting networks within the composite are influenced by the strain states (H. Zhang et al., 2015). With the reinforcing glass fibers oriented in different directions, the deformation mechanisms are altered, leading to variations in the strain distribution and piezoresistive behavior. This warrants further investigation for designing tailored CNT/GFRP composites with optimized piezoresistive performance for SHM applications.

Table 5.1. Summary of fiber orientation dependent piezoresistive behavior of CNT/GFRP composite samples.

Samples	Fiber orientation	Piezoresistivity
Laminates	$[0]_4$, $[\pm15]_2$, $[90/0]_s$	Monotonic
	$[\pm35]_2$, $[\pm45]_2$, $[\pm55]_2$	Nonmonotonic w/ low ε_c
	$[\pm75]_2$, $[\pm80]_2$, $[90]_4$	Nonmonotonic w/ high ε_c
Tubes	[±25], [±35]	Monotonic
	[±45], [±55], [±65]	Nonmonotonic
	[±75], [±80], $[90]_2$	Monotonic

5.4 Conclusion

This chapter establishes that fiber orientation governs the evolution of resistance change in CNT/GFRP laminates and tubes under tensile deformation, leading to distinct piezoresistive behaviors. These findings are critical for the design of self-sensing composite structures, where the desired electromechanical response can be tailored through strategic fiber alignment. The results reveal that for both laminate and tube, the piezoresistive behaviors are monotonic when fibers are aligned perpendicular to the loading direction. When the fiber orientation becomes off-axis, the electromechanical responses are distinctively nonmonotonic. The monotony improves with the fibers approaching parallel to the loading direction. The findings reported here shed new light on the mechanisms that govern the piezoresistive behavior of CNT/GFRP composites, which will be elucidated by further numerical simulations and experimentation.

CHAPTER 6 MICROSTRUCTURAL ORIGIN OF NONMONOTONIC PIEZORESISTIVITY IN CARBON NANOTUBE/EPOXY/GLASS FIBER COMPOSITES

6.1 Introduction

This chapter attempts to elucidate the underlying mechanisms of the fiber orientation dependent piezoresistive behavior of CNT/GFRP composites. A multiscale electromechanical framework is proposed for modeling CNT-modified GFRP composites. The model includes two physical scales, i.e. microscale for unit cells of yarn and matrix, and mesoscale for geometric pattern of yarn and matrix, involving both mechanical and electrical domains. Finite Element Modeling (FEM) is applied for both scales. The proposed approach is demonstrated to evaluate the electromechanical responses of CNT/GFRP composites with arbitrary fiber orientations. DIC and FEA reveal that the strain distribution heterogeneity varies with fiber orientation, and localized transverse compression may lead to the inversion in piezoresistivity. The elemental resistivity changes and weighted means of tunneling distance provide microscopic insights into the changes in the CNT network during the transition from positive to negative piezoresistivity. The study highlights the intricate relationship between fiber orientation, deformation mechanisms, and CNT network reconfiguration in CNT/GFRP composites under tensile loading, providing valuable insights for designing tailored composites with optimized piezoresistive performance for structural health monitoring applications.

6.2 Methods

6.2.1 Materials and Sample Fabrications

The methodology employed here follows that described in Chapter 5.2.1, with the following modifications:

The fabrication process for CNT/GFRP laminate samples is schematically illustrated in Figure 6.1. Unidirectional glass fiber fabrics were wetted with the CNT/epoxy mixture and stacked on a flat aluminum mold to produce laminates with fiber orientations of ±15°, ±55°, and 90°.

Figure 6.1. Procedures for fabricating CNT/GFRP laminates.

6.2.2 Electromechanical Tests

The methodology employed here follows that described in Chapter 5.2.2.

6.2.3 Digital Image Correlation

The methodology employed here follows that described in Chapter 5.2.3.

6.2.4 Gas Pycnometry

To characterize the fiber volume fraction, a Microtrac BELPYCNOL gas pycnometer was used to measure the volume of composite samples (Cook, Forrest, & Goodwin, 1999; Ramsdale-Capper & Foreman, 2018). Measurements were performed on 13 × 50 mm laminate specimens and 20 × 20 mm tube specimens cut from all type of samples at 20.00 ± 0.01 °C using helium gas. Laminate specimens were placed in a standard 60 specimen chambers respectively. The chamber was purged 3 times prior to measurement cycles. The precision of the measurement was controlled by the standard deviation requirement, which was set as 0.2% for 3 out of a maximum of 30 measurements. Density was calculated by dividing the electronic balance-measured specimen mass by the volume. Then, the fiber volume fraction (v_f) is determined using the rule of mixtures as

$$v_f = \frac{\rho_c - \rho_m}{\rho_f - \rho_m} \tag{6.1}$$

where ρ_c is the composite density, ρ_m is the matrix density, and ρ_f is the fiber density. Taking ρ_m = 1.16 g cm^{-3} for epoxy and ρ_f = 2.54 g cm^{-3} for E-glass, the nominal v_f of CNT/GFRP wet-layup laminates were 36.84 ± 7.74 %.

6.2.5 Micro-computed Tomography

X-ray 3D micro-computed tomography (μ-CT) was utilized to characterize the geometry and alignment of fiber bundles (Godara & Raabe, 2007; Gonabadi et al., 2022; López-Santos et al., 2024; Schell, Renggli, van Lenthe, Müller, & Ermanni, 2006). Samples were cut from the cured laminates to a size of 13 × 50 × 2 mm. μ-CT measurements were carried out using a Bruker Skyscan 1276 In Vivo Micro-CT system. The resolution is 10.2 μm. The fiber bundles and their elliptic cross-sections of $[\pm 15]_2$, $[\pm 55]_2$, and $[90]_4$ are shown in Figure 6.2.

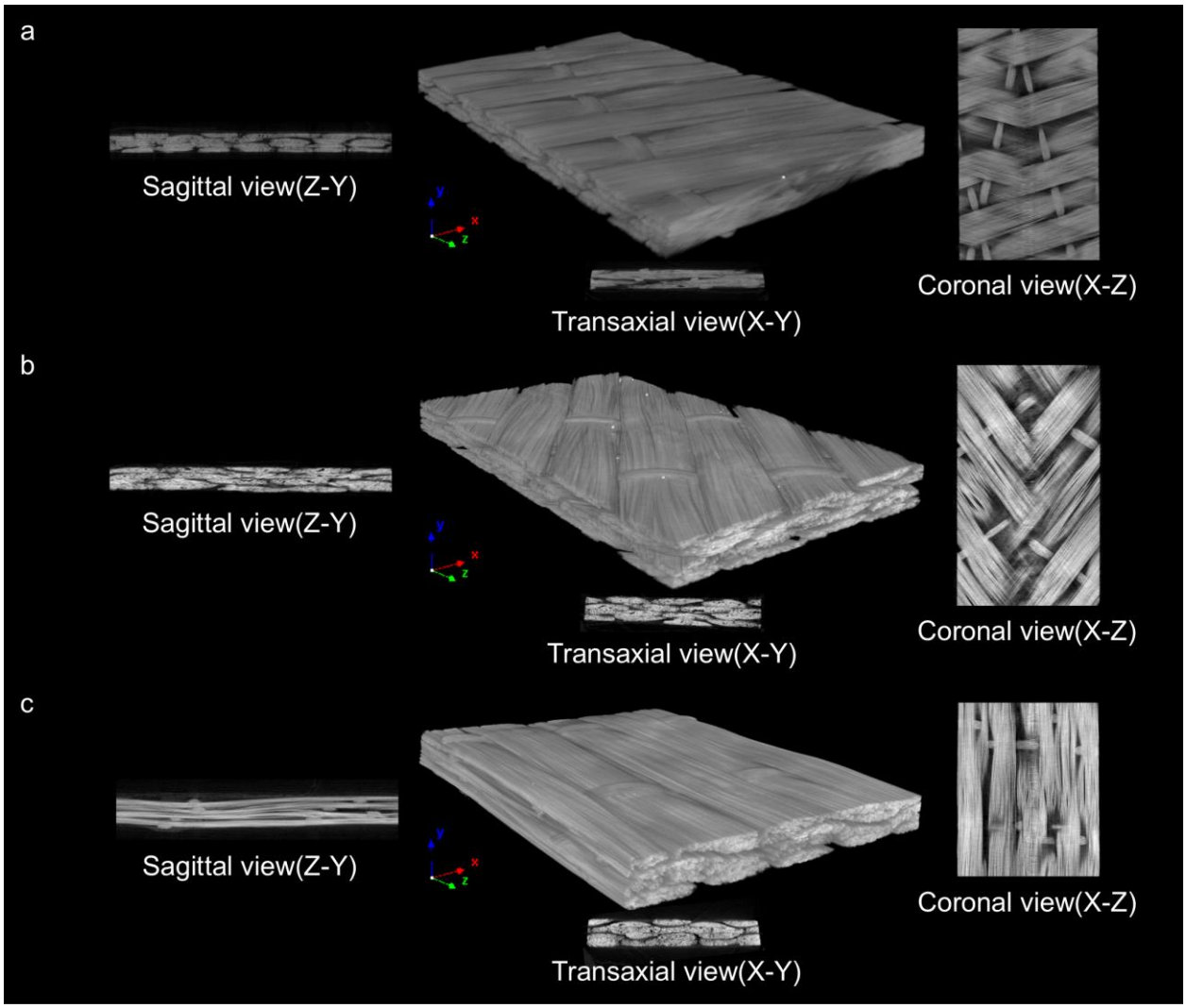

Figure 6.2. 3D reconstruction of fiber bundles in a) $[\pm 15]_2$, b) $[\pm 55]_2$, and c) $[90]_4$ laminate samples by μ-CT.

6.2.6 Optical Microscopy

Optical micrographs were taken using an Olympus BX43 microscope to obtain the fiber diameter. Sample was cut from the cured $[90]_4$ laminates to a size of 13 × 50 × 2 mm and the transaxial cross-section (parallel to the fiber alignment) was polished using sandpaper grade 10 000. The elliptic cross-section of yarn, matrix-rich region, and cross-section of individual fiber are visible in Figure 6.3.

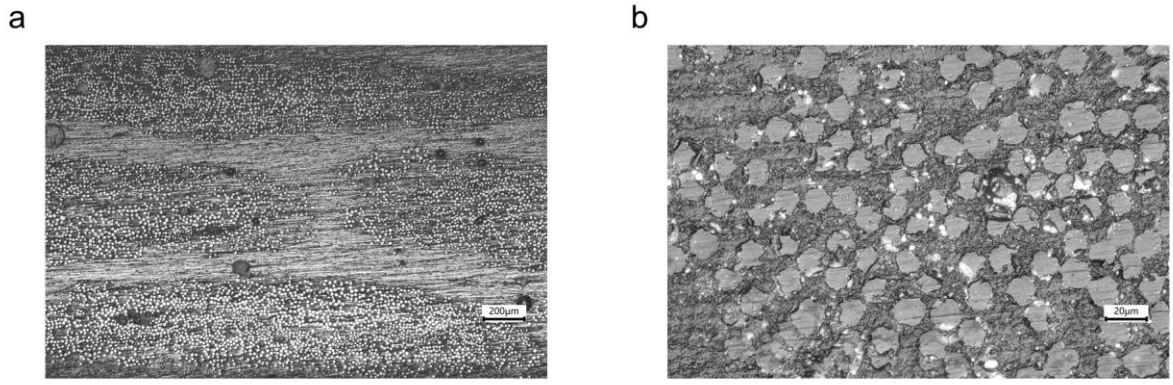

Figure 6.3. Optical micrographs of the transaxial cross-section of $[90]_4$ laminate samples at a) 5× and b) 50× magnifications.

Table 6.1 provides the fabric specifications obtained from µ-CT and optical microscopy analysis. These parameters serve as input for the subsequent multiscale FE simulation.

Table 6.1. Yarn and fiber specifications.

Parameters	Value
Fiber volume fraction (v_f)	35%
Fiber diameter (d_f)	15 µm
Yarn cross-sectional width (w_{yarn})	3 mm
Yarn cross-sectional height (t_{yarn})	0.5 mm

6.2.7 Scanning Electron Microscopy

The fracture surfaces produced in the tensile tests were observed using a field emission scanning electron microscope (FESEM; MAIA3, TESCAN, Czech Republic) operating at 5 kV. The fracture surfaces were coated with a thin layer of gold by sputtering (MCM-200, NanoImages) for FESEM imaging. Figure 6.4 shows the FESEM image of the fracture surface

of the CNT/GFRP composite that reveals the dispersed CNTs in the matrix-rich region between the glass fibers.

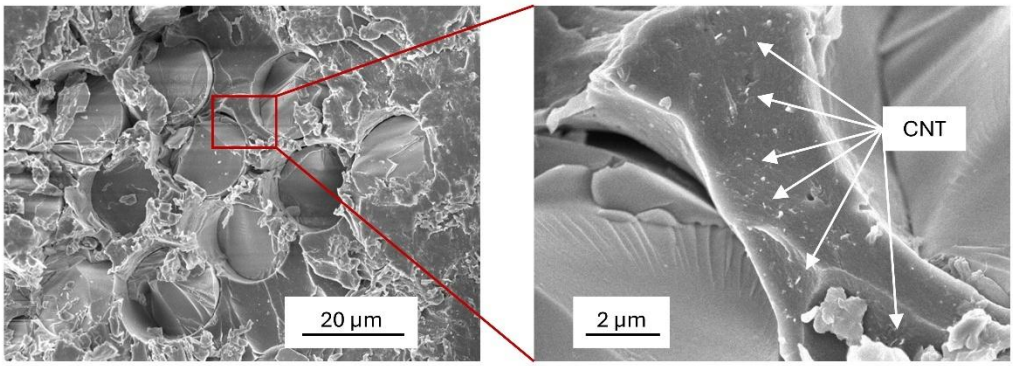

Figure 6.4. FESEM images showing dispersed CNTs in the matrix.

6.2.8 Multiscale Finite Element Modeling

To investigate the microstructural origin of the nonmonotonic piezoresistive behavior in CNT/GFRP composites, a multiscale finite element model was established to simulate and analyze the strain distribution of GFRP composite with different fiber orientations under tensile load, as well as the associated CNT movement and morphological changes in the CNT network during deformation (Grabowski et al., 2017). Figure 6.5 illustrates the schematic of the multiscale FE model for computation of piezoresistive behavior of CNT/GFRP composites with different fiber orientations. The multiscale model consists of two physical scales, namely meso- and micro-scales. The mesoscale model describes the geometries of yarn and matrix in the composites and provides mechanical and electrical responses corresponding to the experimental results. The microscale models are RVEs of yarn and matrix with CNT network, of which its morphological changes in response to the elemental strain states obtained from the mesoscale model are used to extract the elemental resistivity-strain relationship

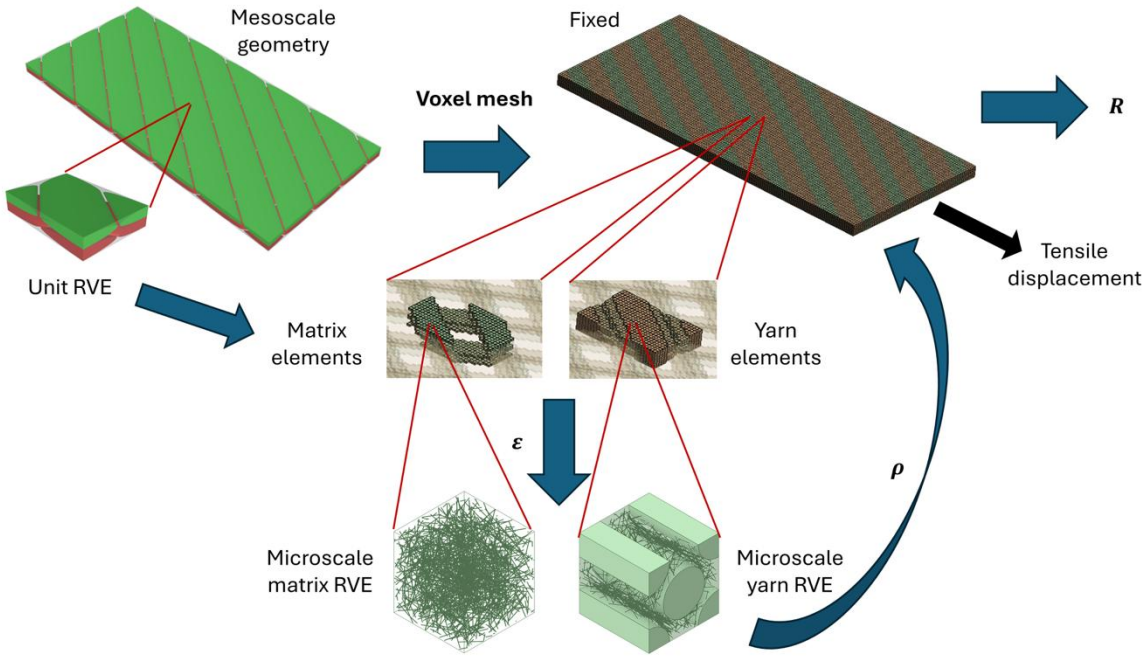

Figure 6.5. Schematic of multiscale FE model for computation of piezoresistive behavior of CNT/GFRP composites with different fiber orientations.

6.2.8.1 Mechanical Part of Mesoscale Model

The properties of FRP composite structures are dependent on the material composition and geometry of the microstructure (H. Li et al., 2024; López-Santos et al., 2024). The geometries of matrix and yarn were obtained by the microstructure analysis described in Chapter 6.2.5-6.2.6 and displayed in Table 6.1. The shape of the yarn was approximated as an ellipse. The gap between yarns (w_{gap}) was taken as 10 μm. The contact between the yarn and the matrix was assumed to be bonded. As such, 3D mesoscale geometric models of glass fiber reinforced composites of different fiber orientations were constructed using TexGen and shown in Figure 6.6 (Brown & Long, 2020). The dimensions of the FE models depended on the fiber orientations. To incorporate periodic boundary conditions (PBCs) of single layer RVE, the size of a unit RVE in longitudinal direction, i.e. y-axis, (l_y) is calculated by

$$l_y = s_{yarn} / \sin\theta \tag{6.2}$$

where $s_{yarn} = w_{yarn} + w_{gap}$ is the yarn spacing and θ is the angle between 90° (y-axis) and the fiber orientation. The size of a unit RVE in transverse direction, i.e. x-axis, (l_x) is calculated by

$$l_x = s_{yarn} / \cos\theta \tag{6.3}$$

A 3D mesoscale geometric model consisted of 8 unit RVEs longitudinally and 4 unit RVEs transversely. Voxel meshes were generated with element sizes of 0.2 mm for in-plane directions (x-y plane) and 0.1 mm for out-of-plane direction (z-axis), respectively. FE simulations were conducted using Ansys software. The element type is SOLID185. The model was loaded in the y direction by fixing the bottom end and applying axial displacement field to the top end. The displacement value was increased linearly from 0 to 3.0% longitudinal tensile strain in a quasi-static manner.

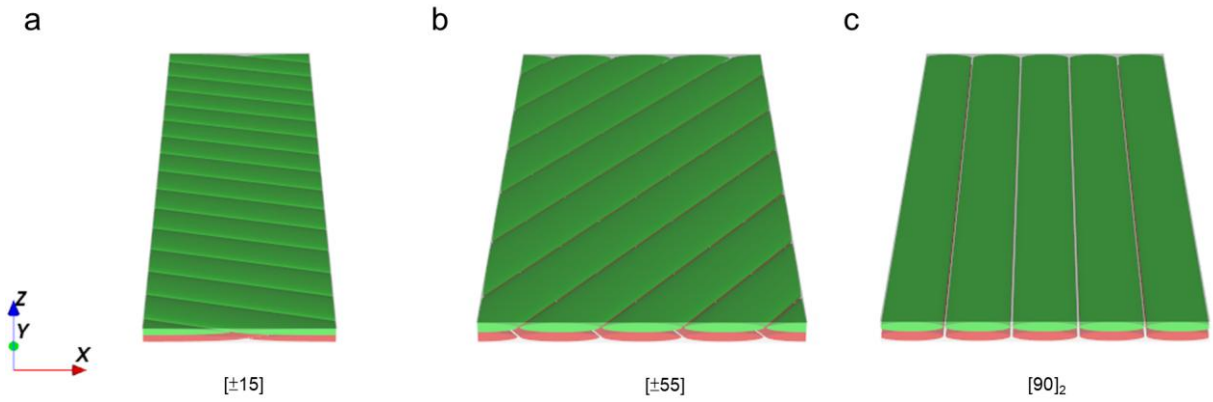

Figure 6.6. 3D mesoscale geometric model of GFRP composites with fiber orientations of a) ±15°, b) ±55°, and c) 90°.

The orthotropic material parameters of yarn, which was modeled as unidirectional GFRP, were assessed by conducting a homogenization using the Material Designer micromechanics plugin in Ansys. A unit RVE of unidirectional FRP with fibers in diamond arrangement was constructed. The orthotropic material parameters of yarn were numerically calculated using the fiber specifications listed in Table 6.1 and the material parameters of the glass fiber and epoxy

matrix listed in Table 6.2. The parameters for epoxy were obtained from electromechanical tensile tests and used for the matrix in the mesoscale model as well. Table 6.3 lists the homogenized material parameters of yarn.

Table 6.2. Material parameters of glass fiber and epoxy matrix.

Material	Young's modulus [GPa]	Poisson's ratio
Epoxy resin	3	0.45
Glass fiber	73	0.22

Table 6.3. Material parameters including Young's modulus (E_{ij}), Poisson's ratio (ν_{ij}), and shear modulus (G_{ij}) of yarn where subscripts 1, 2, and 3 denote longitudinal, transverse, and out-of-plane normal directions, respectively.

Material	E_{11} [GPa]	E_{22} [GPa]	E_{33} [GPa]	ν_{12}	ν_{23}	ν_{13}	G_{12} [GPa]	G_{23} [GPa]	G_{13} [GPa]
Yarn	27.530	6.117	6.117	0.365	0.733	0.365	2.048	2.696	2.048

To incorporate the effects of damage initiation and evolution on the strain response of GFRP composites under uniaxial tensile load, progressive damage analysis (PDA) was performed. The Hashin failure criteria were introduced to determine damage initiation (Hakim et al., 2024; H. Li et al., 2024). The Hashin failure criteria are formulated to consider four damage mechanisms in fiber-reinforced composite materials based on the material strength, which are fiber tension (F_t^f), fiber compression (F_c^f), matrix tension (F_t^m), and matrix compression (F_c^m). The criteria are defined as follows:

For fiber tension where $\sigma_{11} > 0$,

$$F_t^f = \left(\frac{\sigma_{11}}{X_T}\right)^2 + \frac{{\sigma_{12}}^2 + {\sigma_{13}}^2}{{S_{12}}^2} \geq 1 \tag{6.4}$$

For fiber compression where $\sigma_{11} \leq 0$,

$$F_c^f = \left(\frac{\sigma_{11}}{X_C}\right)^2 \geq 1 \tag{6.5}$$

For matrix compression where $\sigma_{22} + \sigma_{33} > 0$,

$$F_t^m = \left(\frac{\sigma_{22} + \sigma_{33}}{Y_T}\right)^2 + \frac{{\sigma_{23}}^2 - \sigma_{22}\sigma_{33}}{{S_{23}}^2} + \frac{{\sigma_{12}}^2 + {\sigma_{13}}^2}{(S_{12})^2} \geq 1 \tag{6.6}$$

For matrix compression where $\sigma_{22} + \sigma_{33} \leq 0$,

$$F_c^m = \frac{1}{Y_C}\left(\left(\frac{Y_C}{2S_{23}}\right)^2 - 1\right)(\sigma_{22} + \sigma_{33}) + \left(\frac{\sigma_{22} + \sigma_{33}}{2S_{23}}\right)^2 + \frac{{\sigma_{23}}^2 - \sigma_{22}\sigma_{33}}{{S_{23}}^2} + \frac{{\sigma_{12}}^2 + {\sigma_{13}}^2}{(S_{12})^2} \geq 1 \tag{6.7}$$

where σ_{ij} are stress tensor components, X_T and X_C are longitudinal tensile and compressive strengths, Y_T and Y_C are transverse tensile and compressive strengths, S_{12} and S_{13} are corresponding in-plane shear strengths, S_{23} is out-of-plane shear strength, respectively. The strength parameters for unidirectional GFRP provided in the material database of Ansys are adopted and listed in Table 6.4.

Table 6.4. Strength parameters of yarn for PDA.

Material	X_T [MPa]	X_C [MPa]	Y_T [MPa]	Y_C [MPa]	S_{12} [MPa]	S_{23} [MPa]	S_{13} [MPa]
Yarn	780	480	31	100	60	35	60

A damage evolution law that controls the stiffness reduction of the yarn after damage initiation is employed for each damage mode. Damage property degradation method was selected in this study (Ferreira et al., 2019; J. Zhang & Zhang, 2015). The material stiffness reduction was based on the damage coefficients that vary from 0 to 1, where 0 corresponds to

no reduction and 1 to complete loss of stiffness in damaged mode. The damage coefficients values of the yarn for fiber tension (d_t^f), fiber compression (d_c^f), matrix tension (d_t^m), and matrix compression (d_c^m) are presented in Table 6.5. Note that these values are set to achieve converged solutions and optimal agreement to experimental evidence. The values of d_t^m and d_c^m are adjusted to 0.85 for models of 0° and ±15°.

Table 6.5. Damage property degradation parameters of yarn for PDA.

Material	d_t^f	d_c^f	d_t^m	d_c^m
Yarn	0.3	0.3	0.3	0.3

The matrix was modeled as a 3D isotropic material in the mesoscale model with parameters listed in Table 6.2. To simulate the nonlinear plastic behavior of the resin, multilinear isotropic hardening was used to describe the development of plastic strain. Beyond the yield strength σ_Y, plastic strain ε_{pl} develops and modulus gradually reduces according to the experimentally obtained stress-strain relationships of the epoxy resin. The ε_{pl}-σ values for the multilinear isotropic hardening properties of the matrix are listed in Table 6.6. The yield strength σ_Y was obtained from electromechanical tensile tests. Once ε_{pl} is larger 0.025, the material becomes perfectly plastic.

Table 6.6. Plastic constants of matrix.

Material	Epoxy resin
Plastic strain ε_{pl}	Stress σ [MPa]
0	40 (σ_Y)
0.005	46

0.01	48
0.015	50
0.02	51.5
0.025	52

6.2.8.2 Mechanical Part of Microscale Model

Determination of resistivity change vs strain relationship of the material was carried out through simulating the changes in CNT network in CNT/epoxy (matrix) and CNT/epoxy/glass fiber (yarn) RVEs in response to deformation. For yarn RVE, the geometric model that was built for homogenization was used, with dispersed CNTs randomly added (Figure 6.7a). Matrix RVE was of the same size but without glass fiber (Figure 6.7c). The volumetric content of CNTs was 1.0 vol.%, which forms percolating CNT network. Periodic boundary conditions were applied to both RVEs.

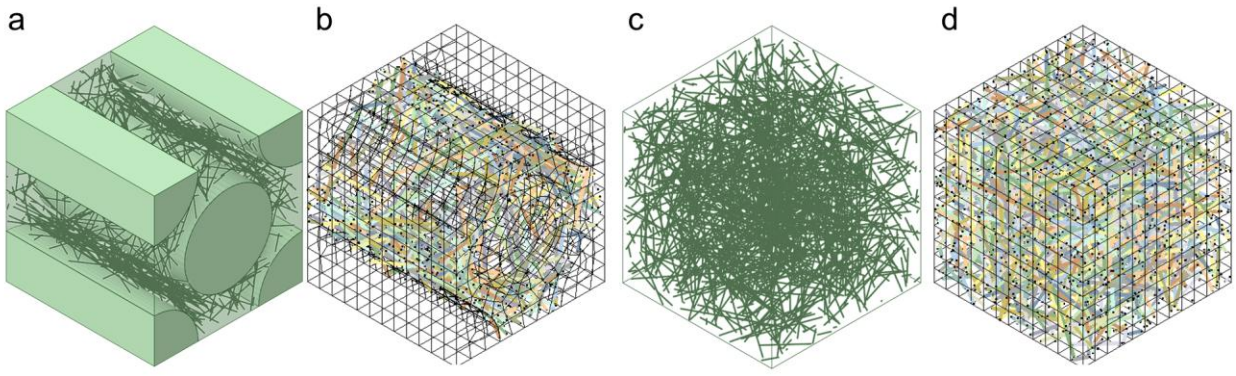

Figure 6.7. Geometries and meshes of a,b) yarn and c,d) matrix RVEs.

The material parameters of the glass fiber and epoxy matrix are listed in Table 6.2. CNTs were modeled as equivalent beam elements with material properties listed in Table 6.7

(Grabowski et al., 2017). To mechanically embed CNTs to the matrix, constraints are imposed on CNT nodes such that the degrees of freedom are coupled with the corresponding degrees of freedom of matrix nodes, as determined by the isoparametric positions of the CNT and matrix elements.

Table 6.7. Material parameters of CNT.

Material	Young's modulus [GPa]	Poisson's ratio
CNT	690	0.16

The strain from the mesoscale model was applied to the microscale yarn and matrix RVEs. A self-consistent clustering approach was employed to improve computational efficiency and maintain the accuracy in transferring the elemental strains of the mesoscale model to microscale RVEs (C. Liu et al., 2025; Z. Liu et al., 2016). By employing the k-means clustering algorithm, voxel elements exhibiting similar strain responses were grouped into one cluster. The clustering was applied to yarn and matrix separately. The number of clusters was adjusted to 10 for both yarn and matrix based on convergence. Displacement field boundary conditions were derived using the cluster centers of elemental strain tensor components output from the mesoscale model using

$$u_i = \varepsilon_{ij} x_i \tag{6.8}$$

where u_i is the normal displacement component, ε_{ij} is the strain tensor component, x_i is the normal position component of vertex, with Einstein summation implied. The displacement field was computed for the eight corners of the RVEs and mapped to the surface nodes using adaptive Kriging technique. To simulate the piezoresistive behavior, the configurations of the CNT networks are output for calculation of electrical resistance using an equivalent resistor network model, as described in Chapter 6.2.8.3.

6.2.8.3 Electrical Part of Microscale Model

The methodology employed here follows that described in Chapter 4.2.8, with the following modifications:

The elemental resistivity-strain relationships were obtained by calculating the electrical resistance of the CNT network in the microscale matrix and yarn RVEs at each strain step using an equivalent resistor network method (N. Hu, Karube, et al., 2008; Jin et al., 2018; C. Li & Chou, 2008). The CNT network was transformed into an equivalent resistor circuit with each CNT end as a node in the circuit such that nodal analysis could be applied to calculate the electrical resistance (Figure 6.8). Two transport mechanisms, intrinsic conductance and the tunnelling effect, are considered to contribute to the electrical conduction path of the CNT network. In the intrinsic conductance mechanism, charge transport along each CNT is described by a series of resistors connecting neighboring nodes with resistance R_{ij}, given by

$$R_{ij} = \frac{4l_{ij}}{\sigma_{\text{cnt}}\pi D^2} \tag{6.9}$$

where l_{ij} is the length of a CNT segment between nodes i and j, σ_{cnt} is the intrinsic conductivity of CNT, D is the CNT diameter. For the tunnelling mechanism, when the distance between two CNTs is smaller than the tunnelling cutoff distance d_{cutoff}, additional nodes are inserted to the CNT pair. The charge transport between the CNT pair R_{tunnel} is described by a resistor connecting the newly added tunneling node pair with separation d_{tunnel}. The transmission probability T_{prob} was estimated by solving the Schrödinger equation with a rectangular potential barrier as follows

$$T_{\text{prob}} = \begin{cases} \exp\left(-\frac{d_{vdW}}{d_{char}}\right), & 0 \le d_{tunnel} \le D + d_{vdW} \\ \exp\left(-\frac{d_{tunnel}-D}{d_{char}}\right), & D + d_{vdW} < d_{tunnel} \le D + d_{cutoff} \end{cases} \tag{6.10}$$

where a soft-core model is applied to handle penetrating CNTs (Bao et al., 2011; N. Hu, Karube,

et al., 2008). Material parameters of CNT used for the microscale resistor network model are listed in Table 6.8.

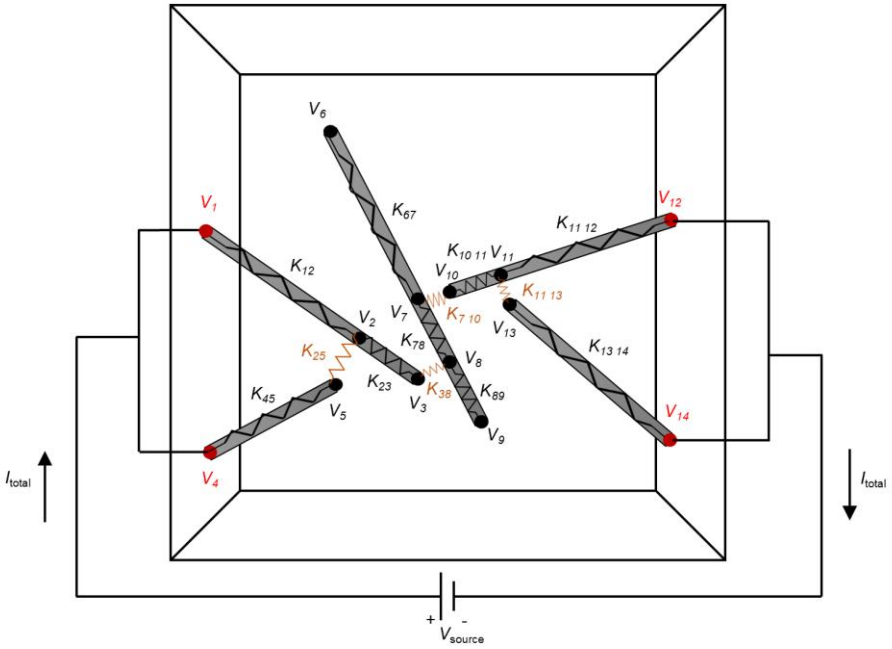

Figure 6.8. Schematic of the microscale equivalent resistor network model.

Table 6.8. Electrical parameters of CNT for microscale resistor network model.

Material	σ_{cnt} [S m^{-1}]	D [nm]	d_{cutoff} [nm]	M	W [eV]
CNT	1×10^4	50	1	400	1.5

The calculation was repeated in the three normal directions to obtain the normal elemental resistivities (ρ_x, ρ_y, and ρ_z).

6.2.8.4 Electrical Part of Mesoscale Model

A mesoscale resistor network model was used to calculate the resistance change-strain relationship of the composite (Ketter, Greb, Bernges, & Zeier, 2025; Lüpke et al., 2017). A

node was defined at each voxel, where a resistor was inserted between each adjacent pair of nodes along the *x*-, *y*-, *z*- directions, resulting in a three-dimensional resistor network. The resistance for each resistor was assigned as the average resistance of the voxel pair based on the directional resistivity-strain relationship of the clusters that the pair of voxels belong to. Boundary conditions were applied to the resistor network, with voxels at the lower face in the longitudinal direction designated as the high-potential boundary and the opposite face as the ground. Using Equation (4.10) to (4.14)

$$R_{\text{equivalent}} = \frac{V_{\text{source}}}{I_{\text{total}}} \quad (4.14),$$

the total resistance of the voxel network at each strain step, that is the composite, was computed. This approach allows for an effective estimation of the overall resistance change-strain relationship of the composite under tensile deformation.

6.3 Results and Discussion

6.3.1 Effect of Fiber Orientation on Piezoresistive Behaviors of CNT/GFRP Composites

To further investigate the influence of fiber orientation, laminate samples with fiber orientations of ±15°, ±55°, and 90° were chosen as the representative configurations for the three types of the fiber orientation dependent piezoresistive behavior observed in Figure 5.10, i.e. monotonic ($[\pm15]_2$), nonmonotonic with relatively low γ_c ($[\pm55]_2$), and nonmonotonic with relatively high γ_c ($[90]_4$). To elucidate the mechanism of the fiber orientation-dependent piezoresistive behavior of CNT/GFRP composites, laminate models with fiber orientations of ±15°, ±55°, and ±90° were constructed and simulated for their electromechanical responses. The resistance change-strain relationships of the laminate models are presented in Figure 6.9.

From the results, it can be seen that there are two types of piezoresistive behavior, i.e. monotonic (Figure 6.9a,c) and nonmonotonic (Figure 6.9b), which qualitatively reproduce the fiber orientation dependent piezoresistive behavior experimentally observed. Composite models containing fibers oriented nearly perpendicular (e.g., [±15]) or parallel to the tensile direction (e.g., $[90]_2$) demonstrate a monotonic increase in resistance as strain increases. Models with fibers oriented around 45° to the tensile direction (e.g., [±55]) exhibit a nonmonotonic resistance change-strain response. The similarity of the fiber orientation dependent piezoresistive behaviors observed in simulations and experiments, despite being qualitative due to the simplifications made in the multiscale FE and CNT network models, indicates that the mechanistic origin of the nonmonotonic piezoresistive behavior can be understood by analyzing the simulations. Future studies may focus on refining the model to achieve a quantitative alignment with experimental data.

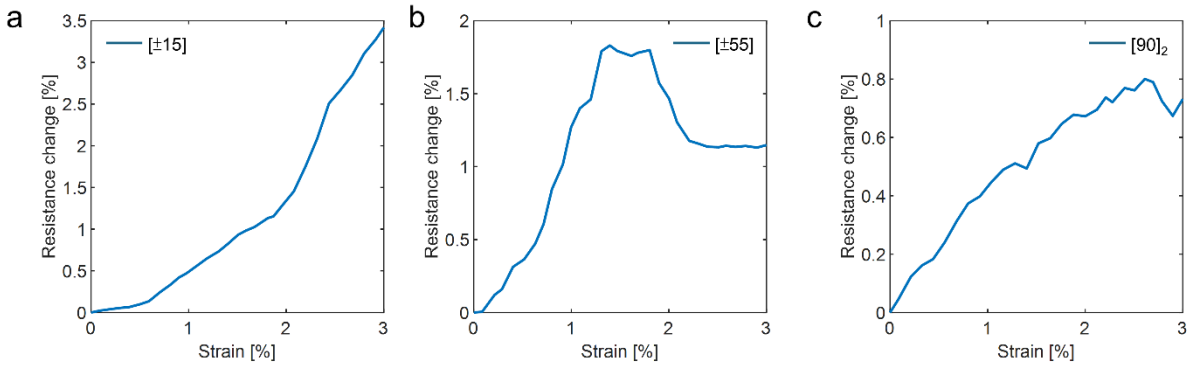

Figure 6.9. Numerical resistance change-strain relationships of a) [±15], b) [±55], c) $[90]_2$ CNT/GFRP composite laminate models.

6.3.2 Effect of Fiber Orientation on Tensile Behaviors of CNT/GFRP Laminates

The fiber orientation in FRP composites exerts a significant influence on the mechanical properties of the composite material due to its impact on load distribution and deformation mechanisms (Bakir & Hashem, 2013; Biswas, Deo, Patnaik, & Satapathy, 2011; Gonabadi et al., 2022; Iquilio et al., 2024; Singh & Shrivastava, 2023; H. W. Wang et al., 2014). The strain data obtained from the DIC measurements, specifically through the use of a virtual extensometer, elucidates the influence of fiber orientation on the tensile stress-strain response and Poisson's effect of the laminate samples in Figure 6.10. FEA results reproduce the influence of fiber orientation on the tensile stress-strain response and Poisson's effect of the laminate samples in Figure 6.11. For fibers oriented perpendicular to the loading direction (e.g., ±15°), the stress-strain curve tends to exhibit a nonlinear and ductile behavior (Figure 6.10a and Figure 6.11a), characterized by relatively low stiffness, yield strain, tensile strength and transverse compression (Figure 6.10d and Figure 6.11d). As the fiber orientation approaches off axis (e.g., ±55°), the stress-strain response becomes increasingly nonlinear and ductile (Figure 6.10b and Figure 6.11b), demonstrating higher stiffness, yield strain, tensile strength and remarkably high transverse compression (Figure 6.10e and Figure 6.11e). When fibers are aligned closer to the loading direction (e.g., 90°), the stress-strain curve manifests more brittle behavior with the highest stiffness, tensile strength (Figure 6.10c and Figure 6.11c) and intermediate transverse compression (Figure 6.10f and Figure 6.11f). The fiber orientation significantly influences the stress-strain curve and Poisson's effect by affecting the load distribution and deformation mechanisms within the laminate structure, as illustrated by the DIC and FEA results (Gonabadi et al., 2022; Iquilio et al., 2024).

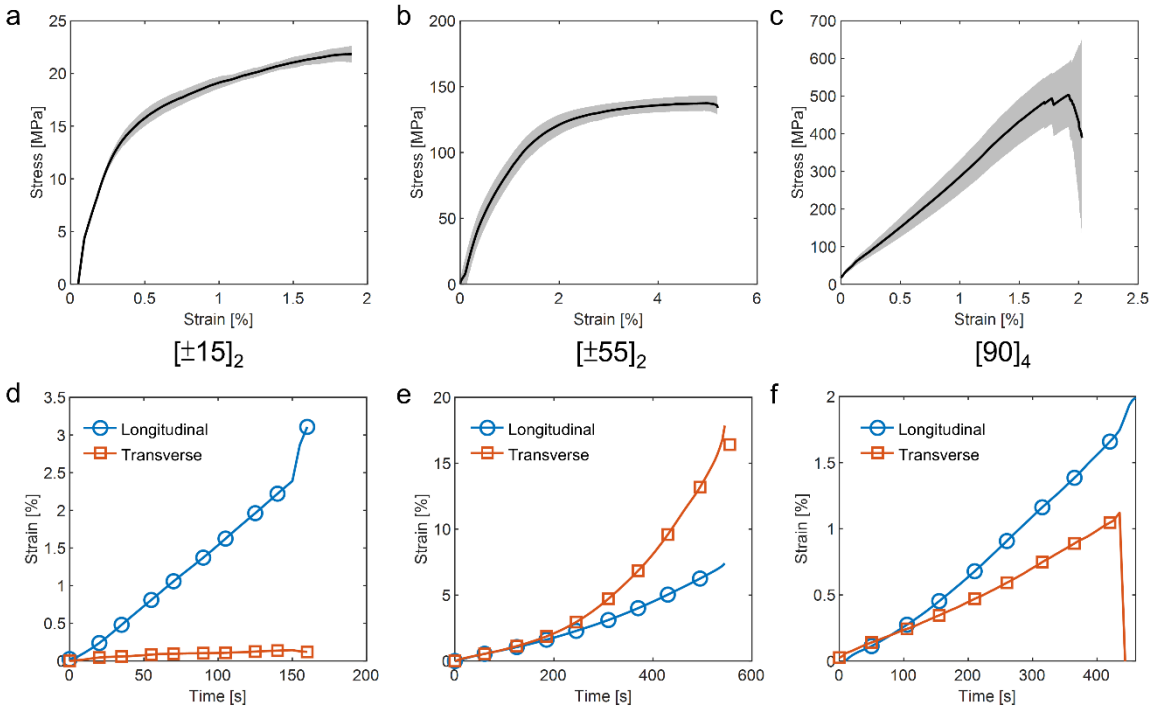

Figure 6.10. a-c) Stress-strain relationships and d-f) comparisons of representative longitudinal and transverse strains of a,d) $[\pm 15]_2$, b,e) $[\pm 55]_2$, and c,f) $[90]_4$ CNT/GFRP composite laminate samples that were cured at room temperature (for stress-strain relationships, three specimens were tested, and the mean±SD response is plotted).

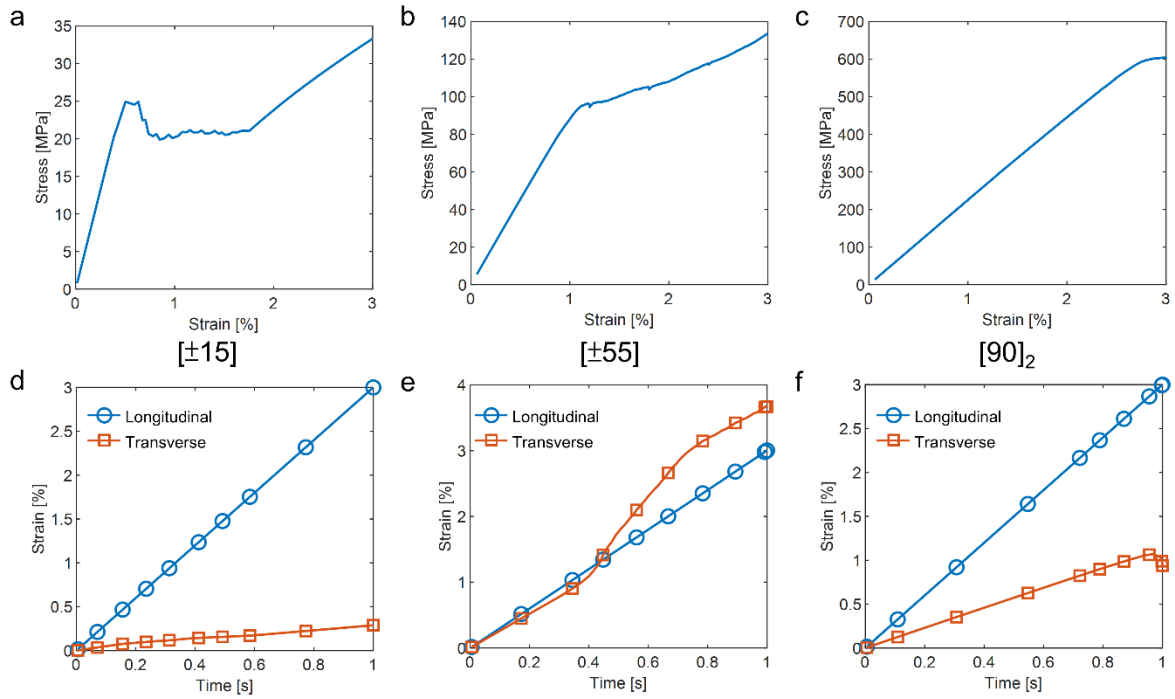

Figure 6.11. a-c) Stress-strain relationships and d-f) comparisons of representative longitudinal and transverse strains of a,d) [±15], b,e) [±55], and c,f) $[90]_2$ CNT/GFRP composite models.

The strain fields measured through DIC techniques reveal varying degrees of heterogeneity dependent on fiber orientation in Figure 6.12. Qualitatively similar strain maps were obtained from FEA and displayed in Figure 6.13. Localized regions of high strain levels can be observed in these strain maps, suggesting that the GFRP laminates exhibit inherent mechanical heterogeneity attributable to their heterogeneous microstructure (Godara & Raabe, 2007; Gonabadi et al., 2022). These localized strains are likely a result of the matrix's localized plastic deformation and micro-damage, such as debonding or micro-cracking. The constraining effect of the surrounding fibers induces additional strain in the matrix, as demonstrated by the localized strains observed in the strain maps. For fiber orientations perpendicular to the loading direction, the ε_{xx} distribution centers around 0% (Figure 6.12a), which is expected from the low transverse compression (Figure 6.10d). However, significant heterogeneity is observed in

the ε_{yy} strain map with high strain bands aligned along the fiber orientation (15°) (Figure 6.12d and Figure 6.13d). This means the strain distribution is dominated by localized longitudinal tension, supported by the same heterogeneous pattern in the ε_{eq} strain maps (Figure 6.12g and Figure 6.13g). As the fiber orientation deviates from the loading axis, more complex and non-uniform strain distributions are observed. Off-axis fiber orientations produce distinct strain patterns due to the interplay between fiber and matrix deformation mechanisms. These orientations can lead to localized strain concentrations in both ε_{xx} and ε_{yy} and the resultant ε_{eq}, particularly at fiber-matrix interfaces or resin-rich region (Figure 6.12b,e and Figure 6.13b,e). The heterogeneous strain fields observed in off-axis orientations contribute to the nonlinear stress-strain behavior and high transverse compression (Figure 6.10b,e). For fiber orientations parallel to the loading direction, the strain distribution tends to be more uniform across the specimen (Figure 6.12c,f,i and Figure 6.13c,f).

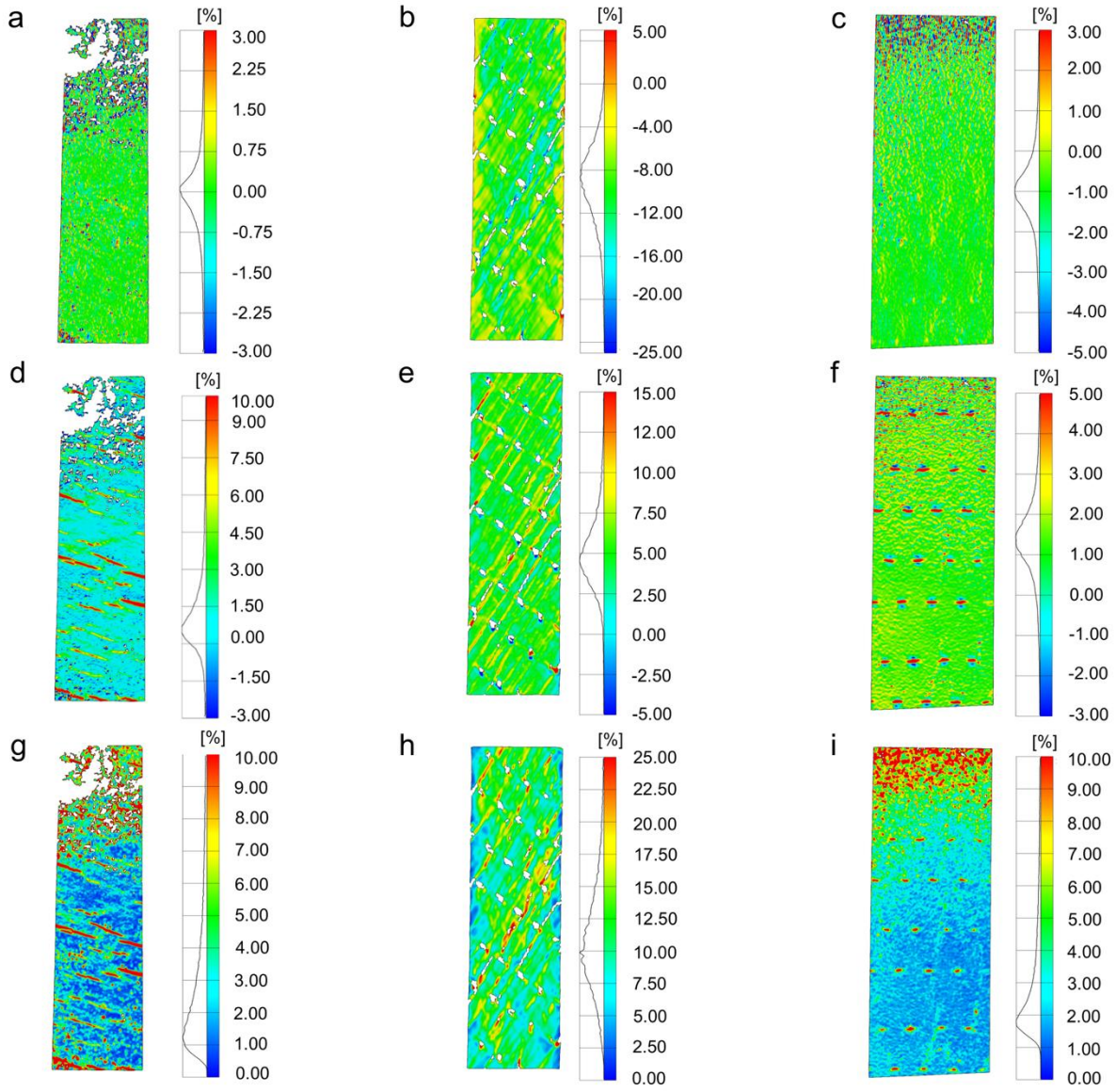

Figure 6.12. DIC strain maps showing heterogeneity distribution in a-c) transverse direction (ε_{xx}), longitudinal direction (ε_{yy}), and equivalent mises (ε_{eq}) for a,d,g) $[\pm15]_2$, b,e,h) $[\pm55]_2$, and c,f,i) $[90]_4$ laminate specimens at tensile strain of 1.5%, 5.4%, and 1.5% respectively.

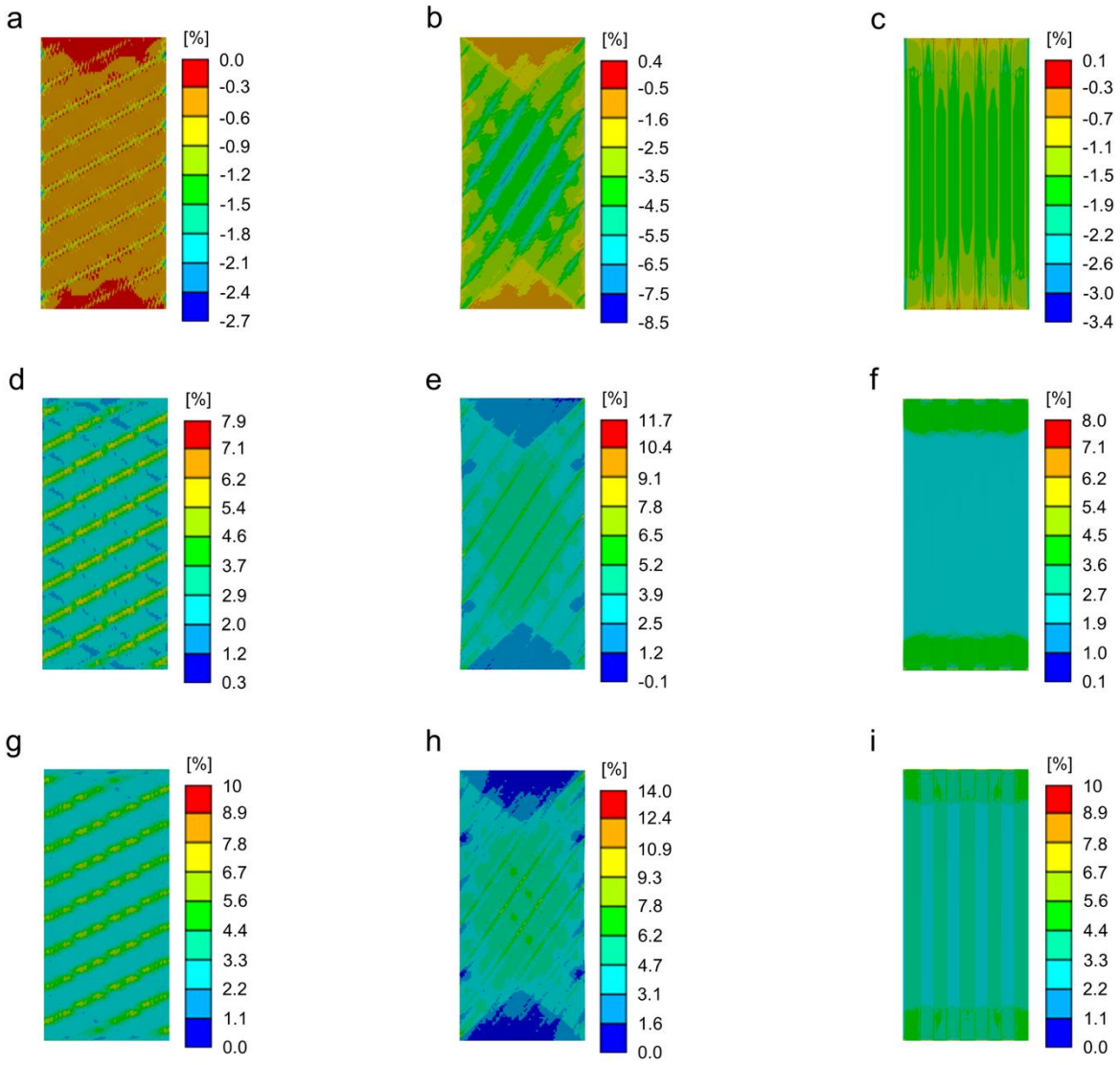

Figure 6.13. FEA strain maps showing heterogeneity distribution in a-c) transverse direction (ε_{xx}), d-f) longitudinal direction (ε_{yy}), and equivalent mises (ε_{eq}) of a,d,g) [±15], b,e,h) [±55], and c,f,i) $[90]_2$ composite models at longitudinal tensile strain of 3.0% respectively.

6.3.3 Analysis of Fiber Orientation Dependent Piezoresistive Behaviors of CNT/GFRP Laminates

The piezoresistive and tensile behaviors of the CNT/GFRP composite laminates and models both exhibit dependence on fiber orientation. This correlation provides valuable

insights into the piezoresistivity and deformation mechanisms of the material as the changes in CNT conducting networks within the composite are influenced by the strain states (H. Zhang et al., 2015). With the reinforcing glass fibers oriented in different directions, the deformation mechanisms are altered, leading to variations in the material's strain distribution and piezoresistive behavior. This warrants further investigation for designing tailored CNT/GFRP composites with optimized piezoresistive performance for specific structural health monitoring applications.

Composites consisting of fibers oriented nearly perpendicular to the tensile direction exhibit monotonic piezoresistive behavior, which is desirable for strain sensing application. This phenomenon is evident in configurations such as $[\pm 15]_2$, where the fibers are primarily aligned transverse to the applied load (Figure 5.10b and Figure 6.9a). When fibers are oriented perpendicular to the loading direction, the stress-strain curve exhibits a nonlinear behavior with low transverse compression (Figure 6.10a,d and Figure 6.11a,d). DIC analysis reveals complex strain field distributions, marked by heterogeneity in the ε_{yy} maps (Figure 6.14c,d), while the ε_{xx} maps remains relatively uniform (Figure 6.14a,b). FEA strain maps show similar patterns (Figure 6.15).

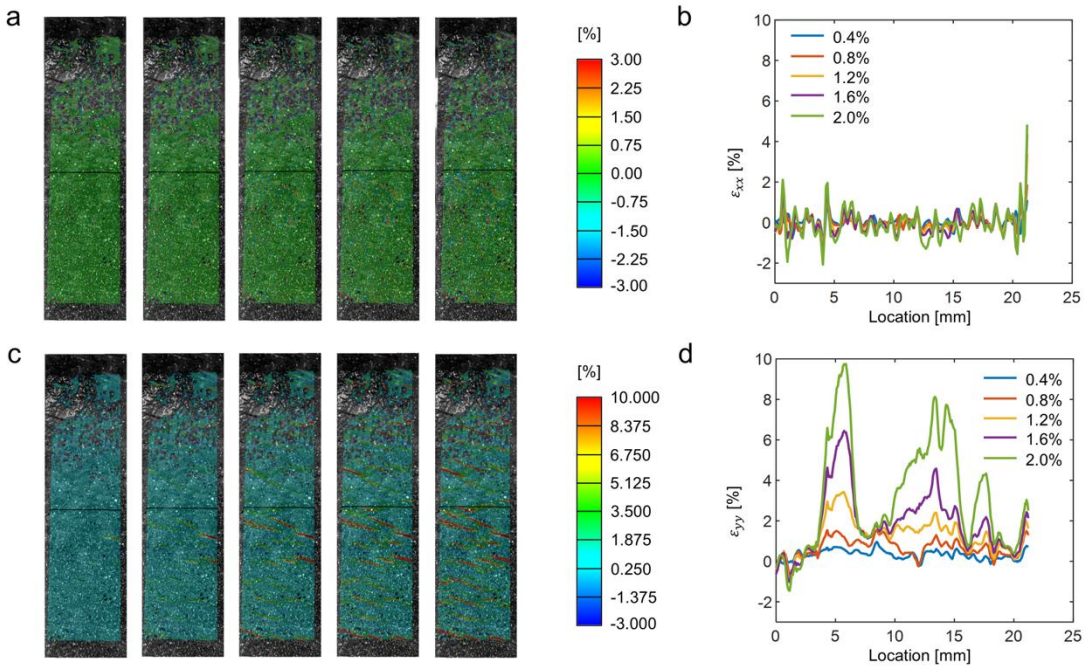

Figure 6.14. Full field a) ε_{xx} and c) ε_{yy} maps of the $[\pm 15]_2$ laminate surface with black lines indicating the section of which b) ε_{xx} and d) ε_{yy} values are displayed.

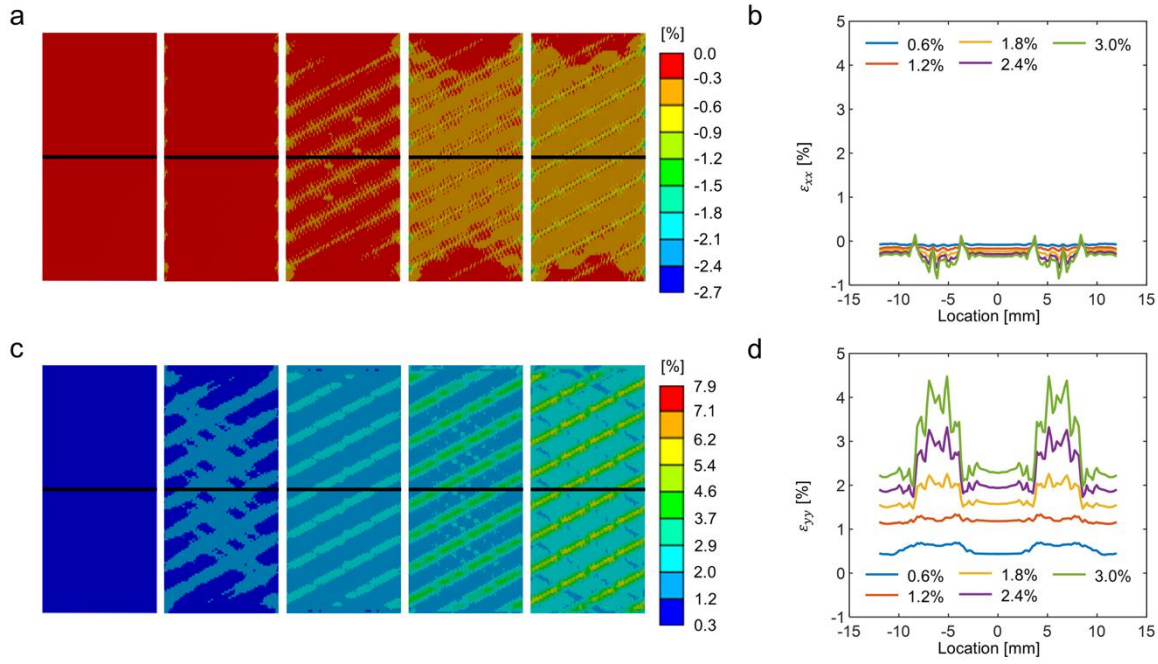

Figure 6.15. a) ε_{xx} and c) ε_{yy} maps of the $[\pm 15]$ composite model *x*-*y* top surface with b) ε_{xx} and d) ε_{yy} values of section line along $y = 0$ indicated by black lines.

The observed monotonic change in electrical resistance can be primarily attributed to the progressive separation of CNTs within the matrix as it undergoes significant tensile deformation. As the matrix and yarn deform, the CNTs are displaced, resulting in an increased separation between CNTs and a corresponding reduction in conductivity. The elemental resistivity changes between 1.2% and 2.4% longitudinal strain are shown in Figure 6.16. Both matrix and yarn elements exhibit monotonic increase in elemental resistivity. The weighted means of tunneling distance of matrix clusters from 0.6% to 3.0% are displayed in Figure 6.17. The resistance increases due to the separation of CNTs that manifest the increasing trend in tunneling distance.

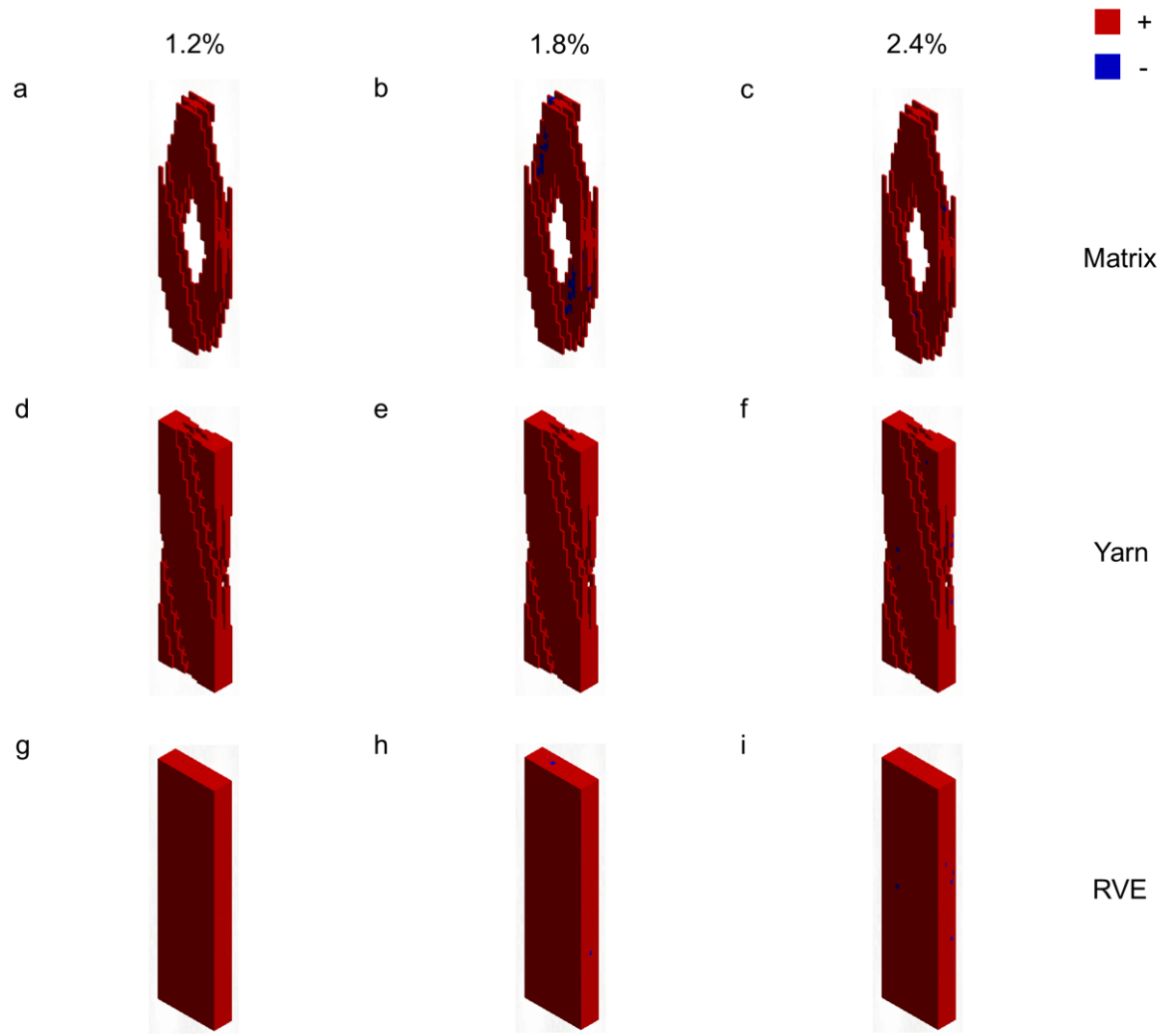

Figure 6.16. Elemental resistivity changes for a-c) matrix elements, d-f) yarn elements, and g-i) unit RVE elements in the [±15] composite model at a,d,g) 1.2%, b,e,h) 1.8%, c-i) 2.4% longitudinal tensile strain.

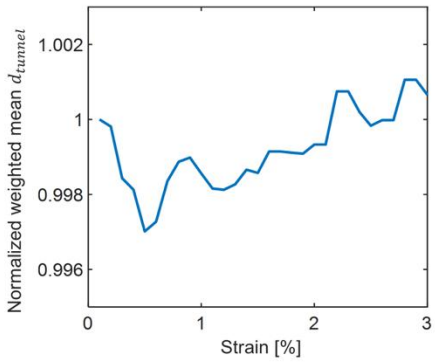

Figure 6.17. Normalized weighted mean of tunneling distance of matrix clusters vs. longitudinal tensile strain in the [±15] composite model.

Laminates with off-axis fibers (e.g., $[\pm 55]_2$) to the tensile direction exhibit distinctive nonmonotonic resistance change-strain responses, characterized by initial increase in resistance followed by decrease after reaching critical strain (Figure 5.10e and Figure 6.9b). The stress-strain response is nonlinear with high transverse compression (Figure 6.10b,e and Figure 6.11b,e). The off-axis fiber alignments allow for greater shear deformation within the matrix, resulting in a more complex load transfer mechanism (Bogusz, 2023; Gonabadi et al., 2022; Iquilio et al., 2024; Liang, Wang, & Gu, 2013). The DIC and FEA strain fields reveal significant heterogeneity in both ε_{xx} and ε_{yy} distributions, indicating complex load transfer and strain localization due to the off-axis fiber alignment (Figure 6.18 and Figure 6.19).

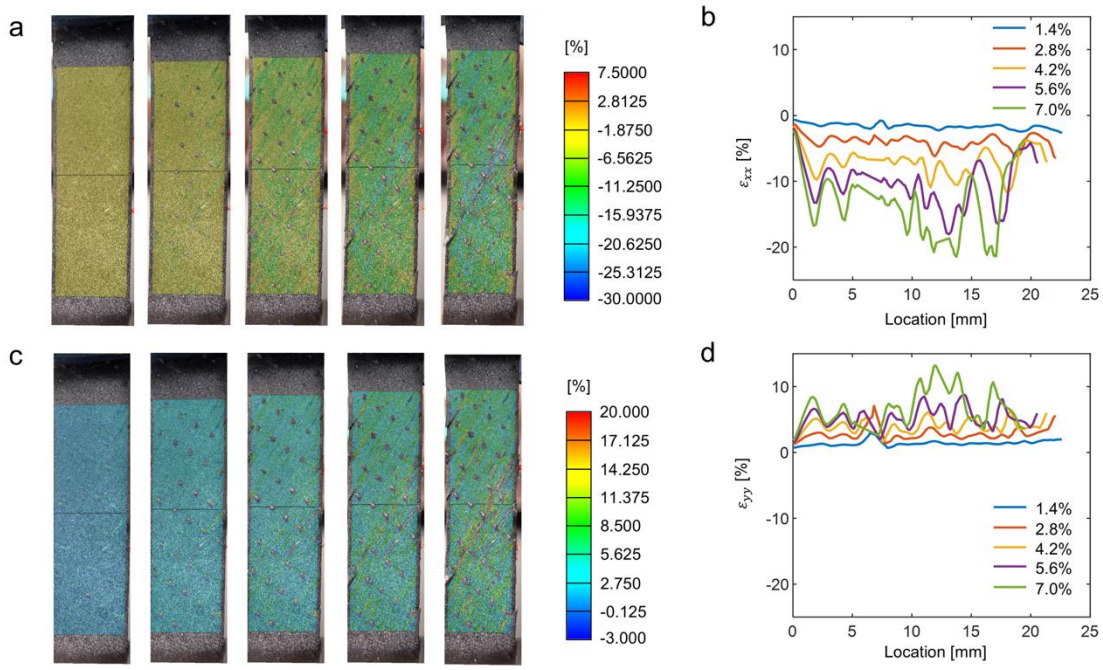

Figure 6.18. Full field a) ε_{xx} and c) ε_{yy} maps of the $[\pm 55]_2$ laminate surface with black lines indicating the section of which b) ε_{xx} and d) ε_{yy} values are displayed.

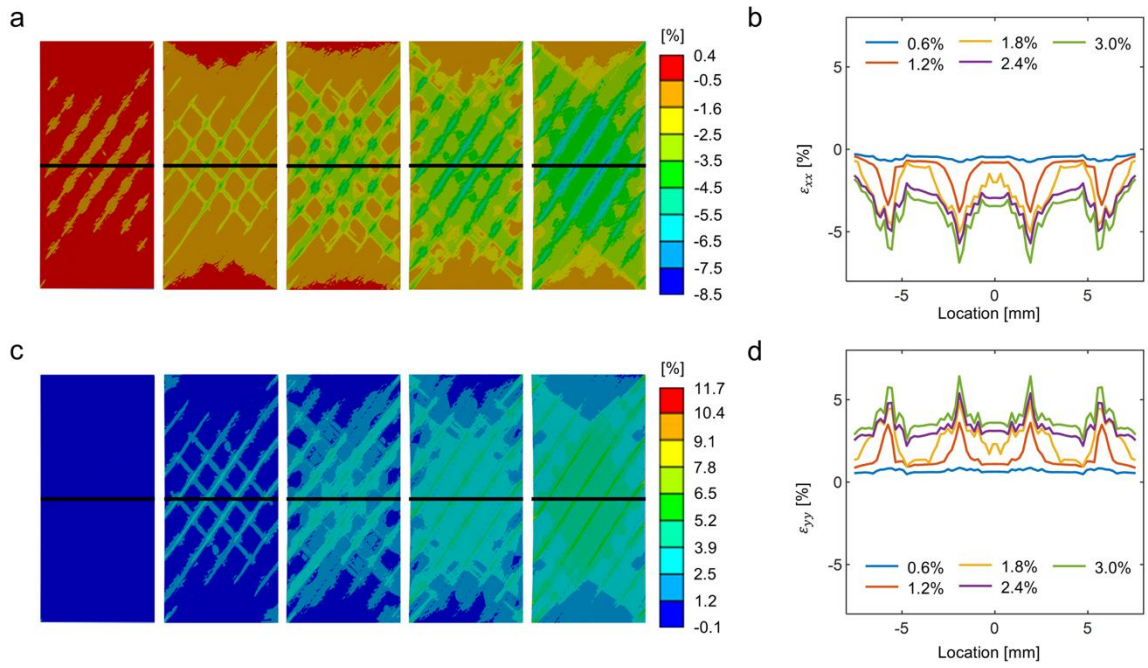

Figure 6.19. a) ε_{xx} and c) ε_{yy} maps of the [±55] composite model *x*-*y* top surface with b) ε_{xx} and d) ε_{yy} values of section line along $y = 0$ indicated by black lines.

The piezoresistive inversion is likely due to the substantial transverse compression under matrix plastic shearing and fiber reorientations by bias tension (Liang et al., 2013; Sen Yang & Chalivendra, 2020), which brings neighboring CNTs closer to each other. The observed nonmonotonic resistance change-strain response in these laminates can be attributed to the fact that the transverse compression outweighs longitudinal tension, despite being under tensile loading (Figure 6.10e and Figure 6.18b,d). The elemental resistivity changes during transition from positive to negative piezoresistivity between 1.2% and 2.4% strain are shown in Figure 6.20. Both matrix and yarn elements exhibit the transition at 1.8%. The weighted means of tunneling distance of matrix clusters against longitudinal tensile strains are displayed in Figure 6.21 and provide microscopic insight into the changes in CNT network. The resistance initially increases due to the separation of CNTs when ε_{xx} and ε_{yy} are still in balance, while the subsequent decrease could be a result of decrease in tunneling distance with transverse compression dominating. The non-monotonic piezoresistive behaviors of laminates with off-axis fibers highlights intricate relationship between fiber orientation, in-plane deformation, and CNT network reconfiguration under tensile loading, warranting further research to optimize the design and performance of such composites.

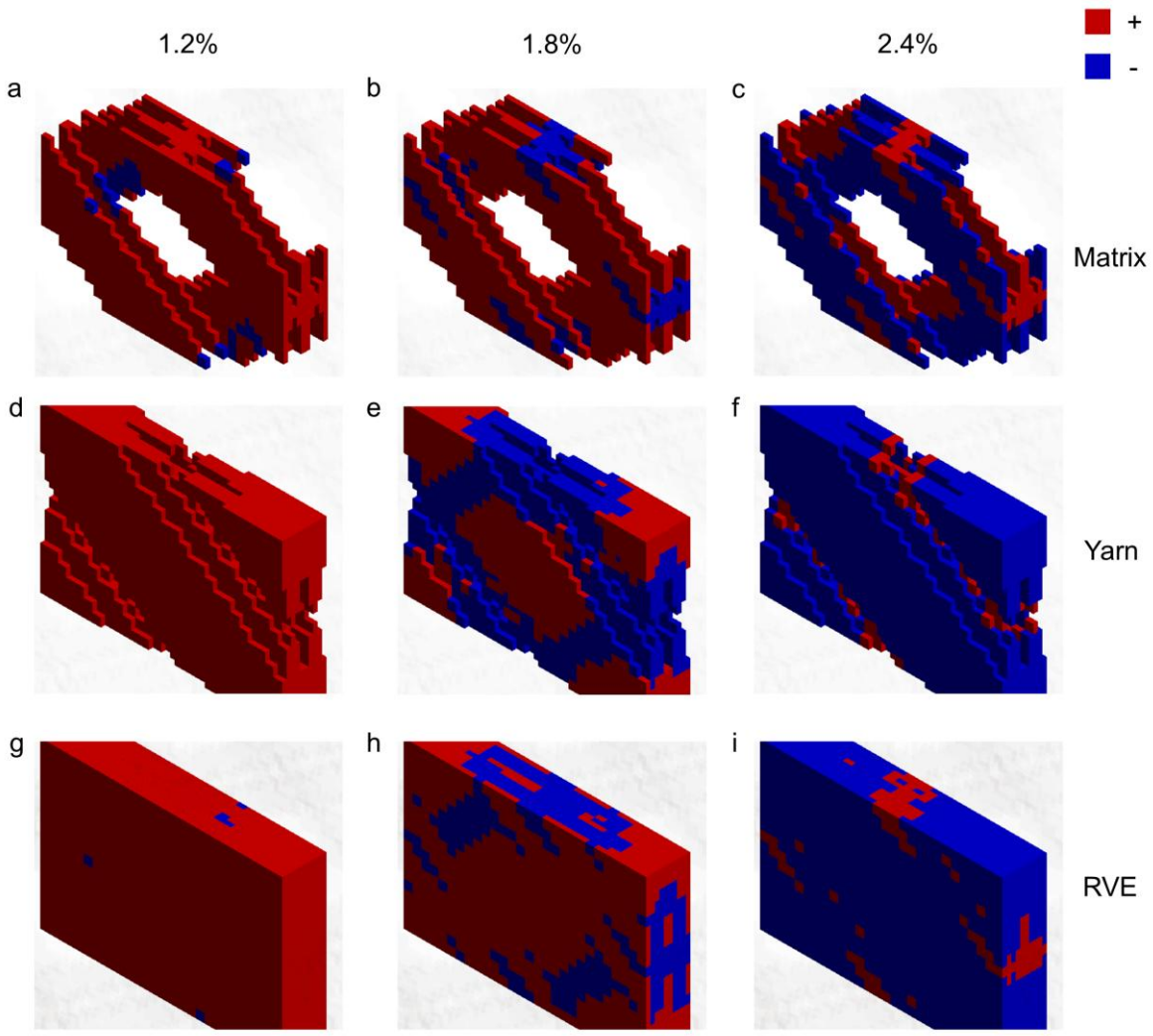

Figure 6.20. Elemental resistivity changes during positive, inverting, negative piezoresistivity for a-c) matrix elements, d-f) yarn elements, and g-i) unit RVE elements in the [±55] composite model at a,d,g) 1.2%, b,e,h) 1.8%, c-i) 2.4% longitudinal tensile strain.

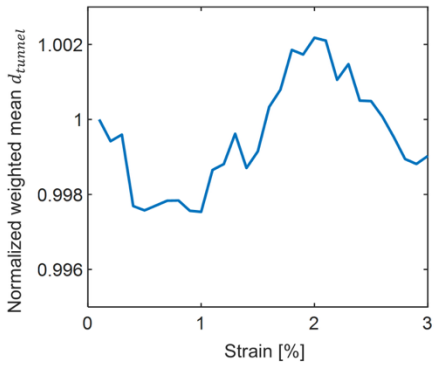

Figure 6.21. Normalized weighted mean of tunneling distance of matrix clusters vs. longitudinal tensile strain in the [±55] composite model.

When fibers are aligned nearly parallel to the tensile axis (e.g., $[90]_4$), the monotony of resistance-strain response improves (Figure 5.10i and Figure 6.9c). When fibers are aligned close to the loading direction, such as at 90°, the stress-strain curve manifests linear behavior with intermediate Poisson's ratio (Figure 6.10c,f and Figure 6.11c,f). In these configurations, the fibers bear a significant portion of the applied load, leading to higher stiffness and strength in the loading direction. However, the limited ability of the fibers to accommodate transverse compression results in intermediate Poisson's effect. The strain fields are comparatively more homogeneous in both ε_{xx} and ε_{yy}, reflecting efficient load transfer along the fiber direction (Figure 6.22 and Figure 6.23). Nevertheless, the sectional values show distinctive strain localizations that grow with applied load (Figure 6.22b,d and Figure 6.23b).

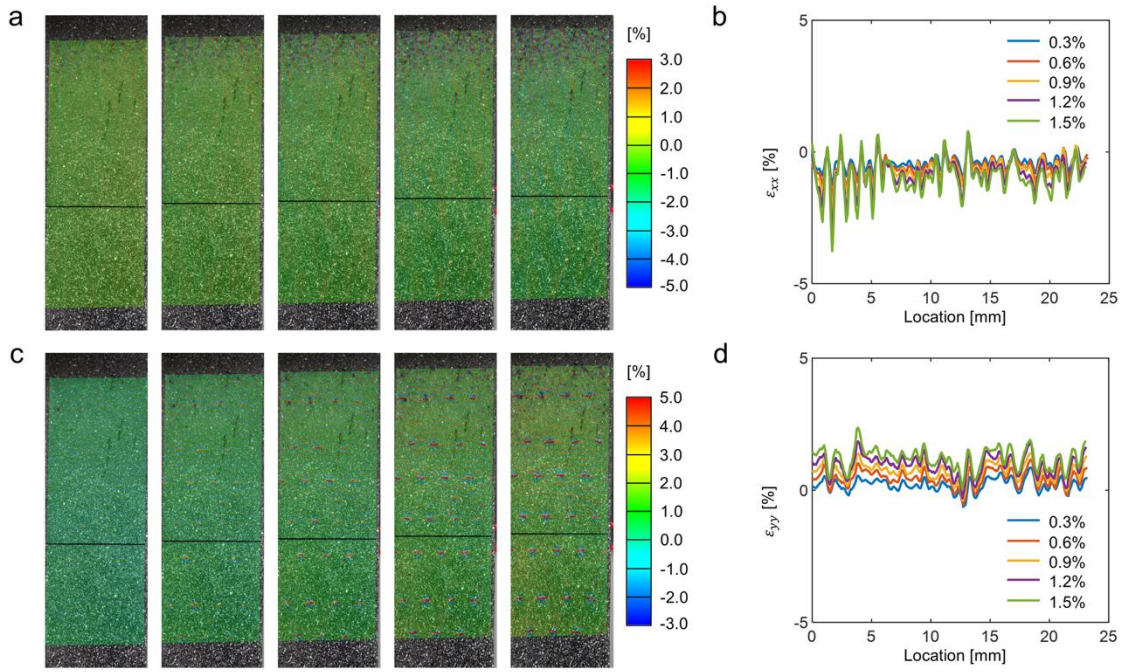

Figure 6.22. Full field a) ε_{xx} and c) ε_{yy} maps of the $[90]_4$ laminate surface with black lines indicating the section of which b) ε_{xx} and d) ε_{yy} values are displayed.

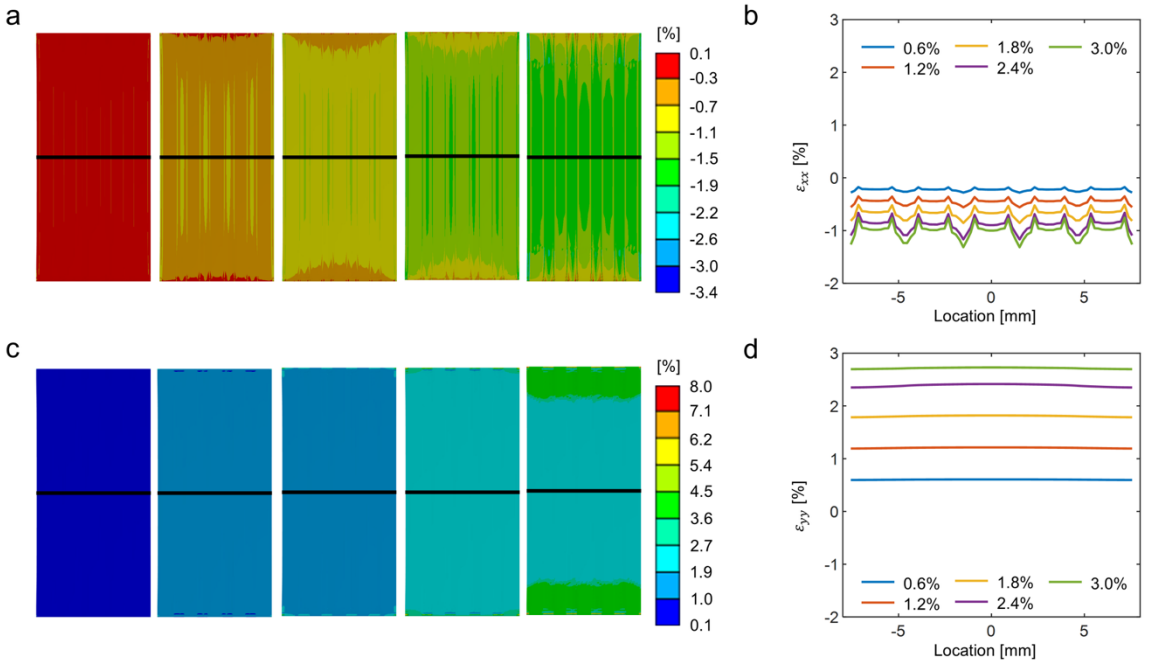

Figure 6.23. a) ε_{xx} and c) ε_{yy} maps of the $[90]_2$ composite model *x*-*y* top surface with b) ε_{xx} and d) ε_{yy} values of section line along $y = 0$ indicated by black lines.

The delayed inversion in resistance near ultimate strain suggests that the separation of CNTs in CNT network remains relatively stable until higher strain levels, after which occurrence of damages induce strain localizations and disrupt the conductive pathways. It can be inferred that heterogenous or localized transverse compression leads to inversion in piezoresistivity as they are observed in tandem in both off-axis and parallel fiber containing samples. Although the simulated resistance change-strain relationship does not display the inversion near ultimate strain observed from experimental results, the elemental resistivity changes reveal some of the yarn elements transition to negative piezoresistivity at 2.4% longitudinal strain (Figure 6.24). The normalized weighted means of tunneling distance of matrix clusters against longitudinal tensile strain are displayed in Figure 6.25. The resistance increases due to the separation of CNTs. However, the tunneling distance levels between 2% and 3% longitudinal strains. This supports that transverse compression in the composite brings CNTs closer, counteracting the separation due to longitudinal tension, and leads to inversion of piezoresistivity.

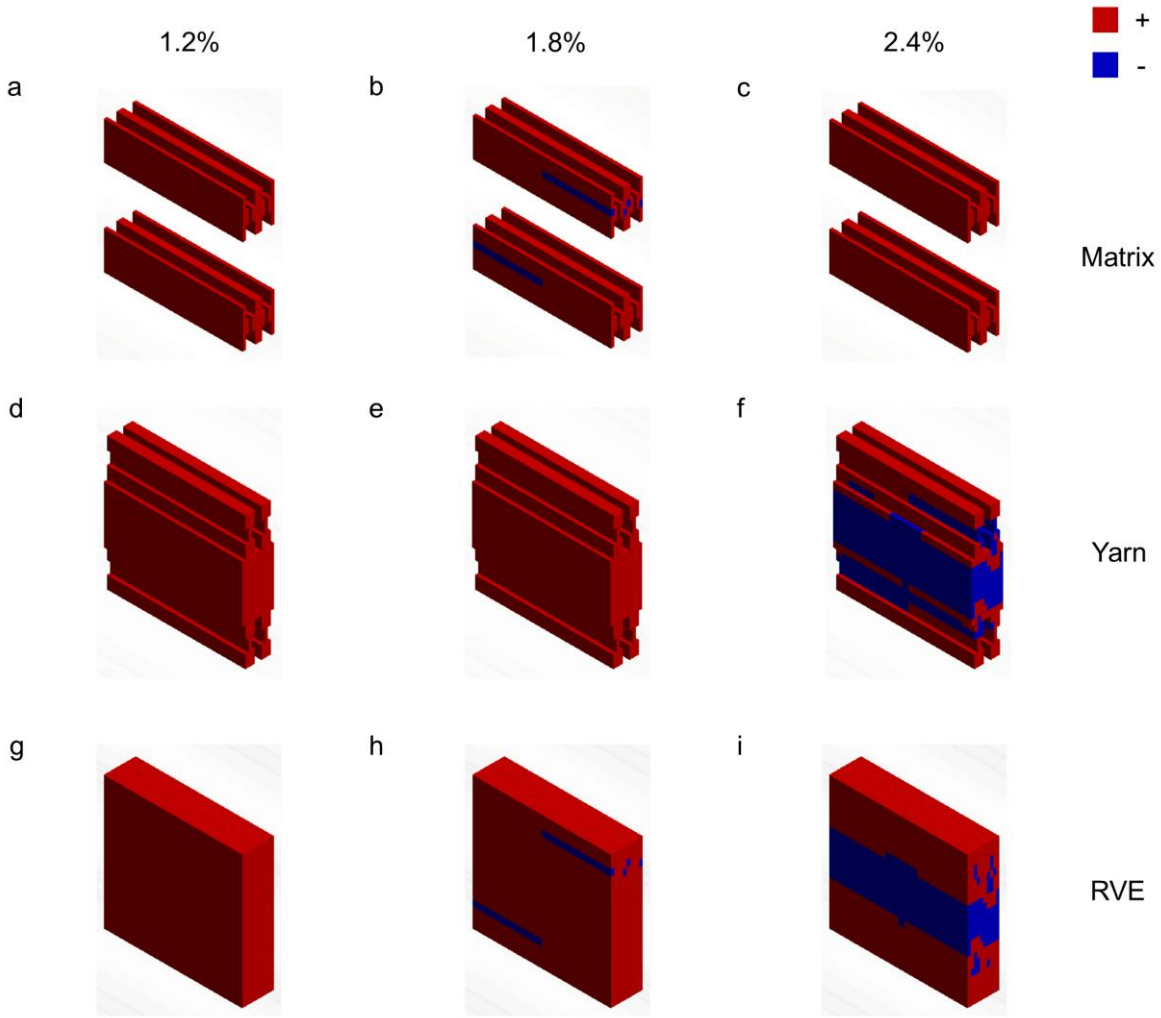

Figure 6.24. Elemental resistivity changes for a-c) matrix elements, d-f) yarn elements, and g-i) unit RVE elements of the $[90]_2$ composite model at a,d,g) 1.2%, b,e,h) 1.8%, c-i) 2.4% longitudinal tensile strain.

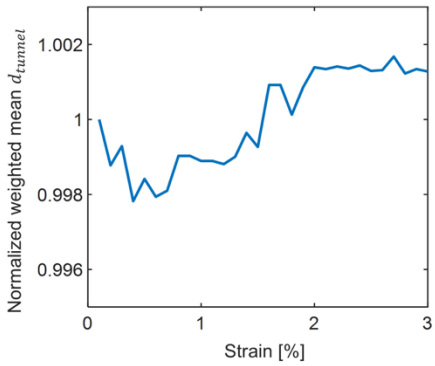

Figure 6.25. Normalized weighted mean of tunneling distance of matrix clusters vs. longitudinal tensile strain in the $[90]_2$ composite model.

6.4 Conclusion

This chapter investigates the microstructural origin of fiber orientation dependent piezoresistive behavior in CNT/GFRP composites using a multiscale FEA-based electromechanical framework. The model consisted of microscale for unit cells of yarn and matrix and mesoscale for geometric pattern of yarn and matrix, involving both mechanical and electrical domains. FEA results successfully reproduced the experimental trends of fiber orientation dependent piezoresistive behavior of CNT/GFRP composites, i.e. monotonic behavior for fibers nearly perpendicular to the tensile direction, nonmonotonic behavior with low critical strain for fibers around ±45°, and nonmonotonic behavior with high critical strain for fibers nearly parallel. DIC and FEA strain maps revealed that the strain distribution heterogeneity varies with fiber orientation, and localized transverse compression may lead to the inversion in piezoresistivity, which was accompanied by increase and then decrease in tunneling distance between CNTs in composites with off-axis fibers. The monotonic or nearly monotonic positive piezoresistive behaviors of composites with parallel or perpendicular fibers were attributed to the increase in tunneling distance under CNT separation. The study provides

mechanistic insights into the intricate relationship between fiber orientation, deformation mechanisms, and CNT network reconfiguration of CNT/GFRP composites under tensile loading.

CHAPTER 7 TAILORING MONOTONIC PIEZORESISTIVE BEHAVIOR IN CARBON NANOTUBE/EPOXY/GLASS FIBER COMPOSITES FOR STRUCTURAL HEALTH MONITORING

7.1 Introduction

Non-monotonic resistance change-strain relation would cause undefined response in strain sensing because there would be two strain levels correspond to one resistance value. However, for [±55] composite that has been widely applied in real-world tube structures due to being known as the optimal angle for balanced axial and hoop strength (Kara et al., 2018; Taşyürek & Tarakçioğlu, 2017; Thomas et al., 2019; Üstün, Eskizeybek, et al., 2016), the piezoresistive behavior is nonmonotonic (Figure 5.10 and Figure 5.11). To achieve self-sensing using CNT/epoxy nanocomposite as matrix in FRP structures, studying the mechanisms that induce the inversion of piezoresistivity (CHAPTER 6) could enable the design of advanced composite materials with desired piezoresistive behavior.

The relationship between fiber orientation, mechanical and piezoresistive properties in GFRP composites is further influenced by factors such as fiber volume fraction (Adekomaya & Adama, 2017) and matrix properties (Kaynak, Erdiller, Parnas, & Senel, 2005). These parameters can modulate the extent to which fiber orientation affects the overall composite behavior.

On the other hand, by strategically aligning fibers in specific orientations or combining multiple orientations in a composite structure, the performance of FRP composite can be optimized for specific applications (Bazli et al. 2019; Y. L. Li et al. 2018; Thirumavalavan and Sarukasan 2022). This customization allows for the development of GFRP components with desired combinations of mechanical and piezoresistive characteristics.

Based on the mechanistic insight gathered from the experimental results and the multiscale simulations, the microstructural origin of fiber orientation dependent piezoresistive behavior in CNT/GFRP composites under tensile loading was stemmed from the intricate relationship between fiber orientation, deformation mechanisms, and CNT network reconfiguration. Here, it is further attempted to design composites with desired piezoresistive behavior, i.e. monotonic one, through stacking sequence, fiber volume fraction, and matrix properties using the multiscale FE model.

7.2 Methods

7.2.1 Materials and Sample Fabrications

The methodology employed here follows that described in Chapter 5.2.1.

CNT/GFRP tubes of [±55] were fabricated via a filament winding process using a X-Winder desktop filament winder.

7.2.2 Electromechanical Tests

The methodology employed here follows that described in Chapter 5.2.2.

7.2.3 Multiscale Finite Element Modeling

To explore the effect of factors related to fiber and matrix properties, simulations were carried out with fiber orientation maintained at ±55° but different width of yarn and matrix Poisson's ratio. The width of yarn (w_{yarn}) was varied from 1.5 to 3 mm to investigate the effect of yarn volume fraction (Figure 7.1). On the other hand, the Poisson's ratio of matrix (v_{matrix})

was tuned from 0.15 to 0.45 to study the effect of matrix property. Other matrix and fiber material parameters remained unchanged. This leaded to different orthotropic material parameters of yarn obtained by the homogenization procedure, which are listed in Table 7.1. The extent of influence of these parameters on the piezoresistive behavior of CNT/GFRP composite can be evaluated.

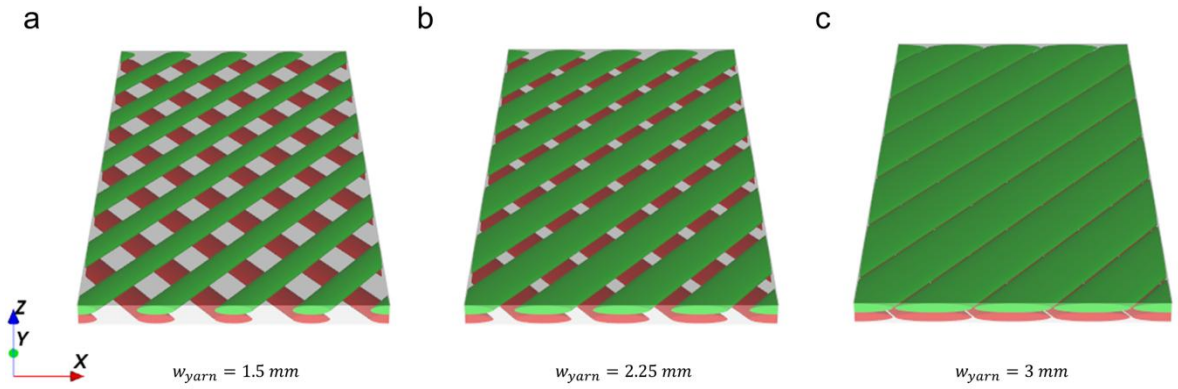

Figure 7.1. 3D mesoscale geometric model of [±55] GFRP composites with w_{yarn} of a) 1.5, b) 2.25, and c) 3 mm.

Table 7.1. Material parameters including Young's modulus (E_{ij}), Poisson's ratio (ν_{ij}), and shear modulus (G_{ij}) of yarn with different v_{matrix}, where subscripts 1, 2, and 3 denote longitudinal, transverse, and out-of-plane normal directions, respectively.

Material	v_{matrix}	E_{11} [GPa]	E_{22} [GPa]	E_{33} [GPa]	ν_{12}	ν_{23}	ν_{13}	G_{12} [GPa]	G_{23} [GPa]	G_{13} [GPa]
Yarn	0.15	27.486	5.156	5.156	0.183	0.236	0.183	2.548	2.447	2.548
	0.3	27.487	5.350	5.350	0.266	0.419	0.266	2.271	2.382	2.271
	0.45	27.530	6.117	6.117	0.365	0.733	0.365	2.048	2.696	2.048

FE models of multi-layered, multiple fiber orientations composites were generated. As the main objective is to achieve monotonic piezoresistive behavior, [0] and [90] layer, which demonstrate the desired behavior as shown in Figure 5.10, are utilized. Additionally, in order to entertain the possibility of developing multi-functional composite materials, all configurations included at least a [90] layer for enhancement of mechanical properties. Specifically, the stacking sequences investigated here were [±55/90], [±55/90_2], [±55/0/90], [±55/90/0] (Figure 7.2). The w_{yarn} and v_{matrix} were maintained at 3 mm and 0.45 respectively. The piezoresistive behaviors of the whole composite and individual layer were computed. This allows the evaluation of the model as a computational tool for the development of GFRP components with desired self-sensing capability.

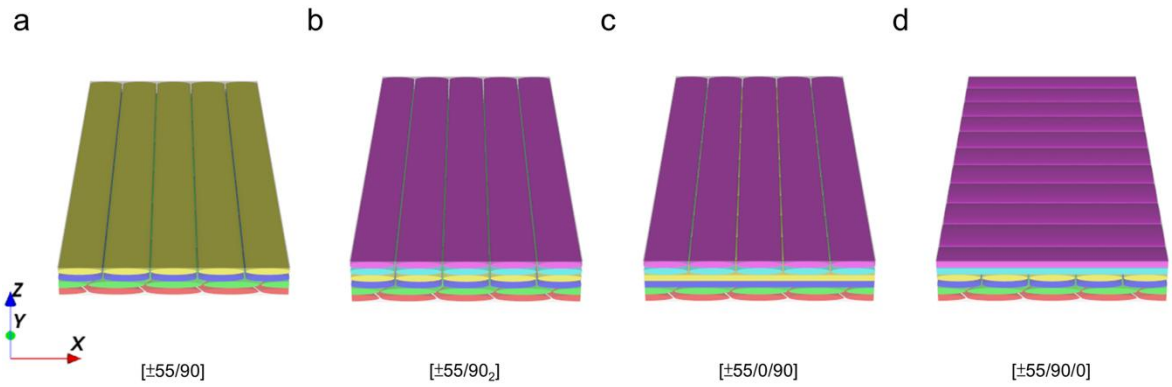

Figure 7.2. 3D mesoscale geometric model of GFRP composites with stacking sequence of a) [±55/90], b) [±55/90_2], c) [±55/0/90], and d) [±55/90/0].

7.3 Results and Discussion

7.3.1 Numerical Results

The effect of yarn width and matrix Poisson's ratio on the resistance change-strain relationship of CNT/GFRP composites with off-axis fibers is explored using the multiscale

model. Figure 7.3 shows the increasing yarn width generally leads to a more pronounced non-monotonic piezoresistive response, likely due to greater fiber-matrix interactions and CNT network reconfigurations. A wider yarn creates more concentrated regions of localized strain, amplifying the transverse compression that induced negative piezoresistive behavior.

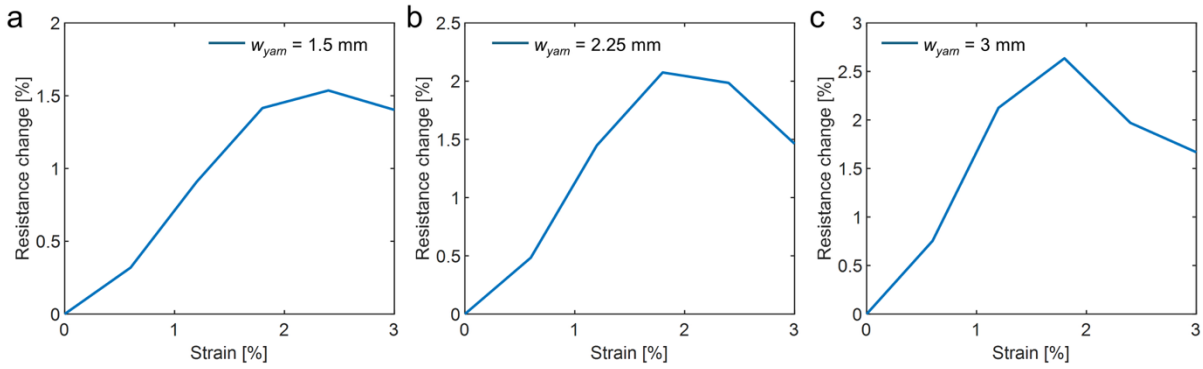

Figure 7.3. Numerical resistance change-stress relationships of [±55] CNT/GFRP composites with w_{yarn} of a) 1.5, b) 2.25, and c) 3 mm under longitudinal (90°) tension.

On the other hand, Figure 7.4 shows that higher Poisson's ratios tend to enhance the non-monotonicity, as the increased lateral contraction of the matrix under tensile loading causes more dramatic changes in the CNT network geometry. This effect is particularly notable in off-axis fiber orientations, where the anisotropic deformation further complicates the strain transfer between fibers and matrix. The interplay between yarn width and matrix properties causes complex and multifaceted piezoresistive behavior in CNT/GFRP composites. Both w_{yarn} and v_{matrix} influence the monotony of the piezoresistive behavior. Although narrower yarns and lower Poisson's ratios generally improve the monotony, the piezoresistive behavior remains nonmonotonic. This suggests that adjusting these material parameters may be insufficient for the design of advanced composite material with desired piezoresistive behavior.

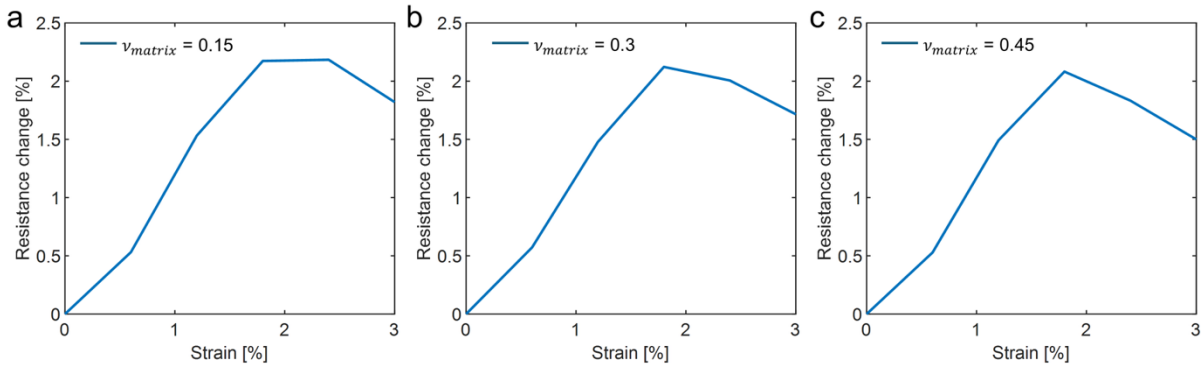

Figure 7.4. Numerical resistance change-stress relationships of [±55] CNT/GFRP composites with ν_{matrix} of a) 0.15, b) 0.3, and c) 0.45 under longitudinal (90°) tension.

The multiscale model is applied to predict the piezoresistive behavior of composites with [±55/90], [±55/90_2], [±55/0/90], [±55/90/0] stacking sequences. Although the piezoresistive behavior of whole composite remains non-monotonic in these layups, it is possible to achieve monotonic piezoresistive behavior in the [0] and [90] layers in the [±55/0/90], and the [0] layer in the [±55/90/0] configurations (Figure 7.5). It can be taken from these results that [0] layer is required for monotonic piezoresistive behavior, likely due to them acting as reinforcement to suppress transverse compression.

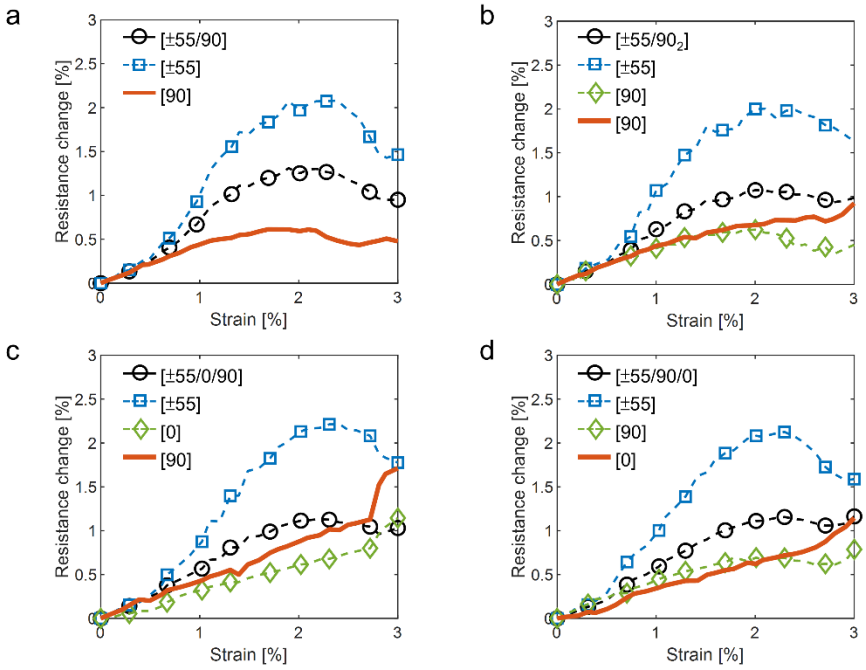

Figure 7.5. Numerical resistance change-stress relationships of CNT/GFRP composites with stacking sequence of a) [±55/90], b) [±55/90$_2$], c) [±55/0/90], and d) [±55/90/0] under longitudinal (90°) tension.

7.3.2 Experimental Validations

In order to validate the numerical results, multi-layered composite tubes were prepared, and electromechanical responses of the specimens were investigated. Using the [±55] filament wound composite tubes, unidirectional glass fiber fabrics were cut to the same width as the ring specimens (20 mm), then wetted with the epoxy resin or CNT/epoxy mixture and wrapped around the ring specimens to fabricate [±55/90], [±55/90$_2$], [±55/0/90], and [±55/90/0] multi-layered composite tubes. Only the outermost layers, which were assigned as the sensing components, were wetted with CNT/epoxy mixture. CNT/epoxy mixture was prepared as described in Chapter 5.2.1. The same epoxy resin was used while multi-walled CNTs from Sigma-Aldrich (purity: >95%, outer diameter: 50–90 nm, aspect ratio: >100) were used. The CNT content is fixed at 0.3 wt. % based on the results in CHAPTER 3.

The evaluation of the self-sensing capability of CNT/GFRP composite tubes with different stacking sequences under hoop tension was undertaken. The self-sensing tubes exhibited distinct resistance change-stress relationships with different stacking sequences, as shown in Figure 7.6. For the [±55/90] tube, the resistance increased up to about 50 MPa, then inversion in piezoresistivity occurred and resistance decreased with stress. Even with an additional [90] layer, the piezoresistive behavior of the [$\pm55/90_2$] tube remained nonmonotonic although the strength is significantly enhanced. Only when a [0] layer is added, the monotony of piezoresistive behavior improved. When the [0] layer was in the middle and the [90] layup was the sensing component, the critical strain remained at about 50 MPs, but the subsequent decrease in resistance was apparently less than the [$\pm55/90_n$] tubes. The optimal stacking sequence was [±55/90/0] as it exhibited monotonic piezoresistive behavior, which is desired for self-sensing purpose. It can be taken from these results that through combinations of cross-ply and [±55] stack-ups, improvements in both monotony of piezoresistive behavior and mechanical properties can be achieved. Nevertheless, the [±55/90/0] tube exhibited better self-sensing performance (monotonic) than the [±55/0/90] tube (nonmonotonic). This suggests the [0] layer should be used as the sensing components for multi-functional multi-layered GFRP composite tubes.

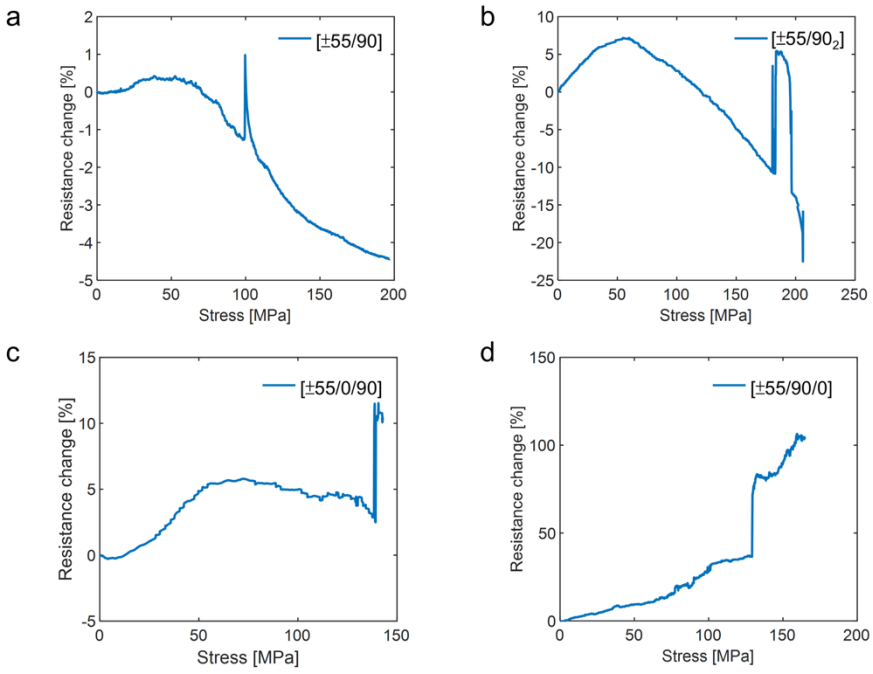

Figure 7.6. Experimental resistance change-stress relationships of CNT/GFRP composite tubes with stacking sequence of a) [±55/90], b) [±55/90$_2$], c) [±55/0/90], and d) [±55/90/0] under split-disk tests.

The piezoresistive behaviors obtained from the numerical model and experimental results show acceptable qualitative agreement. The [±55/90$_n$] configurations exhibited nonmonotonic piezoresistive behaviors in numerical and experimental results, indicating [90] layer is ineffective for improvement in monotony. The numerical and experimental results differed for the [±55/90/0] configuration. While the multiscale model predicted monotonic piezoresistive behavior in the cross-ply layers, the experimental results revealed a nonmonotonic one from the [90] layer. This further supports the ineffectiveness in piezoresistive monotony improvement of [90] layer. The discrepancy between experimental and numerical results can be attributed mainly to oversimplifications in the numerical model, including geometry (planar vs non-planar), CNT characteristics (e.g., waviness), and self-consistent clustering. On the other hand, the numerical results successfully predicted the monotonic piezoresistive behavior

of [0] layer, which demonstrates to a certain degree that the multiscale model (with further optimizations) can be a computational tool aiding the design of advanced composite materials for self-sensing purpose.

Tensile hoop strengths of the composite tubes with different stacking sequences are compared in Figure 7.7. The strengths of [±55/90] and [±55/90_2] samples were higher than that of [±55] by 115.8% and 131.2% respectively. On the other hand, the improvements of [±55/0/90] and [±55/90/0] samples were 53.2% and 60.0% respectively. It is obvious that the [90] layer, which aligns with the direction of loading, provides mechanical reinforcement to the composite tubes.

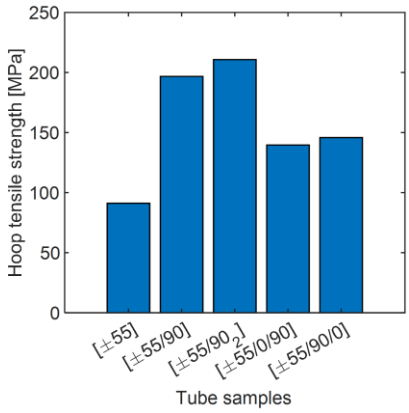

Figure 7.7. Experimental tensile hoop strengths of CNT/GFRP composite tubes with stacking sequence of [±55], [±55/90], [±55/90_2], [±55/0/90], and [±55/90/0] under split-disk tests.

The resistance change-stress relationships of three different specimens of CNT/GFRP composite tubes with stacking sequence [±55/90/0] under split-disk tests are shown in Figure 7.8, demonstrating the repeatability. Under the applied hoop stress until failure, the resistance responses of the specimens increased gradually at the initial stage, while a step increase in resistance was observed at higher stress levels. In addition, the resistance signal fluctuates beyond the initial smooth increase stage, which likely indicates damage initiation and

propagation in the tubes (Yao et al., 2024). Therefore, two stages can be identified from the resistance change-stress curves. The smooth increase in resistance with stress at the initial stage can be attributed to elastic deformation under internal pressure load applied through split-disk. At later stage with higher internal pressure, obvious fluctuations were observed in the resistance signals, with step increases at certain stress levels. The fluctuations can be associated with damage initiation in the form of small matrix cracking (Y. Li, Wang, and Su 2018). The step increase signals the first major damage, which may be interfacial failure in the composite tube. The fluctuations become more aggressive approaching failure, due to damage propagation and development into severe fiber damages like cracking and breaking. The stacking sequence [±55/90/0] shows promise for practical sensing applications.

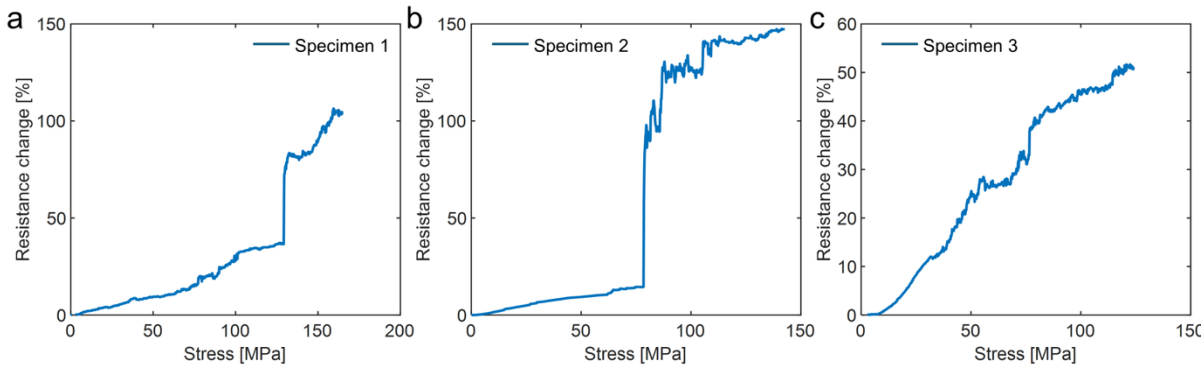

Figure 7.8. Experimental resistance change-stress relationships of three different specimens of CNT/GFRP composite tubes with stacking sequence [±55/90/0] under split-disk tests.

7.4 Conclusion

This chapter explores the design of CNT/GFRP composites with self-sensing capability for structural health monitoring. Multiscale FE modeling was used to investigate the effects of yarn width, matrix Poisson's ratio, and stacking sequence on the piezoresistive behavior of the

composites. The numerical results suggest that narrower yarns and lower matrix Poisson's ratios improve the monotony of the piezoresistive behavior, but adjusting these parameters alone may be insufficient for achieving the desired monotonic response. The inclusion of a [0] layer was found to be crucial for obtaining monotonic piezoresistive behavior using multi-layer, multi-orientation configurations. Experimental validations using multi-layered composite tubes with different stacking sequences confirmed the effectiveness of the [0] layer in improving the monotony of the piezoresistive response. The [±55/90/0] stacking sequence exhibited the best self-sensing performance with a monotonic piezoresistive behavior, demonstrating its potential for practical sensing applications. The study highlights the importance of fiber orientation and stacking sequence in tailoring the mechanical performance and piezoresistive behavior of CNT/GFRP composites for advanced SHM applications.

CHAPTER 8 CONCLUSIONS AND FUTURE WORK

8.1 Summary and Conclusions

This PhD thesis has presented a comprehensive study on the piezoresistive behavior of CNT reinforced epoxy nanocomposites and GFRP composites with strain sensing capability for SHM applications. The first part investigates the piezoresistive behavior of epoxy nanocomposites reinforced with conductive CNTs. This highlights the challenge of achieving monotonic piezoresistivity, which is essential for reliable strain-sensing applications. Through physical experiments and CGMD simulations, the study demonstrates that controlling the initial inter-nanofiller junction geometry can regulate piezoresistive monotony. The curing temperature influences nanofiller mobility and hence the nanoscale conducting network morphology, ultimately affecting the electromechanical responses of the material. This understanding aids in the development of advanced strain-sensing materials with enhanced performance and extended operational ranges by providing a novel approach to control the monotony of the piezoresistive behavior. Understanding and manipulating this behavior is crucial for developing reliable strain-sensing materials, which have wide-ranging applications in fields such as SHM and wearable technology.

The second part explores the piezoresistive properties of GFRP composites with CNT/epoxy nanocomposites as matrices, focusing on the impact of fiber orientation. It is essential to study the impact of fiber orientation, which is a critical performance parameter for FRP composite structures, on the piezoresistive behavior to advance the development of effective self-sensing materials. The experiments reveal that the fiber orientation significantly influenced the self-sensing capabilities of these composites. Non-monotonic piezoresistive behavior is observed, especially when the composites consisted of fibers oriented at 45 °or

similar angles relative to the loading directions. These findings emphasize the need to understand the piezoresistivity mechanisms. Multiscale FEA reveals that the strain distribution heterogeneity varies with fiber orientation, and localized transverse compression may lead to the inversion in piezoresistivity. With highly valuable insights on the microstructural origin of the nonmonotonic piezoresistive behavior in the off-axis CNT/GFRP composites, strategies for tailoring the desired monotonic electromechanical response are proposed. Optimized stacking sequence that contains [0] layer shows encouraging results for developing self-sensing FRP composites. These materials offer a promising solution for reliable, efficient, and multifunctional monitoring systems in engineering structures that utilize FRP composites, enhancing the integrity and safety of civil infrastructure.

The specified and brief conclusions of each main chapter are given below:

1. CHAPTER 3 studied the effect of curing conditions on the piezoresistivity of CNT/epoxy nanocomposites under tensile loading. CNT/epoxy nanocomposite samples with different CNT contents (0.1 wt.%, 0.2 wt.%, and 0.3 wt.%) were prepared under various curing cycles, including room temperature curing followed by post-curing at 60 °C, and direct heat curing at 40-60, 60, and 80 °C. The results showed that the monotony of piezoresistive behavior of the nanocomposites improves with either a reduction in room-temperature curing time or an increase in curing temperature. Samples cured under different cycles exhibited distinct piezoresistive behaviors, with room temperature- and 40-60 °C-cured ones showing nonmonotonic resistance changes and 60 and 80 °C ones demonstrating monotonic piezoresistivity until failure. The findings suggest that the piezoresistivity of CNT/epoxy nanocomposites can be significantly affected by curing conditions, while nanofiller content influences the strain sensitivity but not the monotony of the piezoresistive behavior.

2. CHAPTER 4 elucidated the microstructural origin of nonmonotonic piezoresistive behavior in CNT/epoxy nanocomposites using experiments and CGMD simulations. The experimental results showed that the piezoresistive behavior transitions from nonmonotonic to monotonic with increasing curing temperature. CGMD simulations reproduce this temperature dependence and identify the inter-nanofiller junction geometry as the key microstructural parameter governing the monotony of the piezoresistive behavior. During curing, thermally activated diffusion at high temperatures caused re-agglomeration and direct contact between nanofillers due to van der Waals interactions, leading to monotonic piezoresistivity. At low curing temperatures, re-agglomeration was stimulated during stretching by molecular rearrangements in stress-activated shear transformation zones, resulting in nonmonotonic piezoresistivity. The molecular structure of the polymer matrix also influenced the inter-nanofiller junction geometry and piezoresistive behavior by affecting nanofiller diffusion. Modulating the inter-nanofiller junction geometry enables control over the monotony of piezoresistive behavior in CNT/epoxy nanocomposites.
3. CHAPTER 5 investigated the effect of fiber orientation on the piezoresistive behavior of CNT/GFRP composite laminates and tubes. The samples were fabricated using CNT-dispersed epoxy as the matrix and glass fibers aligned at various angles. The piezoresistive behavior of CNT/GFRP composites is dependent on fiber orientation rather than curing conditions. Laminates and tubes with fibers oriented perpendicular or parallel to the loading direction exhibited monotonic or nearly monotonic piezoresistivity, while those with off-axis fiber orientations demonstrated nonmonotonic behavior. The findings provide valuable insights into designing self-sensing composite structures for SHM applications.

4. CHAPTER 6 investigated the microstructural origin of the fiber orientation-dependent piezoresistive behavior in CNT/GFRP composites using a multiscale FEA based electromechanical framework. The model included microscale for unit cells of yarn and matrix, and mesoscale for geometric pattern of yarn and matrix, involving both mechanical and electrical domains. DIC and FEA revealed that the strain distribution heterogeneity varies with fiber orientation, and localized transverse compression may lead to the inversion in piezoresistivity. The transition from positive to negative piezoresistivity of composites with off-axis fibers was accompanied by increase and then decrease in tunneling distance between CNTs, providing microstructural insights. The monotonic or nearly monotonic positive piezoresistive behaviors of composites with parallel or perpendicular fibers were attributed to the increase in tunneling distance under CNT separation. The study highlights the intricate relationship between fiber orientation, deformation mechanisms, and CNT network reconfiguration in CNT/GFRP composites under tensile loading, providing valuable mechanistic insights for the piezoresistive behavior of nano-engineered FRP composites.
5. CHAPTER 7 explored the design of CNT/GFRP composites with tailored self-sensing capability for SHM. Multiscale FE modeling was used to evaluate the effects of yarn width, matrix Poisson's ratio, and stacking sequence on the piezoresistive behavior of the composites. The numerical results suggested that narrower yarns and lower matrix Poisson's ratios improve the monotony of the piezoresistive behavior, but adjusting these parameters alone may be insufficient for achieving the desired monotonic response. The inclusion of [0] layer was found to be crucial for obtaining monotonic piezoresistive behavior. Experimental validations using multi-layered composite tubes with different stacking sequences confirm the effectiveness of the

[0] layer in improving the monotony of the piezoresistive response. The [±55/90/0] stacking sequence exhibited the desired self-sensing performance with a monotonic piezoresistive behavior, demonstrating its potential for practical sensing applications.

8.2 Future work

Based on the mechanistic insights and promising results of this PhD study, some potential future work directions are recommended and elaborated as follows:

1. While curing temperature has been the primary focus for modulating inter-nanofiller junction geometry in this PhD study, alternative approaches to control piezoresistive behavior can be explored in future work. Promising approaches include applying external fields during curing and manipulating nanofiller-nanofiller interactions through functionalization. These strategies offer potential for fine-tuning piezoresistive response, enabling the development of sensitive and reliable piezoresistive polymer nanocomposites for applications in SHM, wearable electronics, and soft robotics.
2. Exploring different polymer matrices beyond epoxy in piezoresistive nanocomposites could advance the field of self-sensing polymer nanocomposites. Alternative matrices like vinyl ester or polyester may offer unique properties, enhancing monotony, sensitivity, or durability. Investigating synergies between various matrices and conductive nanofillers could reveal novel piezoresistive phenomena, expanding the design space for self-sensing polymer nanocomposite materials.
3. The long-term stability and durability of piezoresistive response in CNT/epoxy and CNT/GFRP composites are crucial for their application in sensing technologies and

SHM. Research focusing on evaluating their piezoresistive behavior under various environmental conditions, including temperature, humidity, UV radiation, and chemical exposure is needed for their further development. Studies can also examine their piezoresistive response under cyclic and long-term static loading to evaluate response stability. This comprehensive approach assesses the reliability and longevity of these composites in real-world applications, where they face complex and changing environmental conditions over time.

4. Multifunctional materials for strain sensing offer promising research opportunities. Combining strain sensing with anti-corrosion or thermal management could address multiple engineering challenges. For example, integrating the self-sensing capability with anti-corrosion could enable advanced FRP structures that monitor integrity while providing corrosion resistance, benefiting marine industry. Incorporating thermal management properties could create advanced composites for harsh environments. These multifunctional capabilities could enhance the performance and reliability of FRP composite structures.
5. To enhance the accuracy of the numerical model, expanding the multiscale modeling approach to include interactions between nanofillers and the polymer matrix is essential. This expansion involves integrating molecular-level simulations (e.g., MD simulations) to capture complex nanofiller-polymer interactions, such as vdW forces, electrostatic interactions, and chemical bonding. Ultimately, this enhanced modeling can serve as powerful computational tool for predicting piezoresistvity of nano-engineered FRP composites, facilitating the design of tailored composite materials for SHM applications.

Appendix

A1 Influence of crosslinking dynamics on dynamic percolation by diffusion of nanotubes and inter-nanotube junction geometry

Thermosetting polymers including epoxy resins are featured by a highly crosslinked network structure, which gives rise to the high performance in terms of mechanical properties, thermal properties, and chemical resistance (Gu et al., 2016). Thus, the network structure is expected to be a critical factor for thermosetting epoxy to attain its desired properties when it is directly applied or used as the matrix of composite. However, heterogenous network structure has been probed using microscopy and scattering techniques (Bai, 1985; Gupta, Drzal, Adams, & Omlor, 1985; Morsch, Liu, Lyon, & Gibbon, 2016; Wu & Bauer, 1986). Several lines of evidence have evinced a correlation between the heterogenous microstructure and the properties of neat epoxy and epoxy nanocomposite such as fracture toughness, solvent resistance, and electrical conductivity (Bahrami et al., 2015; Kishi et al., 2007; Sahagun & Morgan, 2012; W. Zhang et al., 2009; X. Zhang et al., 2013).

Chemical and spatial heterogenous in the network structures of epoxies were revealed by small-angle neutron scattering (SANS) measurements in a study of Wu and Bauer (Wu & Bauer, 1986). Gupta et al. (1985) performed a series of electron microscopy, including scanning electron microscopy (SEM), transmission electron microscopy (TEM), and scanning transmission electron microscopy (STEM), on fracture surfaces and microtomed sections of DGEBA epoxy cured with *m*-phenylenediamine (*m*PDA) in different ratios with or without post-curing. Nodular morphology or heterogeneities of sizes in the range of 5-100 nm were observed on the microscopic images. Heterogeneities were described as regions of higher and lower degree of crosslinking. The size of the heterogeneity was the smallest at stoichiometric

ratio of resin-to-hardener, attributed to the limited growth of heterogeneities due to rapid curing. This finding suggested that the heterogenies are developed during the curing process and depend on the curing conditions.

The highly crosslinked network structure in epoxy-amine thermosets, which determines the physical properties of the cured resin, have been found to be sensitive to curing conditions (Sahagun & Morgan, 2012). Depending on curing temperature, the molecular network developed could vary in term of homogeneity due to different modes of network growth, which could be detected by monitoring the monomer conversion using real-time transmission near-infrared spectroscopy (NIR) during the curing process. A relatively homogeneous network structure is expected when the microgels formed during the pregelation stage are mainly linear chains. These chains are connected to form a molecular network that spans the whole system at gel point. Then the network starts to grow towards vitrification with the formation of crosslinks evenly distributed in space. Another mode of network growth produces heterogeneities in the network structure. The origin of these nanoscale heterogeneities is the presence of both linear segments and crosslinked microgels during the pregelation stage. The occurrence of crosslinked microgels signifies that crosslinks are formed throughout the curing process, instead of mainly between gel point and vitrification, and concentrated in the regions of network developed from crosslinked microgels. The gel structure and subsequently the network structure would be constructed by domains of higher crosslink density with less crosslinked boundary. It should be noted that the values of curing temperature corresponding to the homogeneity of network structure depend on the curing kinetics and differ between different epoxy systems. For the 3,3'-diaminodiphenyl sulfone (DDS)-cured DGEBA epoxy investigated by Sahagun & Morgan (2012), relatively homogeneous microstructure was found in samples cured at 150 °C while heterogeneities were observed in the atomic force microscopy (AFM) images of samples cured at 90 °C and 185 °C. In a recent study of Morsch et al. (2016),

AFM and infrared (IR) technique were combined to characterize that the spatial heterogeneity in epoxy network structure was related to difference in degree of cross-linking, i.e. chemical heterogeneity. The technique was called AFM-IR. Briefly, AFM and IR mapping are conducted simultaneously on the samples so that topological features can be correlated to chemical functionalities in nanoscale. AFM and SEM images of epoxy phenolic resin samples with different isothermal curing times confirmed that the size of heterogeneity depends on the curing kinetics prior to gelation. AFM-IR measurements revealed that the chemical heterogeneity was consistent with the nodular morphology observed by AFM and SEM.

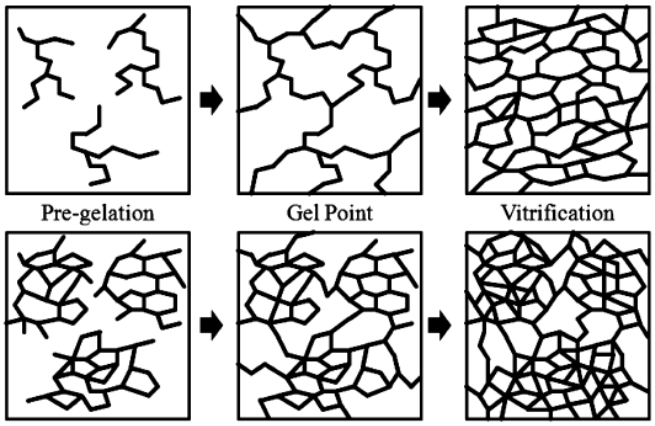

Figure A1. Schematic of two different modes of network growth (Sahagun & Morgan, 2012). (Adapted from Sahagun & Morgan, 2012. Copyright 2025, with permission from American Chemical Society). Top panel shows the growth of a homogeneous network. Bottom panel shows the growth of a heterogeneous network.

The influence of the heterogeneities in the network structure could manifest in the electrical and mechanical properties of the cured epoxies and their composites. Kishi et al. (2007) examined the mechanical and physical properties of dicyandiamide (DICY)-cured DGEBA epoxies with controlled heterogeneities using resin formulations of bimodal molecular weight distribution with different width between the peaks. The differences in viscoelasticity,

solvent resistance, fracture toughness, and ductility could be explained by the size of heterogeneity. Larger heterogeneities lead to lower glass transition temperature (T_g), lower solvent resistance, lower fracture toughness, and lower ductility. Bahrami et al. (2015) performed AFM analysis on TGMDA-amines epoxy system and revealed that difference in degree of curing induced local heterogeneity in degree of cross-linking and hence mechanical response at nanoscale. Zhang et al. (2013) proposed the interphase layer model based on the spatial heterogeneity to explain the difference in percolation dynamics between hexahydro-4-methylphthalic anhydride (HHMPA)-cured DGEBA epoxy nanocomposites with different modes of network growth induced by different catalysts. Crosslinked microgels acted as an interphase layer between the conductive fillers and deteriorated the formation of conductive paths and hence the electrical conductance of the nanocomposite. The thermal sensitivity of the heterogeneity was also noted because increased conductivity was observed when the curing temperature was increased. Zhang et al. (2009) reported that heterogeneous epoxy crosslinking near the nanofillers may produce less crosslinked domains with enhanced molecular mobility and cause the occurrence of crazing in amido-amino-functionalized MWNT (A-MWNT)/DGEBA epoxy composite. Heterogeneity may be localized to the nanotube-matrix interfaces because local curing kinetics may be modified due to the presence of nanofillers. No reduction in macroscale mechanical properties was observed probably due to the localized heterogeneity.

A2 Influence of crosslinking dynamics on dynamic percolation by diffusion of nanotubes and inter-nanotube junction geometry

The observation of a lower free-space length and electrical conductivity in the 100 °C sample compared to the 80 °C sample seems to counter-argue our proposed microstructural origin for the nonmonotonic piezoresistive behavior of CNT/epoxy nanocomposites. It is important to explain this observation in order to validate our claim. A possible explanation is related to the crosslinking dynamics of the epoxy as the network development process determines the physical environment experienced by the nanotubes undergoing diffusion.

Fourier-transform infrared (FTIR) spectroscopy was used to monitor monomer conversion during the curing process of the epoxy and gain insight into the crosslinking dynamics of the matrix DER332/polyetheramine system (Aoki, Shundo, Kuwahara, Yamamoto, & Tanaka, 2019b; Sahagun & Morgan, 2012). Upon mixing the epoxy resin and diamine hardener in a molar ratio of 2:1, the reaction between the epoxy group and the primary amino group forms a secondary amino group (linear segment). Further reaction between another epoxy group and a secondary amino group produces a tertiary amino group (crosslinking). The concentrations of epoxy groups ([E]), primary ([A_1]), secondary ([A_2]), and tertiary amino groups ([A_3]) can be estimated based on the absorbance changes at approximately 4532 and 4940 cm^{-1}, which correspond to the epoxy and primary amino groups, respectively, according to the Lambert-Beer law. As shown in Figure A2a, both the epoxy group and primary amino group bands clearly decreased with curing time. The concentrations of all the monomers at any instant can be determined by

$$[A_2] = [E]_0(\beta B - \alpha) \tag{A1}$$

$$[A_3] = [E]_0\left(\alpha - \beta\frac{B}{2}\right) \tag{A2}$$

where $\alpha = \frac{[E]_0 - [E]}{[E]_0}$ is the degree of epoxy conversion, $\beta = \frac{[A_1]_0 - [A_1]}{[A_1]_0}$ is the degree of primary amine conversion, and $B = \frac{2[A_1]_0}{[E]_0}$ is the ratio between the initial concentration of primary amino group and epoxy group. The initial concentration of the epoxy group $[E]_0$ can be calculated from the epoxy equivalent weight (EEW) (Pramanik, Mendon, & Rawlins, 2012), and that of the primary amino group $[A_1]_0$ can be determined from the molar feed ratio between the epoxy and amine hardener. The values of $[A_2]$ and $[A_3]$ were obtained from the experimentally available values of $[E]$ and $[A_1]$ from their respective absorbance bands at 4532 and 4940 cm^{-1} using Equation (A1) and (A2).

Figure A2b compares the epoxy conversion rate of the DER332/polyetheramine/CNT system cured at 60, 70, 80 and 100 °C. The reaction rate apparently increases with curing temperature as indicated by the more rapid increase in epoxy conversion and the shorter time to reach plateau. Specifically, Figure A2c,d show the concentrations of $[A_1]$, $[A_2]$, and $[A_3]$ as functions of curing time for the DER332/polyetheramine/CNT system cured at 80 and 100 °C. The resulting tertiary amino groups (A_3) or crosslinks, which represent the growth of the network structure, increase viscosity and suppress diffusion (Sahagun & Morgan, 2012). It can be observed that the production of crosslink or the development of network structure is more rapid at 100 °C. The $[A_3]$ values level off at 180 and 60 min at 80 and 100 °C respectively. The level-off time of $[A_3]$ is related to the gelation time, which indicates that an infinite molecular network of epoxy is formed, and diffusion ceases (Aoki et al., 2019).

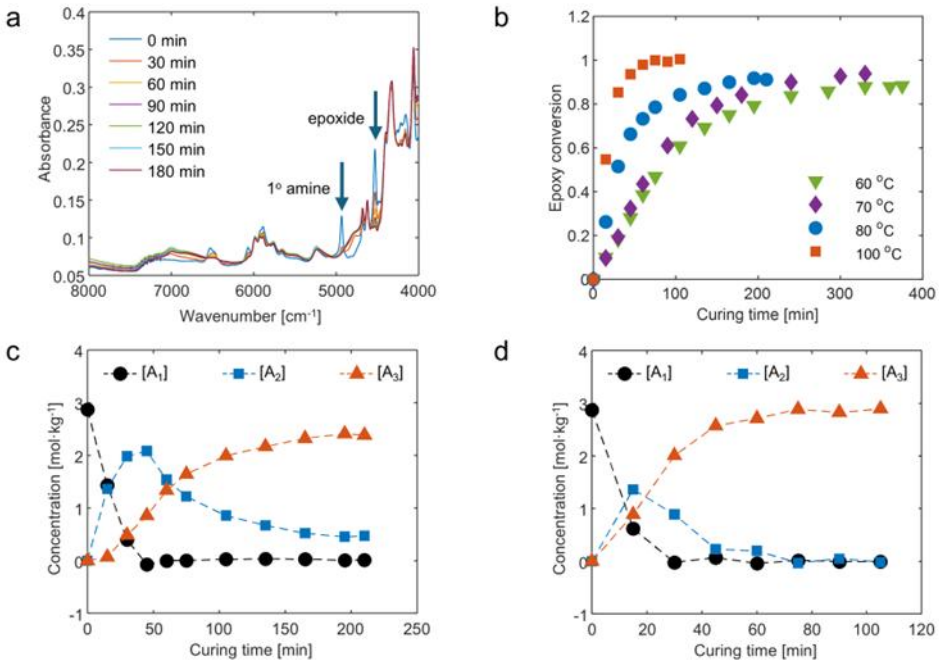

Figure A2. FTIR results of the curing process of DER332/polyetheramine/CNT mixture. a) Time evolution of FTIR spectra for the curing process of DER332/polyetheramine/CNT mixture. b) Epoxy conversion against curing time for the DER332/polyetheramine/CNT mixture at 60, 70, 80 and 100 °C. c,d) Concentration of primary, secondary, and tertiary amino groups against curing time at 80 and 100 °C.

Epoxy curing is a chemical crosslinking process that leads to a continuous increase in viscosity. The nanotubes are mobile and form more connected networks in the low-viscosity stage of the curing cycle before crosslinking halts the movement of nanotubes, and thus, the dynamic percolation process (Boland et al., 2016; X. Zhang et al., 2013). Although a higher temperature can enhance molecular mobility and promote the formation of a percolation network, it simultaneously increases the rate of crosslinking and prematurely suppresses dynamic percolation. Therefore, the lower free-space length and electrical conductivity may be attributed to the shorter time window for the barrier-crossing events that drive the changes in inter-nanotube junction geometry at 100 °C. This may also account for the lower sensitivity of the 100 °C sample.

References

Adekomaya, O., & Adama, K. (2017). Glass-fibre Reinforced Composites: The Effect of Fibre Loading and Orientation on Tensile and Impact Strength. *Nigerian Journal of Technology*, *36*, 782–787.

Alamusi, Hu, N., Fukunaga, H., Atobe, S., Liu, Y., & Li, J. (2011). Piezoresistive strain sensors made from carbon nanotubes based polymer nanocomposites. *Sensors*, *11*, 10691–10723.

Alian, A. R., & Meguid, S. A. (2019). Multiscale modeling of the coupled electromechanical behavior of multifunctional nanocomposites. *Composite Structures*, *208*, 826–835.

Al-Solamy, F. R., Al-Ghamdi, A. A., & Mahmoud, W. E. (2012). Piezoresistive behavior of graphite nanoplatelets based rubber nanocomposites. *Polymers for Advanced Technologies*, *23*, 478–482.

Amjadi, M., Kyung, K. U., Park, I., & Sitti, M. (2016). Stretchable, Skin-Mountable, and Wearable Strain Sensors and Their Potential Applications: A Review. *Advanced Functional Materials*, *26*, 1678–1698.

Aoki, M., Shundo, A., Kuwahara, R., Yamamoto, S., & Tanaka, K. (2019). Mesoscopic Heterogeneity in the Curing Process of an Epoxy-Amine System. *Macromolecules*, *52*, 2075–2082.

Aramoon, A., Breitzman, T. D., Woodward, C., & El-Awady, J. A. (2016). Coarse-Grained Molecular Dynamics Study of the Curing and Properties of Highly Cross-Linked Epoxy Polymers. *Journal of Physical Chemistry B*, *120*, 9495–9505.

Arash, B., Park, H. S., & Rabczuk, T. (2015). Mechanical properties of carbon nanotube reinforced polymer nanocomposites: A coarse-grained model. *Composites Part B: Engineering*, *80*, 92–100.

Avilés, F., Oliva-Avilés, A. I., & Cen-Puc, M. (2018). Piezoresistivity, Strain, and Damage Self-Sensing of Polymer Composites Filled with Carbon Nanostructures. *Advanced Engineering Materials*, *20*, 1–23.

Bahrami, A., Morelle, X., Hông Minh, L. D., Pardoen, T., Bailly, C., & Nysten, B. (2015). Curing dependent spatial heterogeneity of mechanical response in epoxy resins revealed by atomic force microscopy. *Polymer*, *68*, 1–10.

Bai, S. J. (1985). Crosslink distribution of epoxy networks studied by small-angle neutron scattering. *Polymer*, *26*, 1053–1057.

Bakir, B., & Hashem, H. (2013). Effect of Fiber Orientation for Fiber Glass Reinforced Composite Material on Mechanical Properties. *International Journal of Mining, Metallurgy & Mechanical Engineering*, *1*, 341–345.

Balasubramaniam, B., Sathiyan, G., Palani, G. S., Iyer, N. R., & Gupta, R. K. (2019). Fiber Reinforced Polymer Nanocomposites for Structural Engineering Applications. *Materials Science and Technology*, 1–20.

Baltopoulos, A., Polydorides, N., Pambaguian, L., Vavouliotis, A., & Kostopoulos, V. (2015). Exploiting carbon nanotube networks for damage assessment of fiber reinforced composites. *Composites Part B: Engineering*, *76*, 149–158.

Bao, W. S., Meguid, S. A., Zhu, Z. H., & Meguid, M. J. (2011). Modeling electrical conductivities of nanocomposites with aligned carbon nanotubes. *Nanotechnology*, *22*, 485704.

Bauhofer, W., & Kovacs, J. Z. (2009). A review and analysis of electrical percolation in carbon nanotube polymer composites. *Composites Science and Technology*, *69*, 1486–1498.

Bazli, M., Zhao, X. L., Bai, Y., Singh Raman, R. K., & Al-Saadi, S. (2019). Bond-slip behaviour between FRP tubes and seawater sea sand concrete. *Engineering Structures*, *197*, 109421.

Beard, S., & Chang, F. K. (1997). Active damage detection in filament wound composite tubes using built-in sensors and actuators. *Journal of Intelligent Material Systems and Structures*, *8*, 891-897

Biswas, S., Deo, B., Patnaik, A., & Satapathy, A. (2011). Effect of fiber loading and orientation on mechanical and erosion wear behaviors of glass–epoxy composites. *Polymer Composites*, *32*, 665–674.

Böger, L., Wichmann, M. H. G., Meyer, L. O., & Schulte, K. (2008). Load and health monitoring in glass fibre reinforced composites with an electrically conductive nanocomposite epoxy matrix. *Composites Science and Technology*, *68*, 1886–1894.

Bogusz, P. (2023). Digital Image Correlation Analysis of Strain Fields in Fibre-Reinforced Polymer–Matrix Composite under ±45° Off-Axis Tensile Testing. *Polymers*, *15*, 2846.

Boland, C. S., Khan, U., Ryan, G., Barwich, S., Charifou, R., Harvey, A., … Coleman, J. N. (2016). Sensitive electromechanical sensors using viscoelastic graphene-polymer nanocomposites. *Science*, *354*, 1257–1260.

Brown, L. P., & Long, A. C. (2020). Modeling the geometry of textile reinforcements for composites: TexGen. In *Composite Reinforcements for Optimum Performance* (2nd ed.). Elsevier Ltd.

B̈üttiker, M., Imry, Y., Landauer, R., & Pinhas, S. (1985). Generalized many-channel conductance formula with application to small rings. *Physical Review B*, *31*, 6207–6215.

Cao, P., Short, M. P., & Yip, S. (2019). Potential energy landscape activations governing plastic flows in glass rheology. *Proceedings of the National Academy of Sciences of the United States of America*, *116*, 18790–18797.

Cao, X., Wei, X., Li, G., Hu, C., Dai, K., Guo, J., … Guo, Z. (2017). Strain sensing behaviors of epoxy nanocomposites with carbon nanotubes under cyclic deformation. *Polymer*, *112*, 1–9.

Cattin, C., & Hubert, P. (2014). Piezoresistance in polymer nanocomposites with high aspect ratio particles. *ACS Applied Materials and Interfaces*, *6*, 1804–1811.

Cawley, P. (2018). Structural health monitoring: Closing the gap between research and industrial deployment. *Structural Health Monitoring*, *17*, 1225–1244.

Chevalier, J., Brassart, L., Lani, F., Bailly, C., Pardoen, T., & Morelle, X. P. (2018). Unveiling the nanoscale heterogeneity controlled deformation of thermosets. *Journal of the Mechanics and Physics of Solids*, *121*, 432–446.

Chou, T. W., Gao, L., Thostenson, E. T., Zhang, Z., & Byun, J. H. (2010). An assessment of the science and technology of carbon nanotube-based fibers and composites. *Composites Science and Technology*, *70*, 1-19

Chowdhury, S. C., Elder, R. M., Sirk, T. W., & Gillespie, J. W. (2020). Epoxy resin thermo-mechanics and failure modes: Effects of cure and cross-linker length. *Composites Part B: Engineering*, *186*, 107814.

Chung, D. D. L. (2020). A critical review of piezoresistivity and its application in electrical-resistance-based strain sensing. *Journal of Materials Science*, *55*, 15367–15396.

Ci, L., & Bai, J. B. (2006). The reinforcement role of carbon nanotubes in epoxy composites with different matrix stiffness. *Composites Science and Technology*, *66*, 599–603.

Cook, W. D., Forrest, M., & Goodwin, A. A. (1999). A simple method for the measurement of polymerization shrinkage in dental composites. *Dental Materials*, *15*, 447–449.

Cubuk, E. D., Ivancic, R. J. S., Schoenholz, S. S., Strickland, D. J., Basu, A., Davidson, Z. S., … Liu, A. J. (2017). Structure-property relationships from universal signatures of plasticity in disordered solids. *Science*, *358*, 1033–1037.

Dai, G., & Mishnaevsky, L. (2015). Carbon nanotube reinforced hybrid composites: Computational modeling of environmental fatigue and usability for wind blades. *Composites Part B: Engineering*, *78*, 349–360.

de Villoria, R. G., Miravete, A., Cuartero, J., Chiminelli, A., & Tolosana, N. (2006). Mechanical properties of SWNT/epoxy composites using two different curing cycles. *Composites Part B: Engineering*, *37*, 273–277.

De Vivo, B., Lamberti, P., Spinelli, G., Tucci, V., Vertuccio, L., & Vittoria, V. (2014). Simulation and experimental characterization of polymer/carbon nanotubes composites for strain sensor applications. *Journal of Applied Physics*, *116*, 054307.

Elmasry, A., Azoti, W., El-Safty, S. A., & Elmarakbi, A. (2023). A comparative review of multiscale models for effective properties of nano- and micro-composites. *Progress in Materials Science*, *132*, 101022.

Faiella, G., Antonucci, V., Buschhorn, S. T., Prado, L. A. S. A., Schulte, K., & Giordano, M. (2012). Tailoring the electrical properties of MWCNT/epoxy composites controlling processing conditions. *Composites Part A: Applied Science and Manufacturing*, *43*, 1441–1447.

Falk, M. L., & Langer, J. S. (1998). Dynamics of viscoplastic deformation in amorphous solids. *Physical Review E*, *57*, 7192–7205.

Fernberg, P., Nilsson, G., & Joffe, R. (2009). Piezoresistive performance of long-fiber composites with carbon nanotube doped matrix. *Journal of Intelligent Material Systems and Structures*, *20*, 1017–1023.

Ferreira, L. M., Graciani, E., & París, F. (2019). Predicting failure load of a non-crimp fabric composite by means of a 3D finite element model including progressive damage. *Composite Structures*, *225*, 111115.

Frigione, M., & Lettieri, M. (2018). Durability issues and challenges for material advancements in FRP employed in the construction industry. *Polymers*, *10*, 247.

Fu, S., Sun, Z., Huang, P., Li, Y., & Hu, N. (2019). Some basic aspects of polymer nanocomposites: A critical review. *Nano Materials Science*, *1*, 2–30.

Gao, L., Thostenson, E. T., Zhang, Z., & Chou, T. W. (2009). Sensing of damage mechanisms in fiber-reinforced composites under cyclic loading using carbon nanotubes. *Advanced Functional Materials*, *19*, 123–130.

Gao, Y., Cao, D., Liu, J., Shen, J., Wu, Y., & Zhang, L. (2015). Molecular dynamics simulation of the conductivity mechanism of nanorod filled polymer nanocomposites. *Physical Chemistry Chemical Physics*, *17*, 22959–22968.

Gao, Y., Liu, J., Shen, J., Zhang, L., Guo, Z., & Cao, D. (2014). Uniaxial deformation of nanorod filled polymer nanocomposites: A coarse-grained molecular dynamics simulation. *Physical Chemistry Chemical Physics*, *16*, 16039–16048.

Gbaguidi, A., & Kim, D. (2018). Monte Carlo Model for Piezoresistivity of Hybrid Nanocomposites. *Journal of Engineering Materials and Technology*, *140*, 1–11.

Gbaguidi, A., Namilae, S., & Kim, D. (2019). Stochastic percolation model for the effect of nanotube agglomeration on the conductivity and piezoresistivity of hybrid nanocomposites. *Computational Materials Science*, *166*, 9–19.

Ge, T., Kalathi, J. T., Halverson, J. D., Grest, G. S., & Rubinstein, M. (2017). Nanoparticle Motion in Entangled Melts of Linear and Nonconcatenated Ring Polymers. *Macromolecules*, *50*, 1749–1754.

Gholizadeh, S. (2016). A review of non-destructive testing methods of composite materials. *Procedia Structural Integrity*, *1*, 50–57.

Girifalco, L. A., Hodak, M., & Lee, R. S. (2000). Carbon nanotubes, buckyballs, ropes, and a universal graphitic potential. *Physical Review B*, *62*, 13104–13110.

Godara, A., & Raabe, D. (2007). Influence of fiber orientation on global mechanical behavior and mesoscale strain localization in a short glass-fiber-reinforced epoxy polymer composite during tensile deformation investigated using digital image correlation. *Composites Science and Technology*, *67*, 2417–2427.

Gonabadi, H., Oila, A., Yadav, A., & Bull, S. (2022). Investigation of anisotropy effects in glass fibre reinforced polymer composites on tensile and shear properties using full field strain measurement and finite element multi-scale techniques. *Journal of Composite Materials*, *56*, 507–524.

Gong, S., Wu, D., Li, Y., Jin, M., Xiao, T., Wang, Y., … Li, Z. (2018). Temperature-independent piezoresistive sensors based on carbon nanotube/polymer nanocomposite. *Carbon*, *137*, 188–195.

Gong, S., & Zhu, Z. H. (2014). On the mechanism of piezoresistivity of carbon nanotube polymer composites. *Polymer*, *55*, 4136–4149.

Grabowski, K., Zbyrad, P., Uhl, T., Staszewski, W. J., & Packo, P. (2017). Multiscale electro-mechanical modeling of carbon nanotube composites. *Computational Materials Science*, *135*, 169–180.

Gu, H., Ma, C., Gu, J., Guo, J., Yan, X., Huang, J., … Guo, Z. (2016). An overview of multifunctional epoxy nanocomposites. *Journal of Materials Chemistry C*, *4*, 5890–5906.

Guadagno, L., Lamberti, P., Tucci, V., & Vertuccio, L. (2021). Self-sensing nanocomposites for structural applications: Choice criteria. *Nanomaterials*, *11*, 1–13.

Güemes, A., Fernandez-Lopez, A., Pozo, A. R., & Sierra-Pérez, J. (2020). Structural Health Monitoring for Advanced Composite Structures: A Review. *Journal of Composites Science*, *4*, 13.

Gupta, V. B., Drzal, L. T., Adams, W. W., & Omlor, R. (1985). An electron microscopic study of the morphology of cured epoxy resin. *Journal of Materials Science*, *20*, 3439–3452.

Haghgoo, M., Ansari, R., Hassanzadeh-Aghdam, M. K., & Nankali, M. (2022). A novel temperature-dependent percolation model for the electrical conductivity and piezoresistive sensitivity of carbon nanotube-filled nanocomposites. *Acta Materialia*, *230*, 117870.

Haghgoo, M., Ansari, R., Kazem Hassanzadeh-Aghdam, M., Tian, L., & Nankali, M. (2022). Analytical formulation of the piezoresistive behavior of carbon nanotube polymer nanocomposites: The effect of temperature on strain sensing performance. *Composites Part A: Applied Science and Manufacturing*, *163*, 107244.

Hakim, M. L., Nafianto, R., Nugraha, A. D., Wiranata, A., Supriyanto, E., Nugroho, G., & Muflikhun, M. A. (2024). Advanced FEA simulation of GFRP and CFRP responses to low velocity impact: Exploring impactor diameter variations and damage mechanisms. *Composites Part C: Open Access*, *15*, 100541.

Han, J., Sun, L., Li, L., Huang, B., Yang, X., & Wang, T. (2018). 3D Numerical Model for Prediction of Percolation Threshold and Piezoresistive Characteristics of Conductive Polymer Filled With CNT. *ASME 2018 International Mechanical Engineering Congress and Exposition*. 86528

Heider, D., Pandey, G., & Thostenson, E. T. (2016). *Patent No. US9329021B1*. United States.

Homa, L., Sannamani, M., Thomas, A. J., Tallman, T. N., & Wertz, J. (2023). Enhanced damage imaging in three-dimensional composite structures via electrical impedance tomography with mixed and level set regularization. *NDT & E International*, *137*, 102830.

Hoy, R. S., & Robbins, M. O. (2006). Strain hardening of polymer glasses: Effect of entanglement density, temperature, and rate. *Journal of Polymer Science, Part B: Polymer Physics*, *44*, 3487-3500.

Hu, B., Hu, N., Li, J., Alamusi, Liu, Y., Ning, H., & Wu, L. (2012). Numerical simulations on piezoresistivity of nanofiller and polymer based nanocomposites. *ECCOMAS 2012 - European Congress on Computational Methods in Applied Sciences and Engineering, e-Book Full Papers*, 7162–7175.

Hu, N., Karube, Y., Arai, M., Watanabe, T., Yan, C., Li, Y., … Fukunaga, H. (2010). Investigation on sensitivity of a polymer/carbon nanotube composite strain sensor. *Carbon*, *48*, 680–687.

Hu, N., Karube, Y., Yan, C., Masuda, Z., & Fukunaga, H. (2008). Tunneling effect in a polymer/carbon nanotube nanocomposite strain sensor. *Acta Materialia*, *56*, 2929–2936.

Hu, N., Masuda, Z., Yamamoto, G., Fukunaga, H., Hashida, T., & Qiu, J. (2008). Effect of fabrication process on electrical properties of polymer/multi-wall carbon nanotube nanocomposites. *Composites Part A: Applied Science and Manufacturing*, *39*, 893–903.

Iquilio, R., Valín, J. L., Villalobos, K., Núñez, S., González, Á., & Valin, M. (2024). Influence of Fiber Orientation on Mechanical Response of Jute Fiber-Reinforced Polymer Composites. *Polymers*, *16*, 2573.

Jia, X., Zhu, J., Li, W., Chen, X., & Yang, X. (2015). Compressive and tensile response of CFRP cylinders induced by multi-walled carbon nanotubes. *Composites Science and Technology*, *110*, 35–44.

Jin, L., Chortos, A., Lian, F., Pop, E., Linder, C., Bao, Z., & Cai, W. (2018). Microstructural origin of resistance-strain hysteresis in carbon nanotube thin film conductors. *Proceedings of the National Academy of Sciences of the United States of America*, *115*, 1986–1991.

Jung, S., Choi, H. W., Mocanu, F. C., Shin, D. W., Chowdhury, M. F., Han, S. D., … Kim, J. M. (2019). Modeling Electrical Percolation to optimize the Electromechanical Properties of CNT/Polymer Composites in Highly Stretchable Fiber Strain Sensors. *Scientific Reports*, *9*, 1–11.

Kara, M., Kırıcı, M., Tatar, A. C., & Avcı, A. (2018). Impact behavior of carbon fiber/epoxy composite tubes reinforced with multi-walled carbon nanotubes at cryogenic environment. *Composites Part B: Engineering*, *145*, 145–154.

Kaynak, C., Erdiller, E. S., Parnas, L., & Senel, F. (2005). Use of split-disk tests for the process parameters of filament wound epoxy composite tubes. *Polymer Testing*, *24*, 648–655.

Ketter, L., Greb, N., Bernges, T., & Zeier, W. G. (2025). Using resistor network models to predict the transport properties of solid-state battery composites. *Nature Communications*, *16*, 1–9.

Khan, S. U., & Kim, J. K. (2011). Impact and delamination failure of multiscale carbon nanotube-fiber reinforced polymer composites: A review. *International Journal of Aeronautical and Space Sciences*, *12*, 115–133.

Kharchenko, S. B., Douglas, J. F., Obrzut, J., Grulke, E. A., & Migler, K. B. (2004). Flow-induced properties of nanotube-filled polymer materials. *Nature Materials*, *3*, 564–568.

Khare, H. S., & Burris, D. L. (2010). A quantitative method for measuring nanocomposite dispersion. *Polymer*, *51*, 719–729.

Kinloch, I. A., Suhr, J., Lou, J., Young, R. J., & Ajayan, P. M. (2018). Composites with carbon nanotubes and graphene: An outlook. *Science*, *362*, 547–553.

Kishi, H., Naitou, T., Matsuda, S., Murakami, A., Muraji, Y., & Nakagawa, Y. (2007). Mechanical properties and inhomogeneous nanostructures of dicyandiamide-cured epoxy resins. *Journal of Polymer Science, Part B: Polymer Physics*, *45*, 1425-1434.

Koo, G. M., & Tallman, T. N. (2020). Higher-order resistivity-strain relations for self-sensing nanocomposites subject to general deformations. *Composites Part B: Engineering*, *190*, 107907.

Ku-Herrera, J. J., Pacheco-Salazar, O. F., Ríos-Soberanis, C. R., Domínguez-Rodríguez, G., & Avilés, F. (2016). Self-sensing of damage progression in unidirectional multiscale hierarchical composites subjected to cyclic tensile loading. *Sensors*, *16*, 400.

Li, C., & Chou, T. W. (2007). A direct electrifying algorithm for backbone identification. *Journal of Physics A: Mathematical and Theoretical*, *40*, 14679–14686.

Li, C., & Chou, T. W. (2008). Modeling of damage sensing in fiber composites using carbon nanotube networks. *Composites Science and Technology*, *68*, 3373–3379.

Li, C., Thostenson, E. T., & Chou, T. W. (2007). Dominant role of tunneling resistance in the electrical conductivity of carbon nanotube-based composites. *Applied Physics Letters*, *91*, 223114.

Li, C., Thostenson, E. T., & Chou, T. W. (2008). Sensors and actuators based on carbon nanotubes and their composites: A review. *Composites Science and Technology*, *68*, 1227–1249.

Li, H., Liang, J., Zhao, X., Li, Z., Feng, J., Wu, Q., … Guo, Z. (2024). Tensile failure of open-hole composite laminates with yarn gaps: Experimental and numerical study. *Theoretical and Applied Fracture Mechanics*, *131*, 104428.

Li, S., Jeanmeure, L. F. C., & Pan, Q. (2015). A composite material characterisation tool: UnitCells. *Journal of Engineering Mathematics*, *95*, 279–293.

Li, Y. L., Teng, J. G., Zhao, X. L., & Singh Raman, R. K. (2018). Theoretical model for seawater and sea sand concrete-filled circular FRP tubular stub columns under axial compression. *Engineering Structures*, *160*, 71–84.

Li, Y., Liao, Y., & Su, Z. (2018). Graphene-functionalized polymer composites for self-sensing of ultrasonic waves: An initiative towards “sensor-free” structural health monitoring. *Composites Science and Technology*, *168*, 203–213.

Li, Y., Wang, K., & Su, Z. (2018). Dispersed sensing networks in nano-engineered polymer composites: From static strain measurement to ultrasonic wave acquisition. *Sensors*, *18*, 1398.

Li, Y., Wang, K., Wang, Q., Yang, J., Zhou, P., Su, Y., … Su, Z. (2020). Acousto-ultrasonics-based health monitoring for nano-engineered composites using a dispersive graphene-networked sensing system. *Structural Health Monitoring*, *20*, 240-254.

Liang, Y., Wang, H., & Gu, X. (2013). In-plane shear response of unidirectional fiber reinforced and fabric reinforced carbon/epoxy composites. *Polymer Testing*, *32*, 594–601.

Liew, K. M., Pan, Z. Z., & Zhang, L. W. (2019). An overview of layerwise theories for composite laminates and structures: Development, numerical implementation and application. *Composite Structures*, *216*, 240–259.

Liu, C., Ge, J., Zhao, S., Zhang, Q., Liu, X., & Liang, J. (2025). Multiscale analysis method for profiled composite structures considering the forming process. *Journal of the Mechanics and Physics of Solids*, *196*, 106014.

Liu, P. F., & Zheng, J. Y. (2010). Recent developments on damage modeling and finite element analysis for composite laminates: A review. *Materials & Design*, *31*, 3825–3834.

Liu, Z., Bessa, M. A., & Liu, W. K. (2016). Self-consistent clustering analysis: An efficient multi-scale scheme for inelastic heterogeneous materials. *Computer Methods in Applied Mechanics and Engineering*, *306*, 319–341.

López-Santos, F., Hernández-Pérez, A., Ledesma-Orozco, E., & Avilés, F. (2024). Prediction of elastic properties of woven polymer composites using micromechanical models and measured microstructural parameters. *Journal of Reinforced Plastics and Composites*, *0*, 1–17.

Lüpke, F., Eschbach, M., Heider, T., Lanius, M., Schüffelgen, P., Rosenbach, D., … Voigtländer, B. (2017). Electrical resistance of individual defects at a topological insulator surface. *Nature Communications*, *8*, 1–7.

Lyons, A., Devi, A., Hoffer, N. Q., Woodside, M. T., & Ka Shing, L. (2024). Quantifying the Properties of Nonproductive Attempts at Thermally Activated Energy-Barrier Crossing through Direct Observation. *Physical Review X*, *14*, 011017.

Ma, C., Ji, T., Robertson, C. G., Rajeshbabu, R., Zhu, J., & Dong, Y. (2017). Molecular insight into the Mullins effect: Irreversible disentanglement of polymer chains revealed by

molecular dynamics simulations. *Physical Chemistry Chemical Physics*, *19*, 19468–19477.

Malekimoghadam, R., & Icardi, U. (2019). Prediction of mechanical properties of carbon nanotube–carbon fiber reinforced hybrid composites using multi-scale finite element modelling. *Composites Part B: Engineering*, *177*, 107405.

Matos, M. A. S., Pinho, S. T., & Tagarielli, V. L. (2019). Application of machine learning to predict the multiaxial strain-sensing response of CNT-polymer composites. *Carbon*, *146*, 265–275.

Matos, M. A. S., Tagarielli, V. L., Baiz-Villafranca, P. M., & Pinho, S. T. (2018). Predictions of the electro-mechanical response of conductive CNT-polymer composites. *Journal of the Mechanics and Physics of Solids*, *114*, 84–96.

Mayr, S. G. (2006). Activation Energy of Shear Transformation Zones: A Key for Understanding Rheology of Glasses and Liquids. *Physical Review Letters*, *97*, 195501.

Maździarz, M., Rojek, J., & Nosewicz, S. (2018). Molecular dynamics study of self-diffusion in stoichiometric B2-NiAl crystals. *Philosophical Magazine*, *98*, 2257–2274.

Meeuw, H., Viets, C., Liebig, W. V., Schulte, K., & Fiedler, B. (2016). Morphological influence of carbon nanofillers on the piezoresistive response of carbon nanoparticle/epoxy composites under mechanical load. *European Polymer Journal*, *85*, 198–210.

Meng, D., Fan, J., Ma, J., Du, S. W., & Geng, J. (2019). The preparation and functional applications of carbon nanomaterial/conjugated polymer composites. *Composites Communications*, *12*, 64–73.

Montazeri, A., Khavandi, A., Javadpour, J., & Tcharkhtchi, A. (2010). Viscoelastic properties of multi-walled carbon nanotube/epoxy composites using two different curing cycles. *Materials and Design*, *31*, 3383–3388.

Monti, M., Natali, M., Petrucci, R., Kenny, J. M., & Torre, L. (2011). Impact damage sensing in glass fiber reinforced composites based on carbon nanotubes by electrical resistance measurements. *Journal of Applied Polymer Science*, *122*, 2829-2836.

Moreira, L. A., Zhang, G., Müller, F., Stuehn, T., & Kremer, K. (2015). Direct equilibration and characterization of polymer melts for computer simulations. *Macromolecular Theory and Simulations*, *24*, 419–431.

Morsch, S., Liu, Y., Lyon, S. B., & Gibbon, S. R. (2016). Insights into Epoxy Network Nanostructural Heterogeneity Using AFM-IR. *ACS Applied Materials and Interfaces*, *8*, 959–966.

Naghashpour, A., & Hoa, S. Van. (2013). In situ monitoring of through-thickness strain in glass fiber/epoxy composite laminates using carbon nanotube sensors. *Composites Science and Technology*, *78*, 41–47.

Naskar, A. K., Keum, J. K., & Boeman, R. G. (2016). Polymer matrix nanocomposites for automotive structural components. *Nature Nanotechnology*, *11*, 1026–1030.

Nicolas, A., Ferrero, E. E., Martens, K., & Barrat, J.-L. (2018). Deformation and flow of amorphous solids: Insights from elastoplastic models. *Reviews of Modern Physics*, *90*, 045006.

Nofar, M., Hoa, S. V., & Pugh, M. D. (2009). Failure detection and monitoring in polymer matrix composites subjected to static and dynamic loads using carbon nanotube networks. *Composites Science and Technology*, *69*, 1599–1606.

Paliy, M., Trebicky, T., Guo, Q., Kobe, B., Suhan, N., Arsenault, G., … Yang, J. (2016). Nonmonotonic piezoresistive effect in elastomeric composite films. *Journal of Applied Polymer Science*, *133*, 43518.

Panico, M., Narayanan, S., & Brinson, L. C. (2010). Simulations of tensile failure in glassy polymers: Effect of cross-link density. *Modelling and Simulation in Materials Science and Engineering*, *18*, 055005.

Panozzo, F., Zappalorto, M., & Quaresimin, M. (2017). Analytical model for the prediction of the piezoresistive behavior of CNT modified polymers. *Composites Part B: Engineering*, *109*, 53–63.

Papakonstantopoulos, G. J., Doxastakis, M., Nealey, P. F., Barrat, J. L., & De Pablo, J. J. (2007). Calculation of local mechanical properties of filled polymers. *Physical Review E*, *75*, 1–13.

Park, J. M., Kim, D. S., Kim, S. J., Kim, P. G., Yoon, D. J., & DeVries, K. L. (2007). Inherent sensing and interfacial evaluation of carbon nanofiber and nanotube/epoxy composites using electrical resistance measurement and micromechanical technique. *Composites Part B: Engineering*, *38*, 847–861.

Park, J. M., Kwon, D. J., Wang, Z. J., & Devries, K. L. (2015). Review of self-sensing of damage and interfacial evaluation using electrical resistance measurements in nano/micro carbon materials-reinforced composites. *Advanced Composite Materials*, *24*, 197–219.

Pramanik, M., Mendon, S. K., & Rawlins, J. W. (2012). Determination of epoxy equivalent weight of glycidyl ether based epoxides via near infrared spectroscopy. *Polymer Testing*, *31*, 716–721.

Qian, H., Greenhalgh, E. S., Shaffer, M. S. P., & Bismarck, A. (2010). Carbon nanotube-based hierarchical composites: A review. *Journal of Materials Chemistry*, *20*, 4751–4762.

Rahmat, M., & Hubert, P. (2011). Carbon nanotube-polymer interactions in nanocomposites: A review. *Composites Science and Technology*, *72*, 72–84.

Rajak, D., Pagar, D., Menezes, P., & Linul, E. (2019). Fiber-Reinforced Polymer Composites: Manufacturing, Properties, and Applications. *Polymers*, *11*, 1667.

Ramsdale-Capper, R., & Foreman, J. P. (2018). Internal antiplasticisation in highly crosslinked amine cured multifunctional epoxy resins. *Polymer*, *146*, 321–330.

Rana, S., Subramani, P., Fangueiro, R., & Correia, A. G. (2016). A review on smart self-sensing composite materials for civil engineering applications. *AIMS Materials Science*, *3*, 357–379.

Ren, X., Chaurasia, A. K., & Seidel, G. D. (2016). Concurrent multiscale modeling of coupling between continuum damage and piezoresistivity in CNT-polymer nanocomposites. *International Journal of Solids and Structures*, *96*, 340–354.

Ren, X., & Seidel, G. D. (2013). Computational micromechanics modeling of inherent piezoresistivity in carbon nanotube-polymer nanocomposites. *Journal of Intelligent Material Systems and Structures*, *24*, 1459–1483.

Sahagun, C. M., & Morgan, S. E. (2012). Thermal control of nanostructure and molecular network development in epoxy-amine thermosets. *ACS Applied Materials and Interfaces*, *4*, 564–572.

Schell, J. S. U., Renggli, M., van Lenthe, G. H., Müller, R., & Ermanni, P. (2006). Micro-computed tomography determination of glass fibre reinforced polymer meso-structure. *Composites Science and Technology*, *66*, 2016–2022.

Simmons, J. G. (1963). Generalized Formula for the Electric Tunnel Effect between Similar Electrodes Separated by a Thin Insulating Film. *Journal of Applied Physics*, *34*, 1793–1803.

Singh, K. K., & Shrivastava, R. (2023). Influence of fiber orientation on thermo-mechanical response of symmetric glass/epoxy composite. *Journal of the Brazilian Society of Mechanical Sciences and Engineering*, *45*, 1–19.

Spinelli, G., Lamberti, P., Tucci, V., Vertuccio, L., & Guadagno, L. (2018). Experimental and theoretical study on piezoresistive properties of a structural resin reinforced with carbon nanotubes for strain sensing and damage monitoring. *Composites Part B: Engineering*, *145*, 90–99.

Stukowski, A. (2010). Visualization and analysis of atomistic simulation data with OVITO-the Open Visualization Tool. *Modelling and Simulation in Materials Science and Engineering*, *18*, 15012–15019.

Takahashi, Y., Noda, I., & Nagasawa, M. (1985). Zero-Shear Viscosity of Linear Polymer Solutions over a Wide Range of Concentration. *Macromolecules*, *18*, 1002–1008.

Takeda, N., Okabe, Y., & Mizutani, T. (2007). Damage detection in composites using optical fibre sensors. *Proceedings of the Institution of Mechanical Engineers, Part G: Journal of Aerospace Engineering*, *221*, 497–508.

Tallman, T., & Wang, K. W. (2013). An arbitrary strains carbon nanotube composite piezoresistivity model for finite element integration. *Applied Physics Letters*, *102*, 011909.

Taşyürek, M., & Tarakçioğlu, N. (2017). Enhanced fatigue behavior under internal pressure of CNT reinforced filament wound cracked pipes. *Composites Part B: Engineering*, *124*, 23–30.

Taya, M., Kim, W. J., & Ono, K. (1998). Piezoresistivity of a short fiber/elastomer matrix composite. *Mechanics of Materials*, *28*, 53–59.

Tendo Innocent, M., Ma, W., Xiang, H., Zhou, J., Yu, S., & Zhu, M. (2021). Nonmonotonic piezoresistive fibers tuned towards biomechanical sensing. *Materials & Design*, *205*, 109715.

Theodosiou, T. C., & Saravanos, D. A. (2010). Numerical investigation of mechanisms affecting the piezoresistive properties of CNT-doped polymers using multi-scale models. *Composites Science and Technology*, *70*, 1312–1320.

Thirumavalavan, K., & Sarukasan, D. (2022). Experimental investigation on multi-layered filament wound basalt/E-glass hybrid fiber composite tubes. *Materials Research Express*, *9*, 045301.

Thomas, A. J., Kim, J. J., Tallman, T. N., & Bakis, C. E. (2019). Damage detection in self-sensing composite tubes via electrical impedance tomography. *Composites Part B: Engineering*, *177*, 107276.

Thompson, A. P., Aktulga, H. M., Berger, R., Bolintineanu, D. S., Brown, W. M., Crozier, P. S., … Plimpton, S. J. (2022). LAMMPS - a flexible simulation tool for particle-based materials modeling at the atomic, meso, and continuum scales. *Computer Physics Communications*, *271*, 108171.

Thostenson, E. T., & Chou, T. W. (2006). Carbon nanotube networks: Sensing of distributed strain and damage for life prediction and self healing. *Advanced Materials*, *18*, 2837–2841.

Thostenson, E. T., & Chou, T. W. (2008). Real-time in situ sensing of damage evolution in advanced fiber composites using carbon nanotube networks. *Nanotechnology*, *19*, 215713.

Thostenson, E. T., Ren, Z., & Chou, T. W. (2001). Advances in the science and technology of carbon nanotubes and their composites: A review. *Composites Science and Technology*, *61*, 1899–1912.

Tsige, M., Lorenz, C. D., & Stevens, M. J. (2004). Role of network connectivity on the mechanical properties of highly cross-linked polymers. *Macromolecules*, *37*, 8466–8472.

Tsige, M., & Stevens, M. J. (2004). Effect of cross-linker functionality on the adhesion of highly cross-linked polymer networks: A molecular dynamics study of epoxies. *Macromolecules*, *37*, 630–637.

Üstün, T., Eskizeybek, V., & Avci, A. (2016). Enhanced fatigue performances of hybrid nanoreinforced filament wound carbon/epoxy composite pipes. *Composite Structures*, *150*, 124–131.

Üstün, T., Ulus, H., Karabulut, S. E., Eskizeybek, V., Şahin, Ö. S., Avci, A., & Demir, O. (2016). Evaluating the effectiveness of nanofillers in filament wound carbon/epoxy multiscale composite pipes. *Composites Part B: Engineering*, *96*, 1–6.

Vadlamani, V. K., Chalivendra, V. B., Shukla, A., & Yang, S. (2012). Sensing of damage in carbon nanotubes and carbon black-embedded epoxy under tensile loading. *Polymer Composites*, *33*, 1809–1815.

Varshney, V., Patnaik, S. S., Roy, A. K., & Farmer, B. L. (2008). A Molecular Dynamics Study of Epoxy-Based Networks : Cross-Linking Procedure and Prediction of Molecular and Material Properties. *Macromolecules*, *41*, 6837–6842.

Vertuccio, L., Guadagno, L., Spinelli, G., Lamberti, P., Tucci, V., & Russo, S. (2016). Piezoresistive properties of resin reinforced with carbon nanotubes for health-monitoring of aircraft primary structures. *Composites Part B: Engineering*, *107*, 192–202.

Vertuccio, Luigi, Vittoria, V., Guadagno, L., & De Santis, F. (2015). Strain and damage monitoring in carbon-nanotube-based composite under cyclic strain. *Composites Part A: Applied Science and Manufacturing*, *71*, 9–16.

Viets, C., Kaysser, S., & Schulte, K. (2014). Damage mapping of GFRP via electrical resistance measurements using nanocomposite epoxy matrix systems. *Composites Part B: Engineering*, *65*, 80–88.

Vigolo, B., Coulon, C., Maugey, M., Zakri, C., & Poulin, P. (2005). An experimental approach to the percolation of sticky nanotubes. *Science*, *309*, 920–923.

Wang, H. W., Zhou, H. W., Gui, L. L., Ji, H. W., & Zhang, X. C. (2014). Analysis of effect of fiber orientation on Young's modulus for unidirectional fiber reinforced composites. *Composites Part B: Engineering*, *56*, 733–739.

Wang, M., Gurunathan, R., Imasato, K., Geisendorfer, N. R., Jakus, A. E., Peng, J., … Snyder, G. J. (2019). A Percolation Model for Piezoresistivity in Conductor–Polymer Composites. *Advanced Theory and Simulations*, *2*, 1–5.

Wang, Y., Wang, Y., Wan, B., Han, B., Cai, G., & Chang, R. (2018). Strain and damage self-sensing of basalt fiber reinforced polymer laminates fabricated with carbon nanofibers/epoxy composites under tension. *Composites Part A: Applied Science and Manufacturing*, *113*, 40–52.

Wichmann, M. H. G., Buschhorn, S. T., Gehrmann, J., & Schulte, K. (2009). Piezoresistive response of epoxy composites with carbon nanoparticles under tensile load. *Physical Review B*, *80*, 1–8.

Wu, W. li, & Bauer, B. J. (1986). Network structure of epoxies - a neutron scattering study: 2. *Polymer*, *27*, 169–180.

Xie, P., Lin, G., Teng, J. G., & Jiang, T. (2020). Modelling of concrete-filled filament-wound FRP confining tubes considering nonlinear biaxial tube behavior. *Engineering Structures*, *218*, 110762.

Yang, J., Liu, Z., Zhou, Z., Ming, Y., Li, S., Hao, T., & Nie, Y. (2022). Studying the effects of carbon nanotube contents on stretch-induced crystallization behavior of polyethylene/carbon nanotube nanocomposites using molecular dynamics simulations. *Physical Chemistry Chemical Physics*, *24*, 16021–16030.

Yang, Sen, & Chalivendra, V. (2020). Theoretical modeling and experimental validation of electro-shear behavior of carbon nanotubes embedded epoxy nanocomposite. *International Journal of Mechanical Sciences*, *177*, 105594.

Yang, Shaorui, & Qu, J. (2014). Coarse-grained molecular dynamics simulations of the tensile behavior of a thermosetting polymer. *Physical Review E - Statistical, Nonlinear, and Soft Matter Physics*, *90*, 1–8.

Yang, W., Wei, D., Jin, X., & Liao, Q. (2007). Molecular dynamics simulation of the formation of polymer networks. *Macromolecular Theory and Simulations*, *16*, 548–556.

Yao, R., Ge, Z., Wang, D., Shang, N., & Shi, J. (2024). Self-sensing joints for in-situ structural health monitoring of composite pipes: A piezoresistive behavior-based method. *Engineering Structures*, *308*, 118049.

Yin, G., Hu, N., Karube, Y., Liu, Y., Li, Y., & Fukunaga, H. (2011). A carbon nanotube/polymer strain sensor with linear and anti-symmetric piezoresistivity. *Journal of Composite Materials*, *45*, 1315–1323.

Zhang, B., Yu, T., & Teng, J. G. (2015). Behavior of Concrete-Filled FRP Tubes under Cyclic Axial Compression. *Journal of Composites for Construction*, *19*, 04014060.

Zhang, H., Bilotti, E., & Peijs, T. (2015). The use of carbon nanotubes for damage sensing and structural health monitoring in laminated composites: a review. *Nanocomposites*, *1*, 167–184.

Zhang, J., & Zhang, X. (2015). An efficient approach for predicting low-velocity impact force and damage in composite laminates. *Composite Structures*, *130*, 85–94.

Zhang, W., Srivastava, I., Zhu, Y. F., Picu, C. R., & Koratkar, N. A. (2009). Heterogeneity in epoxy nanocomposites initiates crazing: Significant improvements in fatigue resistance and toughening. *Small*, *5*, 1403–1407.

Zhang, X., Sun, H., Yang, C., Zhang, K., Yuen, M. M. F., & Yang, S. (2013). Highly conductive polymer composites from room-temperature ionic liquid cured epoxy resin: Effect of interphase layer on percolation conductance. *RSC Advances*, *3*, 1916–1921.

Zhou, X. W., Jones, R. E., & Gruber, J. (2017). Molecular dynamics simulations of substitutional diffusion. *Computational Materials Science*, *128*, 331–336.

Zhu, R., Pan, E., & Roy, A. K. (2007). Molecular dynamics study of the stress-strain behavior of carbon-nanotube reinforced Epon 862 composites. *Materials Science and Engineering A*, *447*, 51–57.